Oroclines of the Iberian Variscan belt: Tectonic and paleogeographic implications

by

Jessica Shaw
B.Sc., Humboldt State University, 2008

A Dissertation Submitted in Partial Fulfillment
of the Requirements for the Degree of

DOCTOR OF PHILOSOPHY

in the School of Earth and Ocean Sciences

Supervisory Committee

Oroclines of the Iberian Variscan belt: Tectonic and paleogeographic implications

by

Jessica Shaw
B.Sc., Humboldt State University, 2008

Supervisory Committee

Dr. Stephen T. Johnston (School of Earth and Ocean Sciences)
Supervisor

Dr. Dante Canil (School of Earth and Ocean Sciences)
Departmental Member

Dr. Eileen Van der Flier-Keller (School of Earth and Ocean Sciences)
Departmental Member

Dr. Terri Lacourse (Department of Biology)
Outside Member

Abstract

Supervisory Committee
Dr. Stephen T. Johnston (School of Earth and Ocean Sciences)
Supervisor
Dr. Dante Canil (School of Earth and Ocean Sciences)
Departmental Member
Dr. Eileen Van der Flier-Keller (School of Earth and Ocean Sciences)
Outside Member
Dr. Terri Lacourse (Department of Biology)

The Western European Variscan orogenic belt is thought to represent the final in a series of Paleozoic continental collisions that culminated with the amalgamation of the supercontinent Pangea. The Iberian segment of the Variscan belt is characterized by Cantabrian orocline, which is 180º and convex toward the west. Several lines of evidence are at odds with classical interpretation of the Cantabrian orocline as the core of the much larger 'Ibero-Armorican' arc, suggesting instead that it is structurally continuous with a second more southerly and complimentary orocline. Paleocurrent data collected from the Lower Ordovician Armorican Quartzite of the deformed Iberian Paleozoic passive margin sequence confirm the existence of the so-called Central Iberian orocline. Structural continuity between the Cantabrian and Central Iberian oroclines suggests that they formed contemporaneously and in the same fashion. Mesoscale vertical-axis folds deforming slaty cleavage and shear fabric within the Ediacaran Narcea Slates have a dominant vergence toward the hinge of the Cantabrian orocline, suggesting that its formation was in part accommodated by a mechanism of flexural shear during buckling of a linear belt in response to an orogen parallel principle compressive stress. The Cantabrian-Central Iberian coupled oroclines therefore palinspastically restore to an originally linear belt 2300 km in length. Provenance analysis of detrital zircons sampled from the Armorican Quartzite along a 1500-km-long segment of the palinplastically restored Iberian passive margin indicate that it originated in a paleogeographic position stretching east-west along the northern limits of north African Gondwana, from the Arabian-Nubian Shield to the Saharan hinterland. Paleomagnetic data and the distribution of Variscan ophiolites support a model of mid-Paleozoic separation of the Variscan autochthon (Armorican continental ribbon) from north Gondwana preceding or in conjunction with a 90º rotation required to reorient the ribbon to a Late Carboniferous north-south trend. Formation of the Iberian coupled oroclines accommodated 1100 km of orogen parallel shortening. The Western European Variscan belt, North American Cordillera, and Eastern European Alpine system are orogens similarly characterized by both coupled oroclines and paleomagnetic inclinations that are significantly shallower than cratonic reference values. Palinspastic restoration of the Alaskan and Carpathian–Balkan coupled oroclines fully resolves inclination anomalies within the Cordillera and Eastern Alpine system, respectively. Inclination anomalies within the Iberian Variscan belt are only partially resolved through palinspastic restoration of the Iberian coupled oroclines, but the sinuous geometry of the belt is not yet fully deciphered. Oroclines within the Western European Variscan belt, not the orogen itself, provide the true record of Pangean amalgamation.

Table of Contents

List of Tables

List of Figures

Acknowledgments

I am very grateful to my supervisor Stephen Johnston for his mentorship and encouragement, critical insight, open door policy, and initial inspiration for the project at hand. Many thanks to Gabi Gutiérrez-Alonso for his supreme guidance to Spanish culture and geology, and to all my other co-authors for the respective roles they played in bringing this project to completion. I would like to thank my committee members for the thoughtful critiques and questions they have provided throughout the years, and all of those who provided mentorship and/or partnership through all of the teaching opportunities and experiences that I have had at the University of Victoria, from which I have learned so much. These individuals include my committee member Dante Canil, Laurence Coogan, Vera Pospelova, David Nelles, Duncan Johannessen, Kristen Morell, and my supervisor Stephen Johnston. I would like to thank my fellow tectonics graduate students, Duncan McLeish, Laurence Gagnon, Kass del Greco, Travis Dawson, and Gerri McEwen, for their friendship and support. Special thanks are owed to my brother and parents for their tireless encouragement, to Ken Aalto, Lori Dengler, and Brandon Schwab, for the initial push to attend graduate school, and to Sheila-Dale Johnston, for helping me clear countless hurdles, both big and small.

Funding for this project was provided by an NSERC Canada Discovery Grant awarded to Stephen Johnston, the University of Victoria Fellowship Program, a Ministry of Advanced Education Pacific Century Graduate Scholarship awarded through the University of Victoria by the Province of British Colombia, and by a Scholar Award granted by the International Chapter of the P.E.O. Sisterhood. Additional contributions from financial support awarded to co-author and collaborator Gabriel Gutiérrez-Alonso by the Spanish Ministry of Science and Technology through Project Grant O.D.R.E. II ("Oroclines and Delamination: Relations and Effects") CGL2006CGL2009-1367-00902.

Method of Presentation

This thesis is presented as four self-contained papers (Chapters 2, 3, 4 and 5), each contributing to the common goals of deciphering the orogenic geometry of the Iberian Variscan belt and providing insight into the tectonic processes and respective paleogeographic implications of oroclines. This format is intended to facilitate the publication of research presented herein; it does, however, introduce redundancies. Chapters 1 and 6 are introductory and conclusion chapters, respectively. These chapters demonstrate how the self-contained papers form a collective and coherent thesis by outlining the study aims and suggestions for further research. I am the primary author for all manuscripts (Chapters 2, 3, 4 and 5), and each is co-authored by my supervisor, Stephen Johnston. Additional co-author Gabi Gutiérrez-Alonso contributed field assistance and guidance (Chapters 2, 3 and 4), manuscript review (Chapters 2, 3 and 4), and processing of raw zircon isotope data (Chapter 3). Co-author Arlo Weil (Chapter 1) contributed an in field introduction to Spanish regional geology and provided a manuscript review. Co-authors Ulf Linneman and Mandy Hoffman (Chapter 3) provided laboratory assistance and guidance, and co-author Dani Pastor-Galán (Chapter 3) provided assistance with sample processing. Chapter 2 is published in *Earth and Planetary Science Letters*, vol. 329-330, May 2012; Chapter 3 is published in the *Geological Society of America Bulletin*, vol. 126, no. 5-6, May 2014. At the time of submission, Chapter 4 is in press in *Lithosphere* and Chapter 5 is submitted and in review to *Earth-Science Reviews*.

Chapter 1. Introduction

1.1 Presentation of the problem

The Western European Variscan orogenic belt is classically interpreted as having developed during the final collisional stage in the amalgamation of the supercontinent Pangea (Wegener, 1929). Carboniferous continental collision of the southern megacontinent Gondwana with the previously amalgamated Laurussia (Laurentia+Baltica+Avalonia) was achieved following closure of the intervening Rheic Ocean (named for the Titan Rhea of Greek mythology, the sister of Iapetus, who fathered Atlas and gave his name to the ocean that preceded the Atlantic) (e.g. Nance et al., 2010). The Variscan belt extends sinuously across Western Europe and is interpreted to be correlative across the Atlantic and into northwestern Africa, with the Ouachita–Alleghanian and Mauritanide orogens, respectively. Interpretations of the tectonic evolution of the Variscan orogen hinge on a fundamental understanding of the nature and extent of several map-view folds (oroclines) that characterize it. Did the map-view bends develop during Variscan orogenesis and in response to the same regional stress (progressive oroclines), or as 'true' oroclines (*sensu* Carey, 1955) that are secondary features formed subsequent to Variscan orogenesis by lithospheric-scale vertical-axis rotation of an initially linear orogen?

The 180º Cantabrian orocline of the Iberian segment of the Western European Variscan belt is one of the best studied structures of its kind, yet the full geometric extent and developmental nature of the Cantabrian orocline remain topics of debate. Though modern interpretations of Variscan geometry place the Cantabrian orocline at the core of the much larger 'Ibero-Armorican arc' (e.g. Martínez Catalán et al., 2007) (Fig. 1-1), structural and stratigraphic patterns within the Variscan of Iberia are more consistent with an earlier model that predicts the well-exposed convex to the east Cantabrian orocline to be continuous with a more southerly, complementary orocline whose hinge is buried beneath post-Variscan sedimentary cover (Du Toit, 1936). The existence of an *S*-shaped pair of continental-scale coupled Iberian oroclines as implied by Du Toit's interpretation (Fig. 1-2) is difficult to reconcile within the majority of models that interpret the Cantabrian orocline as a

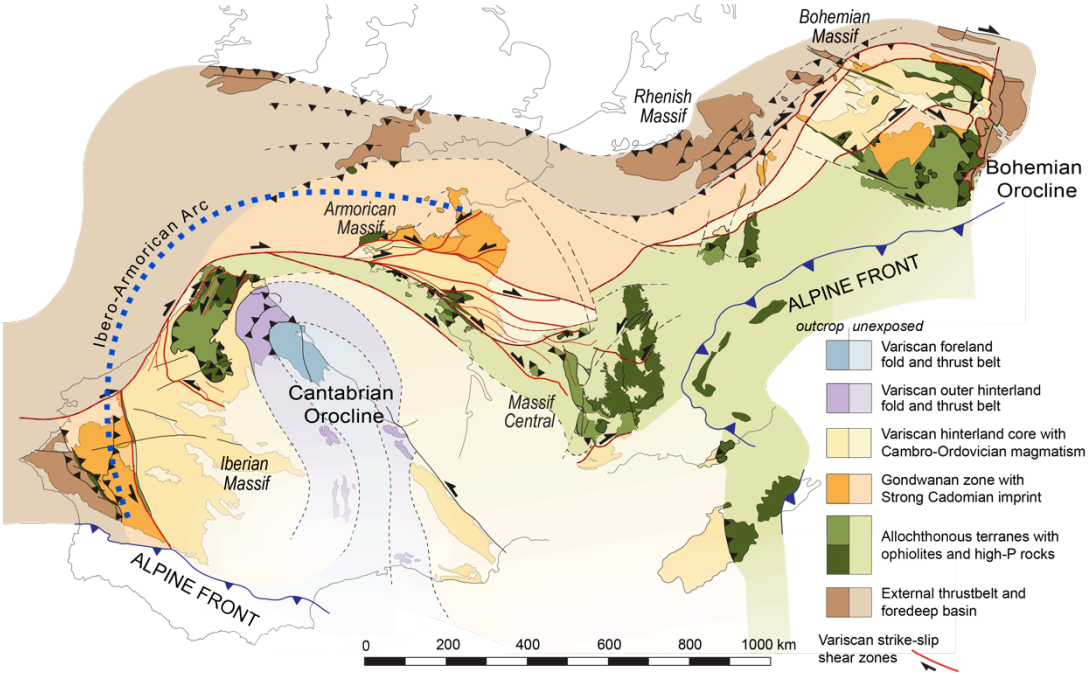

Figure 1-1 Tectonostratigraphic map of the Western European Variscan belt showing the Cantabrian orocline as the core of the larger Ibero-Armorican arc as interpreted by Martínez-Catalán et al. (2007).

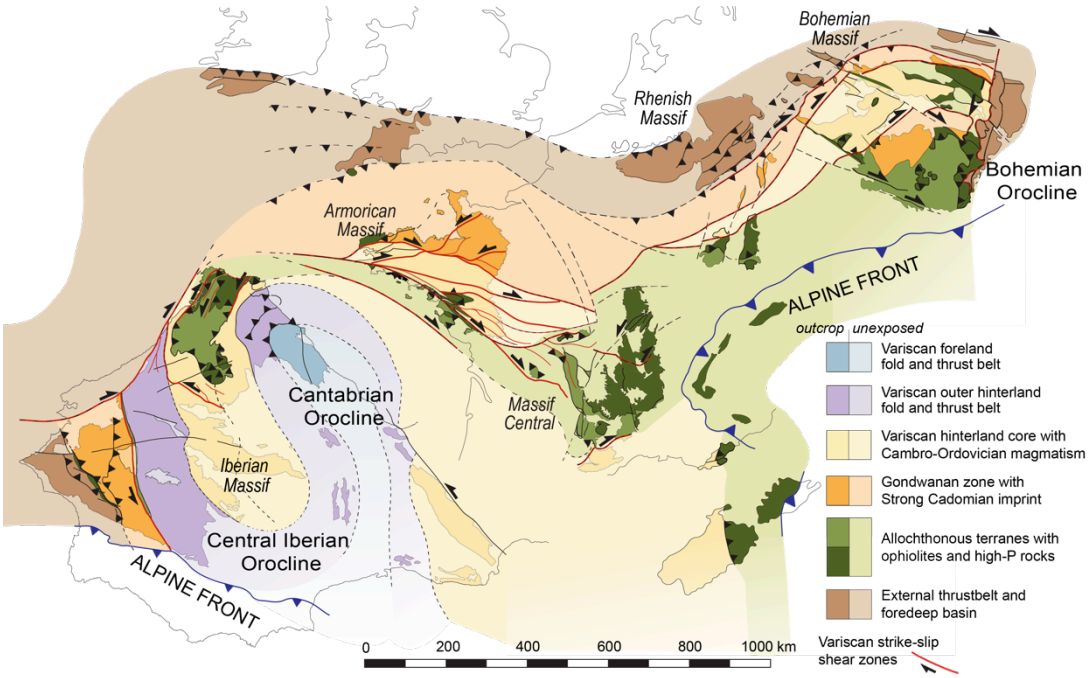

Figure 1-2 Tectonostratigraphic map of the Western European Variscan belt showing the *S*-shaped Iberian coupled oroclines as interpreted by Shaw et al. (2012).

progressive feature developed during Variscan orogenic shortening (Brun and Burg, 1982; Pérez-Estaún et al., 1988; Ribeiro et al., 1995, 2007; Martínez Catalán, 2011). However, an alternative interpretation of the Cantabrian orocline as secondary is supported by conjunctive paleomagnetic and structural studies that document vertical axis-rotations requiring restoration of the Variscan belt to an originally linear geometry in the Late Carboniferous (Parés et al., 1994; Van der Voo et al., 1997; Weil et al., 2000, 2001; Weil, 2006; Merino-Tomé et al., 2009; Weil et al., 2010; Pastor-Galán et al., 2011; Weil et al., 2013a).

Linked or 'coupled' oroclines have been documented in other orogens. For example, the Alaskan portion of the Cordilleran orogen of western North America is characterized by a *Z*-shaped pair of coupled oroclines, or 'terrane wreck' (Johnston, 2001), that formed by vertical-axis buckling of an originally linear segment of the North American Cordillera. Interpretation of an *S*-shaped pair of coupled oroclines within the Iberian Variscan belt therefore has precedent, and may be reconcilable within a model of orocline formation by secondary buckling. A terrane wreck model for formation of the Iberian coupled oroclines makes a number of testable predictions. These include: 1) that orocline formation occurred in response to a change in regional stress from orogen perpendicular during Variscan deformation, to orogen parallel during orocline formation; 2) that >1100 km of orogen-parallel shortening was accommodated by orocline formation; and 3) that palinspastic restoration of the oroclines yields a 2300-km-long, linear Variscan orogen.

The Paleozoic stratigraphic sequence that characterizes the Iberian Variscan belt has been interpreted as an autochthonous element of the northern passive margin of the Gondwana megacontinent (e.g. Nance and Murphy, 1994; Murphy et al., 2004, 2006). However, continuity of the passive margin sequence around the oroclines of a Variscan terrane wreck requires that this Paleozoic sequence was decoupled from Gondwana at the time of orocline formation. Most paleogeographic models interpret Iberia in its modern-geometry and fixed in a position adjacent to the West African craton from the lower Paleozoic onset of passive margin sedimentation through Carboniferous Variscan orogeny (e.g. Robardet, 2003). However, such models are inconsistent with 1) the observation of significant numbers of ca. 0.9-1.1-Ga zircons that have no West African source within Ediacaran to lower Paleozoic clastic rocks of Iberia (Ábalos et al., 2012; Fernández-Suárez et al., 2000a, 2013; Gutiérrez-Alonso et al., 2003; Talavera et al., 2012), and 2) paleomagnetic inclination data that place

autochthonous regions of the Western European Variscan belt at significantly lower latitudes than the north African Gondwana margin from the mid-Paleozoic onward (e.g. Tait et al., 2000a). Separation of the Variscan autochthon from the North Gondwana margin predicts the mid-Paleozoic opening and subsequent Variscan closure of at least one major ocean in addition to the Rheic; however, interpretations of the nature, extent, and number of oceanic sutures within the Variscan belt are entirely dependent on interpretations of its plan-view architecture.

This dissertation is thus concerned with deciphering the orogenic geometry of the Iberian Variscan belt in an effort to provide insight into the tectonic processes and respective paleogeographic implications of oroclines, both within the Variscan belt and in other sinuous orogens worldwide. The most fundamental question at hand is whether the Iberian Variscan belt is characterized by an *S*-shaped pair of coupled oroclines, as predicted by the model of Du Toit (1937). If the orogen is characterized by a pair of coupled oroclines, then what are the paleogeographic implications of the required palinspastic restoration to an originally linear Iberian Variscan belt? Is there evidence to support the existence of post-orogenic orogen parallel compressive stress as required by a model of secondary buckling? Does the Variscan paleomagnetic record reflect the significant amounts of orogen parallel translation necessarily acquired during secondary buckling? What characteristics of the Western European Variscan belt are shared by other orogens that may likewise play host to coupled oroclines? Answering the above questions will improve our understanding of Variscan orogenic evolution, and in turn contribute significantly to our understanding of the mechanisms of orocline formation and the processes involved in supercontinent amalgamation.

1.2 Methodological approach

The most widely accepted means of classifying an orocline as either progressive or secondary involve constraining the timing and magnitude of vertical-axis rotations through coupled paleomagnetic and structural analysis (e.g. Weil and Sussman, 2004). Vertical-axis rotations that post-date orogenic shortening in the foreland core of the Cantabrian orocline vary as a function of strike, implying that the Cantabrian orocline formed by secondary buckling of an initially linear Variscan belt (e.g. Weil et al., 2010). A lack of sufficient

exposure through the central and southern Iberian massif precludes the use of a paleomagnetic test for the presence of a second Iberian orocline. However, the Lower Ordovician Armorican Quartzite is stratigraphically correlatable across the entire massif, and exhibits a dominant paleocurrent direction outward from the core of the Cantabrian orocline (Aramburu and García-Ramos, 1993) that varies as a function of strike in the same manner as paleomagnetic declination data. The implication is that paleocurrent data may be used as a tool for constraining orogenic curvature, and the presence of an *S*-shaped pair of coupled oroclines within the Iberian Variscan belt is therefore tested using paleocurrent data collected from the Armorican Quartzite across its stratigraphically correlatable extent within the Spanish Iberian Massif (Chapter 2; Shaw et al., 2012); this technique has no published precedent. Data were predominantly collected from roadcut exposures over a four-week-long field season in the summer of 2010 by myself, my advisor Stephen Johnston, and our collaborator at the University of Salamanca, Gabriel Gutiérrez-Alonso. I performed all subsequent data entry, analysis, and presentation.

Zircon grains isolated from samples collected from the Armorican Quartzite in the 2010 field season were dated using laser ablation-inductively coupled plasma-mass spectrometry (LA-ICP-MS) U-Pb analysis at the Sektion Geochronologie of the Senckenberg Naturhistorische Sammlungen Dresden, Museum für Mineralogie und Geologie in Dresden, Germany, in February of 2011. Provenance analysis of these LA-ICP-MS U-Pb age data was conducted in order to further constrain the geometry of the Iberian coupled oroclines, and to assess the lower Paleozoic paleogeographic position of the palinspastically restored pre-Variscan Iberian passive margin (Chapter 3; Shaw et al., 2014). Though detrital zircon provenance analysis is typically conducted through comparison of detrital age populations with ages of potential source terranes, this study took the unique approach of comparison with detrital populations from contemporaneous clastic sequences of the North African realms with which the Iberian passive margin sequence is stratigraphically linked. Initial heavy mineral separation was performed by co-author Daniel Pastor-Galán. I performed individual grain selection, grain mounting, and laser ablation. Raw data were converted to concordia ages in *AgeDisplay* (Sircombe, 2004) by Gabriel Gutiérrez-Alonso; I conducted all further data analysis and presentation. No other currently published work offers a single formation detrital zircon study of comparable geographical extent.

Structural data were collected from the exposures of the Ediacaran Narcea Slates around the hinge of the Cantabrian orocline during a second field season lasting six weeks in the summer of 2012. The data consisted of measurements of mesoscale vertical-axis folds deforming sub-vertical slaty cleavage and shear fabrics within the Narcea Slates, which were used for the first true test of a model of formation of the Cantabrian orocline by buckling in response to an orogen parallel compressive stress (Chapter 4). The assumption behind the test is that during buckling of an orogen, layer-parallel stress should be accommodated by the same principle mechanism of flexural shear that is active during buckle folding of horizontal strata. Data were predominantly collected from roadcut exposures by myself and field assistant Glenn Jasechko, following a brief field introduction from Gabriel Gutiérrez-Alonso. I conducted all subsequent data entry, structural analyses, and presentation.

Chapter 5 presents a comparative review-based paper that examines paleomagnetic inclination data sets, and the palinspastic restoration of coupled oroclines within the Western European Variscan belt, North American Cordillera, and Eastern European Alpine system. Paleomagnetic data sets were previously compiled by Enkin (2006) for the North American Cordillera, and by Beck (2001) and Shaw and Johnston (2012) for the Eastern Alpine system. Paleomagnetic data for the Western European Variscan belt are compiled herein.

Chapter 2. Oroclines of the Variscan orogen of Iberia: Paleocurrent analysis and paleogeographic implications[1]

2.1 Abstract

Coupled structural and paleomagnetic analysis have shown that the northern Iberian bend of the Variscan orogen, referred to as the Cantabrian orocline, developed by vertical-axis rotation of an originally linear orogen. However, palinspastic restoration of the orocline has proven difficult owing to (1) an unusually great orogenic width of over 700 km and (2) exposure of shallow water strata of the Gondwanan margin in the northern and southern portions of the orogen. We present paleocurrent data from Lower Ordovician shallow marine clastic sedimentary rocks across the Variscan of northern and central Iberia collected to constrain palinspastic restoration of the orogen. Paleocurrent data were collected from over 50 sites, and include cross-bed foresets, ripple crests and casts, as well as rare ball and pillow structures, syn-sedimentary slump folds and incised channels. Paleocurrent directions fan around the Cantabrian orocline, are consistently oriented at a high angle to structural strike, and yield a consistent offshore direction outward from the oroclinal core. Similarly, changes in structural strike and paleocurrent direction across central Iberia imply the presence of a second more southerly orocline, the Central Iberian orocline, which is continuous with, but convex in the opposite direction of the Cantabrian orocline. Together, the Cantabrian and Central Iberian oroclines define an *S*-shaped pair of continental-scale buckle folds. Palinspastic restoration of the oroclines yields a linear continental margin >1500 km long characterized by consistent offshore paleoflow to the west, defining a westerly oceanic domain (presumably the Rheic Ocean) and an easterly landward direction (presumably Gondwana). Recognition of the southern orocline explains the unusual width of the orogen, the geometry of aeromagnetic anomalies attributable to Variscan rocks, and is consistent with available structural data, paleomagnetic declination data, and the distribution of correlative Paleozoic and older rock sequences including shallow water strata of the

[1] This chapter is published as: Shaw, J., Gutiérrez-Alonso, G., Johnston, S.T., and Weil, A.B., 2012, Oroclines of the Variscan orogen of Iberia: Paleocurrent analysis and paleogeographic implications: Earth and Planetary Science Letters, v. 329-330, p. 60–70, doi: 10.1016/j.epsl.2012.02.014.

Gondwanan margin. The *S*-geometry of the oroclines is similar to the *Z*-geometry of the Alaskan oroclines of the North American Cordillera, suggesting that as in the Cordillera, the Iberian oroclines may record a significant, margin-parallel translation event.

2.2 Introduction

The Variscan orogen (Fig. 2-1) provides the European record of the Late Paleozoic continental collisions that ultimately became the core of the supercontinent Pangea. Understanding the Variscan orogen is, therefore, crucial to constructing robust geodynamic and tectonic models of supercontinent formation. Herein, paleocurrent data from Lower Ordovician passive margin sequences are used to determine the original geometry of the Variscan orogen in Iberia. Present-day structural features define a 180º, hairpin bend in northern Iberia referred to as the Cantabrian orocline (Fig. 2-1). Paleomagnetic and structural data demonstrate that the bend is an orocline that resulted from bending of an originally linear orogen in the Late Carboniferous–earliest Permian (Kollmeier et al., 2000; Merino-Tomé et al., 2009; Pastor-Galán et al., 2011; Weil et al., 2010; Weil et al., 2001; Weil et al., 2000). Palinspastic restoration of the bend is a necessary first step in any attempt to model the paleogeographic and tectonic formation of Pangea.

Several aspects of the Iberian Variscan orogen complicate attempts at palinspastic reconstruction of the orogen. First, the orogen is anomalously broad, extending greater than 700 km across strike when measured from the axis of the Cantabrian orocline. The very low grade orogenic foreland is today exposed in the core of the Cantabrian orocline, implying that the oceanward direction off the Gondwanan paleo-continental margin was (in present-day coordinates) to the south and west, consistent with available Ordovician sedimentological data (Aramburu and Garcia-Ramos, 1993). However, lower Paleozoic shallow water strata are common across much of the orogen, and faunal and sedimentary facies studies of Lower Ordovician strata in southern central Iberia have been interpreted to show that the oceanward direction was (in present-day coordinates) to the north (Robardet, 2002; Robardet and Gutiérrez-Marco, 1990a). This polarity change in direction oceanward (from southward in northern Iberia to northward in southern Iberia) has previously been associated with rifting of Avalonia and opening of the Rheic Ocean. This event is marked by

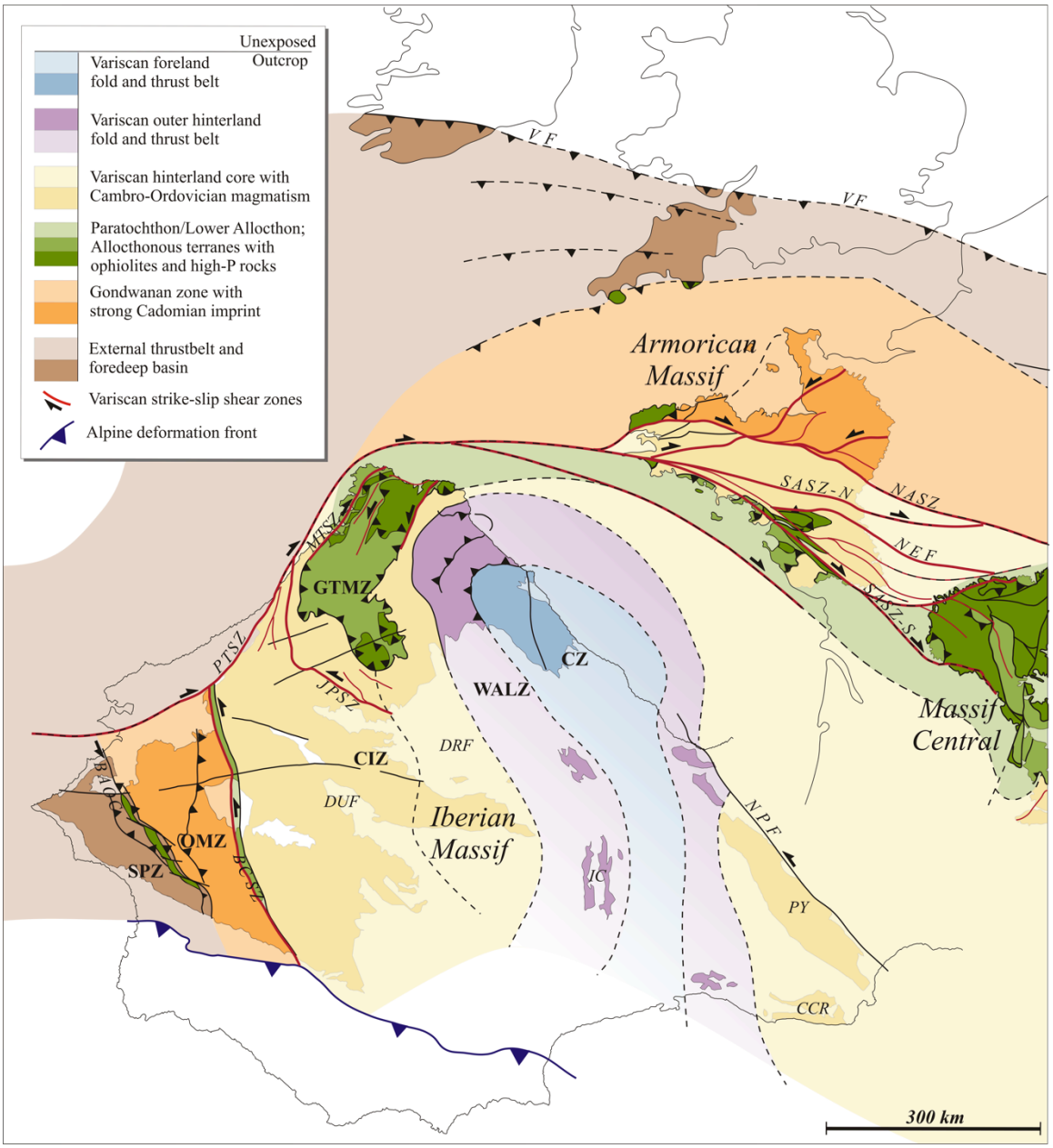

Figurre 2-1 Correlations of tectonostratigraphic zones across the Western European Variscan Belt prior to Cenozoic opening of the Cantabrian Sea (Bay of Biscay); after Martínez Catalán et al. (2007). BAOC—Beja-Acebuches ophiolitic complex; BCSZ—Badajoz-Cordóba shear zone: CCR—Catalonian Coast Ranges; CZ—Cantabrian Zone; CIZ—Central Iberian Zone; DRF—Domain of Recumbent folds; DUF—Domain of Upright folds; GTMZ; Galicia-Trás-os-Montes Zone; IC—Iberian Cordillera; JPSZ—Juzbado-Penalva shear zone; LC—Lizard Complex; MTSZ—Malpica-Tui suture zone; NASZ—North Armorican shear zone; NEF—Nort-sur-Erdre fault; OMZ—Ossa Morena Zone; PTSZ—Porto-Tomar shear zone; PY—Pyrenees; SASZ—South Armorican shear zone (N and S—northern and southern branches); SPZ—South Portuguese zone; VF—Variscan Front; WALZ—West Asturian-Leonese zone.

extension of the Gondwana passive margin (eg. Murphy et al., 2006), and was accompanied by a thermal event that produced large volumes of igneous rocks (Díaz García, 2002; Díez Montes, 2006; Valverde-Vaquero et al., 2005). However, the continental source of Paleozoic sediments (presumably Gondwana) is unexposed, and determining the oceanward direction is complicated by the distribution of fault bound ophiolitic sequences (regarded as Variscan sutures) in Western Iberia, the lack of a single explanation for which allows for accommodation within varying paleogeographic models (Martínez Catalán et al., 2009; Martínez Catalán et al., 2007; Ribeiro et al., 2007; Simancas et al., 2009).

A previous suggestion regarding the geometry of the Variscan Orogen in Iberia may hold the key to resolving at least some of these outstanding problems. Du Toit (1937), in discussing the geometry of the "Hercynian" (what we now include in the Variscan orogen), noted the bends that define the present-day structure of the Variscan in southwestern Europe. He stated that the orogen was "constituted by a series of interlinked wide arcs", and depicted the Variscan orogen of Iberia as being characterized by two bends: the northern, concave eastward towards the foreland, the Cantabrian orocline, and an "interlinked" southern bend (Fig. 2-2), herein referred to as the Central Iberian bend, which is concave westward towards the hinterland and linked into the Cantabrian orocline through the NNW-SSE trending Iberian Cordillera of northeast-central Spain. Together, these two bends define an *S*-shaped fold pair of continental-scale.

The idea of a southern bend in the Variscan has been recently revisited by Aerden (2004) and Martínez Catalán (2011). Aerden (2004) sampled Variscan metamorphic porphyroblasts across allochthonous terranes of the NW Iberian Massif and demonstrated that inclusion trails maintain a constant north-south orientation, reflecting neither the change in strike around the Cantabrian orocline nor the changes in structural strike that define the southern bend. This work suggests that the porphyroblasts preserve the structure of an earlier north-south trending orogen and that the two bends formed contemporaneously as a consequence of secondary rotation during late Variscan orogeny. Martínez Catalán (2011) compiled structural and geophysical data, and argued that the bends are attributable to late-stage dextral transpressional shear of the orogen during final amalgamation of Pangea.

We test Du Toit's suggested southern bend through the use of paleocurrent indicators preserved in pre-orogenic strata of the passive north Gondwana margin. We present new

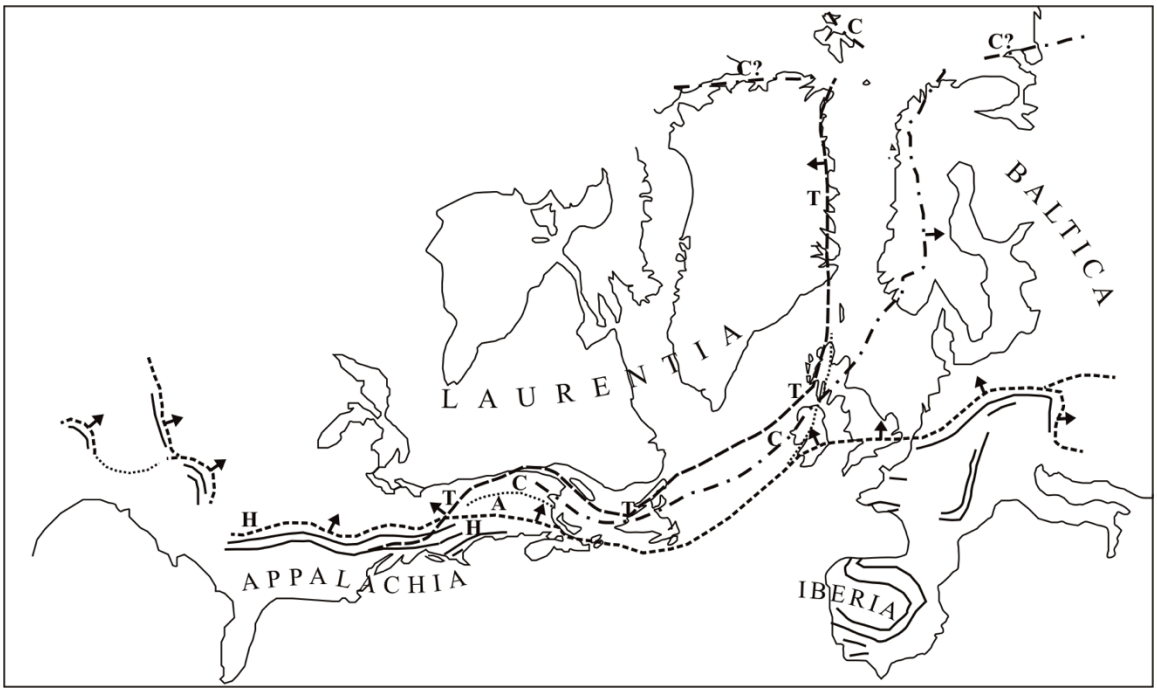

Figure 2-1 Paleozoic fold belts of the circum Atlantic region; C—Cadomian; T—Taconian; A—Acadian; H—Appalachian Hercynian (Variscan). Solid lines indicate structural trends away from orogenic fronts; arrows indicate 'direction of pressure', ie. structural vergence. Redrawn without alteration from Du Toit (1937).

paleocurrent data from Lower Ordovician shallow water clastic rocks collected at over 50 sites across the northern and central Iberian Massif and the Iberian Cordillera. These findings are analysed in conjunction with other available data (geologic, paleomagnetic and aeromagnetic) and used to reassess the pre-orogenic geometry of the Variscan belt in Iberia. Together these data are interpreted as being consistent with the presence of a Central Iberian orocline, which consequently requires a re-examination of the tectonic evolution of Variscan Europe. The revised paleogeography required from such a reexamination might help explain some of the existing problematic aspects of the Variscan orogen in Iberia.

2.3 Geologic setting: The Variscan in Iberia

The Iberian Massif exposes Paleozoic and older rocks that record development of a pre-orogenic passive margin and its subsequent Variscan deformation, though there is little consensus regarding the full Neoproterozoic–Paleozoic paleogeography and tectonic setting of the massif. Within Iberia, correlative rocks are also exposed in the Iberian Cordillera (northeast-central Spain) and within the Pyrenees (Fig. 2-1; see Gibbons and Moreno, 2002).

The Iberian Massif is divided into six tectonostratigraphic zones distinguished on the basis of lithology, stratigraphy, and Variscan deformational style. From the core of the Cantabrian orocline south, these zones are: the Cantabrian (CZ), West Asturian-Leonese (WALZ; extended to include isolated Paleozoic exposures of the Iberian Cordillera), Central Iberian (CIZ), Galica-Trás-os-Montes (GTMZ), Ossa-Morena (OMZ) and South Portuguese (SPZ). Drawing from lithologic and stratigraphic similarities, these zones (with the exception of the CZ) have been tentatively correlated across the length of the Variscan belt (e.g. Martínez Catalán et al., 2007 and references therein). Based on these correlations, the Cantabrian orocline has been interpreted to lie at the core of a much larger orogenic bend, stretching from southern Iberia to southern Britain (Martínez Catalán et al., 1997; Martínez Catalán et al., 2007; Matte, 1991; Robardet, 2002; Robardet and Gutiérrez-Marco, 1990a) (Fig. 2-1), known as the Ibero-Armorican arc (Brun and Burg, 1982).

The CZ, WALZ and CIZ consist of a Neoproterozoic subduction related basin (Fernández-Suárez et al., 2000a) and a Paleozoic passive margin. The foreland CZ is characterized by a thin-skinned fold and thrust belt largely reflective of Mississippian Variscan compression; shallow rooted thrusts that verge toward the core of the Cantabrian orocline overlap passive margin sequences onto syn-kinematic marine to terrestrial foreland basin deposits (Marcos and Pulgar, 1982; Pérez-Estaún and Bastida, 1990; Pérez-Estaún et al., 1988; Pérez-Estaún et al., 1991). Clastic shelf sequences of the hinterland WAL and CI zones deformed under conditions that evolved from early-stage low to medium-grade Barrovian-type metamorphism into late-stage low-pressure metamorphism (Bastida et al., 1986; Díez Balda et al., 1990; Martínez Catalán et al., 1990). Both zones are further characterized by syn-orogenic flysch and syn- and post-kinematic magmatism (Dallmeyer et al., 1997; Gutiérrez-Alonso et al., 2011a; Ugidos, 1990). The WALZ and CIZ are mainly differentiated by the presence of a lower Paleozoic unconformity in the CIZ, which places Lower Ordovician strata atop pre-Cambrian to Cambrian rocks (Gutiérrez-Marco et al., 2002). At 400 km across strike, the CIZ is anomalously wide relative to the other Variscan tectonostratigraphic zones. It was, based on the southward transition to a lower metamorphic grade and a smaller volume of syn-kinematic granitoids, originally subdivided into a northern Galician-Castillian zone, and a southern Luso-Alcudian zone (Lotze, 1945) (Fig. 2-3a); it was later subdivided based on structural style, into a northerly domain of recumbent

folds and a southerly domain of upright folds (Díez Balda et al., 1990) (Fig. 2-1; Fig. 2-3b). Most recently, the northern half of the domain of recumbent folds has been classified as the 'Ollo de Sapo Domain', after the abundant Lower Ordovician calc-alkaline magmatism of its namesake Ollo de Sapo Formation (e.g. Díez Montes et al., 2004 and references therein); the excluded central and southern realms of the CIZ, characterized by a predominance of Neoproterozoic to Lower Cambrian sedimentary rocks, are deemed the 'Schistose-greywacke Domain' (Martínez Catalán et al., 2004).

The GTMZ (Farias et al., 1987) consists of a complex structural stack including a basal schistose unit (referred to as the Paratochthon) atop which ophiolites and far travelled terranes bearing rocks that have been subjected to subduction related high-pressure metamorphism are tectonically juxtaposed (Martínez Catalán et al., 1997; Ribeiro, 1990). Oceanic terranes are commonly interpreted as having originated in the Rheic Ocean domain (eg. Martínez Catalán et al., 2007) which separated Gondwana and Laurussia prior to the amalgamation of Pangea (Nance and Linnemann, 2008 and references therein). It has been suggested that the oceanic allochthons root in, and were thrust northeast out of, the Malpica-Tui suture zone that runs along the west side of the allochthons (Fig. 2-1; Ballevre et al., 1992). Interpretation of the Malpica-Tui zone (Díez Fernández et al., 2011) as a suture has, however, been rejected because (1) the proposed suture cannot be traced along strike into the Central Iberian zone, and (2) southeast of the oceanic allochthons, the Malpica-Tui zone juxtaposes correlative sequences of the Central Iberian zone (Robardet, 2002).

The ESE trending, crustal-scale sinistral Badajoz-Cordóba shear zone (BCSZ) marks the northern boundary of the OMZ. Many consider the OMZ to be autochthonous (e.g. Martínez Catalán et al., 2007; Robardet, 2002, 2003; Robardet and Gutiérrez-Marco, 1990a, 2004) and view lower Paleozoic strata of the OMZ as having accumulated in a more distal passive margin setting than strata of the WAL and CI zones (Robardet and Gutierrez-Marco, 2004). However, interpretation of the BCSZ as an early Variscan (Devonian or younger) suture zone (Azor et al., 1994; Simancas et al., 2001) is supported by the presence of retrograde eclogites and amphibolites with MORB-like geochemical signatures (Ábalos et al., 1991; Gómez-Pugnaire et al., 2003; López Sánchez-Vizcaíno et al., 2003). Available detrital zircon data also suggests a contrasting sedimentary provenance for the OMZ relative to the

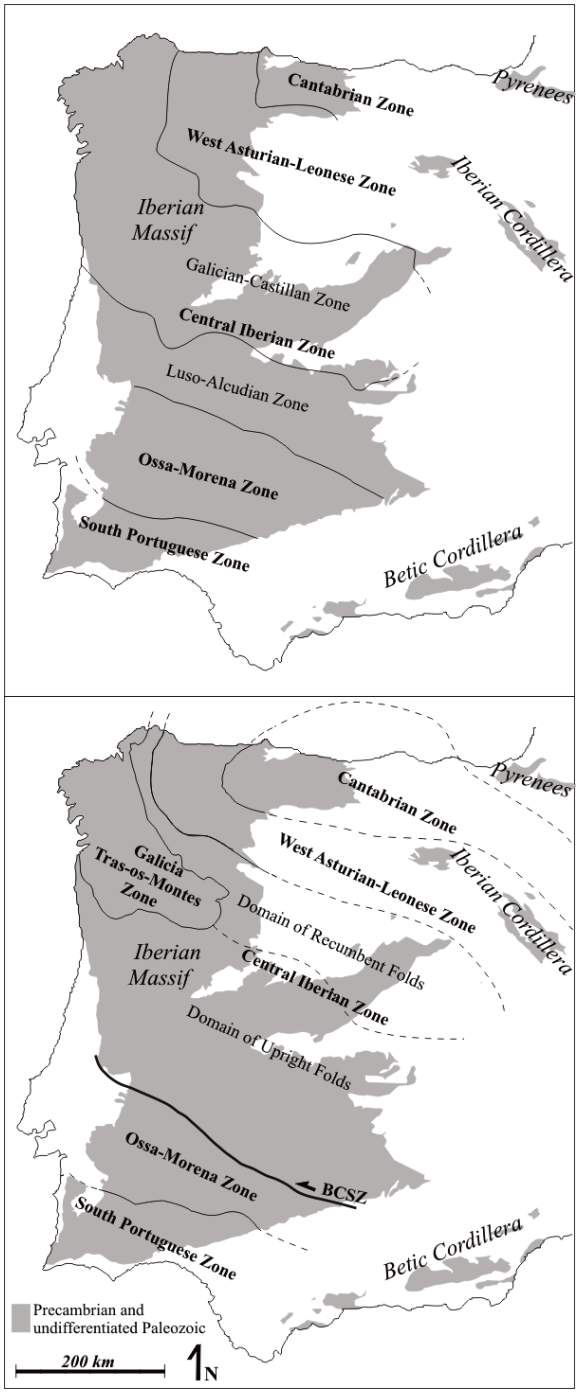

Figure 2-3 The tectonostratigraphic zones of the Iberian massif as originally delineated by Lotze (1945) (a) and as reconstructed in combination of more recent works (b) (Díez Balda et al., 1990; Martínez Catalán et al., 2007). BCSZ—Badajoz-Cordóba shear zone. Galician-Castillan and Luso-Alcudian zones and the domains of Upright and Recumbent folds are early and late divisions of the Central Iberian Zone, respectively.

Cantabrian, WAL and CI zones during the late Neoproterozoic (Fernández-Suárez et al., 2002b; Fernández-Suárez et al., 2000a; Gutiérrez-Alonso et al., 2003), which may have persisted through the Lower Ordovician (see data from the Armorican Quartzite in Fernández-Suárez et al., 2002a; Linnemann et al., 2008)

In the SPZ, a S-verging Variscan thrust belt imbricates an external foredeep basin that is interpreted to have been constructed atop crust of the Avalon terrane (Martínez Catalán et al., 2007 and references therein) (and its associated Meguma terrane?). The Avalon terrane rifted from Gondwana in the Late Cambrian to Early Ordovician (e.g. Braid et al., 2011; Martínez Catalán et al., 200i007; Murphy et al., 2006), opening the Rheic Ocean in its wake as it drifted northward where it accreted with Laurentia in the Siluro-Devonian (e.g. Matte, 2001; McKerrow et al., 2000). A dismembered ophiolite (the Beja-Acebuches) marks the northern boundary of the SPZ, and is commonly interpreted as the suture along which the Rheic Ocean closed (e.g. Crespo-Blanc and Orozco, 1991; Fonseca and Ribeiro, 1993). It is into this suture zone that the allochthonous oceanic terranes of the GTMZ are commonly assumed to have rooted, and out of which they were thrust cratonward over the pericratonic distal margin of Gondwana (Martínez Catalán et al., 2007). The Beja suture is correlated with the Lizard ophiolitic complex of southeastern England and the Rheno-Hercynian ophiolites of northeastern France (Martínez Catalán et al., 2007 and references therein).

2.4 Paleocurrent data

Paleocurrent data were collected from 67 sites spread across the Cantabrian, WAL and CI zones of the Iberian Massif and the WALZ correlative Iberian Cordillera (see Appendix for coordinate data). The Lower Ordovician Armorican Quartzite is a prominent unit of the lower Paleozoic Gondwanan margin sequences with a vast biostratigaphically correlatable extent, from West Africa through Iberia, Armorica, and Western Europe, at least as far east as Serbia, and possibly as far east as Afghanistan (Gutiérrez-Alonso et al., 2007). The Armorican Quartzite is predominantly comprised of thick-bedded clean quartzites, but also contains beds of low-grade metamorphic mature sandstones, phyllitic siltstones, and minor volcanic and shale intercalations. Stratigraphic characteristics suggest a nearshore shallow water depositional environment under the range of tidal, shore current, and storm influences (Gutiérrez-Marco et al., 2002 and references therein). Ridges of the highly resistant quartzite are a ubiquitous feature throughout the Iberian landscape.

Cross bed foresets and ripple crests, marks, and casts, are the most commonly preserved current indicators, the former predominantly found in quartzite and sandstone beds, the latter more prevalent in siltstones and shales. While foreset dip is relatively consistent at outcrop scale, ripples commonly exhibit tidal interference structures (see Fig. 2-4a,b). Other measured flow indicators included ball and pillow structures, slump folds, and incised channels. Primary structures are commonly absent in outcrop due to pervasive bioturbation (ichnofossils, dominantly *Cruziana* and *Skolithos*, are prevalent). Many localities, particularly within the northern CIZ, exhibit a high degree of strain. Data collection from such localities was restricted even in cases where primary structures are preserved, in order to avoid potential errors resulting from undetectable switches in stratigraphic facing direction produced by isoclinal folding, or rotation of primary structures into cleavage planes, etc. (see Fig. 2-4c). Where the Armorican Quartzite was inaccessible or lacked reliable paleocurrent indicators, we utilized the immediately over- and underlying clastic units. Names and correlations of these bounding units vary between and within the different tectonostratigraphic zones. They are, however, representative of the same Lower Ordovician Gondwanan margin, and their inclusion in this study is not believed to have any significant effect on the interpretation of our results (see Gutierrez-Marco et. al., 2002 for the complete Ordovician stratigraphy of Iberia).

2.5 Analysis and results

Data were structurally analysed in sets from individual field sites as well as in the context of regional structures. Bedding was restored on a site-by-site basis unless stereographic analysis of several sites from within the same regional structure yielded a statistically significant fold-axis plunge. If a fold axis could not be determined with accuracy, a site's bedding dip was structurally restored using measured strike and dip; as Variscan structures are generally shallow in plunge, the impact of this analytical simplification was negligible. Data from multiple sites of close proximity from within the same structure or similar-trending structures were grouped for presentation and simplification of analysis. GPS coordinates were averaged for each amalgamate site without weighting the number of data contributed by each site (site location differences yielded by this step would be imperceptible and insignificant given the scale of the study; see Tables A-1 and A-2 in the Appendix).

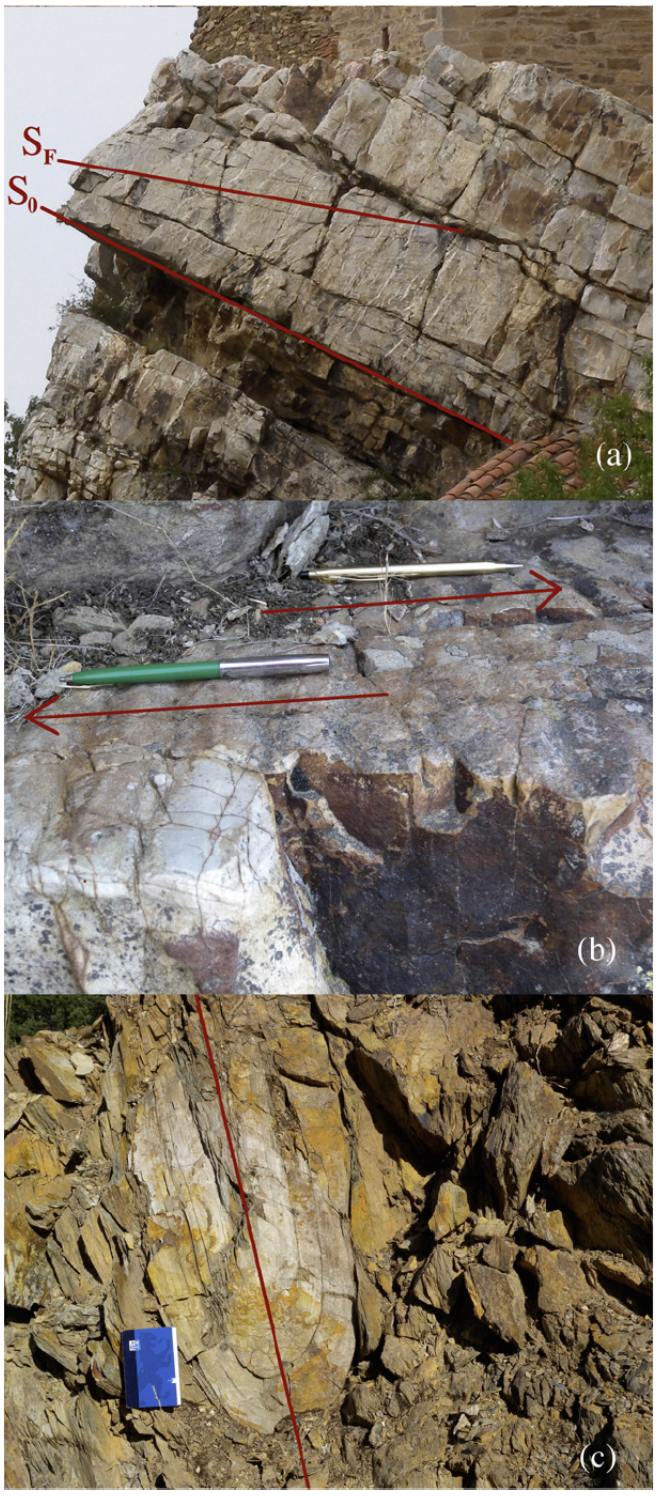

Figure 2-4 (a) Foreset planes dip to the east more shallowly than bedding, indicating westward flow at La Ermita de la Virgen de Herrera, Iberian Cordillera. (**b)** Ripple crests at the top of a quartzite bed exhibit dual asymmetry, influence from tidal currents. (**c)** Isoclinal fold within sandstone layers of the Armorican Quartzite in the CIZ.

Rose diagrams, plotted by site location in Fig. 2-5, are keyed by current indicator type and scaled according to dataset size in order to visually convey comparative robustness. In agreement with the work of Aramburu and Garcia-Ramos (1993), the plot shows current fanning outward from the foreland core of the Cantabrian orocline. Consistent with the pattern in the north, dominant current runs perpendicular to structural trend throughout the peninsula. The implication of paleocurrents being perpendicular to structural strike and outward from the Cantabrian foreland, is that (moving clockwise from the northwest) flow direction transitions from southward in the WNW-ESE trending structures of the CZ, WALZ and northern CIZ (sites 4-7), through westerly in the NNW-SSE trending Iberian Cordillera and eastern Spanish Central System (sites 8,9), and through a northwesterly direction reflective of northward structural deflections in the easternmost southern CIZ (Sites 15, 19) to reach consistently north to northeasterly directions in the WNW-ESE striking southern CIZ (sites 11-14, 16, 17).

2.6 Discussion

Fanning of paleocurrent direction around the Cantabrian orocline is attributable to bending of a formerly linear margin during the Late Carboniferous–earliest Permian; palinspastic restoration of the bend to a north-trending linear orogen (Weil et al., 2010) yields a consistent westward paleocurrent direction and implies an oceanward (Rheic Ocean) direction to the west, and a landward (Gondwana continent) direction to the east. The implication of these findings is that changes in paleocurrent direction can be used to test for the presence of additional bends within the Variscan orogen, such as that originally proposed by Du Toit (1937) or more recently by Martínez-Catalán (2011). As predicted by Du Toit (1937), changes in paleocurrent direction documented across the Iberian Peninsula argue for a second, more southerly bend that is continuous with, but convex in the opposite direction of the Cantabrian orocline. Together the two bends define a continental-scale fold pair with an *S*-geometry. The presence of a southern bend (the Central Iberian) explains the widespread occurrence of shallow water strata, and the faunal and sedimentary data from southern Iberia that imply a northward oceanward direction. This geometric model explains the structural repetition by the bending of a single, originally more linear westward facing, north-south striking (in present day coordinates) passive margin. Furthermore, the model of

post-Variscan bending about the northerly Cantabrian and southerly Central Iberian bends is consistent with observed deflections in the trend of Variscan folds and lithological belts around the southern bend (Fig. 2-5), available paleomagnetic declination data for the Iberian massif (Table 1-1), as well as with the change in structural direction, from northeast to southwest verging thrusts on the north and south sides of the hinge line, respectively. Aeromagnetic anomalies attributable to Variscan rocks constrain the geometry of Variscan structures beneath Mesozoic and younger cover rocks that unconformably overlie much of the hinge region of the Central Iberian bend in eastern Iberia (see Socias and Mezcua, 2002). These geophysical anomalies show that north-northwest–south-southeast trending structures in the Iberian Cordillera deflect westward around the interpreted hinge of the Central Iberian bend and are continuous into the west-northwest–east-southeast trending structures of the southern Central Iberian zone.

Table 2-1 Iberian pre-Variscan paleomagnetic data

Name	Likely age	D	I	D^{-1}	P.Lat.	α_{95}	Reference
San Pedro	Siluro-Devonian	113	+34	293	21 S	10	Perroud & Bonhommet, 1984
Griotte	Siluro-Devonian	224	+51	44	30 S	8.5	Tait et al., 2000b
Almaden-1	Silurian	62	-36	64	20 S	14	Perroud et al., 1991
Almaden-2	Devonian	81	-37	81	20 S	10	Parés & Van der Voo, 1992
Beja	Lower Carboniferous	36	-49	36	29 S	16	Ruffet (1990)

Available paleomagnetic declination (D) and inclination (I) values from the Iberian Massif (north of the Badajoz-Cordoba shear zone) and the Pyrennes. Likely paleolatitude (P.Lat) and an inverted declination (D^{-1}) corresponding to negative inclination are also given; for the southern hemispheric latitudes this implies a north-seeking magnetization and normal polarity (Van der Voo, personal communication).

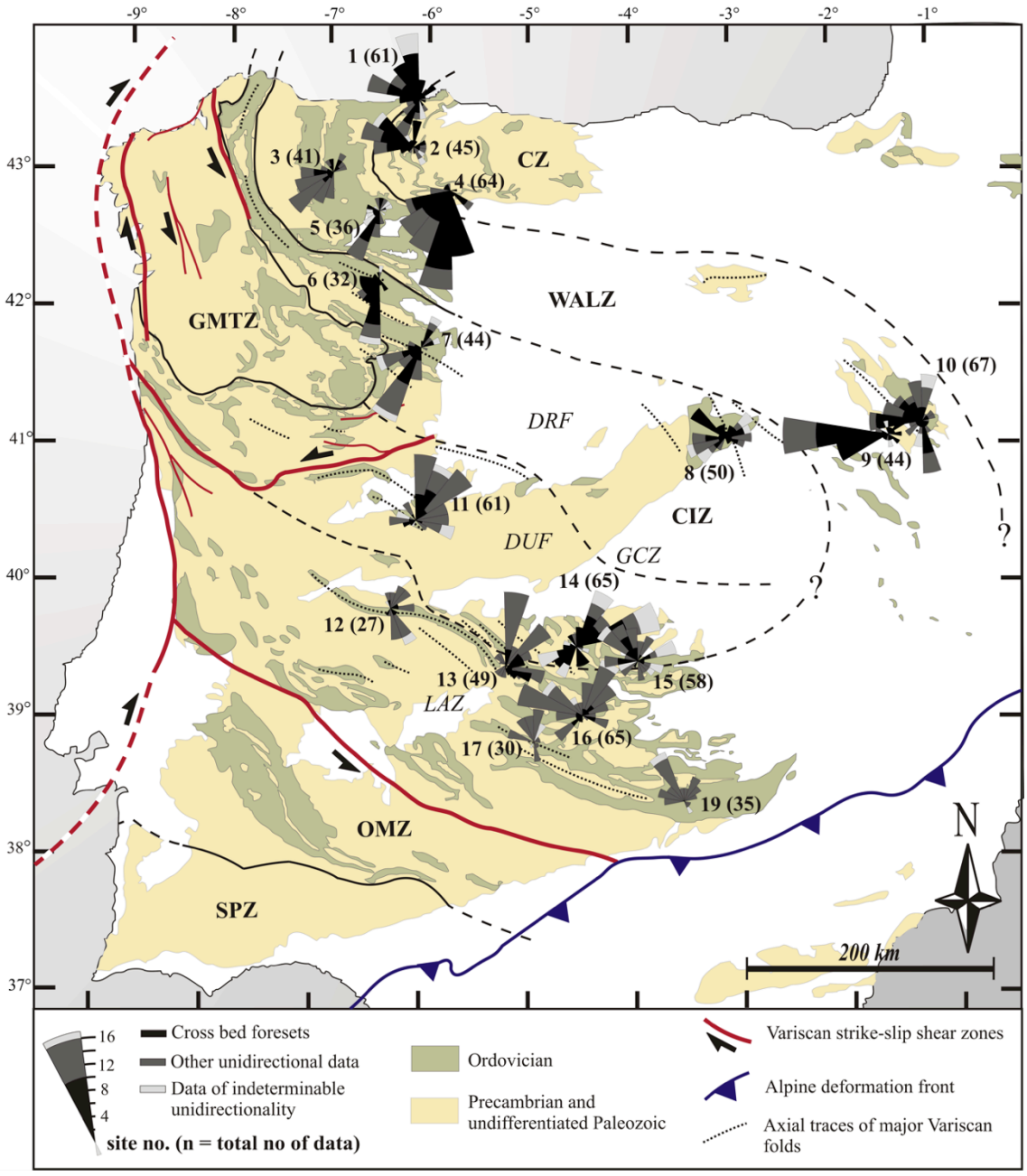

Figure 2-5 Paleocurrent data from Lower Ordovician rocks of the Iberian Peninsula. Coordinate data for each plotted paleocurrent rose are given in the Appendix (Table A-1). Raw field data and calculated paleoflow azimuths are given in the Appendix (Table A-2). CZ—Cantabrian zone; WALZ—West Asturian-Leonese zone; CIZ—Central Iberian zone, GMTZ—allocthonous complexes of the Galicia–Trás-os-Montes zone; OMZ—Ossa Morena zone; SPZ, South Portuguese Zone; DRF Domain of Recumbent Folds and DUF Domain of Upright Folds, northerly and southerly divisions of the CIZ; GCZ—Galician-Castillian zone and LAZ—Luso-Alcudian Zone, northerly and southerly division of the CIZ (Lotze, 1945). Base map and zonal boundaries based on (Ábalos et al., 2002; González Clavijo, 2002; Gutiérrez-Marco et al., 2002; Martínez Catalán et al., 2007; Robardet, 2002).

We assume that the southern bend formed in the same fashion and at the same time as the northern orocline, and is henceforth referred to as the Central Iberian orocline. The inference is based on continuity of structures and strata around the two bends, and the similarity of structural style between them. In addition, the constant and predictable relationship of relative porphyroblast rotation to the bends (Aerden, 2004) argues for them having developed contemporaneously in response to a similar change in the regional stress field. Finally, Early Permian strata that unconformably overlie strata bent during orocline formation in both the northern and southern bends yield expected early Permian paleomagnetic poles, implying that these strata post-date bending and limit formation of the northern and southern bends to a 10 Ma interval straddling the Carboniferous–Permian boundary (Weil et al., 2010). Continuity of structures, including consistency of vergence direction, and stratigraphy, including the regular distribution of continental platform to basin sedimentary facies, requires interpretation of the bends as oroclines that have developed in response to bending of a formerly linear belt. Palinspastic restoration of the Cantabrian–Central Iberian oroclinal pair yields an originally linear orogen of over 1500 km along which paleoflow is consistently offshore to the west (in present-day coordinates), defining a westerly ocean (presumably the Rheic) and an easterly direction landward (presumably towards Gondwana; Fig. 2-6). A slight sense that flow may be directed toward the right along the margin (i.e. to the North) supports a paleogeographic position of the orogen in the southern hemisphere, consistent with a presumed Gondwanan affinity and available paleomagnetic data. Given the extent of the study area and the uncertainties regarding the CIZ–OMZ boundary, palinspastic restoration of the oroclinal pair can, at this time, only be defined within the Cantabrian, WAL and CI zones. Note also, that neither margin parallel shortening assumed prior to oroclinal bending nor strike-perpendicular shortening likely assumed during oroclinal bending are considered here.

Correlation of rocks along strike around the Central Iberian orocline implies that the WAL zone of northern Iberia is correlative with the formerly identified Luso-Alcudian domain of the southern Central Iberian zone, consistent with metamorphic grade and volume of Variscan granitoids increasing southward in the former and decreasing southward in the latter (Fig. 2-7). This correlation implies along strike variation in the lowermost Paleozoic unconformity used to distinguish the WAL and CI zones, resulting perhaps from a

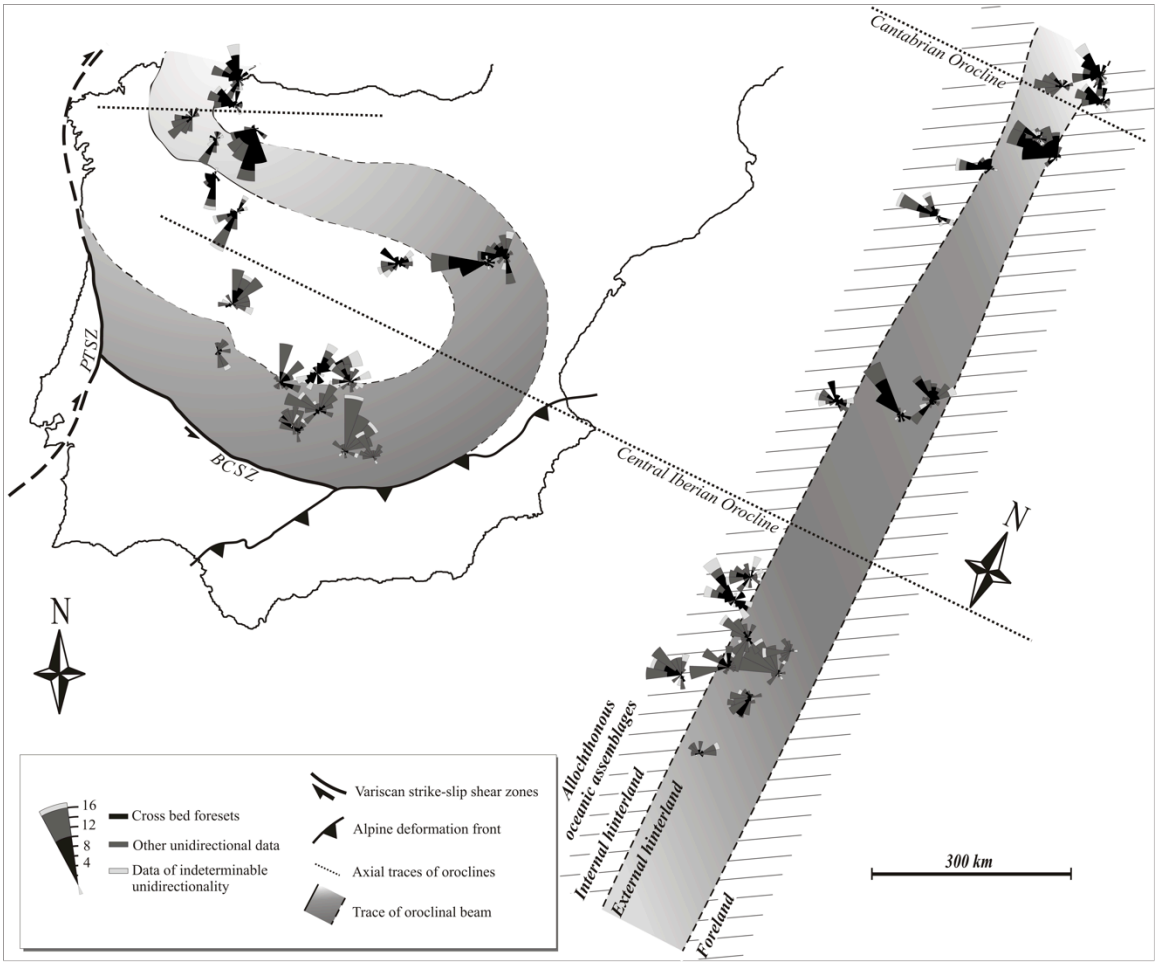

Figure 2-6 Reconstruction of the Iberian double orocline to its originally linear shape yields a uniform direction of offshore current for an originally linear orogen spanning over 1500 km in length. Geometry of the orocline pair is not inferred across major shear zones (PT—Porto Tomar; OM—Ossa Morena), and the palinspastically restored ribbon excludes the Ossa Morena and South Portuguese zones. Neither margin parallel shortening assumed prior to oroclinal bending nor strike-perpendicular shortening likely assumed during oroclinal bending are considered here.

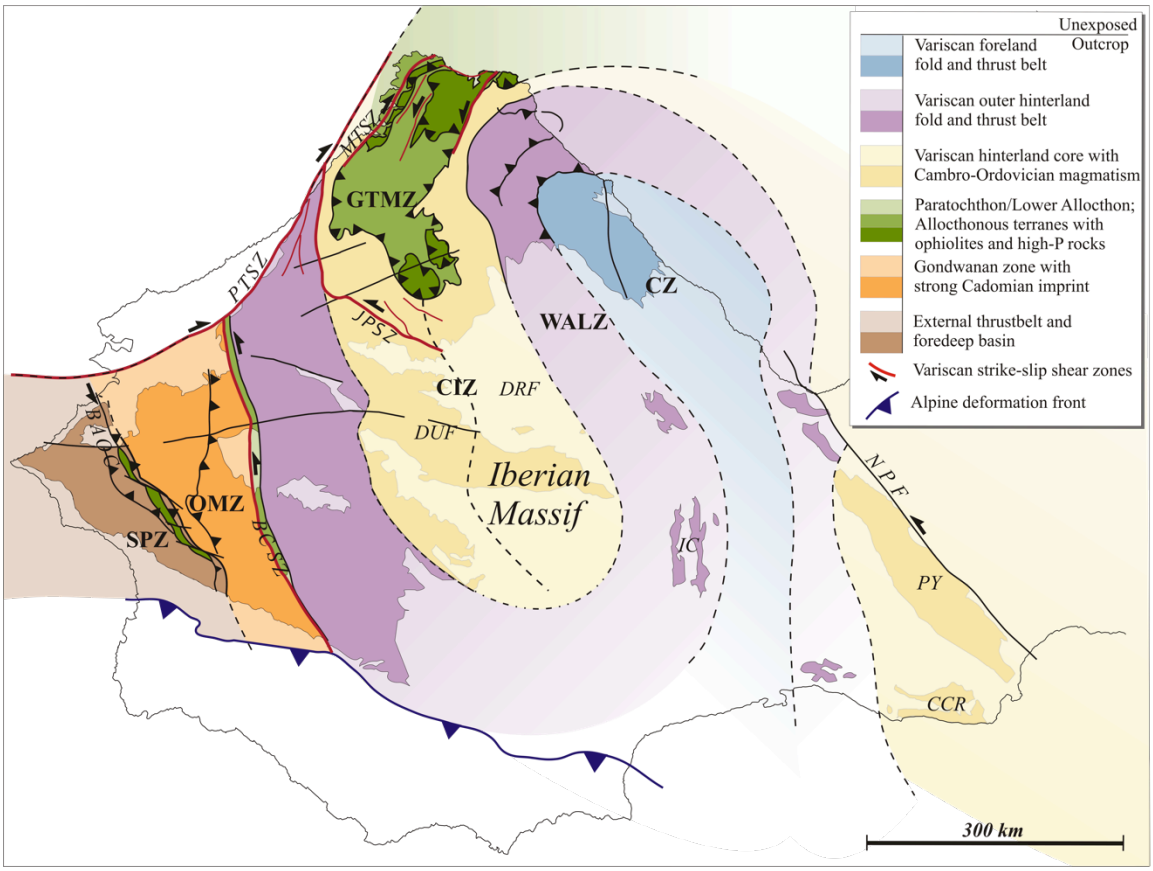

Figure 2-7 Correlations of tectonostratigraphic zones across the Western European Variscan belt prior to Cenozoic opening of the Cantabrian Sea (Bay of Biscay) redrawn in accordance with the double orocline model for the Variscan belt in Iberia. Tectonostratigraphic zones of southern Iberia (southern CIZ, OMZ and SPZ) can no longer be directly correlated to the French Armorican Massif and the Southern British Isles through the 'Ibero-Armorican Arc'. BAOC—Beja-Acebuches ophiolitic complex; BCSZ—Badajoz-Cordóba shear zone: CCR—Catalonian Coast Ranges; CZ—Cantabrian Zone; CIZ—Central Iberian Zone; DRF—Domain of Recumbent folds; DUF—Domain of Upright folds; GTMZ—Galicia-Trás-os-Montes Zone; IC—Iberian Cordillera; JPSZ—Juzbado-Penalva shear zone; MTSZ—Malpica-Tui suture zone; OMZ—Ossa Morena Zone; PTSZ—Porto-Tomar shear zone; PY—Pyrenees; SPZ—South Portuguese zone; WALZ—West Asturian-Leonese zone.

topographic high that was more proximal to the southern portion of the Gondwanan margin. The recently subdivided Ollo de Sapo Domain may also have a southern repetition, the Lower Ordovician calc-alkaline magmatism of the Urra Formation, exposures of which run just north of the Badajoz-Cordóba shear zone (Solá at al., 2008).

In central Iberia, the boundary between the previously identified southerly upright and northerly recumbent structural domains of he Central Iberian zone corresponds with the hinge line of the Central Iberian orocline. Hence, Variscan folds are upright in the southern limb of the Central Iberian orocline and recumbent in the northern limb, implying modification of these structures during oroclinal formation. It may be that the southern limb of the bend overthrust the northern limb during the final stages of oroclinal bending due to space problems in the hinge zone, giving rise to the recumbent geometry of north limb folds. The predominance of Neoproterozoic to Lower Cambrian strata in the southern domain of the CIZ is consistent with a deeper level of achieved erosion in the region, which may further support a model of late-stage overthrusting of the southern oroclinal limb.

Farther to the west, the hinge line of the Central Iberian orocline appears to correspond to the Malpica-Tui suture, with the allochthonous terranes of the GTMZ lying just to the northeast of the hinge/suture line. Paleocurrent data imply an oceanward direction toward the suture zone and allochthonous oceanic terranes in both the southern and northern limbs of the Central Iberian orocline, which is consistent with interpretation of the suture and oceanic terranes originating in an oceanic domain that lay off shore to the west of a formerly more linear, westward-facing Gondwanan passive margin (present-day coordinates). In this model, the Malpica-Tui suture pinches out to the east into the hinge of the Central Iberian orocline. Overthrusting of the oceanic terranes northeast out of the suture is consistent with the southern limb of the bend overthrusting the northern limb during the final stages of bend formation.

One obvious complication of the proposed model is that the Cantabrian zone foreland, which defines the core of the Cantabrian orocline, is not correlative with either the Ossa Morena or South Portuguese zones. This apparent discrepancy could be in part attributable to (1) the possibility that the OMZ and/or SPZ represent a cryptic nappe or nappes not preserved in the core of the Cantabrian orocline and/or (2) significant offset occurred along the Badajoz-Cordóba shear zone (BCSZ), the youngest deformation along which is Variscan

in age (Quesada and Dallmeyer, 1984).

Previous attempts to explain the oroclines have assumed that bending is attributable to shear (Aerden, 2004; Martínez Catalán, 2011). This is unlikely. Aside from the absence of a modern analogue for such significant crustal-scale bending in association with strike-slip faulting, strike-slip models are not 'balanced' and hence cannot be palinspastically restored. The Iberian oroclines are similar in scale and geometry to the Alaskan oroclines that characterize the Cordilleran orogen of western North America (Fig. 2-8). Formation of the Alaskan *Z*-shaped oroclines occurred during northward translation of the bulk of the orogen, resulting in buckling of its northern end (Johnston, 2001). It may be, therefore, that similar, margin-parallel translation, resulting in the buckling of a portion of the orogen, explains the Iberian *S*-shaped oroclines (Weil et al., 2010). A model of oroclinal buckling of a Variscan ribbon (the Cantabrian–Central Iberian ribbon) also offers explanation for the origin of the equidimensional geometry of the Iberian Peninsula, another similarity held with the Alaskan oroclines. Gutiérrez-Alonso et al. (2008a) explained the Cantabrian orocline as the result of

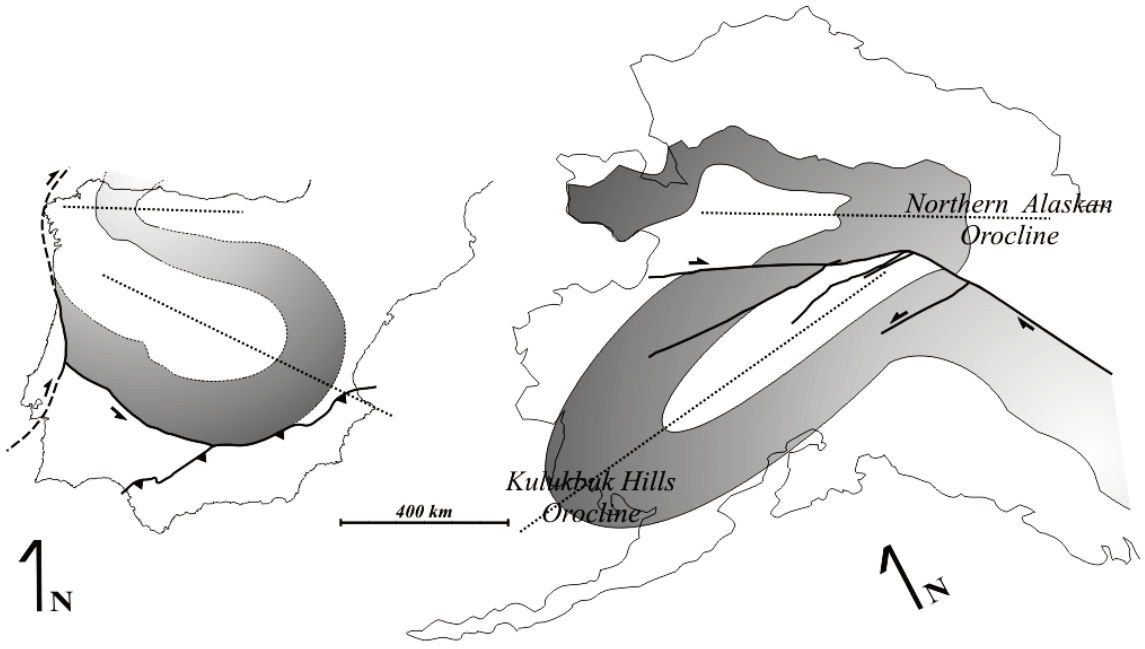

Figure 2-8 The geometry of the Cantabrian and Central Iberian oroclines compared with that of the Northern Alaskan and Kulukbuk Hills oroclines shows that they are near perfect mirrors. Shaded areas for Alaska are hinterland zones of the Alaskan Cordillera; similar to the shaded WALZ and LAZ of Iberia. Alaskan oroclines modeled after Johnston (2001, 2008) and Johnston and Gutiérrez-Alonso (2010).

'self-subduction', a process unique to a supercontinental Earth. Self-subduction cannot be invoked to explain the Alaskan oroclines, and it remains unclear if a modified self-subduction model can be applied to explain the presence of the paired Cantabrian and Central Iberian oroclines. However, while the similar scale and geometry of the Alaskan and Iberian oroclines may point to a common origin (margin parallel translation), it remains possible that the two sets of orocline pairs originated in response to different geodynamic processes.

The *S*-shaped Iberian oroclinal pair is inconsistent with the presence of a large-scale 'Ibero-Armorican Arc' as it is commonly drawn (Martínez Catalán et al., 2007; Matte, 1991; Robardet, 2002; Robardet and Gutiérrez-Marco, 1990a). Though terrane correlations used to support the presence of the Ibero-Armorican Arc are not discredited, direct continuity of the Luso Alcudian and Ossa Morena zones with the French Armorican massif and the South Portuguese Zone with the Southern British Isles is no longer feasible, as it would require oroclinal re-bending of the Iberian oroclines, for which there is no evidence. We suggest that the search for the continuation of the terranes that constitute the south limb of the Central Iberian orocline first focus towards the south, in northern Africa.

2.7 Conclusions

A model of a continental-scale *S*-shaped oroclinal pair for the Variscan in Iberia, in which the Cantabrian orocline is continuous with a complementary Central Iberian orocline, explains sedimentological and structural patterns, requires an orogen of typical across strike width (300-400 km), and fits geometries established by structural trend, distribution of allochthonous terranes, available paleomagnetic data and aeromagnetic anomalies. The model carries strong implications for Variscan and related orogenic processes and for pre-Variscan paleogeography, particularly because it predicts the existence of an independently buckling orogenic ribbon, the Cantabrian–Central Iberian ribbon. Further testing of the model can be accomplished through (1) structural studies focused about the hinge zone of the Central-Iberian orocline (2) detailed paleomagnetic studies that can definitively constrain age and oroclinal nature of bending, and (3) faunal, geochronological and geochemical tests for terrane correlations within Iberia, across the Western European Variscan Belt, and into northern Africa. Pre-established correlations of Iberian tectonostratigraphic zones should also be reassessed in the context of an *S*-geometry double orocline pair.

Chapter 3. Provenance variability along the Lower Ordovician north Gondwana margin: Paleogeographic and tectonic implications of U-Pb detrital zircon ages from the Armorican Quartzite of the Iberian Variscan belt[2]

3.1 Abstract

Detrital zircon laser-ablation-inductively coupled plasma-mass spectrometry U-Pb age data from the Lower Ordovician Armorican Quartzite (deformed passive margin strata of Gondwanan affinity) of the Iberian Massif are presented herein. The *S*-shaped coupled Iberian oroclines defined within these zones palinspastically restore to a 2300 km linear Variscan orogen with a paleomagnetically constrained Late Carboniferous north-south trend. Detrital zircons are used to assess paleogeography and interpreted geometry of the Iberian portion of the Gondwana passive margin. A common signature is identified by (1) Neoproterozoic (ca. 500-850 Ma), (2) Stenian–Tonian (ca. 0.9–1.1 Ga), and lesser (3) Paleoproterozoic and (4) Archean populations (ca. 1.8-2.15 and 2.5-2.7 Ga, respectively). Minor site-to-site variation in relative proportion of widely ranging age groups suggests near-uniform distribution of a highly varied detrital input. Provenance analysis reveals strong similarities with Cambro-Ordovician clastic rocks from northeast African realms. Similarity with underlying sequences suggests a common paleogeography from the Ediacaran through early Paleozoic and persistence of a provenance distinction within the autochthonous Iberian Massif. Consistent northward paleoflow within widespread northeast African lower Paleozoic sedimentary cover suggests long-distance sedimentary transport across a North African peneplain from outlying basement terranes. We propose that the 2300 km long Cantabrian–Central Iberian portion of the early Paleozoic Gondwana margin stretched east-west along the northern limits of the then low-lying Saharan hinterland and Arabian-Nubian Shield. Accepting paleomagnetic constraints, a 90° counterclockwise rotation is required to reorient the Iberian portion to a pre-oroclinal (Late Carboniferous) north-south trend. The mechanisms for accommodating such a rotation are unclear.

[2] This chapter is published as: Shaw, J., Gutiérrez-Alonso, G., Johnston, S.T., and Galán, D.P., 2014, Provenance variability along the Early Ordovician north Gondwana margin: Paleogeographic and tectonic implications of U-Pb detrital zircon ages from the Armorican Quartzite of the Iberian Variscan belt: Geological Society of America Bulletin, v. 126, p. 702–719, doi: 10.1130/B30935.1.

3.2 Introduction

Detrital zircon age dating is a powerful tool in deciphering sedimentary provenance, and constraining paleogeography and tectonic evolution of continental realms. Sampling within restricted areas through thick stratigraphic successions can address questions regarding local tectonic evolution (e.g. May et al., 2013; LeMaskin, 2012). Alternatively, sampling over a wide area within a single stratigraphic level (formation), can yield formidable constraints on a variety of spatial variables at the point in time of interest, from relative location between continental masses, to continental geometry and orientation.

This study presents detrital zircon age data sampled from the Lower Ordovician Armorican Quartzite (*sensu lato*) over a geographical area of roughly 150,000 km^2 within the Variscan orogen of Iberia. The Variscan orogen of Iberia is characterized by the continental-scale *S*-shaped Cantabrian–Central Iberian coupled oroclines (Aerden, 2004; Martínez Catalán, 2011; Shaw et al., 2012) (Fig. 3-1), and is divisible into a series of tectonostratigraphic zones. From the core of the Cantabrian orocline south, four of these zones, the (1) Cantabrian, (2) West Asturian–Leonese, (3) Central Iberian and (4) Ossa-Morena, are considered parts of autochthonous Gondwana. Allochthonous terranes of the Iberian Variscan belt include (1) an ophiolite bearing structural stack that overrides the hinterland zone 3 at the core of the Central Iberian orocline (e.g. Pérez-Estaún et al., 1991 and references therein), and (2) a swath of presumed-exotic continental crust independently sutured to the south of zone 4 (e.g. Martínez Catalán et al., 2007).

The Armorican Quartzite is characteristic of the lower Paleozoic Gondwana passive-margin sequence of zones 1 to 3. A 5-40 km wide fault-bound band of rock at the boundary between zones 3 and 4 has, on the basis of structural data and stratigraphic correlations, been interpreted as being transitional between them (Pereira and Silva, 2001; Solá et al., 2008). The Ossa Morena–Central Iberian transition zone, hereafter referred to as the transition zone (Fig. 3-1), extends north from the sinistral Badajoz-Cordoba shear zone to the Los Pedroches batholith (Linnemann et al., 2008 and references therein). It is characterized by a zone 4-type lower Ediacaran–Cambrian stratigraphic sequence overlain by a zone 3-type Ordovician sequence (Bandres et al., 2002; Pereira and Silva, 2002; Pereira et al., 2010). Though it is generally believed that no Armorican Quartzite equivalent exists within the Ordovician stratigraphic sequence of zone 4 (Robardet and Gutiérrez-Marco, 1990a, b, 2004), the Sierra

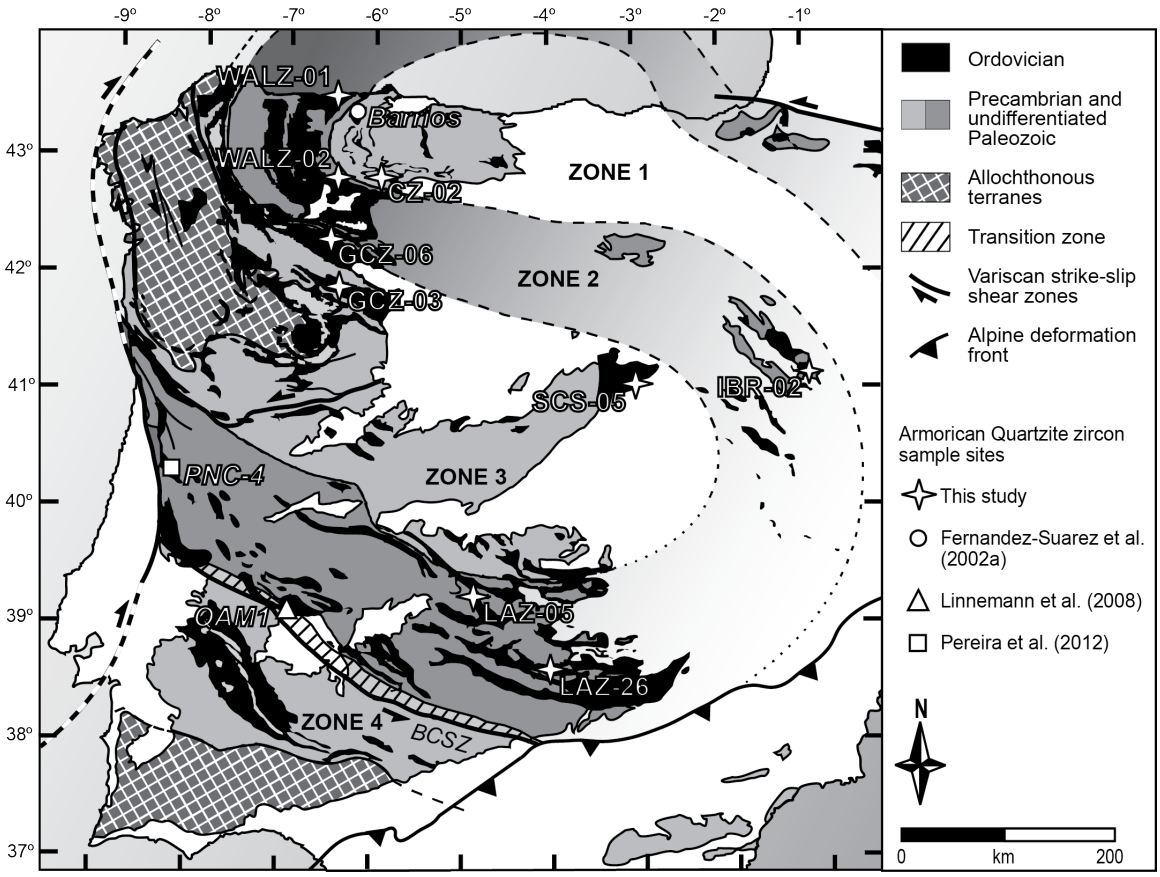

Figure 3-1 Collection sites for detrital zircons from the Iberian Armorican Quartzite from this and from previous studies in (the Cantabrian) zone 1 (Fernández-Suarez et al., 2002a), (the Central Iberian) zone 3 of Portugal (Pereira et al., 2012), and the zone 3–4 (Ossa Morena) transition zone (Linnemann et al., 2008). Sample coordinate data for this study are given in the Appendix (Table A-3). The more darkly shaded external hinterland of the Variscan orogen reveals the geometry of the coupled Cantabrian–Central Iberian oroclines. The external hinterland (West Asturian–Leonese) zone 2 is continuous with the southern zone 3 through the unexposed hinge of the Central Iberian orocline, after Shaw et al. (2012). BCSZ—Badajoz-Cordoba shear zone.

Albarrana Quartzites, exposed just south of the transition zone boundary and loosely constrained as early Paleozoic in age (Azor et al., 1991; Marcos et al., 1991), have been suggested as possible correlatives (Azor et al., 1991). The Cantabrian–Central Iberian coupled oroclines were defined in, and affect that portion of, the Variscan orogen located north of the transition zone; the nature of the relationship between the coupled oroclines and that portion of the Iberian Massif that lies to their south (zone 4 and the southern allochthon) remains unclear.

Paleomagnetic and structural studies have demonstrated that the Cantabrian orocline formed by lithospheric-scale vertical-axis rotation of an originally linear Variscan orogen in the Late Carboniferous–earliest Permian (Kollmeier et al., 2000; Merino-Tomé et al., 2009; Pastor-Galán et al., 2011; Weil et al., 2000, 2001, 2010, 2013b). Continuity between the Cantabrian and Central Iberian oroclines is supported by structural (Aerden, 2004), geophysical (Ardizone et al., 1989), sedimentological, and faunal data (Aramburu and García-Ramos, 1993; Robardet, 2002; Robardet and Gutiérrez-Marco, 1990a). Coeval development of the Cantabrian and Central Iberian oroclines is consistent with their coupled nature and with available paleomagnetic data (Table 3-1 and references therein). Palinspastic restoration of the coupled Iberian oroclines to a paleomagnetically constrained north-south trend (Weil et al., 2010) yields a 2300 km long segment of the Variscan orogen (Fig. 3-2). The easterly autochthonous portion of the orogen consists primarily of a deformed west-facing (in present-day coordinates) lower Paleozoic passive-margin sequence of Gondwanan affinity (Murphy et al., 2008) referred to as the Cantabrian–Central Iberian margin (CCIM).

Table 3-1 Available paleomagnetic data for the Iberian Massif and Pyrennees

Name	Relative location within oroclinal pair	Likely age	D	I	D^{-1}†	Paleo-Latitude§	α_{95}	Reference
San Pedro	Common limb of fold pair	Siluro-Devonian	113º	+34º	293º	21ºS	10	Perroud & Bonhommet, 1984
Griotte	North limb of Cantabrian orocline	Siluro-Devonian	224º	+51º	44º	30ºS	8.5	Tait et al., 2000b
Almaden-1	South limb of Central Iberian orocline	Silurian	62º	-36º	64º	20ºS	14	Perroud et al., 1991
Almaden-2	South limb of Central Iberian orocline	Devonian	81º	-37º	81º	20ºS	10	Parés & Van der Voo, 1992
Beja	South limb of Central Iberian orocline	Early Carboniferous	36º	-49º	36º	29ºS	16	Ruffet, 1990

Note: D—declination; I—inclination.
* North of the Badajoz-Córdoba shear zone.
† Inverted declination corresponding to negative inclination implying, for the southern hemispheric latitudes, a north-seeking magnetization and normal polarity (R. Van der Voo, personal communication, 2011).
§Likely paleo-latitude based on a north-seeking magnetization and normal polarity.

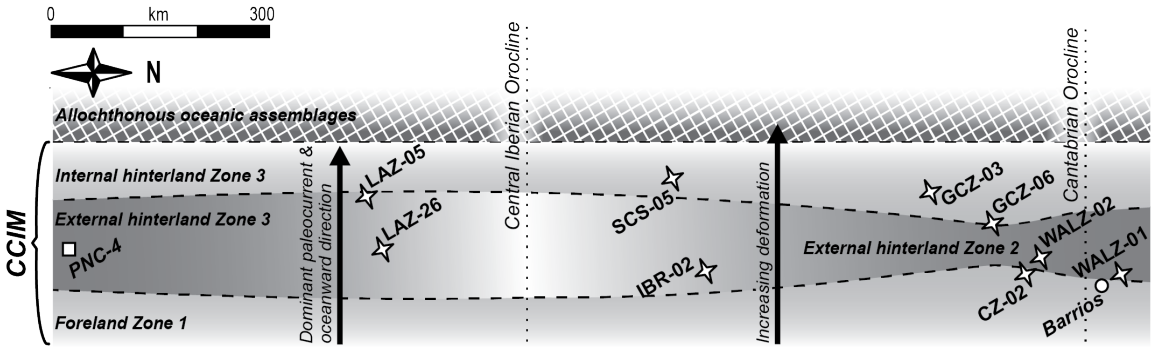

Figure 3-2 Relative locations of sample collection sites along the ca. 1500 km long studied segment of the palinspastically restored Iberian Variscan belt, after Shaw et al. (2012). Neither margin-parallel shortening preceding oroclinal formation nor strike-perpendicular shortening likely to have been assumed during bending are restored. The deformed CCIM (Cantabrian–Central Iberian margin) consists of, from coastal to distal shelf, autochthonous zones 1, 2 and 3.

Interpretation of the Ibero-Variscan orogen as having originated as a north-south striking linear belt requires along-strike continuity of stratigraphic units through the 2300 km length of the CCIM. This requirement is testable. If stratigraphic continuity along the margin can be demonstrated, efforts must be made to (1) constrain the paleogeographic origin of the CCIM along the Gondwana margin and (2) assess the relationship between the stratigraphic sequence of the CCIM and the passive-margin strata of southwestern Iberia that are also thought to be of Gondwanan affinity. Detrital zircon age data presented herein stem from samples of the Armorican Quartzite collected along a 1500 km length of the CCIM. Sampling a single formation (and hence a narrow time slice) over a large area enables us to (1) assess interpretation of the CCIM as having originated as a north-striking, west-facing, linear and coherent segment of the early Paleozoic Gondwana passive margin, (2) provide further constraints on the nature of the boundary between tectonostratigraphic zones 3 and 4 by assessing provenance distinctions across it, and (3) limit the paleogeography of the CCIM through sedimentary provenance analysis. Our study demonstrates that paleogeography can be effectively and reliably constrained using zircon provenance analyses that focus on comparison of contemporaneous clastic sequences rather than on the comparison of clastic sequence against potential basement source. The detailed Early Ordovician ‘snapshot’ of the Iberian Gondwana margin revealed through detrital zircon ages yields broad and significant

implications for the pre-Ordovician paleogeography and post-Ordovician tectonic evolution of the Variscan orogen.

3.3 Geologic setting

3.3.1 The Armorican Quartzite

The Armorican Quartzite consists of thick-bedded (decameter to meter scale) clean quartzites, meta-sandstones, phyllitic siltstones, and rare layers of volcanic rock and shale. Sedimentological studies indicate a range of depositional facies that grade outward from proximal deltaic in zone 1 (Aramburu, 1989; Aramburu and García-Ramos, 1993; Aramburu et al., 2004) to shallow-water nearshore with tidal, shore-current and storm influences in zones 2 and 3 (Gutiérrez-Marco et al., 2002 and references therein). Paleocurrent data indicate that dominant transport direction in the Armorican Quartzite is offshore, fanning outboard of the foreland core of the Cantabrian orocline in the north (Aramburu and García-Ramos, 1993; Shaw et al., 2012), and focusing inward toward allochthonous terranes at the core of the Central Iberian orocline in the south (Shaw et al., 2012). A K-bentonite (altered ash-fall tuff) interbedded within the Armorican Quartzite of zone 1 yielded a U-Pb zircon age of 477 ± 1 Ma (Gutiérrez-Alonso et al., 2007). Units correlative with the Armorican Quartzite occur in North and West Africa, as far east as Serbia, and in the Armorican and Bohemian massifs of France and Germany, respectively (Fernández-Suárez et al., 2002a; Gutiérrez-Alonso et al., 2007).

3.3.2 Existing Provenance Constraints

Autochthonous Iberia (zones 1-4) is stratigraphically linked with the North African Gondwanan realm (Noblet and Lefort, 1990), and Neoproterozoic–early Paleozoic paleogeographic reconstructions commonly place it adjacent to Morocco and the West African craton (e.g. Murphy et al., 2004, 2006; Nance and Murphy, 1994). Several recent models have proposed a variety of Central to East African early Paleozoic paleogeographic locations for Iberia, based on (1) paleontological grounds (Gutiérrez-Marco et al., 2002 and references therein) (2) detrital zircon studies within para-allochthonous terranes of northwestern Iberia (Díez Fernández et al., 2010, Fernández-Suárez et al., 2013), and (3) isotopic and inherited zircon studies of Central Iberian Cambro-Ordovician magmatic rocks

(Bea et al., 2010). However, the assumption of a common paleogeographic history for a cohesive Iberian Massif may be flawed. Detrital zircons from Ediacaran–Cambrian clastic strata of zone 4 display a signature thought to be characteristic of a West African provenance (Fernández-Suárez et al., 2002b). In contrast, Ediacaran–lower Paleozoic clastic rocks of zones 1-3 contain significant numbers of Stenian–Tonian aged (ca. 0.9-1.1 Ga) zircons (Ábalos et al., 2012; Fernández-Suárez et al., 2000a, 2013; Gutiérrez-Alonso et al., 2003; Talavera et al., 2012) for which there is no known source within the West African Craton (Rocci et al., 1991). As Stenian–Tonian zircons have also been documented within Devonian and Carboniferous clastic rocks of zone 3 (Martínez Catalán, 2008) and Silurian through lowermost Permian clastic rocks of zone 1 (Pastor-Galán et al., 2013), they may be characterisitic of the entire pre-Variscan Paleozoic sequence within northern and central Iberia.

How to reconcile the contrasting Ediacaran–early Paleozoic provenance of strata from zones 3 and 4 across the transitional boundary between them remains unclear, and complex late Neoproterozoic–Devonian histories have been postulated for the outlying zone 4 (Azor et al., 1994; Gómez-Pugnaire et al., 2003). Paleobiological data have been used to suggest a deep-water distal origin for the early Paleozoic Gondwanan zone 4 platform (Robardet and Gutiérrez-Marco, 1990a, b, 2004), the manner and timing by which it arrived at its present-day relative position with respect to zone 3 remaining unclear. Owing to the inherent ambiguities, the geometry of the coupled Iberian oroclines cannot yet be defined across the transition zone, and we consider the palinspastically restored (pre-orocline) CCIM independently of both the transition zone and zone 4.

3.4 Sampling

The laser ablation-inductively coupled plasma-mass spectrometry (LA-ICP-MS) U-Pb age analyses of detrital zircons presented in this study are from samples collected at nine locations within zones 1, 2 and 3 (Fig. 3-1). Collection was aimed at covering the ~1500-km-long portion of the CCIM that today constitutes the northern and central Iberian Massif (Fig. 3-2). No samples were collected from the less discrete Pyrenean continuation of the northern limb of the Cantabrian orocline. Sample WALZ-01, which represents the study's northernmost sampling site, was collected at Playa de Cueva in Canero, Asturias. Sample

WALZ-02 was taken within the upper sequence of the Los Cabos Group (local formation name), just south of the Presa (dam) de las Ondinas, Palacios del Sil, León. Sample CZ-02 was collected on the western side of the dam at Barrios de Luna, León, from which the local formation name Barrios de Luna is taken, at a stratigraphic height of 20 m above the K-bentonite bed dated at 477 ± 1 Ma by Gutiérrez-Alonso et al. (2007). Samples GCZ-03 and GCZ-06 are from within the Galician–Castillian Zone, a northern subdivision of zone 3 (Lotze, 1945), from the northern limb of the Alcañices syncline at San Pedro de Las Herrerias, Zamora, and the northern limb of the Truchas syncline north-northwest of Corporales, Truchas, Zamora, respectively. Sample SCS-05 was collected within the Spanish Central System (easternmost Galician-Castillian subzone) NW of Bustares, Guadalajara, in a basal unit of the Armorican Quartzite formation. Sample IBR-02 was taken at La Ermita de la Virgen de Herrera, south of Herrerra de los Navarros, Zaragoza, in the eastern Iberian Cordillera, discontinuous in exposure but commonly correlated with zone 2. Samples LAZ-26 and LAZ-05 were collected from within the Luso Alcudian southern subdivision of zone 3 (Lotze, 1945). LAZ-26 was collected from west of Puertollano, Ciudad Real, and LAZ-05 from the northeastern limb of the Anticlinorio de Guadalupe west of Helechosa de los Montes, Toledo, where the base of the Armorican Quartzite formation is locally conglomeratic and which represents the southernmost sampling site along the palinspastically restored CCIM. Coordinate data for each collection site are provided within Table A-3 in the Appendix.

Samples were selected in the field based on grain size and textural maturity. Petrographic and geochemical analyses reveal the samples to be mineralogically mature, consisting mainly of quartz grains (up to 99%; see Table 3-2 for major element geochemistry; trace element geochemistry is provided in Table A-4 in the Appendix). Most of the samples studied are unmetamorphosed or were recrystallized under low-grade conditions, excepting sample SCS-05, for which metamorphic grade is slightly higher. Previous detrital zircon studies of the Armorican Quartzite within the Iberian massif are limited to three publications providing single-sample analyses, one of which is based on a sample collected within the transition zone (Fernández-Suárez et al., 2002a; Linnemann et al., 2008; Pereira et al., 2012) (see Figs. 1, 2). Other samples from lower Paleozoic Iberian clastic rocks not including the Armorican Quartzite are reported in Martínez Catalán et al. (2004) and Talavera et al. (2012).

Table 3-2 Major element geochemistry for the Armorican Quartzite of the Iberian Massif

		CZ-02	WALZ-01	WALZ-02	IBR-2	GC-03	GCZ-06	SCS-05	LAZ-05	LAZ-26
SiO_2	(%)	98.25	91.55	98.51	97.41	97.43	95.56	89.2	91.87	93.48
TiO_2	(%)	0.16	0.178	0.13	0.152	0.199	0.578	0.623	0.176	0.313
Al_2O_3	(%)	0.56	4.22	0.5	0.88	1	1.7	6.1	2.51	2.83
Fe_2O_3	(%)	0.2	0.28	0.34	0.19	0.51	0.33	0.54	3.91	2.34
MnO	(%)	0*	0*	0.016	0.002	0.005	0*	0*	0.004	0*
MgO	(%)	0*	0*	0*	0*	0*	0.01	0.09	0*	0*
CaO	(%)	0.01	0.01	0.01	0.01	0.01	0.01	0.01	0.01	0.01
Na_2O	(%)	0*	0*	0*	0*	0*	0.06	0*	0*	0*
K_2O	(%)	0.15	1.95	0.14	0.23	0.31	0.38	1.93	0.13	0.4
P_2O_5	(%)	0.027	0.029	0.015	0.029	0.026	0.032	0.034	0.053	0.056
LOI	(%)	0.19	0.77	0.00	0.20	0.09	0.50	1.18	1.08	0.89
Sum†	(%)	99.55	98.99	99.66	99.10	99.58	99.16	99.71	99.74	100.32

Note: SuperQ quantitative analysis of glass discs conducted using a Phillips PW2400 spectrometer at the Regional Geochemical Centre, St Mary's University, Halifax, Nova Scotia B3H 3C3.
* Negative calculated quantity, assumed to be zero.
† Total values do not include trace elements.

3.5 Analytical techniques

Initial preparation of field samples was conducted at the Salamanca and Complutense (Madrid) universities. Fresh samples were crushed with a jaw crusher then pulverized with a disc mill. Zircons were isolated by heavy-fraction enrichment on a Wilfley table followed by density separation using diodomethane (CH_2I_2) and magnetic separation in a Franz isodynamic separator. Final stages of sample preparation and LA-ICP-MS-U-Pb analysis were conducted at the Sektion Geochronologie of the Senckenberg Naturhistorische Sammlungen Dresden, Museum für Mineralogie und Geologie (Germany). A representative suite of zircon grains were mounted, and set in resin blocks. Resin-mounted zircons were then hand polished to approximately half their thickness, bringing a full cross section flush with the surface; each mount was cleaned in a 5% HNO_3 bath prior to ablation. Each sample is characterized by a similar range of zircon morphology. Grains are rose coloured to colourless and relatively fine. Larger grains (up to 350 μm c-axis in LAZ-05) are euhedral to subrounded prisms whereas smaller grains (as little as 25 μm diameter) are well rounded.

Zircons were analysed for U, Th and Pb isotopes by LA-ICP-MS techniques using a Thermo-Scientific Element 2 XR sector field ICP-MS coupled to a New Wave UP-193 Excimer Laser System. Each analysis consisted of 15 s of background acquisition followed

by 35 s of data acquisition with laser pits 20, 25, or 35 μ wide, depending on the crystal size, and no more than 15 μ deep. A common-Pb correction based on the interference-and background corrected ^{204}Pb signal and a model-Pb composition (Stacey and Kramers, 1975) was carried out where necessary. The necessity of the correction was judged on whether the corrected ^{207}Pb/^{206}Pb lay outside of the internal errors of the measured ratios. Raw data were corrected for background signal, common Pb, laser-induced elemental fractionation, instrumental mass discrimination, and time-dependent elemental fractionation of Pb/Th and Pb/U using a Microsoft Excel spreadsheet program developed by Axel Gerdes (Institute of Geosciences, Johann Wolfgang Geothe-University Frankfurt, Frankfurt am Main, Germany). Reported uncertainties were propagated by quadratic addition (the square root of the sum of squares) of the external reproducibility obtained from the standard zircon GJ1 (~0.6% and 0.5-1% for the ^{207}Pb/^{206}Pb and ^{206}Pb/^{238}U, respectively) during individual analytical sessions and the within-run precision of each analysis. For further detail on analytical protocol and data processing see Frei and Gerdes, (2009).

3.6 Detrital zircon ages

3.6.1 Data Treatment

A minimum of 120 U-Pb age determinations, as required for statistical adequacy in detrital provenance analysis, were performed on each sample (one analysis in the center of each grain) (see Vermeesch, 2004; Anderson, 2005; Link et al., 2005). Analyses with discordance higher than 10% (i.e. concordance <90% or >110%) were rejected. The remaining U-Pb data are represented in concordia diagrams (Fig. 3-3) drawn using *Isoplot 3.7* (Ludwig, 2009), and in relative probability plot and histogram combined displays (Fig. 3-4), generated with the *AgeDisplay* Excel®-based macro (Sircombe, 2004). Complete data tables are available as Table A-5 in the Appendix. Age assignment for each analysis (*Reported Age* column in Table A-5) is as follows: for analyses whose 2σ error ellipses overlap the concordia curve, the chosen age (and 2σ error) are the concordia age and error (Ludwig, 2009) as calculated by *Isoplot 3.7*. For analyses that are less than 10% discordant but whose corresponding 2σ ellipses do not intercept the concordia curve we have chosen either the ^{207}Pb/^{206}Pb or the ^{206}Pb/^{238}U age depending on which corresponding isotope ratio was measured with greater precision in that particular analysis.

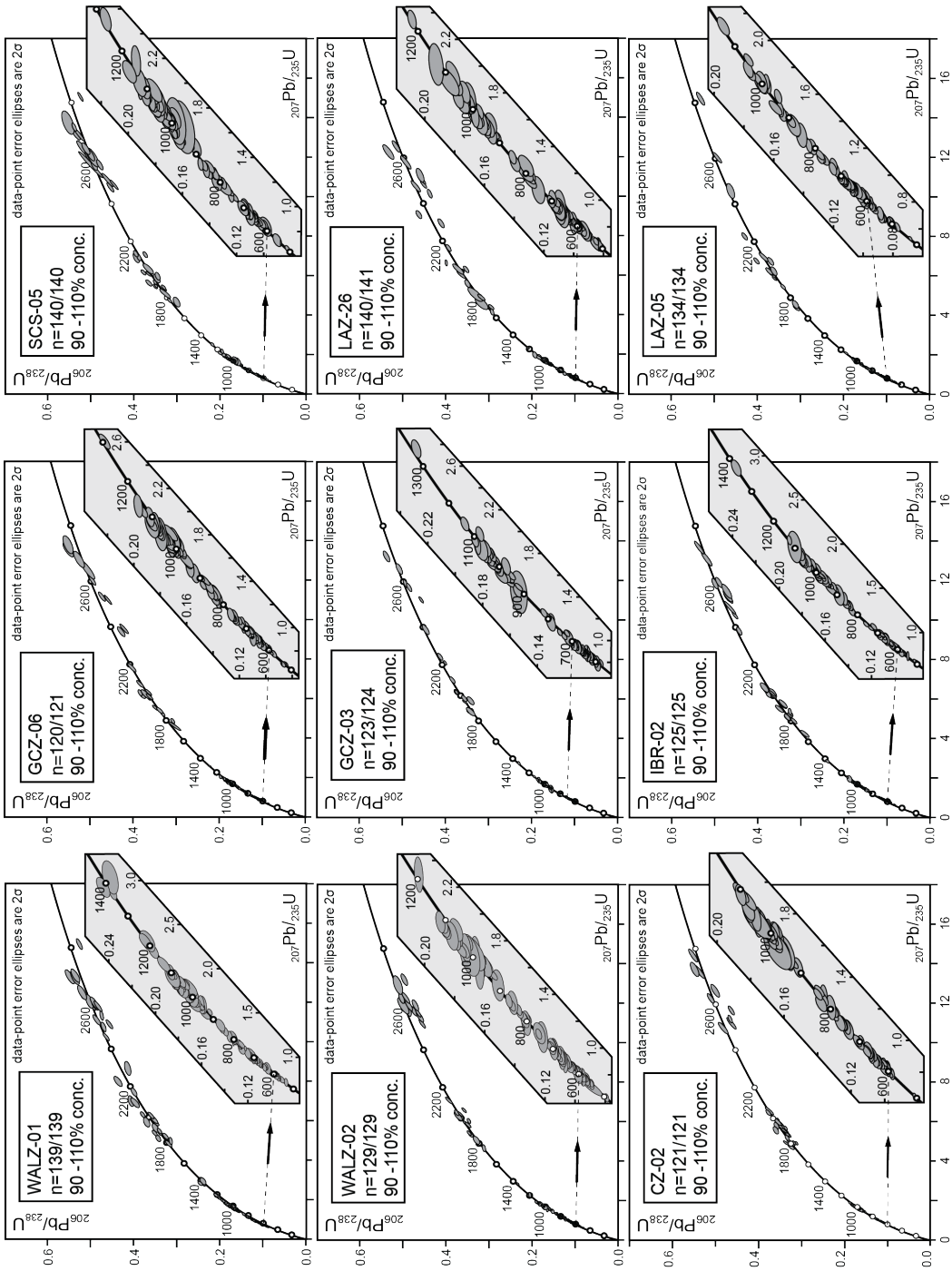

Figure 3-3 Concordia plots of laser inductively-coupled plasma-mass spectrometry U-Pb analyses of detrital zircon grains for each of the nine sample sites from within the Lower Ordovician Armorican Quartzite of the Cantabrian–Cantral Iberian margin. Insets show enlargement of younger ages; n = number of grains displayed/number of concordant analyses. For graphical clarity, outlying Archean aged grains from samples GCZ-03 (3434 Ma; ±30 2σ error; 98% concordance), GCZ-06 (3434 Ma; ±21 2σ error; 101% concordance) and LAZ-26 3382 Ma; ±15 2σ error; 96% concordance) are not plotted.

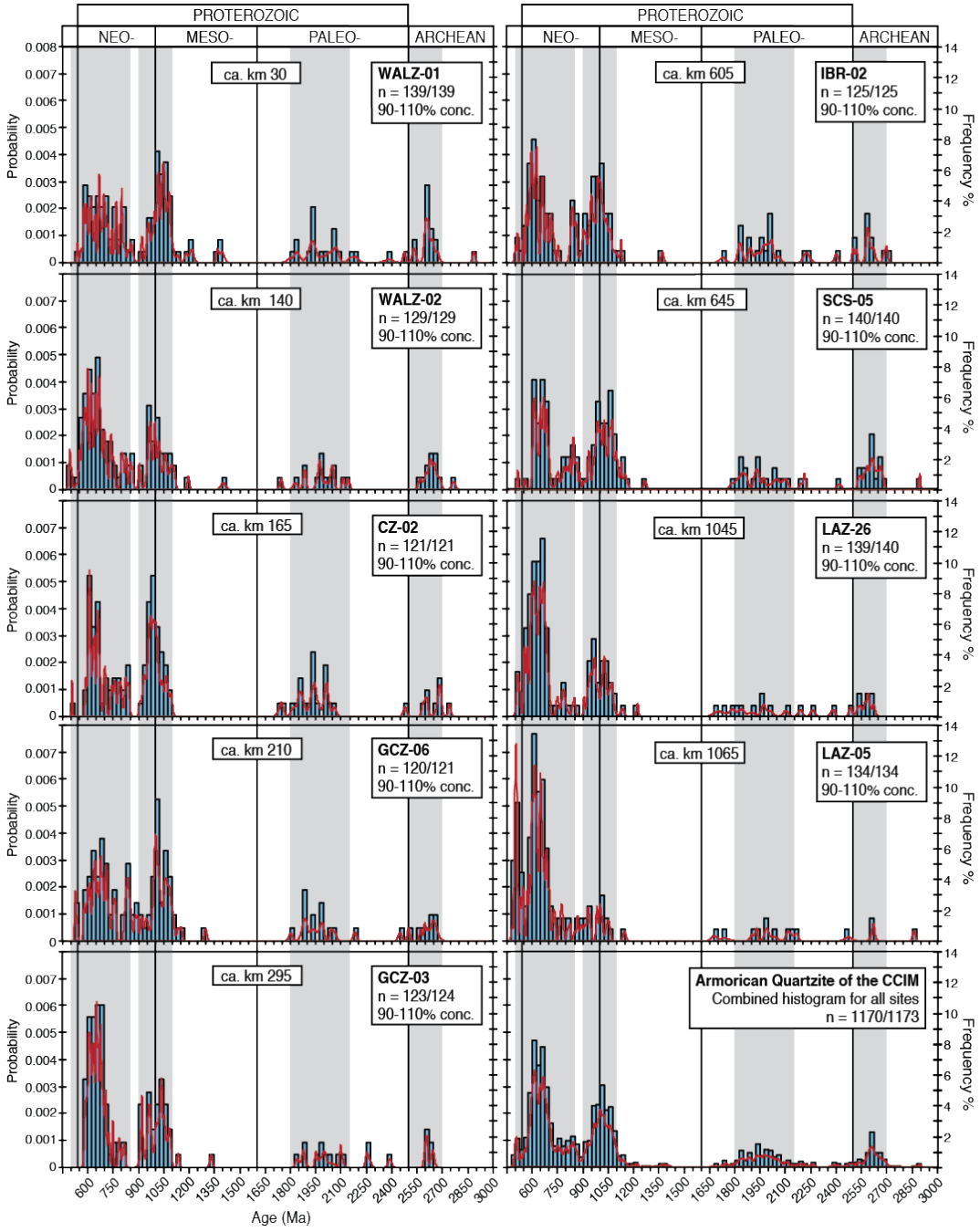

Figure 3-4 Combined histogram and probability distribution density plots of detrital zircon grains for each of the nine sample sites within the Lower Ordovician Armorican Quartzite of the Cantabrian-Central Iberian margin (CCIM) and for all samples combined. The shaded bars highlight the ranges of the four main age populations. Distances south along the studied 1500 km segment of the palinspastically restored CCIM are given from a northernmost reference, site WALZ-01. n = number of grains displayed/number of concordant analyses. For graphical clarity, outlying Archean aged grains from GCZ-03 (3434 Ma; ±21 2σ error; 98% concordance), GCZ-06 (3232 Ma; ±30 2σ error; 101% concordance) and LAZ-26 (3382 Ma; ±15 2σ error; 96% concordance) are not plotted.

3.6.2 Data analysis

Detrital zircon ages are examined in the context of the coupled Iberian oroclines; samples are ordered by relative north-to-south location along the palinspastically restored 1500 km long segment of the CCIM (Fig. 3-2). Four dominant U-Pb age population groups define a detrital zircon signature common across the studied area. Each sample contains a nearly continuous suite of zircon ages between ca. 550 and 1100 Ma, accounting for 70-80% of the total number of concordant grains analysed per sample. Two peaks sandwiching a prevalent 850-900 Ma minimum within this range suggest two dominant age populations, (1) Neoproterozoic (ca. 500-850 Ma) and (2) Stenian–Tonian (ca. 0.9-1.1 Ga). Less dominant Paleoproterozoic (ca. 1.8-2.15 Ga) and Archean (ca. 2.5-2.7 Ga) populations have more poorly defined peaks at 1.9 and 2.6 Ga, respectively. The greatest degree of variability between samples is expressed within Paleozoic zircons. Most samples contain fewer than 5% grains with concordant Cambrian–earliest Ordovician ages; sample LAZ-05 is the exception, with 18.6%. The youngest concordant age (481 ± 11 Ma) was measured in sample LAZ-05. Our samples are characterized by a paucity of Late Paleoproterozoic to early Mesoproterozoic zircons, with only a fraction of a percent of all concordant grains within the range of 1.3–1.7 Ga.

Statistical comparison of age distributions between sampling sites and with external datasets during provenance analysis is carried out through multiple two-sample Kolmogorov-Smirnov (K-S) tests in a manner similar to those employed by previous studies seeking to assess common provenance (Amidon et al., 2005; Barbeau et al., 2009; Berry et al., 2001; DeGraaf-Surpless et al., 2003; Dickinson et al., 2010). The K-S test assigns a value of difference (D) that corresponds to a probability value (P) that both sample groups were randomly selected from identical parent populations. This analysis incorporates the errors on each individual zircon age date. We accept any two samples that are not significantly different at a 5% significance level ($P > 0.05$) as derived from erosion of the same source area. Any two samples that are not significantly different at a 0.1% significance level ($0.05 > P \geq 0.001$) are interpreted as possibly derived from erosion of the same source area. Any two samples that are significantly different at the 0.1% significance level ($P < 0.001$) are interpreted as derived from erosion of different source areas. We caution, however, that use of the K-S is best reserved as a quantitative supplement to first-order qualitative visual

comparisons of detrital zircon age spectra, particularly when assessing common provenance on a regional scale. K-S tests were performed using an Excel®-based macro developed at the Arizona LaserChron Center (ALC) in the Department of Geosciences at the University of Arizona (Guynn and Gehrels, 2010). As the Armorican Quartzite is characterized by rare volcaniclastic layers, the observed high variability of Paleozoic zircons may be attributable to intermittent input from local volcanic sources. In an effort to buffer against this variability detrital zircon ages < 500 Ma were excluded from the two-sample K-S tests ("reported age" values in Table A-5 and preferred age values from external datasets).

3.7 Interpretation and discussion

3.7.1 Provenance relationships within Iberia

The detrital zircon age spectra identified within each of the nine studied samples provide constraints on the nature and geometry of the CCIM. Our samples are characterized by an age spectra consistent with those reported by previous studies from zone 1 (sample *Barrios*; Fernández-Suárez et al., 2002a) and zone 3 (sample *PNC-4*; Pereira et al., 2012), which represent north and south end-member locations along the palinspastically restored CCIM, respectively. An along-strike trend, characterized by a southward decrease in the Stenian–Tonian signature balanced by a southward increase in the Neoproterozoic signature, is apparent. The trend is made most evident by comparison of our palinspastically restored northern and southern end-member sites (WALZ-01 and LAZ-05, respectively) with the previously published data sets (Fig. 3-5). Northern samples, WALZ-01 and *Barrios,* are characterized by robust Stenian–Tonian populations (31.6% and 22% concordant grains, respectively). In contrast, the southernmost samples, LAZ-05 and *PNC-4,* have similar Stenian–Tonian populations (10.4 and 8%, respectively), but greater numbers of middle to late Neoproterozoic (59.7 and 60%), as well as many Cambrian (17.9 and 20%) zircons. The degree of along-strike variability is also apparent within the site-to-site two-sample K-S test results (Table 3-3). Sites along the first 650 km of the restored margin appear to be derived from erosion of the same or similar source regions, with the possible exception of GCZ-03, which is significantly different from 70% of the northern sites at the 5% significance level. Southern sites LAZ-26 and LAZ-05 are not significantly different from one another at the 5% significance level, but significantly different from 60% and 100% of the northern sites,

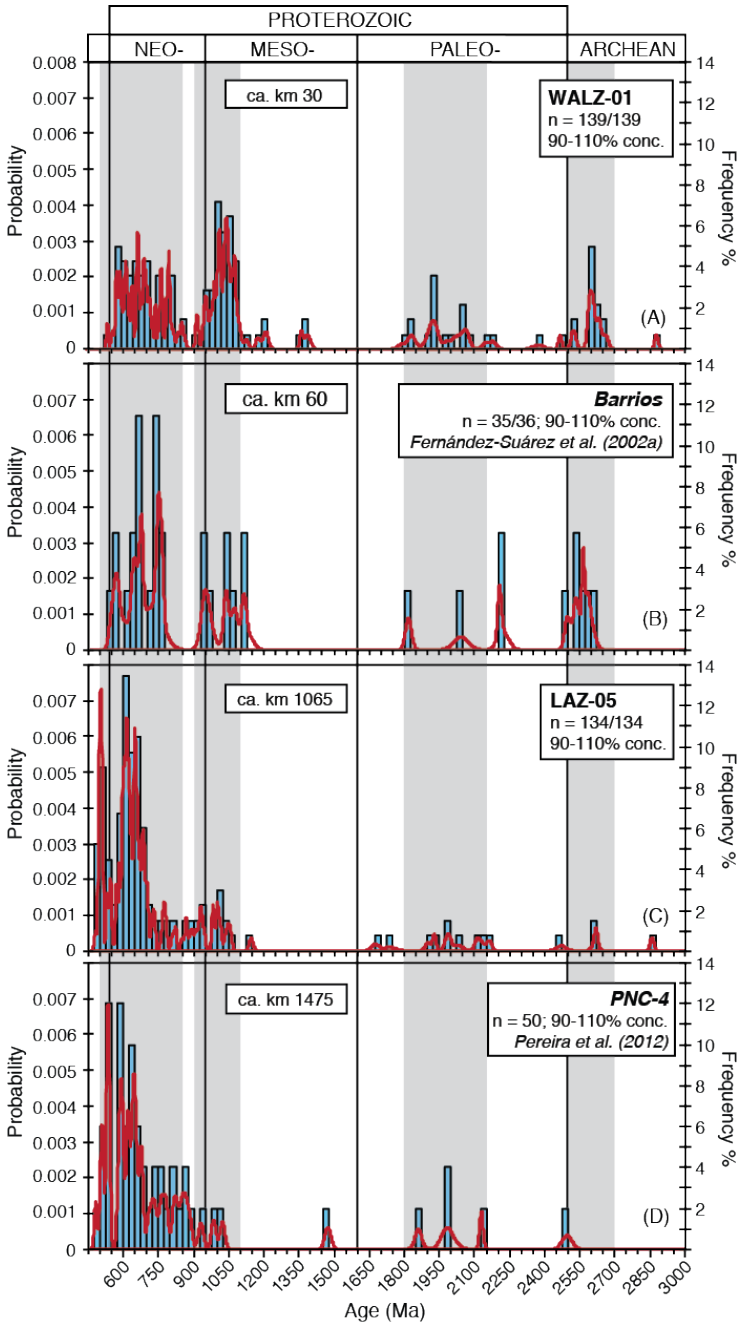

Figure 3-5 Sample size-normalized histogram and probability density plots comparing previous U-Pb detrital zircons studies form the Armorican Quartzite of the Cantabrian-Central Iberian margin (CCIM) with the most proximal sample sites from this study. Samples represent northern (A) WALZ-02, (B) *Barrios,* and southern (C) LAZ-05, (D) *PNC-4*, end member locations along the palinspastically restored CCIM. Displayed preferred ages are selected on the criteria established in each original publication; originally published data with greater than 10% discordance are excluded. n = number of grains displayed/number of concordant analyses; concordant analyses excluded for graphical clarity are single grains > 3.0 Ga. The shaded bars highlight the ranges of the four main CCIM age populations.

Table 3-3 Comparison of detrital zircon age spectra with the Armorican Quartzite using the K-S statistical test

P < 0.001	(statistically different at the 0.1% significance level)	0.05 > P ≥ 0.001	(statistically different at the 5% significance level)	P > 0.05	(not statistically different at the 5% significance level)

	WALZ-01	***Barrios****	**WALZ-02**	CZ-02	**GCZ-06**	**GCZ-03**	**IBR-02**	**SCS-05**	**LAZ-26**	**LAZ-05**	***PNC-4***†	***QAM-1***§
WALZ-01 n = 139/139		0.496	0.019	0.111	0.378	0.001	0.074	0.998	< 0.001	< 0.001	< 0.001	< 0.001
Barrios* n = 36/36	0.155		0.509	0.329	0.437	0.313	0.524	0.335	0.057	0.001	0.015	< 0.001
WALZ-02 n = 127/129	0.188	0.155		0.076	0.181	0.826	0.199	0.015	0.121	< 0.001	0.010	< 0.001
CZ-02 n =121/121	0.149	0.180	0.162		0.906	0.005	0.752	0.239	< 0.001	< 0.001	< 0.001	< 0.001
GCZ-06 n = 118/121	0.113	0.165	0.139	0.073		0.019	0.468	0.626	< 0.001	< 0.001	< 0.001	< 0.001
GCZ-03 n = 121/124	0.239	0.182	0.079	0.221	0.195		0.031	0.001	0.320	0.003	0.019	< 0.001
IBR-02 n = 124/125	0.158	0.154	0.135	0.086	0.108	0.183		0.169	0.003	< 0.001	< 0.001	< 0.001
SCS-05 n = 140/140	0.047	0.176	0.191	0.128	0.093	0.246	0.137		< 0.001	< 0.001	< 0.001	< 0.001
LAZ-26 n = 141/141	0.319	0.249	0.145	0.277	0.276	0.118	0.225	0.285		0.051	0.095	< 0.001
LAZ-05 n = 127/134	0.431	0.370	0.256	0.404	0.391	0.227	0.365	0.431	0.166		0.964	< 0.001
PNC-4† n = 49/50	0.430	0.343	0.273	0.418	0.352	0.258	0.368	0.435	0.205	0.084		< 0.001
QAM-1§ n = 31/31	0.687	0.647	0.648	0.716	0.687	0.706	0.657	0.725	0.614	0.546	0.513	

D Values

P Values

Note: Ages <500 Ma excluded from analyses, error incorporated.

*Fernandez-Suarez et al. (2002a)

†Pereira et al. (2012)

§Linnemann et al. (2008)

respectively. This statistical difference may reflect the large gap in data (400 km along strike between sites SCS-05 and LAZ-26) through the buried hinge of the Cantabrian orocline. The consistency of detrital age populations across zones 1-3 is nevertheless suggestive of the CCIM having constituted a coherent component of the Early Ordovician Gondwanan passive margin characterized by deposition on a uniform shelf receiving detrital input from both stable cratonic sources and areas of relatively recent tectonic activity.

The age spectra in our data differ from those reported by Linnemann et al. (2008) for the Armorican Quartzite of the transition zone (Fig. 3-6). Sample *QAM-1* fails each two-sample K-S test with high D values (> 0.5; Table 3-3), and though Linnemann et al. (2008) reported only a small number of concordant ages (n = 31), a paucity of Mesoproterozoic zircons in their sample contrasts with the strong Stenian–Tonian signal that is characteristic of Armorican Quartzite samples from the CCIM. An absence of Mesoproterozoic zircons, as that observed in the transition zone sample, is commonly considered a hallmark of West African provenance (e.g. Abati et al., 2010), and is likewise a defining characteristic of Ediacaran–Cambrian clastic sedimentary strata of zone 4 (Fernández-Suárez et al., 2002b).

Though recent studies have revealed a minor Stenian–Tonian signature within Middle Cambrian clastic rocks of the Moroccan Anti-Atlas (Avigad et al., 2012), the population is absent within older (Ediacaran and Lower Cambrian) sequences in the region, as well as absent within lower Paleozoic sequences of the Algerian Tuareg Shield (Linnemann et al., 2011). It was previously recognized that zones 3 and 4 could be distinguished based on detrital zircon provenance in Ediacaran rocks (e.g. Fernández-Suárez et al., 2000a, 2002b; Gutiérrez-Alonso et al., 2003). The boundary between the 'West African-type' zone 4 and the CCIM (zones 1-3), characterized by clastic detritus of Stenian–Tonian age, can now be located along the northern boundary of the transition zone. This provenance distinction, previously thought to be restricted to Ediacaran strata, persists through the Early Ordovician deposition of the Armorican Quartzite.

3.7.2 Ordovician paleogeography

Our detrital zircon data places limits on the sedimentary provenance of the Armorican Quartzite, and hence the Early Ordovician paleogeographic location of the CCIM. The

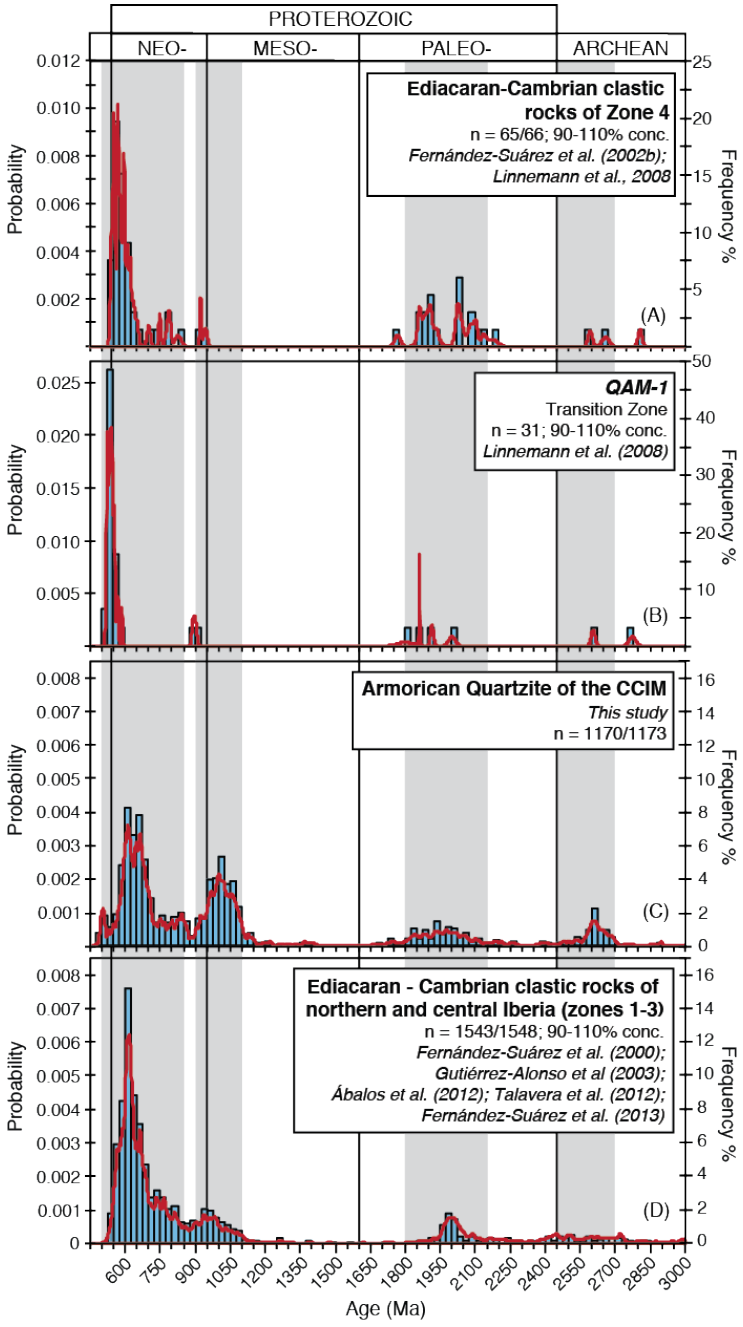

Figure 3-6 Sample size-normalized histogram and probability density plots comparing U-Pb detrital zircon ages for (A) Ediacaran–Cambrian clastic rocks of zone 4, (B) sample *QAM-1* of the (zone 3–4) transition zone, (C) the Armorican Quartzite of this study, and (D) Ediacaran and Cambrian clastic rocks from zones 1-3. Displayed preferred ages are selected on the criteria established in each original publication; originally published data with greater than 10% discordance are excluded. n = number of grains displayed/number of concordant analyses; concordant analyses excluded for graphical clarity are single grains > 3.0 Ga. Note that the y-axis scale in A and B has been changed in order to accommodate significant Neoproterozoic peaks. The shaded bars highlight the ranges of the four main CCIM age populations.

dominant Cryogenian–Ediacaran population is consistent with derivation from basement within West Gondwana. Neoproterozoic igneous rocks and related immature sedimentary sequences in West Gondwana are attributed to long-lived subduction along the northern Gondwana margin forming the Cadomian-Avalonian arc (Nance et al., 2008 and references therein), and to the Pan-African—Brasiliano orogenic belts, which record the amalgamation of Gondwana (500-800 Ma) (eg. Cawood and Buchan, 2007; Hoffman, 1991; Unrug, 1997). Younger zircons (<500 Ma) can be attributed to Cambro-Ordovician magmatism likely related to rifting of the north margin of Gondwana. Rifting explains the Cambro-Ordovician departure of peri-Gondwanan terranes, including Avalonia, (Díaz García, 2002; Díez Montes, 2006; Montero et al., 2007; Valverde-Vaquero et al., 2005) the opening and growth of the Rheic Ocean, and the development of the north-Gondwanan passive margin upon which the Armorican Quartzite was deposited. The youngest concordant age (481 ± 11 Ma) is in agreement with the previously established 477 Ma depositional age of the Armorican Quartzite (Gutiérrez-Alonso et al., 2007).

Stenian–Tonian crustal material is typically associated with the supercontinent Rodinia (e.g. Hoffman, 1991), but known material within the specific range of 0.9-1.1 Ga is limited within the stable cratonic realms of West Gondwana. The younger component of the range (0.9-1.0) exists within the Sunsas-Aguapei belts of the Amazonian craton (Teixeira et al., 1989). Older Mesoproterozoic rocks (1.0-1.6 Ga) are documented within the Namaqua-Natal belt along the southern limit of the Kaapvaal Craton (Eglington, 2006), within the Kibaran and Irumide belts along the respective western and southern margins of the Tanzania Craton (Cahen et al., 1984; De Waele et al., 2009; Johnson et al., 2007), and as lesser components within the dominantly Neoproterozoic Mozambique belt along the eastern margin of the Tanzania Craton (Kröner, 2001). The Armorican Quartzite, however, contains very few Mesoproterozoic zircons older than 1.1 Ga. Isolated regions within the Neoproterozoic Arabian–Nubian Shield that contain 0.9-1.1 Ga components (Be'eri-Shlevin et al., 2009; Eyal et al., 2013; Hargrove et al., 2006; Morag et al., 2012) are not substantial enough to account for the robust 0.9-1.1 Ga population within the Armorican Quartztite of the CCIM. In addition, the low topographic relief and widespread sedimentation that characterized north-central and northeast Africa during the early Paleozoic (e.g. Avigad et al., 2012; Noblet and Lefort, 1990), yielded Cambro-Ordovician clastic sequences that are distinct from local

basement, both in terms of detrital age range and geochemistry (Avigad et al., 2012, 2005; Morag et al., 2011). Though the source of Stenian–Tonian material deposited along the early Paleozoic north Gondwana passive margin remains enigmatic, a dominant northward sediment transport direction recorded within the widely distributed Cambro-Ordovician sedimentary cover (Morag et al., 2011) supports a model of long-distance sediment transport across a North African peneplain from basement terranes exposed somewhere to the south (in modern-day coordinates). Long distance transport is consistent with deposition of the uniform and mineralogically mature Armorican Quartzite along the north Gondwana margin, and with the presence of rare Paleoarchean zircon (3434 Ma ±21 in GCZ-03, 3232 Ma ±30 in GCZ-06, and 3382 Ma ±15 2in LAZ-26) that have known basement sources within the eastern Kapvaal craton of southern Africa (e.g. Byerly et al., 1996; Lowe and Byerly, 1999).

Available North African detrital zircon age data are divisible, by basement geology and geographic sampling location, into four main groups. These are, from east to west, (1) the Arabian–Nubian Shield of the Red Sea region, (2) the Saharan hinterland of north-central Africa (Saharan Metacraton of Abdelsalam et al, 2002), (3) the Tuareg Shield of Algeria, and (4) the Anti-Atlas of Morocco. Each of the four distinct age populations present within the Armorican Quartzite are observed within contemporaneous clastic sedimentary rocks preserved within the north-central and northeast African realms of the Saharan hinterland and Arabian Nubian Shield. Sampled Ordovician units from the Saharan hinterland are the Cambrian Hasawnah (Altumi et al., 2013; Meinhold et al., 2011), Middle Ordovician Hawaz (Meinhold et al., 2011) and Upper Ordovician Mamuyinat (Morton et al., 2012) formations of the Murzuq and Kufra basins. Units sampled in and around the Arabian–Nubian Shield are the Cambro-Ordovician Tabuk Group in Saudi Arabia (Garzanti et al., 2013), the Ordovician Enticho sandstone of northwestern Ethiopia (Avigad et al., 2007), Cambrian sandstones from the Elat region of southern Israel (Avigad et al., 2003; Kolodner et al., 2006), and stratigraphically correlatable Cambro-Ordovician sandstones from the Aqaba region of southern Jordan (Kolodner et al., 2006). With the exception of the Cambrian Hasawnah Formation whose detrital zircons are dominantly Neoproterozoic, each of these units exhibits (1) Neoproterozoic (ca. 500-800 Ma), (2) Stenian–Tonian (ca. 0.9-1.1 Ga), (3) Paleoproterozoic (ca. 1.8-2.1 Ga) and (4) Archean (2.5-2.7 Ga) age populations in magnitudes similar to those observed in the Armorican Quartzite. In the Cambro-Ordovician

Aijer Fur, Middle Ordovician d'In Azaoua, and Upper Ordovician Tamadjut formations of the Tuareg Shield to the east, Mesoproterozoic and Archean populations are virtually absent, replaced by stronger Neoproterozoic, and older Paleoproterozoic (2.0–2.2 Ga) populations (Linnemann et al., 2011). In the Anti-Atlas, the age spectra within the Lower Cambrian Serie de Base are similar to those in the Tuareg. However, a small Stenian–Tonian population is evident by the Middle Cambrian within the quartz rich sandstones of the Grés de Tabanit and Schistes á Paradoxies (Avigad et al., 2012). Detrital age data from Ordovician clastic rocks of the Anti-Atlas are unavailable for comparison.

Two-sample K-S tests were run between individual sample sites from the Armorican Quartzite of the CCIM and datasets amalgamated from sample sites of the best age equivalence (ideally Early Ordovician) from each North African region (both independently and then partnered with each neighbour). From the test results, we can confirm the affinities deduced by first-order visual comparison and examine the degree to which the length-parallel trends of the CCIM are mirrored within North Africa (Table 3-4). A pattern is immediately evident, with Armorican Quartzite sites of the northern and central CCIM showing the greatest degree of similarity with the Saharan hinterland and Arabian–Nubian Shield, and with southerly sites (LAZ-26, LAZ-05 and *PNC-4*) showing similarities with the Anti-Atlas and Tuareg Shield. However, as the along strike distance from the northerly WALZ-01 to the southerly *PNC-4* is less than half the length of the North African Gondwana margin (with the Red Sea closed), the apparent similarities cannot be simultaneously supported.

The provenance comparisons for which the K-S tests were conducted are further examined by visual comparison of kernel function probability distributions for which a moderate bandwidth *(h*) of 50 was employed (e.g. Vermeesch, 2012). Each individual and partnered North African dataset is plotted against the full dataset for the Armorican Quartzite, and against a small grouping (2-3 sites) of those Armorican Quartzite sites assumed (based in part on the K-S test results) to be of the nearest along-strike proximity (Fig. 3-7). Datasets from northwestern Africa are also compared with a combined dataset for southern Iberia, which includes transition zone sample *QAM-1* (Linnemann et al., 2008) and the available ages from Ediacaran–Cambrian clastic rocks of zone-4 (Fernández Suárez et al., 1999; Linnemann et al., 2008). The kernel functions reveal strong similarities between

Table 3-4 Comparison of detrital zircon age spectra from the Armorican Quartzite of Iberia with detrital zircon age spectra from North African realms using the K-S statistical test

P < 0.001 (statistically different at the 0.1% significance level)

0.05 > P ≥ 0.001 (statistically different at the 5% significance level)

P > 0.05 (not statistically different at the 5% significance level)

W → E

N ↓ S

	AA* n = 212 M. Cam.	AA + TS n = 553/555	TS† n = 341/343 U. Cam.(?) - M. Ord.	TS + SH n = 575/579	SH§ n = 234/236 M. Ord.	SH + ANS n = 428/432	ANS# n = 196/198 L-M Ord.
WALZ-01 n = 138/139	P < 0.001 D = 0.339	P < 0.001 D = 0.361	P < 0.001 D = 0.380	P < 0.001 D = 0.250	P = 0.348 D = 0.100	P = 0.090 D = 0.122	P < 0.001 D = 0.251
Barrios n = 35/36	P = 0.022 D = 0.270	P = 0.004 D = 0.304	P = 0.002 D = 0.326	P = 0.170 D = 0.191	P = 0.598 D = 0.137	P = 0.460 D = 0.148	P = 0.344 D = 0.170
WALZ-02 n = 127/129	P = 0.011 D = 0.181	P < 0.001 D = 0.196	P < 0.001 D = 0.214	P = 0.143 D = 0.113	P = 0.015 D = 0.172	P = 0.251 D = 0.103	P = 0.416 D = 0.101
CZ-02 n =120/121	P < 0.001 D = 0.323	P < 0.001 D = 0.346	P < 0.001 D = 0.360	P < 0.001 D = 0.226	P = 0.128 D = 0.131	P = 0.371 D = 0.094	P = 0.001 D = 0.226
GCZ-06 n = 118/121	P < 0.001 D = 0.308	P < 0.001 D = 0.317	P < 0.001 D = 0.339	P < 0.001 D = 0.218	P = 0.041 D = 0.156	P = 0.494 D = 0.086	P = 0.014 D = 0.182
GCZ-03 n = 124/ 124	P = 0.091 D = 0.141	P = 0.053 D = 0.134	P = 0.002 D = 0.196	P = 0.008 D = 0.165	P = 0.002 D = 0.205	P = 0.009 D = 0.167	P = 0.094 D = 0.142
IBR-02 n = 122/125	P < 0.001 D = 0.307	P < 0.001 D = 0.302	P < 0.001 D = 0.299	P = 0.006 D = 0.168	P = 0.082 D = 0.140	P = 0.707 D = 0.071	P = 0.008 D = 0.191
SCS-05 n = 139/140	P < 0.001 D = 0.364	P < 0.001 D = 0.366	P < 0.001 D = 0.380	P < 0.001 D = 0.246	P = 0.693 D = 0.076	P = 0.091 D = 0.121	P < 0.001 D = 0.251
LAZ-26 n = 136/140	P = 0.286 D = 0.107	P = 0.140 D = 0.109	P = 0.019 D = 0.153	P = 0.005 D = 0.162	P < 0.001 D = 0.255	P < 0.001 D = 0.245	P < 0.001 D = 0.233
LAZ-05 n = 127/134	P = 0.001 D = 0.220	P = 0.024 D = 0.147	P = 0.002 D = 0.190	P < 0.001 D = 0.227	P < 0.001 D = 0.395	P < 0.001 D = 0.357	P < 0.001 D = 0.340
PNC-4†† n = 49/50	P = 0.044 D = 0.219	P = 0.198 D = 0.160	P = 0.066 D = 0.199	P = 0.006 D = 0.253	P < 0.001 D = 0.436	P < 0.001 D = 0.335	P = 0.002 D = 0.292

Note: Ages <500 Ma excluded from analyses, error incorporated.

* Anti Atlas of Morocco (Avigad et al., 2012)

† Tuareg Sheild of Algeria (Linneman et al., 2011)

§ Saharan hinterland (Meinhold et al., 2011; Morton et al., 2013)

Arabian Nubian Shield (Avigad et al., 2007; Garzanti et al., 2013; Kolodner et al., 2006)

**Fernandez-Suarez et al. (2002a)

†† Pereira et al. (2012)

northern sites (WALZ-01, WALZ-02, *Barrios)* and the Arabian–Nubian shield (Fig. 3-7H), between north-central sites (CZ-02, GCZ-03 and GCZ-06) and the combined Arabian-Nubian Shield and Saharan hinterland dataset (Fig. 3-7I), and between central sites (SCS-05 and IBR-02) and the Saharan hinterland (Fig 7J). The K-S tests and kernel function comparisons give strong and consistent evidence that the northern 650 km of the studied 1500 km segment of the CCIM formed a portion of the early Paleozoic Gondwana passive margin that ran the length between the Saharan hinterland and Arabian–Nubian Shield. Though the K-S tests show a statistical difference between southern sites (LAZ-05, LAZ-26,

PNC-4) and the Saharan hinterland, it is implied that the remaining 850 km of the CCIM continued along its northern limit, reaching just short of the Tuareg Shield to the West. Kernel function comparisons support this implication; aside from the magnitude and location of respective Paleoproterozoic peaks, the age spectra of the southern sites and the combined Saharan hinterland–Tuareg Shield dataset are highly similar (Fig. 3-7k).

The kernel function for the southern sites does not fit well with that of the independent Tuareg Shield dataset (Fig. 3-7l). Despite diminishing in frequency southward along strike, Paleoproterozoic (2.1 Ga) peak in the Tuareg spectra is absent within the southern sites. With a strong Neoproterozoic peak and an absence of Mesoproterozoic zircon, the detrital age spectra of the Tuareg Shield is much more similar to those of sample *QAM-1* and the Ediacaran–Cambrian clastic rocks of zone-4 (Fig. 3-7l). Though the comparison between the southern sites and the combined Tuareg Shield–Anti Atlas dataset is also relatively weak (Fig. 3-7m), the southern sites compare well with the independent Anti-Atlas data (Fig. 3-7n). However, given the strong similarities between the northern to central CCIM and more easterly African realms, a West African provenance for the southern sites implies that parts of the margin separated by a comparable along-strike distance during the Early Ordovician were juxtaposed during the Variscan orogeny and are now separated by an as yet unrecognized tectonic boundary. The age spectra within southerly sites LAZ-26, LAZ-05 and *PNC-4*, are best described as Saharan hinterland-type signatures perturbed by an increased input of the strong Neoproterozoic component identified within the Tuareg Shield.

We propose that the 2300 km long Cantabrian-Central Iberian portion of the Gondwana margin was situated in an Early Paleozoic Central to East African position stretching E-W along the northern limits of the then low-lying Saharan hinterland and Arabian Nubian Shield (Fig. 3-8). Of all the North African datasets, the age spectra of the Tuareg Shield and the combined Tuareg Shield–Anti Atlas dataset most closely resemble those of sample *QAM-1* and the Ediacaran–Cambrian clastic rocks of zone-4, though Paleoproterozoic and Archean ages do not correlate strongly (Fig. 3-7l, m). This suggests that the southernmost regions of Iberia, heretofore excluded from palinspastic restorations of the CCIM, may represent its westerly continuation. The reappearance of a Stenian-Tonian population in the Middle Cambrian clastic rocks of the Anti-Atlas argues against a common provenance with zone 4,

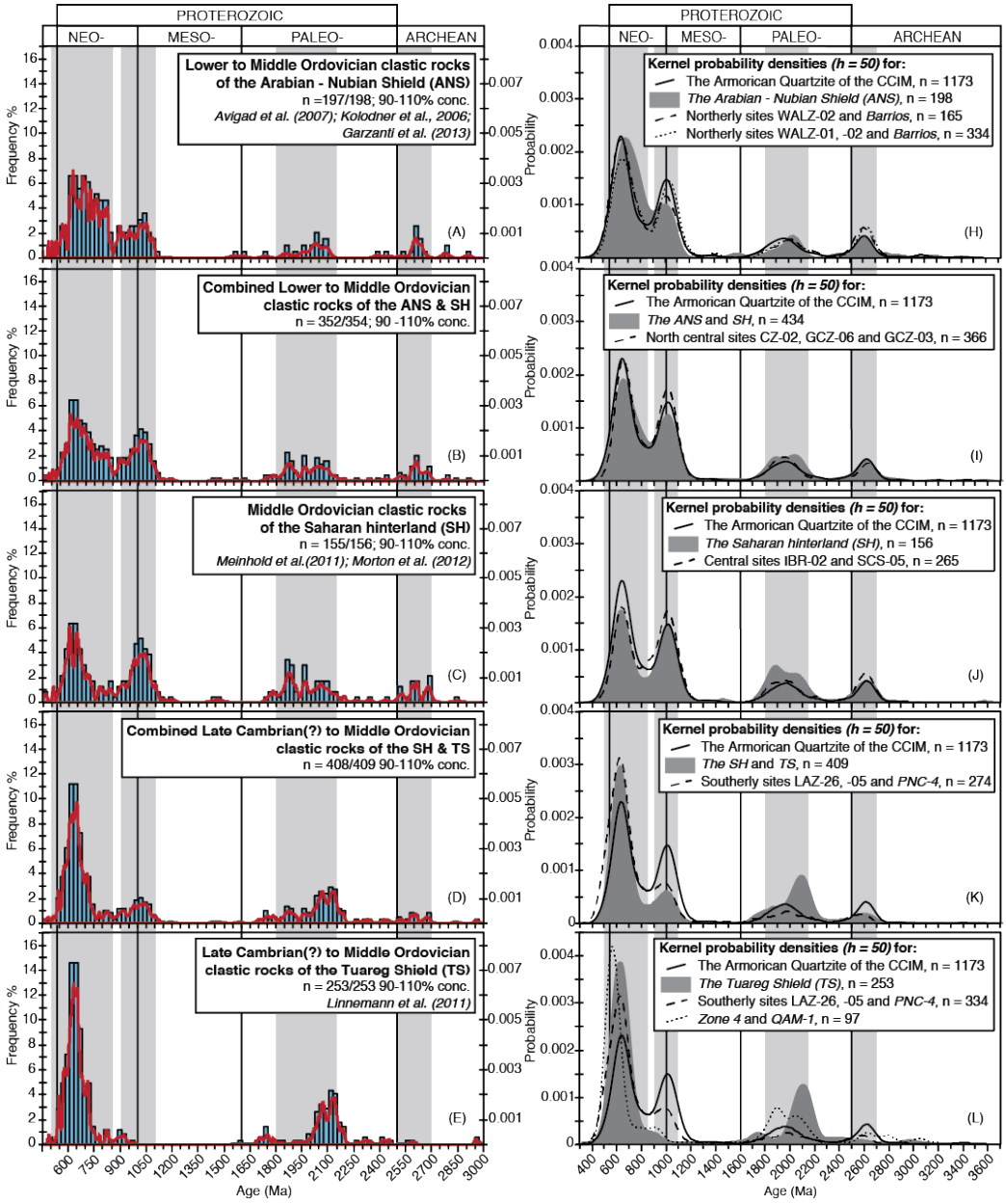

Figure 3-7 ***(on this and following page).*** Sample size-normalized histograms of U-Pb detrital zircons ages for lower Paleozoic clastics of North African realms (A-G) and kernel probability density plots comparing those data with the data set from Armorican Quartzite of this study (CCIM–Cantabrian-Central Iberian margin). (H) Lower to Middle Ordovician clastic rocks of the Arabian–Nubian shield versus northern sites (WALZ-01, -02 and *Barrios*). (I) Combined Lower to Middle Ordovician clastic rocks of the Arabian–Nubian Shield and the Saharan hinterland versus north-central sites (CZ-02, GCZ-06 and GCZ-03). (J) Middle Ordovician clastic rocks of the Saharan hinterland versus central sites (IBR-02 and SCS-05). (K) Combined Late Cambrian (?) to Middle Ordovician clastic rocks of the Saharan hinterland and Tuareg Shield versus southerly sites (LAZ-26, -05 and *PNC-4*). (L) Late Cambrian(?) to Middle Ordovician clastic rocks of the Tuareg Shield versus southerly sites and a combined southern Iberian dataset.data set including transition zone sample *QAM-1* and available ages from Ediacaran–Cambrian clastic rocks of zone 4.

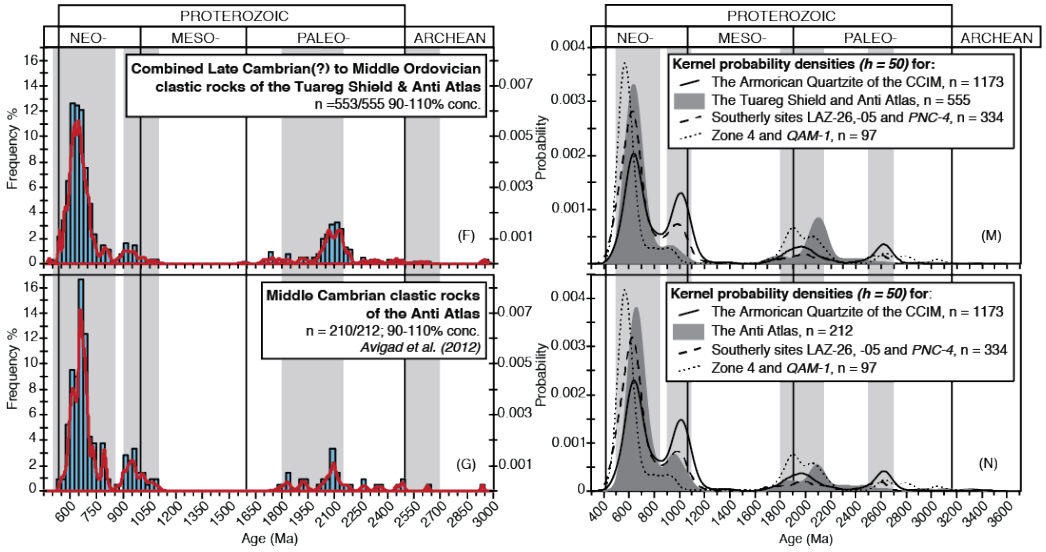

Figure 3-7 ***(continued)*** (M) Combined Late Cambrian (?) to Middle Ordovician clastic rocks of the Tuareg Shield and Anti Atlas versus southern sites, and the combined southern Iberian dataset. (N) Middle Cambrian clastic rocks of the Anti Atlas versus southern sites and the combined southern Iberian dataset. Displayed preferred ages are selected on the criteria established in each original publication; originally published data with greater than 10% discordance and post-depositional (secondary growth rim) age data are excluded. The shaded bars highlight the ranges of the four main CCIM age populations.

suggesting that no part of autochthonous Iberia originated directly adjacent to the West African Craton.

A range of factors hinder the precision with which clastic sedimentary rocks can, through detrital zircon geochronology, be matched with their basement source terrane or terranes (e.g. Cawood et al., 2003; Lawrence et al., 2011). The strength with which the length-parallel trends of the CCIM systematically correlate with east-west variability in North African clastic rocks, despite a lack of correlation with the known age range of North African basement terranes, demonstrates the (1) precision with which paleogeographic affinities can be drawn through comparison of detrital zircon age range in contemporaneous clastic rocks, (2) dangers of making paleogeographic assumptions based on comparison of clastic sequence and potential basement source(s) and, (3) importance of conducting detrital zircon provenance studies at appropriate geographic scale (see Sircombe et al., 2001).

Previous interpretations of Iberia as having originated in a Central to East African realm during the Ordovician have been supported by (1) paleontological data (Gutiérrez-Marco et al., 2002 and references therein), (2) detrital zircons studies of Ediacaran–lower Paleozoic rocks in northwestern Iberia (Díez Fernández et al., 2010, 2012, 2013; Fernández Suárez et

al., 2013) and (3) isotopic and inherited zircon studies of Central Iberian Cambro-Ordovician magmatic rocks (Bea et al., 2010). Bea et al. (2010) observed that the age range and geochemical characteristics of xenocrystic zircon entrained in Cambro-Ordovician granitoids of zone 3 are consistent with derivation of these intrusions from melting of crust similar to that of the Egyptian Western Desert. The Western Deserts is a sub-region of the northwestern Saharan hinterland whose age is constrained by whole rock Nd model ages.

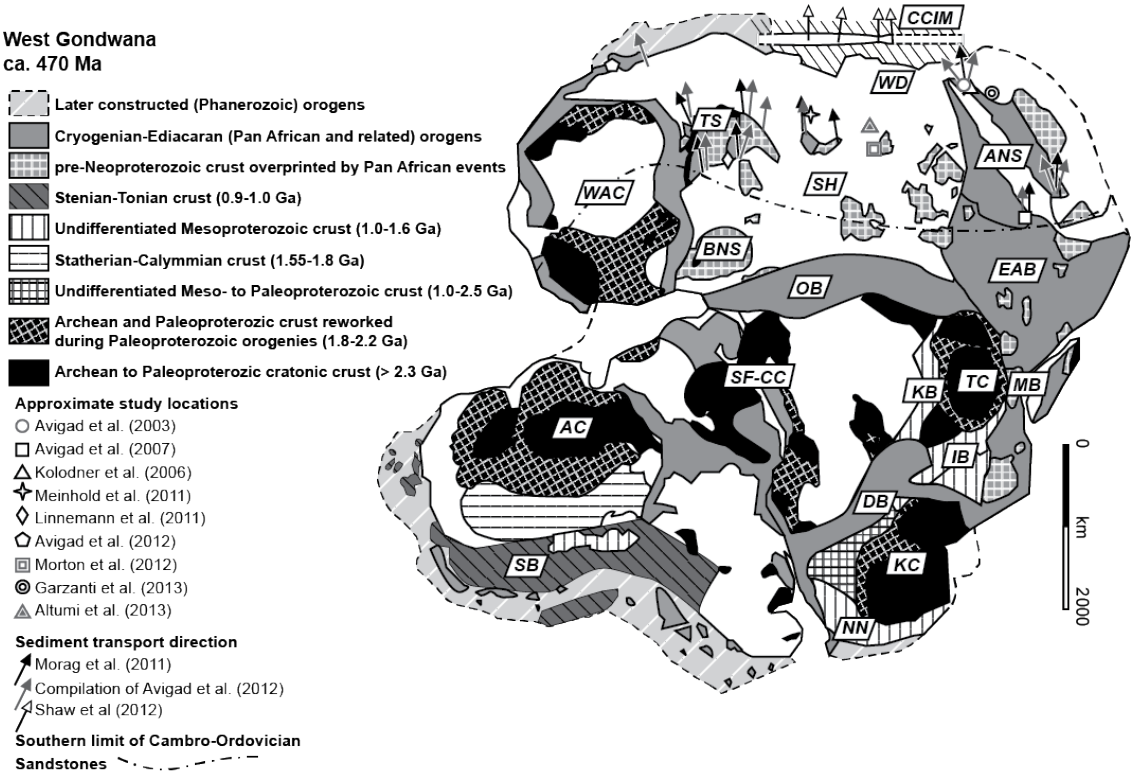

Figure 3-8 Ca. 470 Ma reconstruction of West Gondwana showing the Cantabrian-Central Iberian passive margin (CCIM) in the proposed paleogeographic location adjacent to the Saharan hinterland (SH) and Arabian-Nubian Shield (ANS); relative locations of other peri-Gondwanan Variscan terranes are not considered. North African detrital zircon study location sites are, based on sample age and geographic location, those used for statistical and detailed visual comparison (black), and those excluded from statistical and detailed visual comparison (grey). Modified from the compilation of Linnemann et al. (2011), North African sedimentary data after (Morag et al., 2011). Geology of Madagascar after Kröner (2001). AC—Amazonian Craton; BNS—Benin-Nigeria Shield; DB—Damara belt; EAB—East African belt; KB—Kibaran belt; KC—Kaapvaal Craton; IB—Irumide belt; MB—Mozambique belt; NN—Namaqua Natal belt; OB—Oubanguide belt; SB—Sunsás belt; SH—Saharan hinterland TC—Tanzania Craton; TS—Tuareg Shield; WAC—West African Craton; WD—Western Desert; SF-CC—São Francisco–Congo Craton.

The observation of Bea (2010) suggests that zone 3 was 'pinned' to the Western Desert, but requires further examination in the context of the Central Iberian orocline. The 62 samples of Bea et al. (2010) are from three different domains (Ollo de Sapo, Schistose Greywacke, and Urra) spanning a length of roughly 1000 km along the restored CCIM. The resolved paleogeographic constraints are therefore of no greater precision than those obtained by the detrital zircon provenance analysis presented herein. Ranges of the species of West Algerian to Saudi-Arabian-type fauna within the Lower Ordovician sequences of zones 1-3 (Gutiérrez-Marco et al., 2002 and references therein) do not exhibit dependence on location along strike. Paleontological correlations can therefore offer no precise constraints on the location of the CCIM along the north Gondwana margin. However, continuity of faunal assemblages along the margin further supports a latitude parallel (E-W) orientation during the Early Ordovician.

3.7.3 Pre-Ordovician paleogeography

The interpreted Neoproterozoic to early Paleozoic evolution of the north Gondwana margin consists of long-lived subduction forming the Cadomian-Avalonian arc superseded by (1) its Cambro-Ordovician departure, (2) the opening of the Rheic Ocean, and (3) the development of a passive margin. Despite the changing tecontic environments, each defining age population identified within the Armorican Quartzite is characteristic within nearly every studied sample from the Ediacaran and Cambrian clastic sequences that underlie it in northern and central Iberia (zones 1-3) (Ábalos et al., 2012; Fernández Suárez et al., 2013; Gutiérrez-Alonso et al., 2003; Talavera et al., 2012). The one exception is sample *OD-1* from the Cambrian Candána-Herrería Sandstones of zone 1 (Fernández Suárez et al., 2013), for which an anomalous absence of Stenian–Tonian zircons and accentuated Paleoproterozoic and Archean populations can only be explained as reflecting a change detrital input into a comparatively local depositional basin. The Armorican Quartzite is, by comparison with the detrital zircon age spectra typical for most Ediacaran–Cambrian clastic rocks in zones 1-3, characterized by a weakened Neoproterozoic signature, a more robust Stenian–Tonian signature, and definable Paleoproterozoic and Archean peaks (Fig. 3-9). The occurrence of Stenian–Tonian zircons in the Ediacaran sequences, which predate passive margin development and presumably the low-relief delivery pathway of such material from southerly sources, cannot be directly explained.

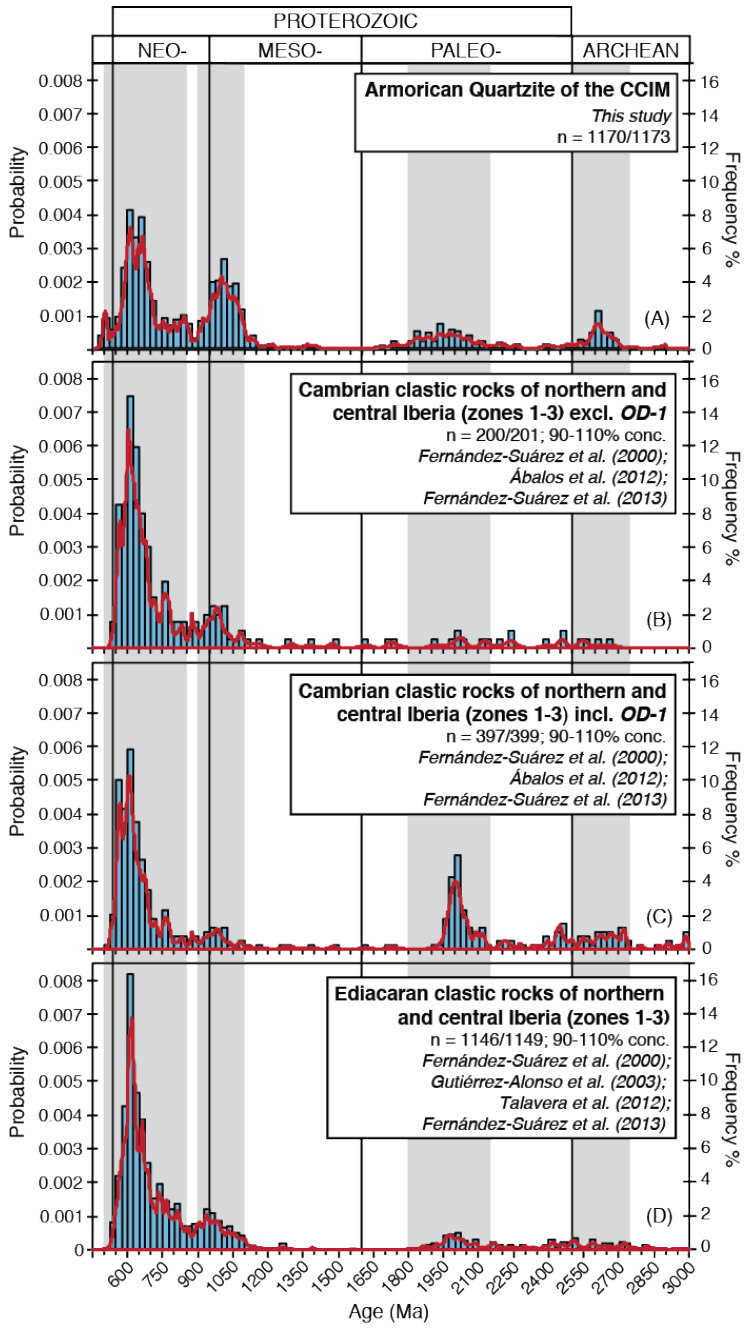

Figure 3-9 Sample size-normalized histograms and probability density plots comparing U-Pb detrital zircons ages of (a) the Armorican Quartzite of this study with U-Pb detrital zircons ages of Cambrian clastic rocks from zones 1-3, both (b) excluding and (c) including anomalous sample *OD-1*(Fernández Suárez et al., 2013), and (d) Neoproterozoic clastic rocks from zones 1-3 (CCIM–Cantabrian-Central Iberian margin). Displayed preferred ages are selected on the criteria established in each original publication; originally published data with greater than 10% discordance are excluded. n = number of grains displayed/number of concordant analyses; concordant analyses excluded for graphical clarity are single grains > 3.0 Ga.

When Stenian–Tonian zircons were first identified in Ediacaran sequences of northern and central Iberia (Fernández-Suárez et al., 2000a, 2002b; Gutiérrez-Alonso et al., 2003) the Amazonian Craton contained the only known source within north Gondwana, leading to suggestion that these strata originated in an Amazonian realm. But as the stratigraphic ties between the Armorican Quartzite and north African Gondwana were well understood, Fernández-Suárez et al. (2002a,b) and Gutiérrez-Alonso et al. (2003) interpreted the Gondwanan margin of zones 1-3 to have been translated at least 4000 km eastward from an Amazonian location in the latest Neoproterozoic along a dextral transcurrent fault system to reach an African position prior to deposition of the Armorican Quartzite. Stenian-Tonian zircons known within the *Barrios* sample of Zone 1 were attributed to recycling of 0.9-1.0 Ga material from underlying sedimentary sequences in a West African depositional realm (Fernández-Suárez et al. 2002a). The maturity of the Armorican Quartzite seems to imply long-distance transport and argue against recycling from immediately underlying strata as an explanation for the Stenian-Tonian zircons contained within it. However, its maturity has also been attributed to in situ chemical weathering related to elevated pCO_2 within a post-Pan-African greenhouse global climate (Avigad, 2005). As we have also now identified the depositional realm of the Armorican Quartzite as Central to East African, the required translation distance (from an Amazonian to a Central African realm) increases significantly, to an excess of 5000 km. An assumed 50 million year transit time (between 540 and 490 Ma) would require relative plate motions in excess of 10 $cm \cdot yr^{-1}$. Such sustained and rapid translation along a strike-slip fault system is unlikely; there is no modern analogue strike-slip fault characterized by such high rates of relative translation. The likelihood of a Neoproterozoic Amazonian origin is further countered by an absence of zircons attributable to Rondonian—San Ignacio (ca.1.25-1.45 Ga) or Rio Negro—Jurunea (ca. 1.5-1.75 Ga) orogenic belts (Nance and Murphy, 1994; Teixeira et al., 1989), both of which are considered characteristic of clastic sediments of Amazoninan provenance (Barr et al., 2003; Friedl et al., 2000; Keppie et al., 1998). Detrital micas from the Cambrian Candána- -Herrería Sandstones of zone 1 (same formation and locality as anomalous zircon Sample *OD-1*; Fernández-Suárez et al., 2013) that yield 1.58-1.78 Ga Ar-Ar ages (Gutiérrez-Alonso et al., 2005) have no known source.

There is little evidence suggesting a significant change in the paleogeographic location of Iberia from the Ediacaran through the Early Ordovician. The increasing magnitude of Stenian-Tonian, Paleoproterozoic, and Archean populations observed over this time period may reflect a decrease in the diluting effect of a strong Neoproterozoic signature. This is consistent with the interpreted evolution of regional geodynamic setting from a Neoproterozoic (Cadomian) subduction environment to an early Paleozoic stable (Rheic) passive margin, and with the rapid erosion of local Neoproterozoic basement as indicated by the development, by the Late Cambrian, of a North African peneplain.

3.7.4 Post-Ordovician tectonic implications

Models of Gondwanan paleogeography during the early to middle Paleozoic suggest that the CCIM occupied a portion of the Gondwana passive margin that shifted from an Early Ordovician south-polar position into an east west-striking, north-facing orientation as Gondwana drifted steadily northward (e.g. Stampfli and Borel, 2002; Torsvik et al., 2012). The east-west strike of the margin during deposition contrasts with the paleomagnetically constrained north-south strike of these rocks in the Late Carboniferous during Variscan orogenesis. A Central to East African paleogeographic position during the Early Ordovician therefore implies that the CCIM rotated 90 degrees counterclockwise after deposition of the Armorican Quartzite but prior to the termination of the Variscan orogeny. How to accommodate such a rotation is unclear. Though the Paleozoic drift history of Gondwana is not well constrained, current paleomagnetic data do not support significant counterclockwise rotation of Gondwana between the Early Ordovician and the Late Carboniferous (e.g. Tait et al., 2000a; Torsvik et al., 2012). If Gondwana did not rotate during this time period, post-depositional separation of the CCIM from autochthonous Gondwana, an event for which there is no known geologic evidence, would be required.

3.8 Conclusions

We interpret the CCIM as having originated as a continuous linear portion of the north Gondwana Cambro-Ordovician passive margin. The detrital zircon age spectra of the CCIM is best explained as a product of erosion of source terranes exposed, in modern day coordinates, to the south of the Saharan hinterland and Arabian Nubian shield. A paleogeographic model in which the palinspastically restored CCIM is a component of the

Ediacaran–Early Paleozoic Central to East African Gondwanan margin extending along the northern limits of the then low-relief Saharan hinterland and Arabian–Nubian Shield satisfies known sedimentary, petrologic and paleontological constraints. The suggested east-west trend maintained by the CCIM prior to and during deposition of the Armorican Quartzite contrasts with the N-S trend it held immediately prior to buckling of the orogen about a vertical axis of rotation giving rise to the coupled secondary Ibero-Variscan Cantabrian and Central Iberian oroclines. Ninety degrees of counterclockwise rotation are required to bring the CCIM from an Ediacaran–Early Paleozoic position as a component of the north facing Gondwana passive margin to a pre-oroclinal (Late Carboniferous) north-south trend.

Chapter 4. Orocline formation at the core of Pangea: A structural study of the Cantabrian Orocline, NW Iberian Massif[3]

4.1 Abstract

The Variscan orogen provides the European record of the latePaleozoic continental collisions that culminated with formation of the supercontinent Pangea. An *S*-shaped pair of isoclinal coupled oroclines characterizes the Variscan orogen of the Iberian Massif. Though oroclines are common features of the world's orogenic belts, the mechanisms that drive oroclinal formation, and the manner in which these continental-scale vertical-axis folds of orogens are accommodated, are poorly understood. The northerly Cantabrian and the southerly Central Iberian oroclines are structurally continuous and contemporaneous, suggesting that they formed in the same fashion. Exposures of the Ediacaran Narcea Slates within the so-called Narcea Antiform trace a 150-km-long arcuate belt around the 180º Cantabrian orocline. In the Western flank of the Narcea Antiform, the Narcea Slates are characterized by a penetrative steep to vertical rough to slaty cleavage (S1) and subparallel 2-km-wide reverse shear zones with a penetrative fabric (S2) that are postdated by asymmetric meso- to outcrop-scale vertical-axis folds (plunge >65°) with a dominant vergence toward the oroclinal hinge; i.e. fold geometry is dominantly dextral (*Z*-shaped) in the southern limb of the Cantabrian orocline and dominantly sinistral (*S*-shaped) in its northern limb. Axial planes are consistently steeply dipping, but typically oriented at a high-angle to S1/S2 and are therefore variable in strike about the orocline hinge. Vertical-axis folds affecting the Narcea Slates are of the appropriate scale and geometry to be interpreted as parasitic structures developed in response to a component of flexural shear within the limbs of the forming Cantabrian orocline. A model of formation of the Iberian coupled oroclines by buckling accommodating significant orogen-parallel shortening along an initially linear Iberian Variscan belt is therefore supported, providing new insight into the complexities associated with the final stages of Pangean amalgamation.

[3] This chapter will be published as: Shaw, J., Johnston, S.T., and Gutiérrez-Alonso, G., 2015, Orocline formation at the core of Pangea: A structural study of the Cantabrian orocline, NW Iberian Massif: Lithosphere, in press.

4.2 Introduction

Progressive oroclines are thin-skinned structures that develop curvature over the course of orogen formation through local vertical-axis rotations driven by the same stress field responsible for orogen perpendicular shortening. Secondary, or 'Carey' oroclines, are thick-skinned and extra-orogenic, involving strike-parallel shortening of an entire orogen in response to a regional stress field distinct from that responsible for initial orogenic shortening (Johnston et al., 2013 and references therein); see Marshak (2004) for further review of the terminology of map-view orogenic curvature.

An *S*-shaped pair of coupled oroclines characterizes the Iberian segment of the Western European Variscan belt (Fig. 4-1). The more northerly and convex towards the west Cantabrian orocline hosts the Variscan foreland in its core; allochthonous terranes occupy the core of the southerly convex towards the east Central Iberian orocline (Du Toit, 1937; Aerden, 2004; Martínez Catalán, 2011; Shaw et al., 2012). The hinge of the Central Iberian orocline is mostly buried beneath post-Variscan sedimentary cover; the Cantabrian orocline, in contrast, is incredibly well exposed and is hence one of the best-studied structures of its kind. Despite a wealth of research aimed at deciphering the dynamics, mechanics, kinematics, and lithospheric-scale effects of the Cantabrian orocline, (e.g., Julivert, 1971; Julivert and Marcos, 1973; Brun and Burg, 1982; Pérez-Estaún et al., 1988; Ribeiro et al., 1995; 2007; Weil et al., 2000; 2001; Weil, 2006; Gutiérrez-Alonso et al., 2004; 2008a; Weil et al., 2010; Gutiérrez-Alonso et al., 2011a; 2011b; Pastor-Galán et al., 2011; Gutiérrez-Alonso et al., 2012; Weil et al., 2013a; Gutiérrez-Alonso et al., 2015) there remains debate with regard to the nature of its development.

Of the many distinct models for its formation, most interpret the Cantabrian orocline as progressive. Progressively developed curvature is postulated to have resulted from (1) the impingement of a rigid Gondwanan continental indenter (Ribeiro et al., 1995; 2007), (2) a gradual and continuous change in thrust transport direction (e.g., Pérez-Estaún et al., 1988), (3) sinistral transpression confined to the upper-plate and driven by collision at a transform-trench triple junction (Brun and Burg, 1982), or (4) lithospheric-scale dextral transpression driven by oblique collision (Martínez Catalán, 2011). Alternatively, the Cantabrian orocline has been interpreted as secondary, formed by buckling accommodating significant orogen

parallel shortening along the length of an initially linear Variscan orogen in response to a reorientation of the regional stress field (e.g., Weil et al., 2000; 2013b; Johnston et al., 2013).

Interpretation of the Cantabrian orocline as secondary is supported by paleomagnetic and structural studies that demonstrate significant post-Variscan vertical-axis rotations that, when restored, indicate an initially linear north-south Variscan trend (Parés et al., 1994; Van der Voo et al., 1997; Weil et al., 2000; 2001; Weil, 2006; Merino-Tomé et al., 2009; Weil et al., 2010; Pastor-Galán et al., 2011; Weil et al., 2013a). Consistent paleomagnetic poles within Early Permian strata unconformably deposited above strata deformed about both the Cantabrian and Central Iberian oroclines suggest that they formed contemporaneously over a 10-20 My period immediately following the Late Carboniferous cessation of east-west Variscan shortening (in modern-day coordinates) (Weil et al., 2010). Variscan porphyroblasts characterized by inclusion trails that preserve a constant north-south orientation about the axes of both the Cantabrian and Central Iberian oroclines provide further evidence in support of their contemporanous formation from an initially linear north-south trending Variscan orogen (Aerden, 2004). Magmatism, metamorphism, mineralization and associated isotopic data suggest that orocline formation involved the entire lithosphere (Fernández-Suárez et al., 2000b; Gutiérrez-Alonso et al., 2004; 2011a; 2011b; Ducea, 2011).

A model of secondary formation of the Iberian coupled oroclines implies that significant components of orogen parallel shortening were accommodated by buckling of an initially linear Variscan orogen, and makes testable predictions. Buckle folding is accommodated within the fabric being folded by a principal mechanism of flexural shear identifiable by parasitic folds that reside in the limbs and verge towards the hinge of the larger-scale structure. Buckle folding about a vertical axis requires existing vertical structures or fabrics that are likewise subject to modification by flexural shear (Fig. 4-2). A buckled orogen (secondary orocline) should therefore host, within existing fabrics that are deformed about its axis, a predicable array of mesoscale vertical-axis structures with a characteristic vergence towards the oroclinal hinge (Fig. 4-2). In any given orogen, existing vertical fabrics may include axial planar cleavage of upright folds, and axial planar cleavage of recumbent folds or thrust-ramp shear zones subsequently imbricated during fold and thrust belt propagation. In addition, buckle folding on a lithospheric scale is likely to require an orogen bound by lithospheric-scale free surfaces, i.e. plate boundaries.

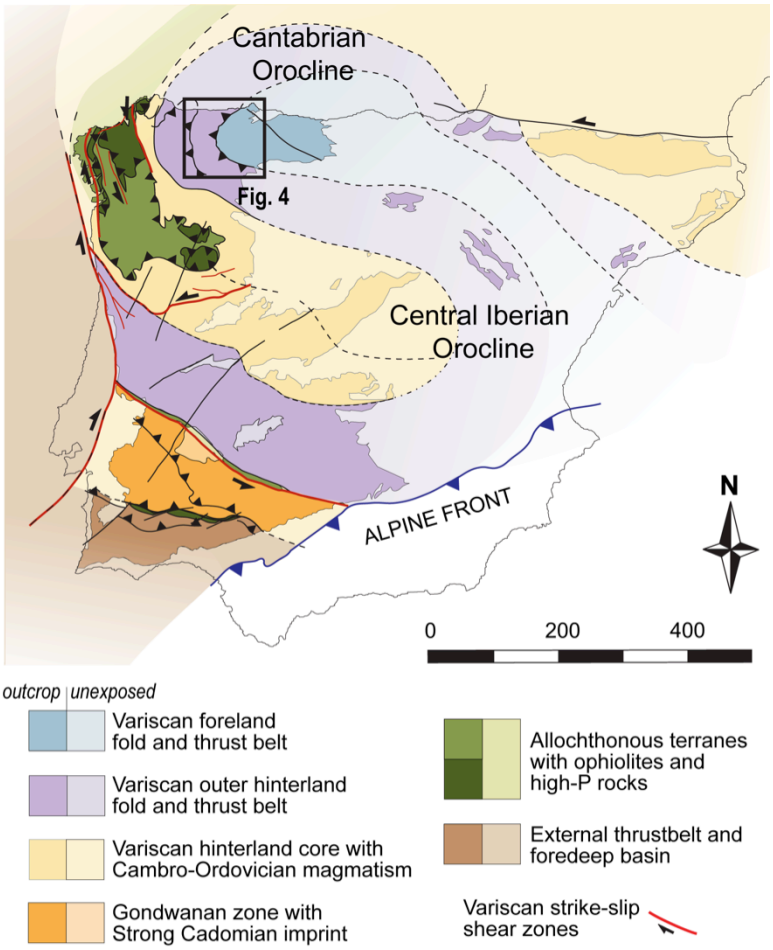

Figure 4-1 The *S*-shaped coupled Cantabrian and Central Iberian oroclines of the Western European Variscan belt. After Shaw et al. (2012).

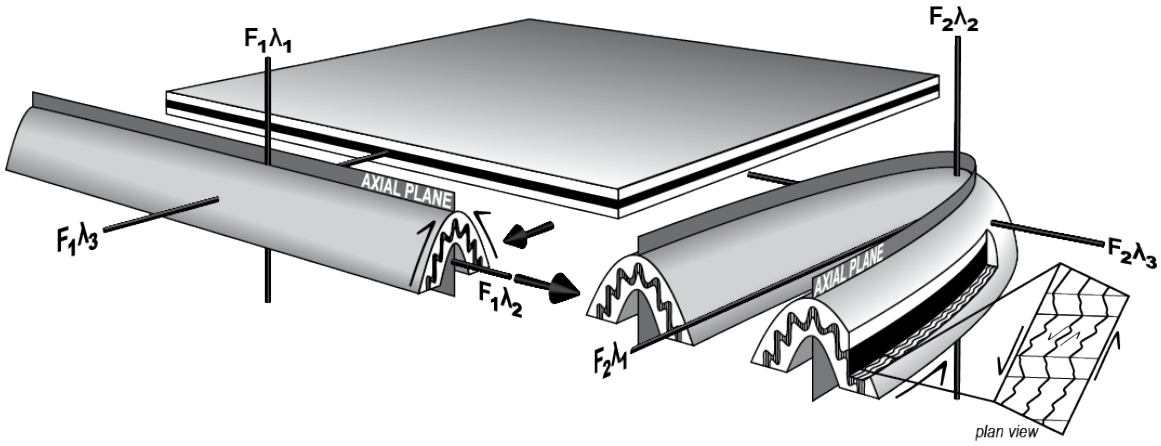

Figure 4-2 A schematic illustration of the reorientation of regional shortening required for oroclinal buckling. Folding about a vertical axis requires the preexistence of vertical structures and/or fabrics. The rectangular inset shows the predicted plan-view geometries of measurable mesoscale vertical-axis folds, with dominant vergence directed toward the orocline hinge.

We present analyses of structural data collected from steeply plunging mesoscale folds affecting steep to sub-vertical Variscan fabrics that bend around and define the Cantabrian orocline. Our primary aim is to assess whether these structures are of the appropriate scale and geometry to be parasitic to the Cantabrian orocline, as is predicted by an interpretation of the orocline as a secondary feature formed by orogen parallel shortening of an initially linear Variscan orogen.

4.3 Geologic Setting: The Narcea antiform

Ediacaran to Paleozoic strata of the Iberian Massif record the late Neoproterozoic to early Paleozoic evolution of a segment of the North African Gondwana margin and its subsequent Variscan deformation. The coupled Iberian oroclines are defined within and affect a series of tectonostratigraphic zones that are distinguished on the basis of lithology, stratigraphy, and Variscan deformational style (Shaw et al., 2012; Shaw et al., 2014). From the core of the Cantabrian orocline outward, autochthonous Iberia is divisible into (1) a foreland domain, (2) an external hinterland domain, and (3) an internal hinterland domain (Shaw et al., 2012 and references therein). The internal hinterland domain is overthrust from the west by an exotic ophiolite bearing allochthonous package. In southern Iberia, an additional distal Gondwanan zone, a continental allochthon, and an intervening suture (Fig. 4-1), are separated from the remainder of the massif by a major sinistral shear zone, the youngest motion along which is Variscan in age (e.g. Quesada and Dallmeyer, 1994).

Variscan structures predate and are deformed about the axis of the 180º Cantabrian orocline. A broad antiformal culmination in the footwall of a major nappe stack, the Narcea antiform, lies along the margin between the foreland and hinterland domains, and traces deflections in structural trend along the Variscan foreland–hinterland transition at the apex of the Cantabrian orocline in the northwestern massif (Fig. 4-3). The core of the antiform exposes the Ediacaran Narcea Slates, the stratigraphically lowermost unit of the massif, for 150 km along strike. The Narcea Slates consists of a distal turbiditic succession of metamorphosed shales and graywackes with minor volcaniclastic layers (Gutiérrez-Alonso, 1996) and Neoproterozoic orthogneisses (Fernández-Suárez et al., 1998). The sequence is interpreted to have originated in a back-arc basin (Fernández-Suárez et al., 2013; Rubio-Ordóñez et al., 2015). In the hinterland western flank of the Narcea antiform, the Narcea

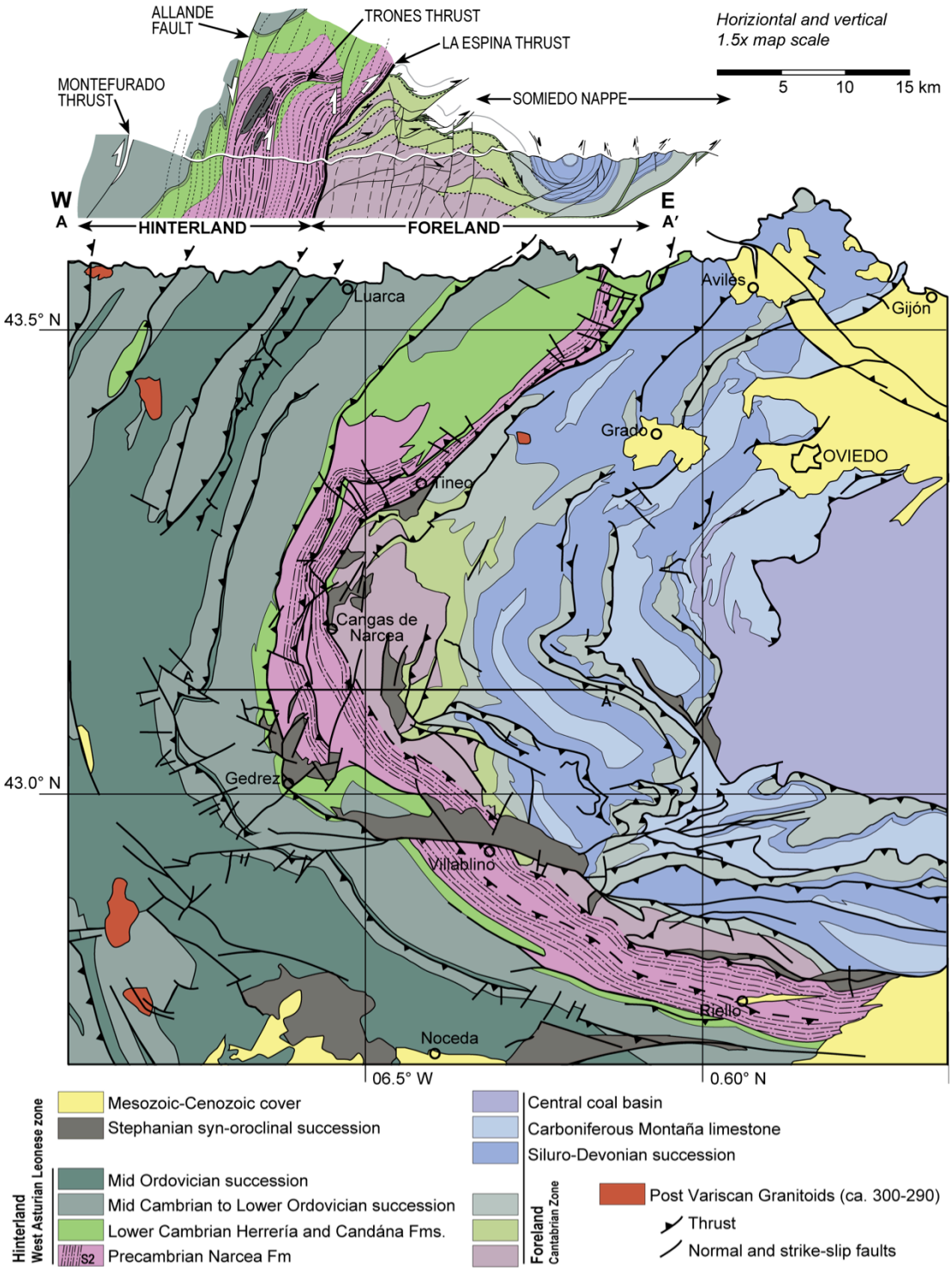

Figure 4-3 Geologic map and cross section illustrating the extent of exposures of the Ediacaran Narcea Slates within the core of the Narcea antiform, tracing deflections in structural trend along the foreland-hinterland transition at the apex of the Cantabrian orocline in the northwestern Iberian Massif. Cross-section after (Gutiérrez-Alonso, 1996).

Slates are characterized by a penetrative steep to vertical rough to slaty cleavage (S1) and two km-wide bands of subparallel shear fabric (S2). The S1 cleavage is axial planar to Variscan structures and characteristic of rocks within which primary structures are still evident. The S2 foliation is a late Variscan fabric developed within discrete km-wide thrust-ramp shear zones under low-grade metamorphic conditions. S2 is sub-parallel to but obliterates the older S1 cleavage and is phyllonitic to mylonitic, characterized by abundant kinematic indicators (primarily C-S fabric and asymmetric quartz porphyroblasts), which indicate shear up dip and towards the foreland core of the Cantabrian orocline. An ^{40}Ar-^{39}Ar study of S2 phyllonite yielded cooling ages of 321 Ma (Dallmeyer et al., 1997). Both the S1 and S2 foliations predate formation of the Cantabrian orocline and are therefore deflected around it.

4.4 Structural Analysis

Structural data were collected for mesoscale vertical-axis folds at ~200 roadcut exposures within the Narcea slates of the hinterland western flank of the Narcea Antiform in northwest Iberia. Shallowly plunging folds could only be considered parasitic to the steeply plunging Cantabrian orocline if they were subsequently titled (note: constraining the timing of post-orocline deformational events was outside the scope of this study). Most of the measurements are of folds of S2 fabrics, as S2 is better developed than S1 and is more likely to be refolded. Individual folds were assessed in terms of their symmetry and the orientation of both limbs and axial planes, where apparent, were recorded. We employed a 2:1 cut-off for fold asymmetry; the long limb of a fold had to be at least twice the length of its short limb in order to be classified as asymmetric. Fold vergence was then defined by limb-length asymmetry as directed toward the short limb; *S*-shaped folds are sinistral, *Z*-shaped folds are dextral. The number of measurable vertical-axis folds at any given field site was variable and depended on (1) the extent and quality of outcrop, and (2) the extent of development and dip of the S1 cleavage and/or S2 shear fabric. Most sites contained five or fewer individual folds. Measured structures included more minor brittle contractional kink folds and ductile folds of variable geometries, all steeply plunging. While there is no penetrative cleavage associated with the vertical-axis folds, some folds were characterized by a local and spaced axial planar cleavage. Seventy-five percent of all measured folds were classifiable as gentle, with interlimb angles of 120 degrees or greater. Folds ranged in size from cm-scale to

outcrop-scale deflections. The frequency of mesoscale vertical-axis folds does not vary as a function of along-strike distance from oroclinal hinge.

A beta-plot analysis was conducted for each individually measured fold. Following a cylindrical best-fit analysis constrained by the axial plane and limb measurements, the Fisher mean vector of the calculated intersection (beta point) and pi- axis was taken as the final preferred fold-axis orientation. Assuming that fold limbs were measured with greater accuracy than axial planes, the dip of the measured axial plane was adjusted about its fixed strike as necessary in order intersect the preferred fold axis. A first order error on the calculated fold axis is thus given as a small circle centered on the preferred fold axis with a radius equal to the dip adjustment on the measured axial plane. If no axial plane was directly measured, fold axis errors could be similarly calculated from any disagreement between axes of folds with shared limbs, including box folds. Fold axes with errors greater than 15 degrees, interlimb angles greater than 160 degrees, or plunges shallower than 65 degrees were eliminated from further analysis.

Beta plots were grouped for individual field sites to assess internal consistency/variability, and then further grouped by geographic location for clarity of presentation. Final plots express regional fabric (S1/S2) as great circles and distinguish measured axial planes from calculated bisecting surfaces plotted as poles, as well as the corresponding fold axes with or without calculable error (Figs. 4-4, -5 and -6). Final plots also include average axial plane orientations for either fold symmetry, taken as the group site mean vector for poles to bisecting surfaces and axial planes. All structural analyses were conducted in Stereonet (Allmendinger et al., 2012).

Vertical-axis folds of the slaty cleavage (S1) and shear fabric (S2) characteristic of the Narcea slates in the hinterland western flank of the Narcea Antiform are dominantly sinistral in the northern limb of the Cantabrian Orocline (Fig. 4-4) and dominantly dextral in its southern limb (Fig. 4-5). Large-scale deflections in S1/S2 (most apparent in the northern limb) reveal the presence of somewhat cryptic km-scale folds with the same orientations and symmetries expressed by their mesoscale counterparts. An even proportion of dextral and sinistral folds accompanied by a higher proportion of symmetric folds characterize the hinge region (Fig. 4-6). Dual fold symmetry in both limbs is attributable to box folding and the development of parasitic folds at diminishing scales (Fig. 4-7). At every diminishing scale of

subsidiary fold, parasites formed on the long limb of an asymmetric host will share its sense of asymmetry and necessarily outnumber those with an opposing sense of asymmetry developed on its shorter limb. The dominant vergence within mesoscale structures is therefore reflective of the sense of shear recorded by first-order parasitic fold on the largest-scale structure (the Cantabrian orocline).

Idealized flexural buckling predicts the axial planes of parasitic folds to parallel that of the largest-scale structure. While the axial planes of vertical-axis folds of the S1 and S2 fabrics in the Narcea Slates are at moderately high angles to the axial plane of the Cantabrian orocline, the overall distribution of fold symmetry (Fig. 4-8) illustrates dominant shear sense toward the oroclinal hinge in both limbs, suggesting that these structures are parasitic folds formed in response to a component of flexural shear during formation of the Cantabrian orocline. A model of secondary buckling accommodating orogen parallel shortening of an initially linear Iberian Variscan orogen is therefore supported.

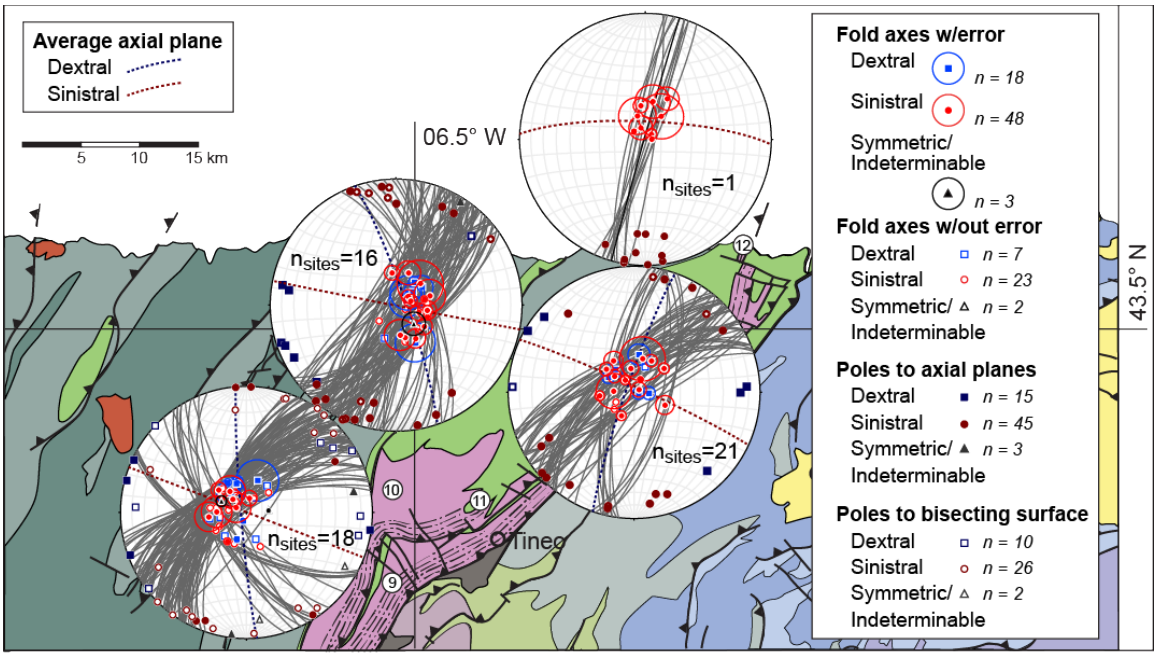

Figure 4-4 Stereonet plots for steeply plunging mesoscale folds of S1/S2 measured within the northern limb of the Cantabrian orocline. Solid gray great circles on each stereoplot show the local orientation of the dominant S1/S2 foliations, which equate to local structural strike and are the long-limb orientations for the majority of measured folds; folds that developed on the short limb of a larger-scale parasitic fold have long limbs oriented at some angle to local structural strike.

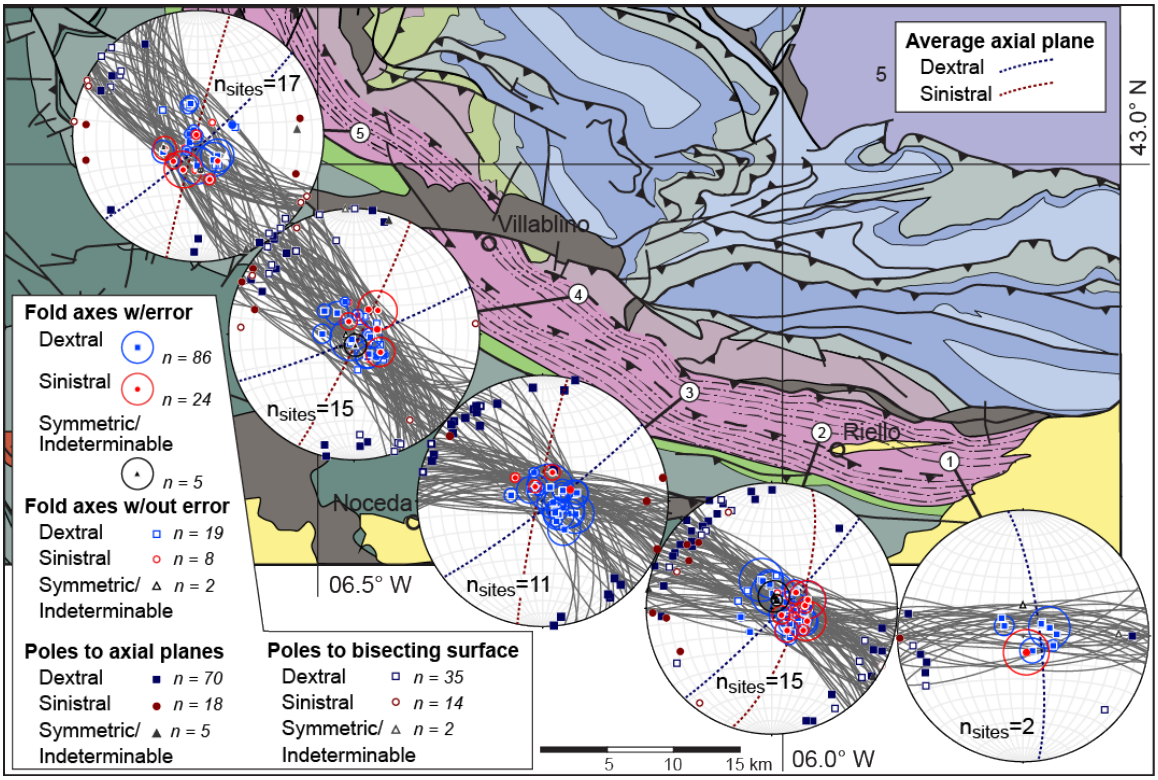

Figure 4-5 Stereonet plots for steeply plunging mesoscale folds S1/S2 measured within the southern limb of the Cantabrian orocline. Solid gray great circles on each stereoplot show the local orientation of the dominant S1/S2 foliations, which equate to local structural strike and are the long-limb orientations for the majority of measured folds; folds that developed on the short limb of a larger-scale parasitic fold have long limbs oriented at some angle to local structural strike.

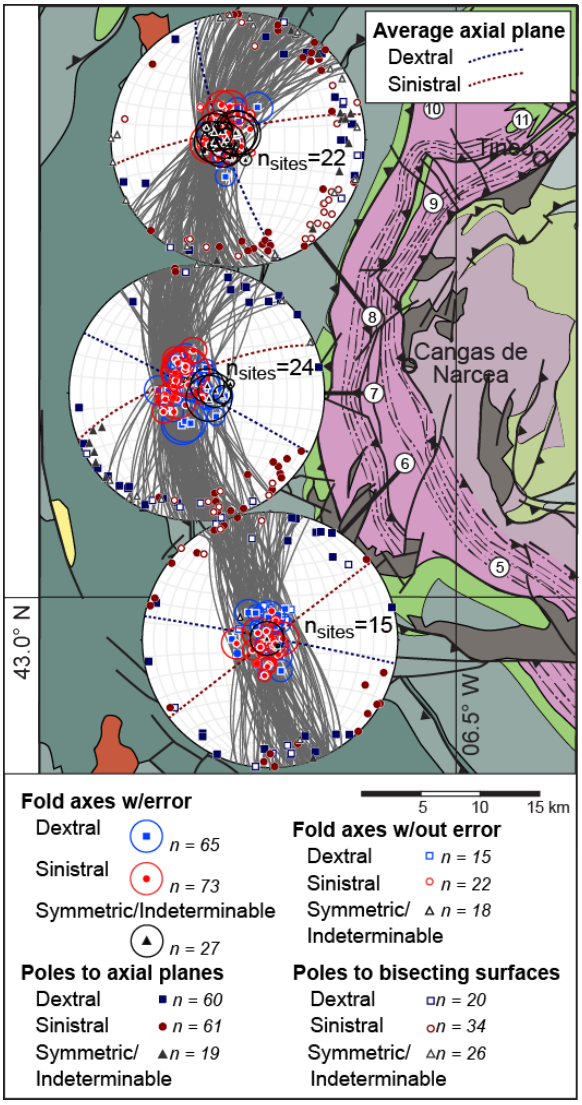

Figure 4-6 Stereonet plots for steeply plunging mesoscale folds of S1/S2 measured within the hinge region of the Cantabrian orocline. Solid gray great circles on each stereonet plot show the local orientation of the dominant S1/S2 foliations, which equate to local structural strike and are the long-limb orientations for the majority of measured folds; folds that developed on the short limb of a larger-scale parasitic fold have long limbs oriented at some angle to local structural strike.

Figure 4-7 (opposite) Annotated field photographs of measured mesoscale vertical-axis (>65º plunge) folds and accompanying stereonet plots within which the bold great circle represents the long limb of the fold, i.e. the dominant orientation of S1/S2. Axial planes (or hinge lines in the case of photograph PC70B-01) are traced by and plotted as dashed lines in blue, indicating dextral asymmetry, or red, indicating sinistral asymmetry. The fabric being folded (S1/S2) is traced in either solid white or solid black. Dual asymmetry is not uncommon and most often attributable to the development of parasitic folds at diminishing scales (photographs PC107-05 and PC26-01). Similar relationships are more cryptic at larger scales, e.g. the dominant outcrop-scale ENE-WSW trend of S2 in PC107-05 is high-angle to the dominant regional-scale N-S trend of the fabric in the hinge zone where the outcrop is located. Note that the dextral folds in photographs PC07-r1 and PC98-01 appear *S*-shaped because they are being viewed up-plunge.

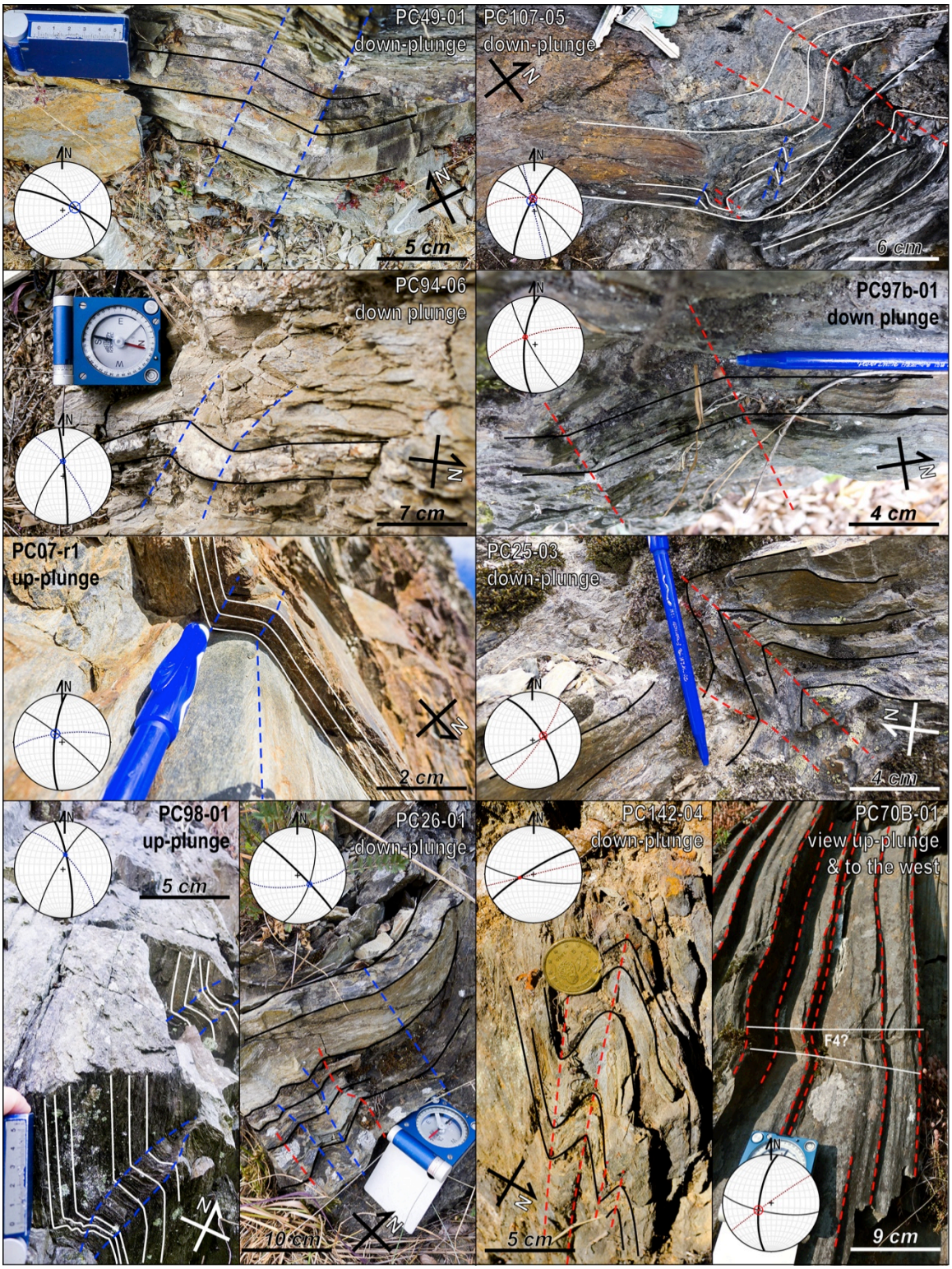
PC49-01
down-plunge
5 cm
PC107-05
down-plunge
6 cm
PC94-06
down plunge
7 cm
PC97b-01
down plunge
4 cm
PC07-r1
up-plunge
2 cm
PC25-03
down-plunge
4 cm
PC98-01
up-plunge
5 cm
PC26-01
down-plunge
10 cm
PC142-04
down-plunge
5 cm
PC70B-01
view up-plunge
& to the west
F4?
9 cm

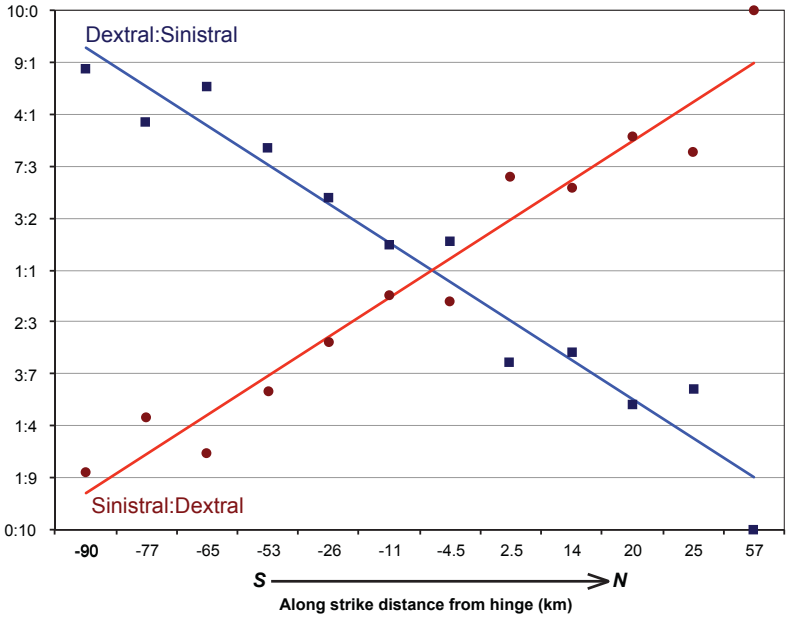

Figure 4-8 Plot showing the ratios of dextral to sinistral folds (blue) and sinistral to dextral folds (red) decreasing and increasing along-strike from south to north, respectively. Individual points correspond to the groupings of proximal data collection points represented by stereonet plots in Figures 4-4,-5 and -6. Lines of best fit were calculated by linear regression in Excel®.

4.5 Discussion and conclusions

The structural data presented herein point to formation of the Iberian coupled oroclines by buckling accommodating significant orogen-parallel shortening along an initially linear Variscan orogen. Along strike variations in paleomagnetic declination (e.g. Weil et al., 2010) and offshore paleocurrent flow direction (Shaw et al., 2012) about the axes of the Cantabrian and Central Iberian oroclines indicate a negligible degree of initially inherent curvature within the pre-orocline Iberian Variscan orogen. Here we discuss the potential implications of these findings for our understanding of the processes involved in Pangean amalgamation. Palinspastic restoration of the Iberian coupled oroclines yields a 2100 km long linear segment of the Variscan orogen (Fig. 4-9) and shows that >1100 km of orogen parallel shortening occurred during orocline formation (Johnston et al., 2013; Shaw et al., 2014) over a 10-20 My time interval between the Late Carboniferous cessation of east-west Variscan shortening (in modern-day coordinates) and the onset of Early Permian deposition of post-oroclinal terrigenous sedimentary successions (Gutiérrez-Alonso et al., 2004; Weil et al., 2010; Gutiérrez-Alonso et al., 2011a; 2011b; Pastor-Galán et al., 2011). Formation of the Iberian coupled oroclines therefore required comparatively rapid relative plate motions of between 5.5 and 11 cm • yr^{-1}, suggesting a subduction-related driving mechanism as initially proposed by Johnston et al., (2013). The Variscan is interpreted as the European record of

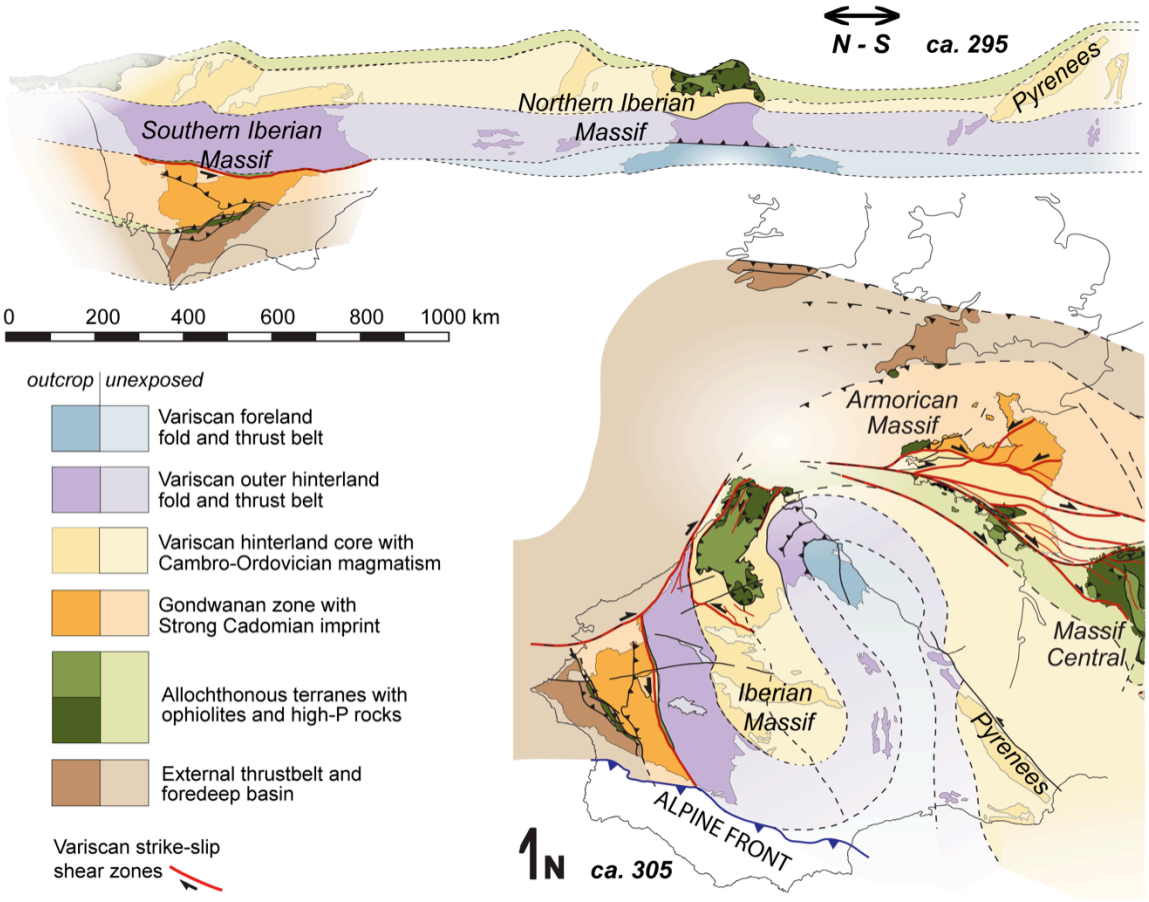

Figure 4-9 Palinspastic restoration of the Iberian coupled oroclines reveals a 2300 km long initially linear Variscan belt whose formation accommodated >1100 km of orogen parallel shortening.

Pangean amalgamation (e.g. Matte, 1991; 2001; Martínez Catalán et al., 1997; 2007; Nance et al., 2010); however, the requirements for formation of the Iberian coupled oroclines, including the accommodation of >1100 km of orogen parallel shortening at rates consistent with subduction driven convergence, are difficult to reconcile with paleogeographic and tectonic models that place orocline formation within the continental core of the Pangean supercontinent. Thorough reviews of the existing paleotectonic models for formation of the Iberian coupled oroclines can be found in Johnston et al. (2013) and Weil et al. (2013b).

The Iberian coupled oroclines are an isoclinal continental scale fold pair; oroclines of similarly expansive scale and tightly sinuous geometry are common features, but models invoking secondary buckling are rare. For example, formation of the Fleurieu orocline in the

Adelaide fold and thrust belt of South Australia and the Kingston orocline of the central Appalachians is proposed to have been accommodated by the development of strike-slip shear zones along lithologic boundaries (Marshak and Tabor, 1989; Marshak and Flöttmann, 1996), whereas the Makran orocline of the Eastern Himalaya and Umbrian arc of the central Apennines are proposed to be thin-skinned features accommodated by the development or reactivation of conjugate strike-slip systems (Marshak et al., 1982; Marshak, 1988; 2004). Orocline formation by secondary buckling requires an orogen bound by free surfaces and may also require a subduction-related driving mechanism (Johnston et al., 2013). Johnston (2001) proposed that the Alaskan coupled oroclines formed by vertical-axis buckling of an originally linear Cordilleran orogen; the bends are traditionally interpreted as derived from an initially sinuous North American continental margin (e.g. Box, 1985; Dover, 1994). The Carpathian orocline is coupled with the more southerly and isoclinal Balkan orocline, and buckling of an originally linear Carpathian–Balkan belt is both spatially and temporally linked with ongoing westward tectonic escape of the Anatolian block out of the Arabian–Eurasian collision zone (Burtman, 1986; Shaw and Johnston, 2012). These eastern Alpine oroclines are most commonly interpreted as the relict of a preexisting European embayment (e.g. Burchfiel, 1980; Csontos and Vörös, 2004). Ongoing vertical-axis rotations in the actively tightening Andean oroclines are popularly explained by differential shortening driven by along strike variations in upper plate rheology and/or degree of coupling between upper plate and subducting Nazca slab (e.g. Isacks, 1988; Lamb, 2001; Allmendinger et al., 2005; Medvedev et al., 2006). Johnston et al. (2013) proposes an alternative model of buckling in response to an orogen parallel stress derived from subduction-collision at the E-W striking (orogen perpendicular) South American–Caribbean plate margin.

The identification of a component of flexural shear accommodated during formation of the Iberian coupled oroclines is consistent with the interpretation of the oroclines as secondary features formed by buckling of an initially linear Variscan orogen in association with a regional stress field distinct from that responsible for initial orogen perpendicular shortening. A similar mechanism of vertical-axis buckling is suggested for oroclines that are similarly extra-orogenic (developed after initial orogenic shortening) and continental in scale.

Chapter 5. Terrane wrecks and inclination anomalies

5.1 Abstract

Three major orogenic belts that are host to coupled oroclines (terrane wrecks) are likewise characterized or directly associated with paleomagnetic inclination anomalies: (1) the North American Cordillera, (2) the Western European Variscan belt, and (3) the Eastern European Alpine system. Implied paleolatitudinal discrepancies in each orogen are of similar magnitude to the translation required by orogen parallel shortening during oroclinal formation. The Alaskan coupled oroclines accommodated >3000 km of orogen parallel shortening in the North American Cordillera, where primary remanent paleomagnetic inclinations in Late Cretaceous rocks require the bulk of the belt to have been translated 2000 to 3000 km northward relative to cratonic North America over a 20-30 My time span. The Iberian coupled oroclines accommodated >1100 km of orogen parallel shortening in the Western Variscan belt, within which mid-Paleozoic paleomagnetic inclinations are shallow with respect to stable Gondwana. The implied existence of a 3500-km-wide Paleotethys Ocean between the Variscan autochthon and the north Gondwana margin is seemingly at odds with paleontological constraints. The Carpathian–Balkan oroclines accommodated >1000 km of orogen parallel shortening in the Eastern Alpine system, immediately north-northeast of an eastern Mediterranean region, where primary remanent inclinations in Late Oligocene to Miocene rocks require northward translation between 500 and 1000 km. Palinspastic restoration of the Alaskan and Carpathian–Balkan oroclines fully accounts for the translations recorded by the Cordilleran and Eastern Mediterranean inclination anomalies, respectively. Restoration of the Iberian coupled oroclines confirms the existence of the Paleotethys Ocean, but only accounts for one third of the paleolatitudinal discrepancy recorded by the Variscan inclination anomaly. Fully resolving the Variscan inclination anomaly requires: (1) a paleomagnetic data set of greater temporal and spatial extent, and (2) refinement of the geometric and geological continuity of the Variscan belt across Western Europe.

5.2 Introduction

Paleomagnetic studies of stable cratonic realms are instrumental in constraining Earth's paleogeographic evolution. Paleomagnetic data from the mobile belts that flank the Precambrian cratons, however, are often difficult to interpret. Problems arise when such data are seemingly at odds with the cratonic reference values to which all apparent geological evidence suggests they should conform; the solution has commonly been to discredit and ignore the 'anomalous' paleomagnetic data sets, no matter how robust (e.g. Westphal, 1993; Robardet, 2003.

Secondary oroclines (sensu Johnston et al., 2013) are orogens expressing lithospheric-scale curvature developed secondarily in response to a reorientation of principle compressive stress from orogen perpendicular to orogen parallel. Coupled oroclines, or "terrane wrecks" (Johnston, 2001) result from buckling into two or more contiguous bends. Although the processes and mechanisms involved with oroclinal buckling are not well understood, it is apparent that the formation of coupled oroclines requires a significant component of orogen parallel shortening implying a comparable magnitude of translation in plan.

Three major orogenic belts that are host to coupled oroclines are likewise characterized by or directly associated with paleomagnetic inclinations that are anomalously shallow with respect to cratonic reference values. These orogens are: (1) the North American Cordillera, host to the Alaskan coupled oroclines, (2) the Western European Variscan belt, host to the Iberian coupled oroclines, and (3) the Eastern European Alpine system, host to the coupled Carpathian–Balkan oroclines. The paleomagnetic inclination anomalies associated with each of these orogens imply paleolatitudinal discrepancies of strikingly similar magnitude to the degree of orogen parallel shortening acquired during oroclinal buckling. The discussion herein aims to show that these so-called inclination anomalies are in fact records of the translation required for the formation of coupled oroclines. We will begin with a geologic overview of each orogenic system, present the nature and timing constraints on the formation of each set of coupled oroclines, discuss the nature of the paleomagnetic inclination anomalies that characterize each orogen, and finally, show how these inclination anomalies may be either fully or partially resolved through palinspastic restoration of the coupled oroclines.

5.3 The North American Cordillera

5.3.1 Geologic overview

The North American Cordillera extends the length of the Pacific flank of the continent, from Alaska to Mexico, but is segmented in nature. The Cordillera has long been considered the archetypal accretionary orogen, constructed in conjunction with the steady westward growth of North America through successive terrane accretions beginning with the Devono-Mississippian emplacement of the Roberts Mountains allochthon (e.g. Burchfiel et al., 1992). However, the widely accepted accretionary model for Cordilleran orogenesis has been called into question (Moores, 1970, 1998; Tempelman-Kluit, 1979; Mattauer et al., 1983; Chamberlain and Lambert, 1985; Lambert and Chamberlain, 1988). Johnston (2001, 2008), whose research focus lies within the northern (Canadian and Alaskan) segment of the belt, and Hildebrand (2009, 2013), principally focused in the contiguous United States, have independently argued for an alternative model of collisional orogenesis. The alternative model involves Late Cretaceous collision of North America with a composite continental mass resulted in the main (Sevier–Laramide) episodes of Cordilleran mountain building. Protracted aggregation of the colliding composite Cordilleran ribbon continent occurred within the Panthalassan (proto-Pacific) realm, far to the west of the ancestral North American margin.

The coincidental proximity of the US–Canada international border to the locus of change in numerable along-strike variations has made such contrasts appear all the more prevalent and further complicates the inherently difficult task of formulating a cohesive model of formation for the length of the belt. As the most salient concerns of this Cordilleran discussion are associated with the Canadian sector of the belt, employment of nomenclature and terminology unique to that sector is unavoidable; U.S. equivalents are provided where possible.

The fundamental architecture of the Canadian Cordillera may be described as consisting of (1) an eastern foreland fold and thrust belt developed within sedimentary strata of continental affinity, (2) a central accretionary domain (the Intermontane belt) consisting of pericratonic, arc and oceanic assemblages traditionally assumed to have formed in close proximity to North America and (3) a western accretionary domain (the Insular belt)

containing a mixture of exotic assemblages with both continental and oceanic affinities (Fig. 5-1; Johnston, 2008). Paleozoic to Middle Jurassic strata of the foreland domain are internally divisible into eastern and western shallow-water platforms; the eastern, westward-deepening Rocky Mountain platform and the western, eastward-deepening Cassiar platform (termed the Antler platform in the Basin and Range; Hildebrand, 2009, 2013) separated by a central deep-water facies domain (the Medial basin).

Passive margin sedimentation within the Rocky Mountain platform is ongoing until at least 155 Ma (Ross et al., 2005), unperturbed by the Late Paleozoic to Early Mesozoic orogenic episodes that characterize and constrain the docking of outboard terranes within traditional accretionary models. Collisional models for Cordilleran orogenesis require the suture joining autochthonous North America with the Cordilleran ribbon continent to exist within the eastern reaches or along the eastern boundary of the Medial basin (Johnston, 2008); both the Intermontane domain and Cassiar platform record a major Late Triassic-Early Jurassic orogenic event (Johnston, 2008) and Devono–Mississippian deformation (related to the Antler orogeny of the western U.S.?) is recorded by the development of recumbent nappe stack within Medial basin facies of the Kechika trough (McLeish et al., 2010; McLeish and Johnston, 2011). Allochthoneity of the east-facing Cassiar platform is supported by the presence of Eurasian fauna conodont species *Epigondolella* and *Paragondolella* (Orchard, 2006), which are similarly characteristic of arc and accretionary assemblages of the Intermontane domain (e.g. Orchard, 2000; Johnston and Borel, 2007). Geochemical and geochronological data from the Cretaceous Omineca magmatic belt, which stitches the Intermontane, Cassiar platform, and Medial basin (Fig. 5-2), suggest that closure of the ocean basin separating North America and the Cordilleran ribbon continent was achieved through westward directed subduction (Johnston, 2008 and references therein). Diachronous Late Cretaceous collision of the Cordilleran ribbon continent with the western margin of North America coincides with the onset of foreland basin sedimentation and formation of the Sevier and Rocky Mountain fold and thrust belts from ~120–60 Ma (Hildebrand, 2009 and references therein) and ~80–50 Ma (Price, 1981; McMechan et al., 1992; Enkin et al., 2000; van der Pluijm et al., 2006), respectively.

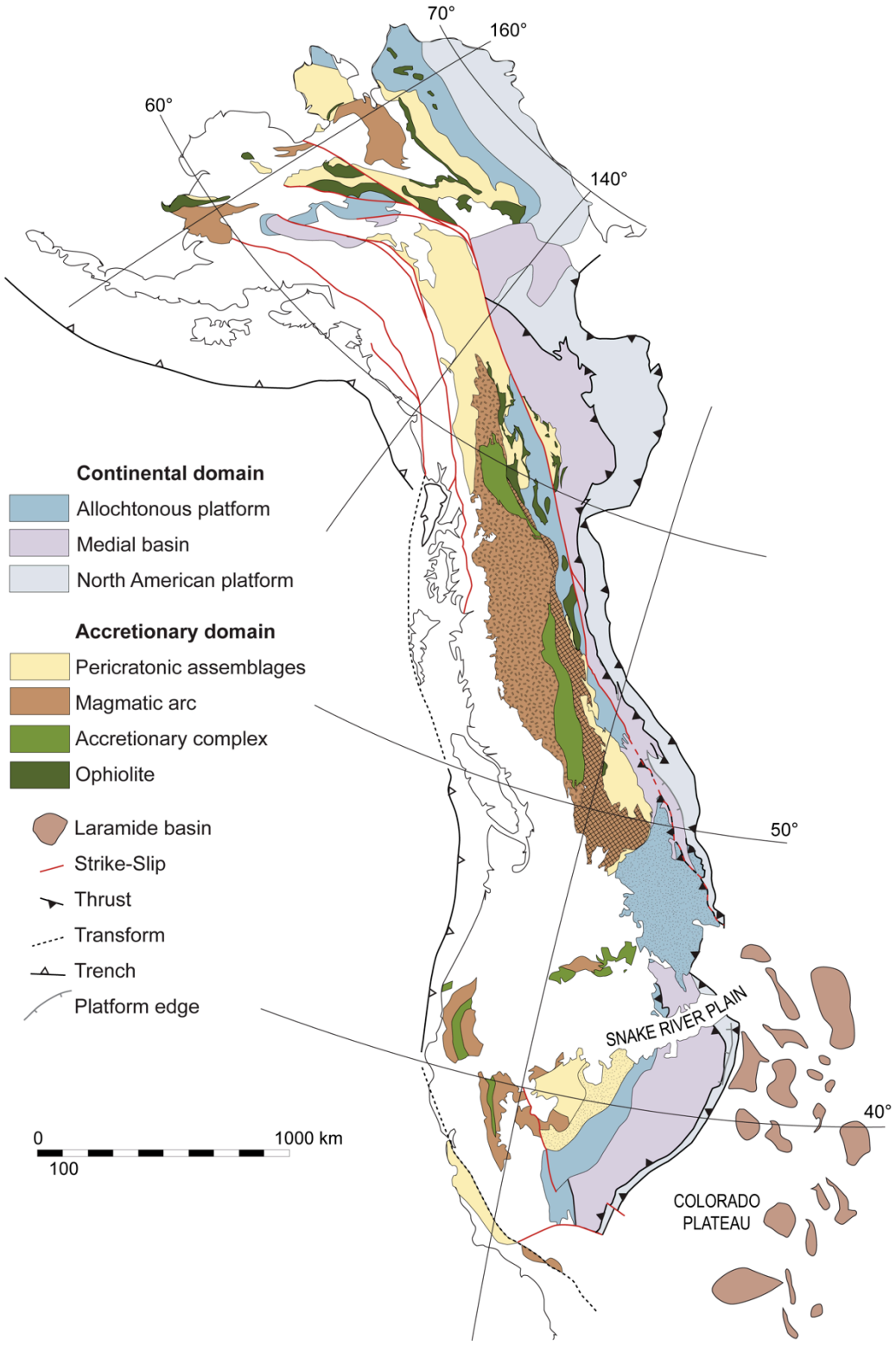

Figure 5-1 Generalized tectonostratigraphic map of the North American Cordillera, after Johnston (2008) and Hildebrand (2013).

5.3.2 The Alaskan coupled oroclines

Alaska, in striking contrast to the relatively well-ordered northwest-southeast trending collage of the more southerly Cordillera, is characterized by a series of belts of variable orientation (Fig. 5-1). Continuity between east–west-trending Brooks Range, the central southwest-trending Ruby Range and the southerly east–west trending Dillinger belt defines a *Z*-shaped oroclinal pair within the Alaska promontory (Fig. 5-3). Early observers of the 'Z' pattern attributed its existence to successive terrane accretion along an initially irregular North American continental margin (Box, 1985), or to a combination of a relict continental margin irregularities and mid-Cretaceous tectonism (Dover, 1994). Formation of the Alaskan oroclines by secondary buckling of an initially linear 300 km-wide Cordilleran ribbon was initially proposed by Johnston (2001). Johnston's model of a "great Alaskan terrane wreck" is supported by (1) a continuity of ophiolites and accreted terranes about both bends, (2) consistently strike-perpendicular structural vergence, (3) consistent and predictable variations in slope-basin facies transition within sediments of the Cassiar platform, and (4) available paleomagnetic data showing significant and opposing vertical axis rotations (Johnston, 2001 and referenes therein).

Westward continuity of the Brooks Range through the Seward Peninsula into the Chukotsk Peninsula of eastern Siberia and southeastward continuity of the Dillinger belt into Yukon require that the 'Z' of the Alaskan coupled oroclines occupy the core of a four-member oroclinal fold train. Palinspastic unbuckling of the Alaskan oroclines restores >3000 km of orogen parallel shortening and places the bulk of the Cordillera at significantly more southerly latitudes in the Late Mesozoic. The timing of formation of the Alaskan coupled oroclines is constrained to the latest stages of Cordilleran orogenesis in the Late Cretaceous through Paleocene by the involvement of mid-Cretaceous plutons as young as 95 Ma and by the subsequent overlap of Late Paleocene sedimentary rocks yielding paleomagnetic poles that are concordant with those of cratonic North America (Johnston, 2001, 2008). The relatively short (20–30 My) time window for orocline formation requires sustained translation at relatively rapid rates of 10 $cm \cdot yr^{-1}$ (Johnston et al., 2013). Modern measurable relative plate motions of similar magnitude are exclusive to plates with subducting slabs (Gordon, 1998), prompting Johnston (2001, 2008) to conclude that buckling of the Alaskan

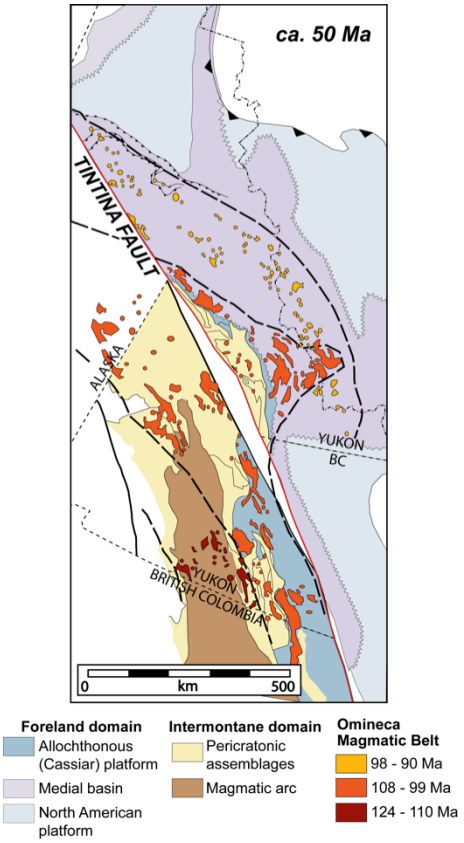

Figure 5-2 (left) Extent and age ranges of the northern Omineca magmatic belt prior to Eocene displacement along the Tintina–Rocky Mountain trench dextral transform system.

Figure 5-3 (below) The Alaskan coupled oroclines. Formation by secondary buckling of an originally linear orogen is supported by continuity of ophiolites and accreted terranes and by consistently strike perpendicular structural vergence. After Johnston (2001, 2008).

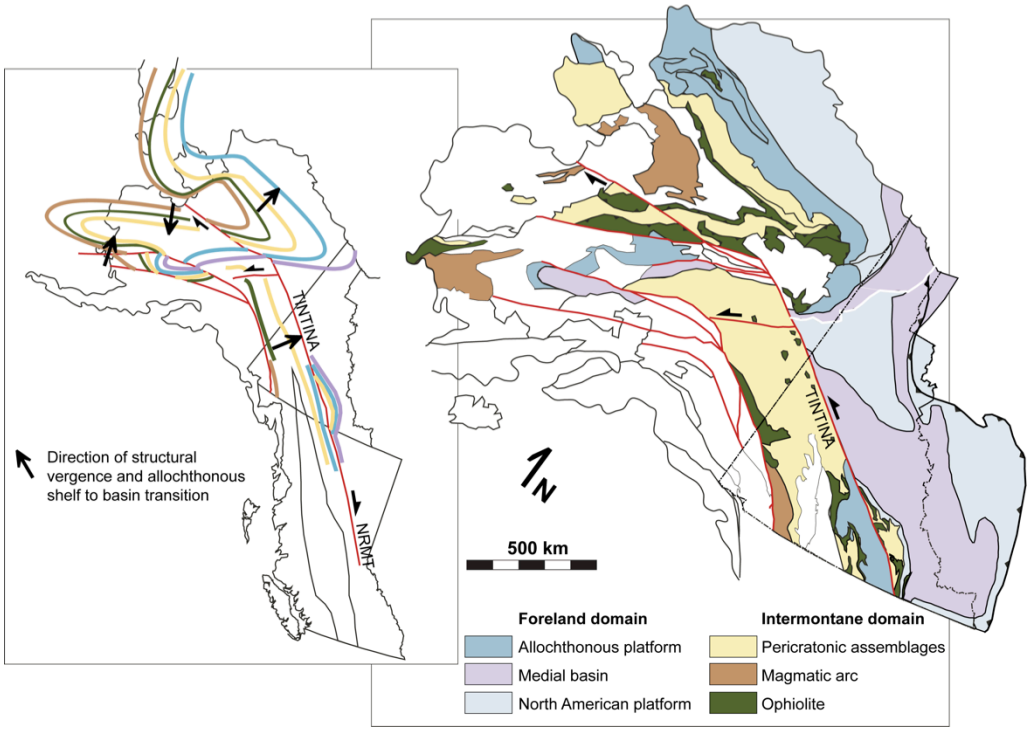

oroclines was driven by northward directed subduction of oceanic lithosphere with which the Cordilleran ribbon continent was either continuous or coupled.

5.3.3 The "Baja BC" hypothesis

Primary remanent magnetizations from Late Cretaceous layered volcanic, and sedimentary rocks of the Intermontane and Insular domains yield paleomagnetic inclinations that are anomalously shallow with respect to reference poles for cratonic North America (see compilation of Enkin, 2006). The data indicate that the bulk of the western Canadian Cordillera, often collectively referred to as "Baja BC" (Irving, 1985), occupied a latitudinal position 2000-3000 km to the south relative to cratonic North America between 90–70 Ma. Paleomagnetic studies of Cretaceous intrusive rocks yield less consistent results, likely attributable to difficulties in constraining paleohorizontal and/or age of remanent magnetization. Paleomagnetic data from some plutons have been interpreted as showing little evidence for displacement relative to the craton (Symons et al., 2005; McCausland et al., 2006); however, the majority of data from intrusive rocks are consistent with the data obtained from supracrustal stratified rocks (Enkin et al., 2006; Irving and Wynne, 1992).

Included among the Late Cretaceous rocks with shallow inclinations yielding far-sided paleopoles are volcanic flows and interlayered sedimentary rocks of the 70 Ma Carmacks Group of Yukon. Paleomagnetic studies of the Carmacks Group indicate cooling and deposition 1950±600 km to the south relative to cratonic North America (Enkin et al., 2006; Johnston et al., 1996; Marquis and Globerman, 1988; Wynne et al., 1998). The Carmacks Group unconformably overlies pericratonic and arc terranes of the Intermontane belt; the Intermontane belt, as earlier stated, is stitched to the Cassiar platform and much of the Medial basin by the mid-Cretaceous (124-90 Ma) Omineca magmatic belt (Woodsworth et al., 1992). Paleomagnetic data for the Carmacks Group must therefore be extrapolated through the Cassiar platform to the eastern limit of the Omineca Magmatic belt within the Medial basin (Gladwin and Johnston, 2006), implying that the eastern limit of Baja BC is coincident with the eastern limit of the Cordilleran ribbon continent and the cryptic suture.

The mean latitudinal difference between Baja BC and cratonic North America as determined from Late Cretaceous stratified rocks (mean age 80 Ma) is 18.6º ± 6.1º, or 2100 ± 700 km (Fig. 5-4; Enkin 2006, and references therein). Paleomagnetic poles from Eocene

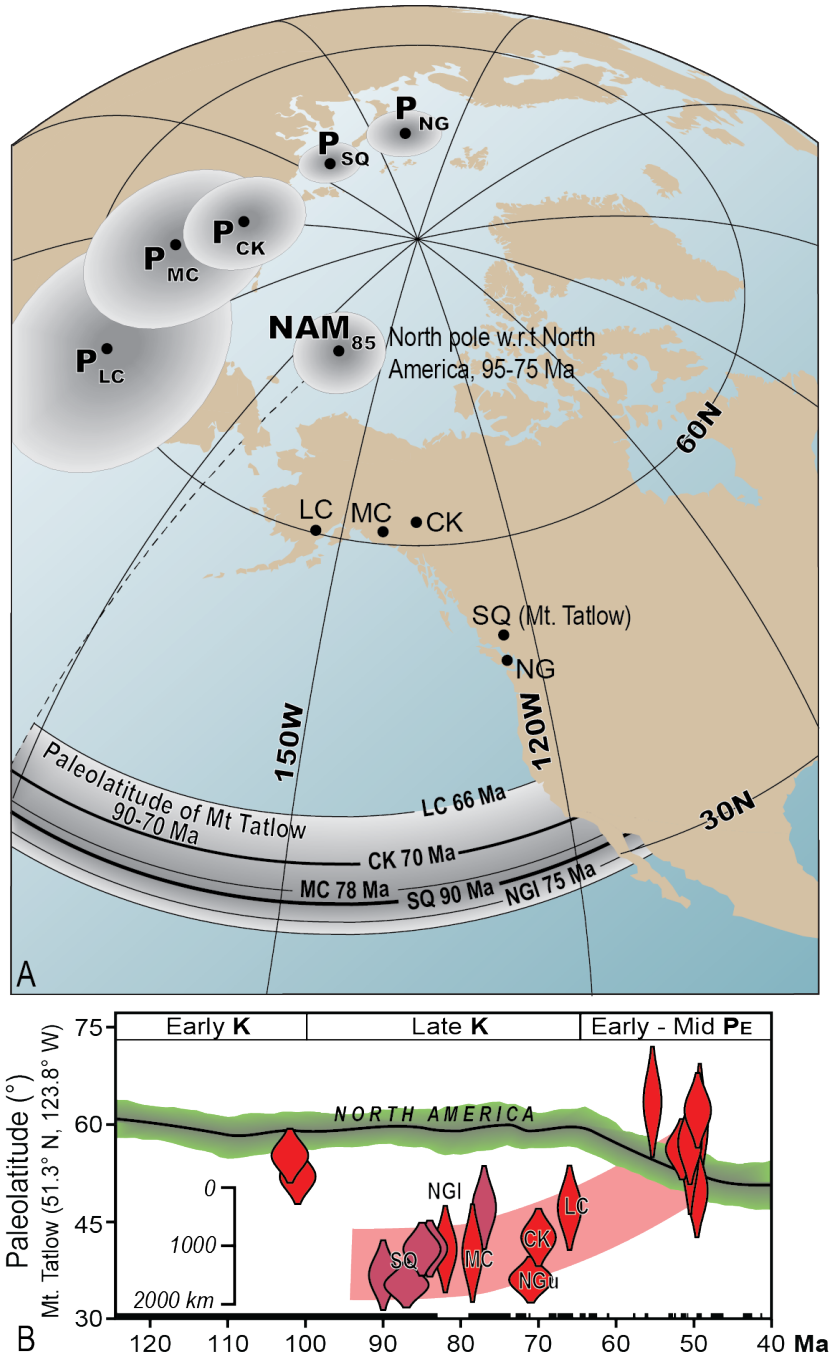

Figure 5-4 Paleomagnetic data from layered sedimentary and volcanic rocks of the Intermontane and Insular belts of the North American Cordillera presented as (A) paleomagnetic poles with their 95% confidence radii, all far-sided with respect to North America, and (B) corresponding paleolatitudes calculated for a reference location at Mt. Tatlow (51.3ºN, 123.8º W) compared with that of North America. After Enkin (2006). CK—Carmacks Group volcanics, YK; LC—Lake Clark lavas, AK; MC—MacColl Ridge formation, AK; NG—Nanaimo Group clastic sediments (upper and lower), BC; SQ—Combined Silverquick and Powell Creek formations, BC.

(55-50 Ma) rocks for the western Canadian Cordillera are concordant with North American reference poles (Enkin 2006 and references therein), requiring that Baja BC reached its current position adjacent to cratonic North America by ~55 Ma. Although Late Cretaceous–Paleogene convergence forming the Foreland fold and thrust belt was accompanied by dextral strike-slip faulting, mappable offset (860 km in the outermost Cordillera; Gabrielse et al., 2006) is a fraction of the translation required by far-sided Cretaceous paleopoles. In addition, half (460 km) of the mappable dextral offset in the Cordillera is accommodated along Eocene structures (e.g. the Tintina–Rocky Mountain Trench; Gabrielse et al., 2006) and therefore post-dates the 80–55 Ma window for northward translation indicated by the paleomagnetic record. The consistency of the paleomagnetic data argues for the existence of a cryptic structure or structures along which thousands of kilometers of margin-parallel displacement were accommodated at relatively rapid rates of translation. Formation of the Alaskan oroclines is coincident with northward translation of Baja BC and requires a magnitude of margin parallel shortening equivalent to the magnitude of margin parallel translation recorded by the "anomalous" Cordilleran paleomagnetic data.

5.4 The Western European Variscan belt

5.4.1 Geologic overview

The Western European Variscan belt provides the European record of Pangean amalgamation, which culminated with the Late Paleozoic closure of the Rheic Ocean and the juxtaposition of Gondwana against the previously amalgamated Laurussia (Laurentia+Baltica+Avalonia) (e.g. Martínez Catalán et al., 1997, 2007; Nance et al., 2010, 2012). The belt extends sinuously across western Europe, from southwestern Portugal to eastern Poland, and correlates across the Atlantic and into northwestern Africa with the Ouachita-Alleghanian and Mauritanide belts, respectively. The Variscan autochthon is of Gondwanan affinity, consisting of a limited Ediacaran sequence deformed through Late Neoproterozoic Cadomian orogenesis and unconformably overlain by a Paleozoic sedimentary sequence recording the development of a pre-orogenic North Gondwanan passive margin and its subsequent Variscan deformation. The autochthon is preserved most completely in the Iberian Massif, where it is divisible into (1) a thin-skinned foreland fold and thrust belt, (2) an external metamorphic hinterland, and (3) an internal metamorphic

hinterland characterized by higher metamorphic grade and a higher occurrence of Variscan granitoids (Shaw et al., 2012) (Fig. 5-5).

In northwestern Iberia, the autochthon is overridden by the ophiolite and high-P assemblage-bearing nappe-stack of the Galicia–Trås-os-Montes zone, most often interpreted as a Rheic Ocean remnant but with no definitive deep crustal root (e.g. Martínez Catalán et al., 2007, 2009). In southwestern Iberia, a fourth "Ossa Morena" zone of Gondwanan affinity is separated from the remainder of the autochthon by the sinistral Badajoz-Cordoba shear zone. Though the Ossa Morena zone is traditionally interpreted as merely a more distal portion of the Gondwanan platform (Robardet and Gutiérrez-Marco, 1990a, 1990b, 2004), its Neoproterozoic, Cambrian and Ordovician detrital zircon signatures are unique with respect to the remaining autochthon, indicating that it occupied a distinctly different position along strike on the North Gondwanan margin at least through these times (Shaw et al., 2014). A dismembered ophiolite (the Beja-Acebuches) along the southern margin of the Ossa Morena zone marks the location of the 'true' Rheic suture, equivalent to the Lizard ophiolitic

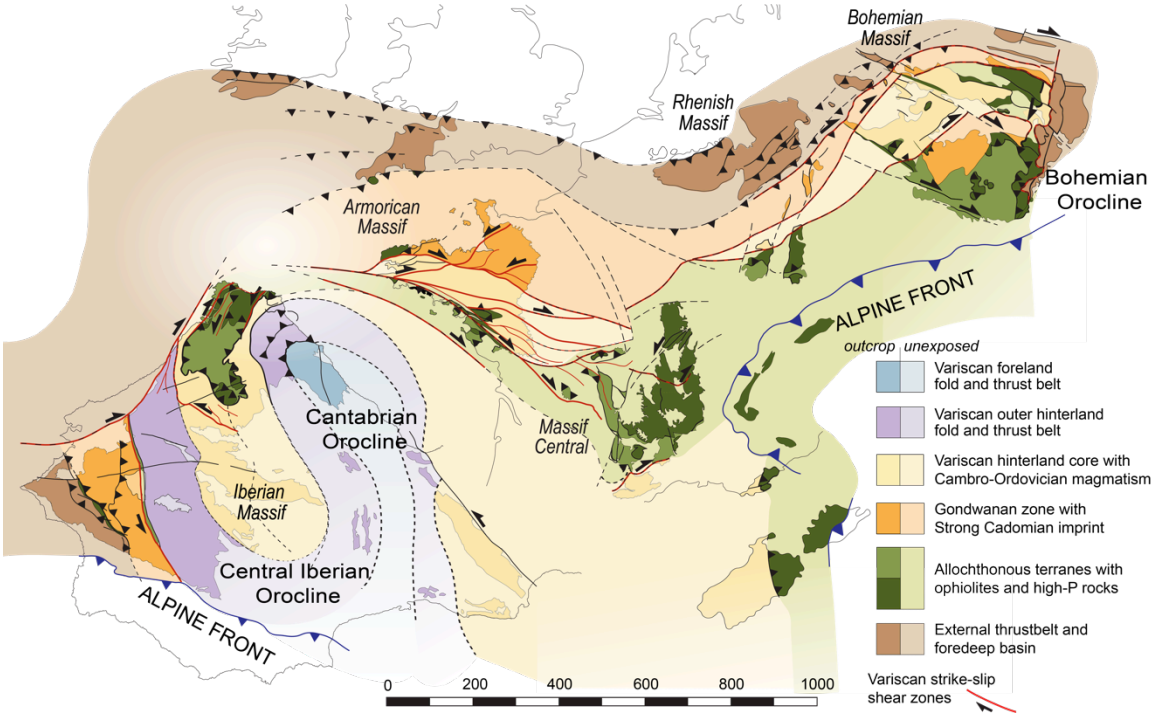

Figure 5-5 General tectonostratigraphic map of the Western European Variscan belt. The Iberian massif is host to the *S*-shaped coupled Cantabrian–Central Iberian oroclinal pair. After Martínez Catalán et al (2007) and Shaw et al. (2012).

complex of southeastern England and the Rheno-Hercynian ophiolites of northeastern France (Martínez-Catalán et al., 2007 and references therein). Outboard of the suture, allochthonous terranes with continental affinity are interpreted as peri-Gondwanan in origin, having departed in conjunction with the opening of the Rheic Ocean at the Cambro-Ordovician boundary (Murphy et al., 2006; Nance et al., 2010, 2012). Though the Beja-Acebuches ophiolitic suture is commonly interpreted as the root to the ophiolite bearing nappes of northwestern Iberia, this interpretation is at odds with contrasting cooling ages determined from the ultramafic rocks in either realm. Ophiolites of the Galicia–Trås-os-Montes zone with protolith ages of 395 Ma (Martínez Catalán et al., 1997; Sanchez Martinez et al., 2007; Murphy and Gutierrez-Alonso, 2008) were obducted at 377 Ma ($^{40}Ar/^{39}Ar$ cooling ages; Dallmeyer et al., 1997); the Beja Acebuches ophiolite was formed and emplaced around 350-340 Ma (Azor et al., 2008; Dahn et al., 2014).

Closure of the Rheic Ocean by northward-directed subduction beneath the Laurussian margin (in present day coordinates) may have accelerated with the coupling of both oceanic margins following (mid-Devonian) subduction of the mid-ocean ridge by 395 Ma (Woodcock et al., 2007; Gutiérrez-Alonso et al., 2008b). Collisional orogenesis initiated with subduction of the outermost Gondwanan margin in the latest Devonian, as indicated by the age of earliest metamorphism in northwest Iberia (Dallmeyer et al., 1997), but may have begun as early as the mid-Devonian in southwest Iberia, southern Britain, and Bohemia (Nance et al., 2010). Subsequent shortening within the autochthon resulted in extensional collapse of the over-thickened hinterland by 320 Ma (Pérez-Estaún et al., 1994). Coeval development of the foreland fold and thrust belt continued into the Pennsylvanian but was complete by 310 Ma (Parés et al., 2000, 2001, 2010a, 2012a, Weil, 2006.)

5.4.2 The Iberian coupled oroclines

The Iberian segment of the European Variscan belt is characterized by the *S*-shaped and isoclinal Cantabrian–Central Iberian oroclinal pair. The Variscan foreland is preserved at the core of the more northerly and convex towards the west Cantabrian orocline, while allochthonous complexes occupy the core of the more southerly and convex towards the east Central Iberian orocline (Du Toit, 1937; Aerden, 2004; Martínez Catalán, 2011; Shaw et al., 2012). The Central Iberian orocline, whose hinge is mostly buried beneath post-Variscan

sedimentary cover, was only recently documented; the well-exposed Cantabrian orocline is, in contrast, one of the best studied structures of its kind. Structural continuity between the Cantabrian–Central Iberian orocline pair confirms their coupled nature and suggests that they formed contemporaneously and in the same fashion. Though the Iberian coupled oroclines are defined to the north of the Badajoz-Córdoba shear zone, $^{40}Ar/^{39}Ar$ age determinations on amphibole and mica sampled from within the shear zone range from 370 Ma to 330 Ma (Quesada and Dallmeyer, 1994), implying that the shear zone predates formation of the oroclines, and that it and the Ossa Morena zone to its south should be continuous around them.

The Iberian coupled oroclines formed by orogen-parallel shortening of an initially linear segment of the Variscan belt (Chapter 4). Evidence for buckling having been a lithospheric-scale process involves the development of coeval metamorphism, mineralization, and magmatism with juvenile mantle sources that contrast those of earlier Variscan mantle sources, suggesting high heat flow associated with lithospheric mantle delamination (Fernández-Suárez et al., 2000b; Gutiérrez-Alonso et al., 2004; 2011; 2011; Ducea, 2011). The timing of oroclinal buckling is constrained by structural, stratigraphic, and paleomagnetic data to a 10-20 My time interval between the Late Carboniferous cessation of east-west Variscan shortening (in modern-day coordinates) and the onset of Early Permian deposition of post-oroclinal terrigenous sedimentary successions (Gutiérrez-Alonso et al., 2004; Weil et al., 2010; Gutiérrez-Alonso, Fernández-Suárez, et al., 2011; 2011; Pastor-Galán et al., 2011). Formation of the Iberian coupled oroclines accommodated a minimum of 1100 km of orogen parallel shortening in the Iberian segment of the Variscan belt (Shaw et al., 2014), requiring rates of translation between 5.5 and 11 $cm \bullet yr^{-1}$. The relatively rapid rates of translation required for formation of the Iberian coupled oroclines suggests, as is the case with the Alaskan coupled oroclines, a subduction-related driving mechanism (Johnston et al., 2013).

5.4.3 The Armorica Microplate

Gondwanan affinity of the Variscan Paleozoic continental platform is established through strong sedimentological and paleontological ties (Noblet and Lefort, 1990; Robardet, 2003). Early Paleozoic placement of the 2300 km-long palinspastically restored Iberian segment of the Variscan belt along the (present-day) northern limits of the Saharan hinterland and

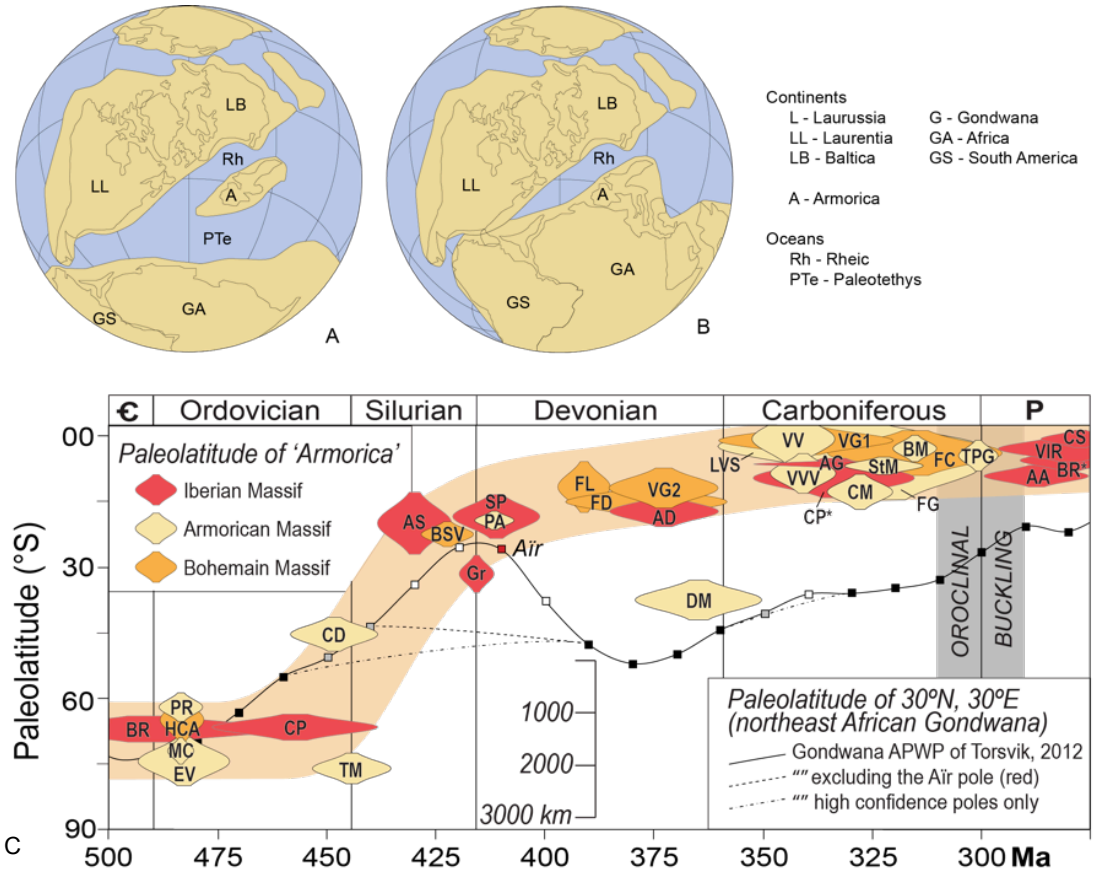

Figure 5-6 Contrasting global paleogeographic models for the mid-Devonian as constrained by paleomagnetic data that require 30º latitudinal separation between Armorica and North African Gondwana (A, B) and by paleontological data that require continuity between Armorica and North African Gondwana. (C) Plot of Paleozoic paleolatitudes for Armorica, as recorded by paleomagnetic inclination data from the Variscan autochthon (raw data and location acronyms listed in Table A-6), against the paleolatitude of northeast African Gondwana calculated from the apparent polar wander path of Cocks and Torsvik (2002) for a reference location at 30ºN, 30ºE. A and B after (Johnston and Gutierrez-Alonso (2010).

Arabian-Nubian Shield is well-constrained by detrital zircon provenance and in agreement with all other petrological, paleontological, and paleomagnetic constraints for these times (Shaw et al., 2014 and references therein). However, mid-Paleozoic paleomagnetic data from the Iberian, Armorican, and Bohemian massifs (Table A-6 in the appendix) place these regions at significantly lower paleolatitudes than the North African Gondwanan margin to which they are linked (Fig. 5-6). The implied separation and independent northward drift of the European Variscan autochthon, collectively referred to as "Armorica" (Van der Voo, 1979, 1982), requires the growth of a second major ocean (the Paleotethys) at the expense of

the more northerly Rheic. Though paleomagnetic data indicate that Paleotethys reached a maximum width ca. 3500 km during the Devonian, the existence of a wide Paleotethys is seemingly at odds with faunal and stratigraphic studies (Robardet, 2003; Linneman et al., 2004) that indicate little or no separation between the Variscan autochthon and Gondwana.

Constraining the timing of separation of Armorica is complicated by a paucity of Siluro-Devonian paleomagnetic poles for stable Gondwana, allowing for a range of interpretations of the apparent polar wander path of the Gondwana megacontinent during this time (see compilation of Torsvik and Cocks, 2013). A rapid (~6.5 cm•yr^{-1}) northward excursion of Gondwana during the Silurian allows for Armorica to remain fixed to the north African margin through the Early Devonian, but is constrained by a single paleomagnetic pole during the 450-400 Ma time interval, the 409 Ma Aïr intrusives of Niger (Hargraves et al., 1987). Exclusion of the 409 Ma Aïr pole, for which there is no direct constraint on paleohorizontal, implies a steady northward drift for Gondwana over the course of the Paleozoic, and requires separation of Armorica in the Early to mid-Silurian (Fig. 5-6). Early Devonian opening of the Paleotethys, as implied by the inclusion of the Aïr pole, requires an average full spreading rate along a mid-ocean ridge in excess of 11.5 cm•yr^{-1} in order to reach a maximum width of 3500 km at 380 Ma.

Armorica sensu Van der Voo (1979) was defined on the basis of, and thus included, the peri-Gondwanan arc Avalonia. As Cambro-Ordovician separation (from Gondwana) and Silurian accretion (to Laurentia–Baltica) of Avalonia was later constrained by a range of geologic, paleomagnetic and paleontological data, allochthoneity of the Avalonian regions of western Europe (southern Britain, Saxo-Thurungia and perhaps southern Iberia) was established. Both paleomagnetic declination data implying differential rotations between massifs (e.g. Tait et al., 2000a) and the distribution of ophiolites and/or high-pressure terranes interpreted as oceanic sutures (e.g. Matte, 2001), have been used to argue for the existence of an "Amorican Terrane Assemblage", as opposed to a singular and continuous Armorica microplate. However, differential rotations are a necessity of orocline formation, oceanic sutures may themselves be involved in oroclinal buckling, and the full extent and nature of oroclinal bends within the Western European Variscan belt has yet to be determined (Warr, 2012). In addition, faunal similarities indicate that any potential separation between the Variscan massifs would have been minimal (McKerrow and Cocks,

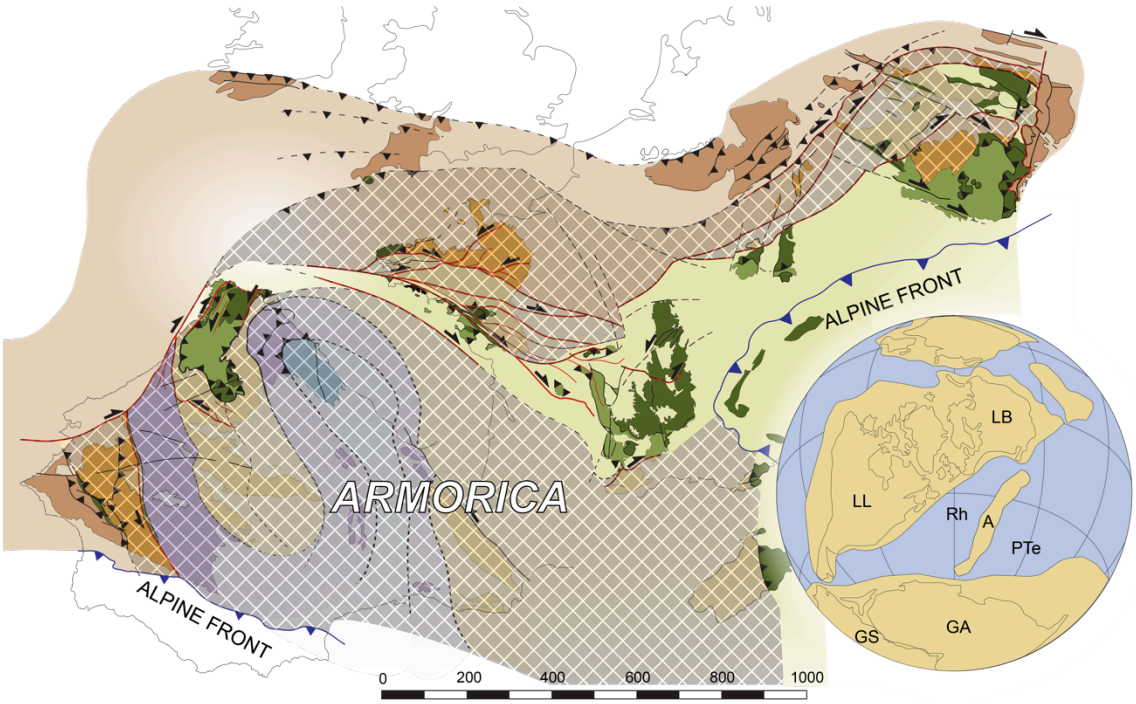

Figure 5-7 The geographical extent of the Armorica corresponds to the entirely of the Variscan autochthon. Insert shows alternative mid-Devonian global paleogeography where a hypothesized north-south elongate Armorican continental ribbon satisfies both paleontological and paleomagnetic data sets.

1986). We therefore consider Armorica as a singular entity consisting of the full extent of the once continuous Western European autochthon (Fig. 5-7), and propose that the apparent dilemma of faunal and stratigraphic continuity across a wide Paleotethys may be resolved if Armorica were an elongate continental ribbon outstretched across it. Testing this hypothesis requires paleomagnetic data of greater temporal and spatial extent than is currently available in addition to a refinement of the geometry and geological continuity of the Variscan orogen across Western Europe.

5.5 The Eastern European Alpine system

5.5.1 Geologic Overview

The Alpine orogenic system stretches sinuously across the southern flank of continental Europe (Fig. 5-8), providing a complex record of interactions between the African and Eurasian plates spanning from at least the Late Jurassic to recent times (e.g. Burchfiel, 1980; Schmid et al., 2008). The Carpathian–Balkan and Dinaride–Hellenide belts constitute the

Figure 5-8 Satellite image of Europe overlain by the approximate traces of major orogenic fronts of the Alpine system, (solid upper plate indicators), modern subduction trenches (hollow upper plate indicators) and major transform systems. Imagery courtesy of NASA earth observatory.

respective northeastern and southeastern segments of the Alpine system, and are characterized by opposing structural vergence and contrasting structural trends (Fig. 5-9). The Carpathian–Balkan belt traces a broad hook across northeastern Europe before doubling back to terminate against the western margin of the Black Sea. Structural vergence is toward the European foreland, but directionally variable as maintains perpendicularity to structural strike around the coupled Carpathian–Balkan oroclines (Burtman, 1986; Csontos and Vörös, 2004). The Dinaride–Hellenide belt forms a roughly linear southeast-trending belt spanning from the southeastern limit of the Eastern Alps through the Grecian peninsula, with structural vergence facing consistently southwest (Burtman, 1986; Handy et al., 2015).

Deformation within the Eastern Alpine system relating to closure of the Tethyan seaway is long-lived, polyphase, and complex, involving the subduction-collision of debatable numbers of intervening continental fragments and associated ocean basins (e.g. Burchfiel, 1980; Csontos and Vörös, 2004; Schmid et al., 2008). The European basement to the Eastern Alpine system is variable, consisting of Variscan, Caledonian, and Precambrian components

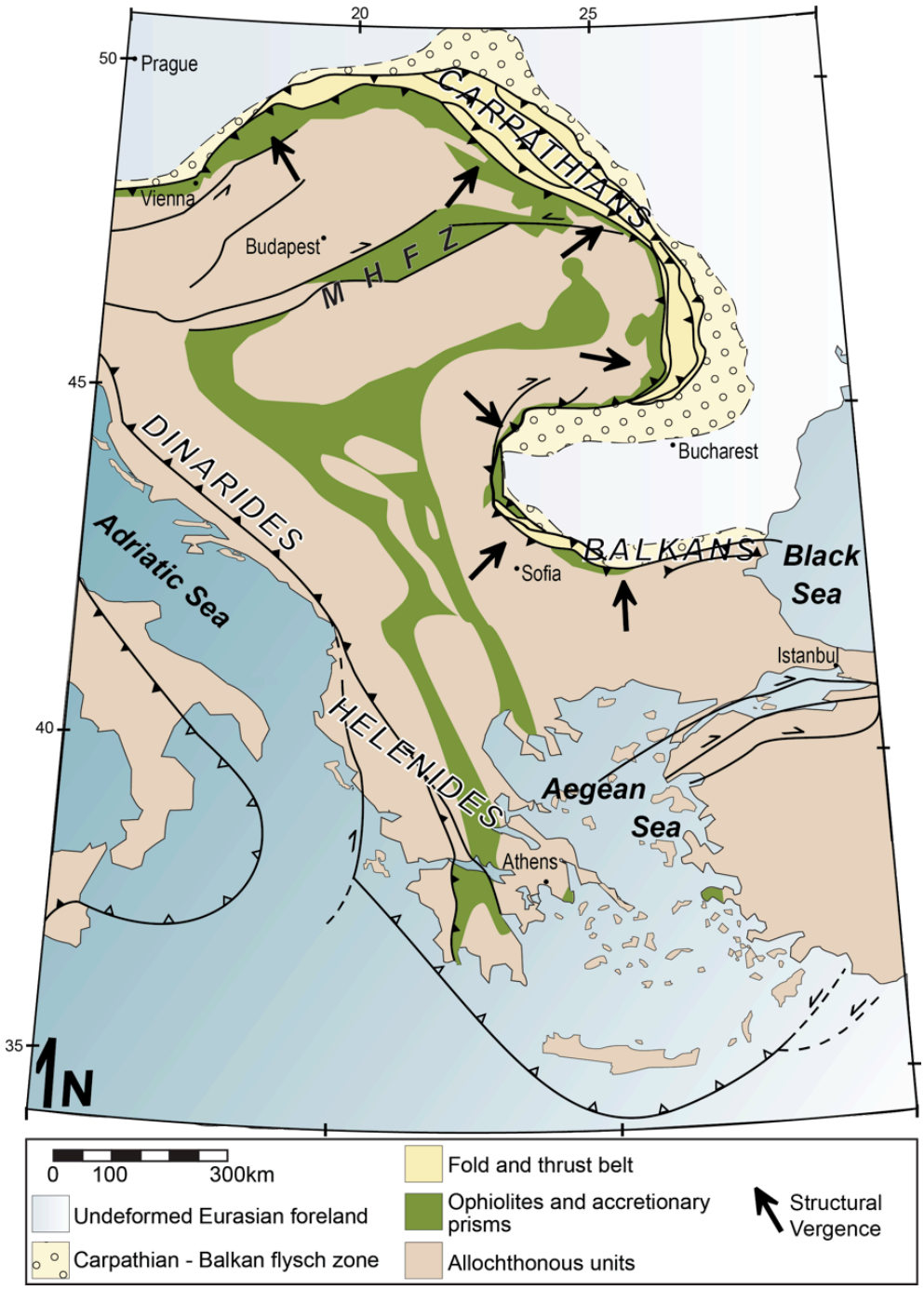

Figure 5-9 General tectonostratigraphic map of the Eastern European Alpine system illustrating consistent strike-perpendicular structural vergence directed toward the European foreland about the Carpathian–Balkan oroclines and opposing southwest directed structural vergence in the Dinaride–Hellenide belt. MHFZ—Mid Hungarian Fault zone. Simplified geology modeled after Burchfiel (1980), Horvath (1993), and Tischler (2008). Extent of Balkan flysch zone after Burtman (1986); extent of ophiolites and accretionary complexes in Grecian peninsula after van Hinsbergen et al. (2005).

(Schmid et al., 2008). From the undeformed Eurasian foreland to the southwest, the fundamental architecture of the Eastern Alpine system consists of (1) an external foredeep (molasse) domain; (2) a thin-skinned fold and thrust (external flysch belt); (3) ophiolitic and accretionary nappe complexes that form a continuous band along-strike aboutboth the Carpathian and Balkan oroclines (e.g. Handy et al., 2015); (4) a complex arrangement of variably derived allochthonous terranes and intervening suture zones,including components emplaced through late-stage (Neogene) lateral extrusion from the west (e.g. Alcapa sensu Csontos and Vörös, 2004); and 5) a southward verging fold and thrust belt deforming the leading edge of the Apulia(–Adria) microplate, whose specific independent Mesozoic drift history remains a matter of debate (e.g. Stampfli, 2005).

The main phases of Alpine deformation within the Carpathian–Balkan belt consist of (1) mid-Cretaceous long-distance nappe transport directed toward the Eurasian foreland, (2) Late Cretaceous to Paleocene folding of the nappe stacks into a system whose axial traces run parallel to the modern actuate trend of the belt (Burchfiel, 1980) , and 3) Late Oligocene to Miocene formation of the foreland fold and thrust belt and external foredeep (Schmid et al., 2008; Burchfiel, 1980; Royden and Burchfiel, 1989). Oceanic closure in the region was complete by the Eocene (Nemcok et al., 1998; Royden and Burchfiel, 1989), and achieved through subduction of Eurasian oceanic lithosphere as indicated by nappe transport directed toward the Eurasian foreland, and by calc-alkaline to alkaline magmatism within the accreting terranes (Schmid et al., 2008; Burchfiel, 1980). Subduction polarity is reversed in the Dinaride–Hellenide belt, with Adria forming the lower plate during the Late Jurassic emplacement of ophiolitic nappes and through the main phases of Cretaceous to Cenozoic fold and thrust belt development (Schmid et al., 2008).

5.5.2 The Carpathian–Balkan coupled oroclines

The Alpine orogenic system is characterized by a number of arcuate segments (Fig. 5-8), all of which are commonly interpreted as primary features inherited from an initially convolute southern European margin. The most widely accepted tectonic models for formation of the Carpathian–Balkan oroclines propose variable styles of terrane accretion into an existing Carpathian embayment, most commonly driven by roll-back of the southwestward dipping Eurasian-Tethys slab (e.g. Channell and Horváth, 1976; Burchfiel,

1980; Csontos and Vörös, 2004). However, reconciliation of such models is made difficult by the along-strike continuity of orogenic structures and tectonostratigraphic units about both bends. Palinspastic restoration of the internal (mid-Cretaceous to Paleocene) Carpathian–Balkan fold and thrust belt is not possible within any model invoking primary curvature; an excess line length through the Carpathians would require all nappes to restore to a common origin; a line length deficit around the Balkan orocline would require thrust nappes to have been either originally discontinuous or shortened in plan simultaneous with emplacement. In addition, rollback-driven terrane accretion into a pre-existing continental embayment predicts a significant component of syn-accretion transform motion, for which there is no evidence (Shaw and Johnston, 2012).

An alternative model for formation of the Carpathian–Balkan coupled oroclines by buckling of an originally linear northwest-southeast trending fold and thrust belt about a vertical-axis is not possible within any model invoking primary curvature; an excess belt was initially proposed by Burtman (1986), and more recently supported by Shaw and Johnston (2012). Secondary buckling of an originally linear Carpathian–Balkan belt is supported by both the consistency of strike-perpendicular vergence and the continuity of ophiolites and accreted terranes about both bends. Though paleomagnetic data constraining the timing and extent of vertical-axis rotations within the belt are limited, rocks older than 35 Ma consistently show significant rotations (Fig. 5-10), implying that buckling likely initiated closely after the Eocene termination of collision and accretion. Oroclinal buckling was therefore coeval with (1) eastward-directed lateral extrusion of the so-called Alcapa block out of the Eastern Alpine collision zone, (2) continued shortening in the outer flysch belt and development of the molasse foredeep, and (3) a significant high-temperature magmatic event attributed to asthenospheric upwelling following gravity-driven slab break-off beneath the modern-day Pannonian Basin (Nemcok et al., 1998). Burtman (1986) proposed that lateral extrusion of the Alcapa block bifurcated the Carpathian and Dinaric belts, which originally formed a singular bivergent orogen. Palinspastic restoration of the coupled Carpathian–Balkan oroclines reveals that oroclinal buckling of an originally linear 2100-km-long Carpathian–Balkan orogen trending northwest-southeast and parallel to the Dinaride-Hellenide chain (Burtman, 1986) accommodated >1000 km of orogen parallel shortening (Shaw and Johnston, 2012).

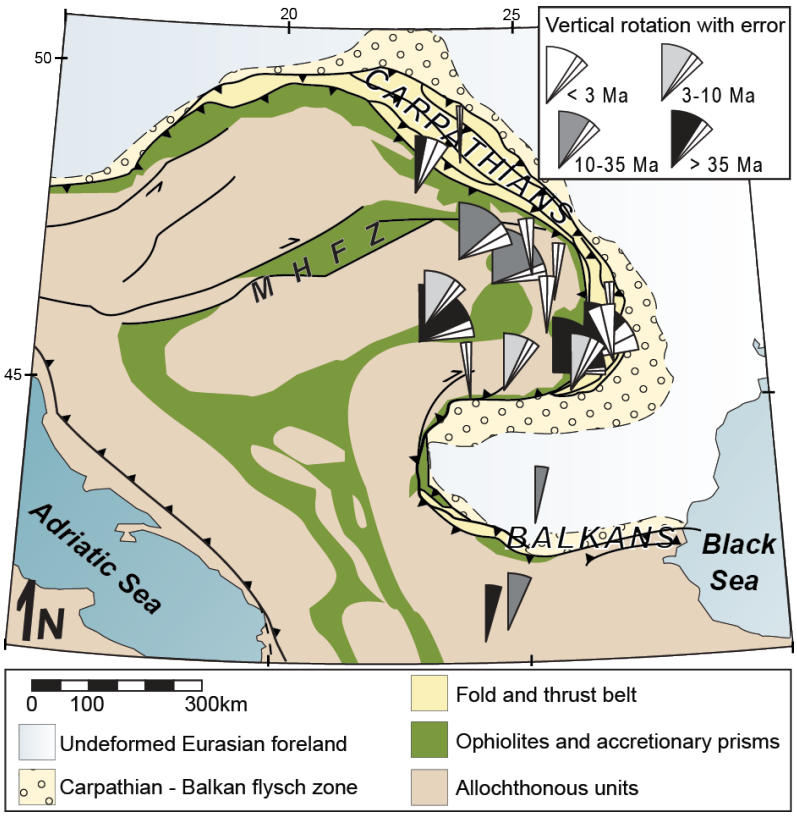

Figure 5-10 Vertical-axis rotations constrained by available paleomagnetic declination data from the Carpathian–Balkan belt. See compilation in Shaw and Johnston (2012).

5.5.3 The Eastern Mediterranean Inclination Anomaly

The oroclinally buckled Carpathian–Balkan belt lies immediately north-northeast of the eastern Mediterranean Aegean Sea region, within which Late Eocene to Miocene volcanic and plutonic rocks consistently record paleomagnetic inclination values that are anomalously shallow with respect to stable Europe (Fig. 5-11; see compilations of Beck et al., 2001; Shaw and Johnston, 2012). The data, representing the so-called eastern Mediterranean inclination anomaly (EMIA), indicate that the crust underlying the greater Aegean region of the eastern Mediterranean was displaced 500-1000 km northward since ~35 Ma (Fig. 5-12; Shaw and Johnston, 2012).

The most robust dataset recording the EMIA comes from Early Miocene volcanics on the island of Lesbos, which have been the subject of several paleomagnetic studies yielding consistent results (Kondopoulou and Lauer, 1984; Kissel, Kondopoulou, et al., 1986; Beck et al., 2001). Lesbos volcanics record an average ΔI (local inclination minus reference) of -5.6º

± 4.7º, corresponding to ca. 500 km of northward displacement (Beck et al., 2001). Older volcanic sequences; e.g. 30 Ma volcanics from the western Greek Rhodope (Atzemoglou et al., 1994) and 35.5 Ma volcanics and plutonics from Thrace (Kissel, Kondopoulou, et al., 1986) record an extent of inclination shallowing consistent with 1000 km of northward displacement. The Lesbos volcanics are therefore likely to be younger than the onset of northward translation, and the 500 km of displacement they record is accepted as a minimum value for total northward displacement of the eastern Mediterranean. At 3 Ma, volcanics

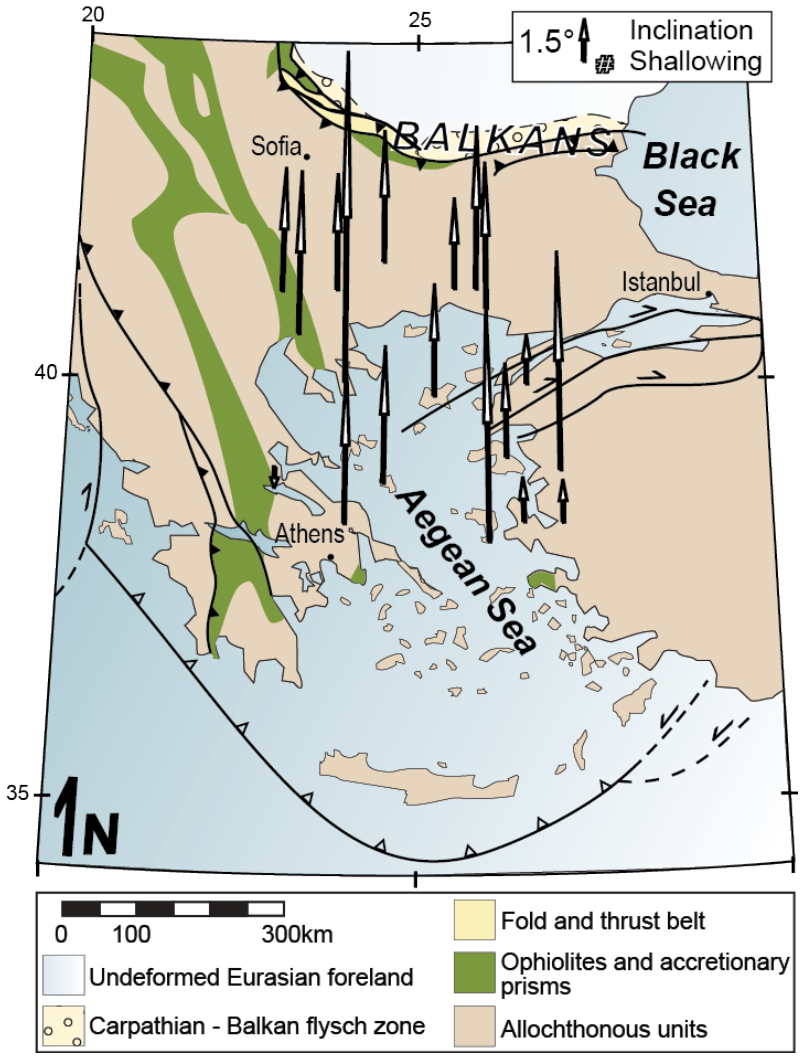

Figure 5-11 Scaled arrows representing degrees of latitude of northward displacement of the greater Aegean eastern Mediterranean region corresponding to calculated ΔI (local minus reference paleomagnetic inclination) values. See compilations within Beck (2001) and Shaw and Johnston (2012).

from the island of Volos (Kissel, Laj, et al., 1986), yield inclinations consistent with those for stable Europe, indicating that the eastern Mediterranean crust block had reached its current latitude by this time. Assuming a maximum value of 1000 km northward displacement between approximately 35 and 3 Ma, a moderate translation rate of just over 3 cm•yr^{-1} is implied.

It has been suggested that the EMIA is a record of a large (18º) and abrupt shift in the geomagnetic dipole, and therefore not indicative of significant crustal mobility (Westphal, 1993). A dipole shift of such scale should, however, be recorded in contemporaneous rocks worldwide, which does not appear to be the case (Beck and Schermer, 1994). No such shift, for example, is recorded in the well-constrained Cenozoic apparent polar wander path for North America (Torsvik et al., 2012). Furthermore, the extended time period and localized scale of the EMIA argue against its being attributable to geomagnetic irregularities such as dipole shifts or non-dipole components. The eastern Mediterranean inclination anomaly is therefore considered to be a true record of significant (500-1000 km) northward crustal mobility of the eastern Mediterranean region since 35 Ma, contemporaneous with the current age constraints on formation of the Carpathian–Balkan orocline and of a similar magnitude to the degree of orogen parallel shortening recorded therein.

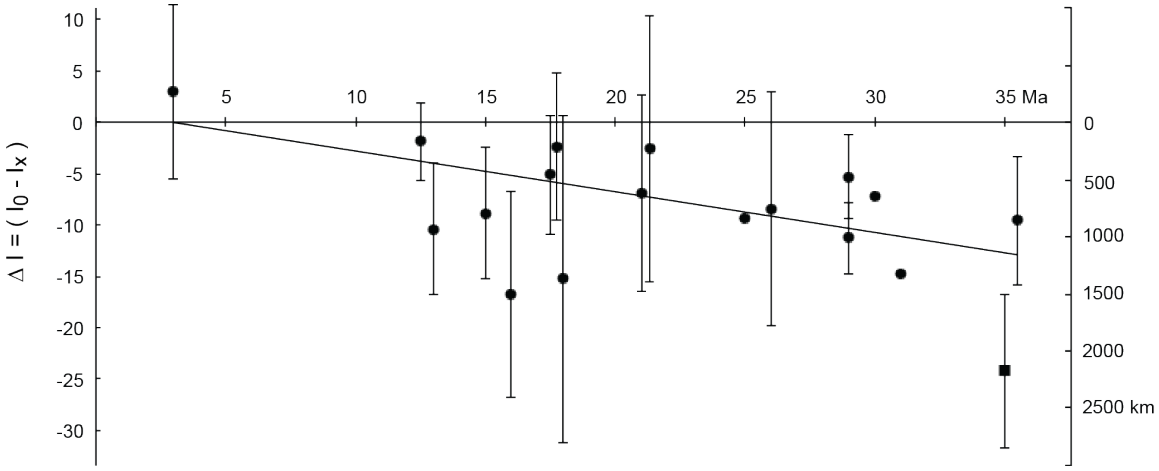

Figure 5-12 Plot of ΔI vs. average age estimates for lithological units sampled for paleomagnetic study within the greater Aegean eastern Mediterranean region. Error bars are 95% confidence limits, incalculable where not shown. The solid line of best fit, corresponding to a gradual translation northward since 35 Ma, excludes the outlying Chalkadiki plutonics (plotted as a square). See compilations within Beck (2001) and Shaw and Johnston (2012).

5.6 Resolution of paleomagnetic inclination anomalies through palinspastic restoration of oroclines

5.6.1 The North American Cordillera: The Alaskan coupled oroclines and Baja BC

Formation of the Alaskan coupled oroclines accommodated greater than 3000 km of orogen parallel shortening between approximately 95 and 55 Ma. Paleomagnetic data from Late Cretaceous layered volcanic and sedimentary rocks of the Intermontane and Insular domains indicate that the bulk of the Western Cordillera, from the eastern limit of the Omineca Magmatic belt westward, occupied a latitudinal position 2000-3000 km south of cratonic North America between 90 and 70 Ma. Palinspastic restoration of the Alaskan coupled oroclines (Fig. 5-13) brings the Insular and Intermontane domains of Yukon and British Colombia 2000-3000 km south of their Early Eocene (pre-Tintina–Rocky mountain trench transform displacement) positions to lower latitudes consistent with the inclinations recorded by their primary remanent magnetizations. The so-called paleomagnetic anomalies of the North American Cordillera are therefore a valid and robust record of the orogen parallel translation and shortening required for the formation of the Alaskan coupled oroclines.

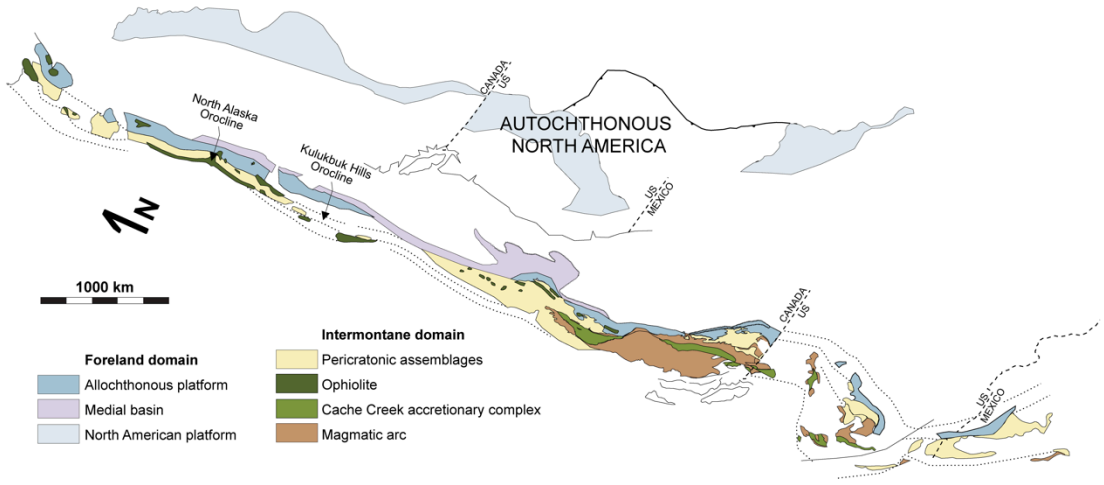

Figure 5-13 Palinspastic restoration of the Alaskan coupled oroclines restores > 3000 km of orogen parallel shortening and brings the Insular and Intermontane domains of Yukon and British Colombia 2000-3000 km south of their early Eocene (pre-Tintina–Rocky mountain trench transform displacement) positions to lower latitudes consistent with the inclinations recorded by their primary remanent magnetizations. After Johnston (2001).

5.6.2 The Western European Variscan belt: The Iberian coupled oroclines and Armorica

Formation of the Iberian coupled oroclines accommodated 1100 km of orogen parallel shortening over the course of a 10-20 My time period straddling the Carboniferous–Permian boundary. The concept of an Armorica microplate was founded and persists on the observation that paleomagnetic data from the Iberian, Armorican and Bohemian massifs place these regions at significantly lower mid-Paleozoic paleolatitudes than North African Gondwana. The paleolatitudinal discrepancy requires the Silurian opening of a major ocean, the Paleotethys, which grew at the expense of the more northerly Rheic to reach a maximum width of ca. 3500 km during the mid-Devonian. The concept of Paleotethys has been repeatedly challenged on the grounds that (1) the North African affinity of the Variscan autochthon is persistent though the Paleozoic and (2) the geologic record holds no evidence of its opening, its closure, or the oceanic lithosphere that floored it. Each of these lines of reasoning is, however, refutable bearing consideration of the palinspastic restoration of the Iberian coupled oroclines (Fig. 5-14). Palinspastic restoration of the Iberian coupled oroclines reveals (1) the existence of an elongate continental ribbon that could have feasibly spanned the width of Paleotethys, and (2) the presence of two distinct oceanic sutures on opposite sides of the initially linear Iberian Variscan orogen.

Paleomagnetic data suggest that the originally linear Iberian segment of the European Variscan belt was oriented north-south during the Late Carboniferous, immediately prior to oroclinal buckling (e.g. Weil et al., 2010). A north-south trending Armorican ribbon may have thus served as an adequate paleontological link between itself and the north Gondwana realm. Although the known 2100 km length of the restored Armorican ribbon is less than the maximum 3500 km width of Paleotethys, this restoration does not include the Armorican and Bohemian massifs, within which at least one other orocline (the Bohemian) is known. If Armorica were elongate north-south, its latitudinal range should be recorded by analogous ranges in paleomagnetic inclination along the length of the ribbon, and should be visible in a more detailed and well-constrained paleomagnetic data set.

The contrasting emplacement ages for ophiolites of the northwest Iberian Galicia–Trás-os-Montes and southern Iberian Beja-Acebuches complexes supports the notion that they are representative of distinct oceanic realms; the Galician ophiolites were emplaced >35 Ma

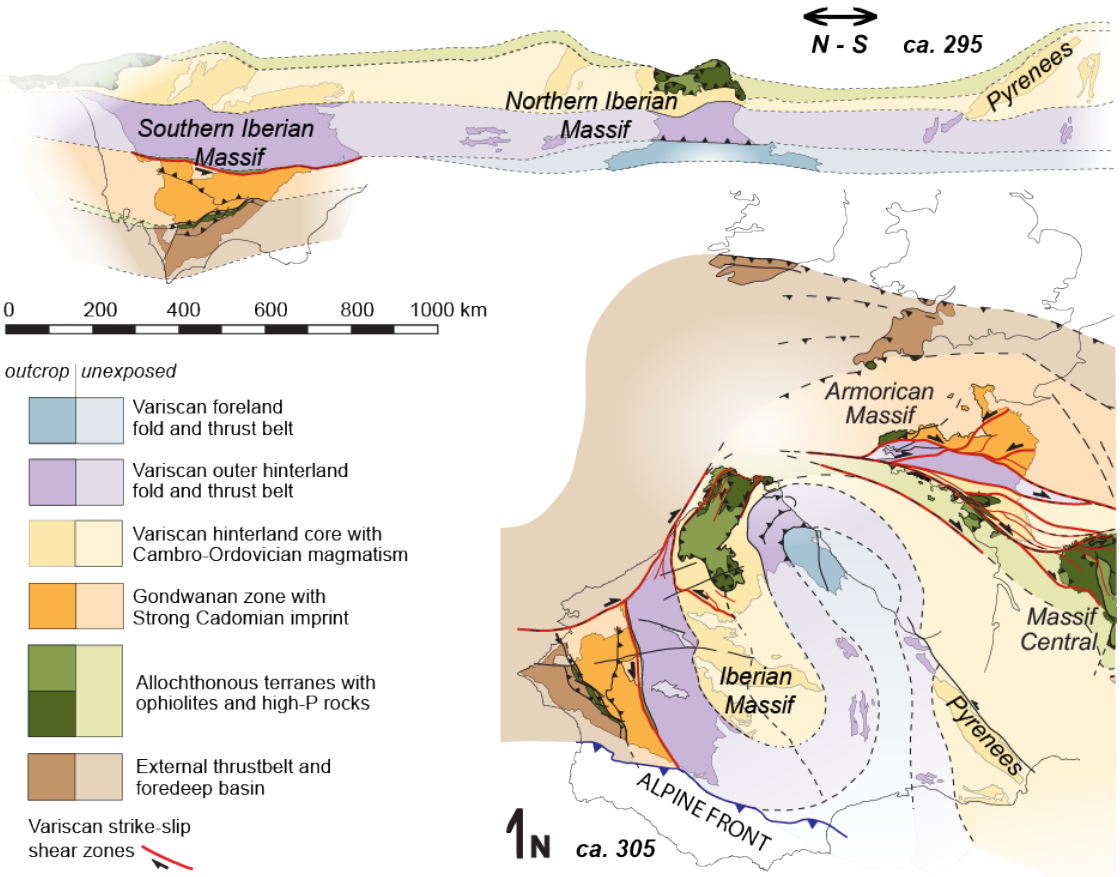

Figure 5-14 Palinspastic restoration of the Iberian coupled oroclines restores 1100 km of orogen parallel shortening in an originally 2300 km-long segment of the orogen flanked on either side by oceanic sutures.

prior to the formation of the Beja suture and therefore cannot root into it. In addition, an orogen or elongate continental ribbon may require flanking free surfaces such as suture zones in order to accommodate lithospheric flexure about a vertical axis (Johnston et al., 2013). An additional implication of a north-south elongate Armorican continental ribbon is that the Rheic and Paleotethys oceans lay side by side, separated only by the north-trending Armorican ribbon continent. However, determining which Iberian suture is representative of which Paleozoic ocean is difficult given the current conceptual framework of Variscan geology. Interpretation of the Galicia–Trás-os-Montes allochthon as a Rheic Ocean remnant is consistent with its direct emplacement above an Ordovician passive margin that faced towards it (Shaw et al., 2014); interpretation of the Beja-Acebuches complex as the true

Rheic suture is supported by its affinity with the Lizard complex of southern Britain, and by the Avalonian affinity of allochthonous terranes to its south (in modern-day coordinates). Nonetheless, a plot of the paleolatitude of Armorica versus that of the North Gondwana margin referenced at 30ºN, 30ºE (Fig. 6), indicates that Gondwana collision is not coincident with Variscan orogeny (i.e. closure of the Rheic), but with formation of the Iberian coupled oroclines. This suggests that Pangea was not amalgamated by Variscan orogenesis, but by the closure of Paleotethys and associated buckling of a preexisting Variscan orogen.

5.6.3 The Eastern European Alpine system: The Carpathian–Balkan oroclines and the EMIA

The Carpathian–Balkan coupled oroclines record 1100 km of post-Eocene orogen parallel shortening. Paleomagnetic data from the greater Aegean sea region immediately to the southeast of the Carpathian–Balkan belt record paleomagnetic inclinations consistent with 500-1000 km of northward displacement with respect to stable Europe since ~35 Ma, contemporaneous with formation of the Carpathian–Balkan oroclinal pair. A geometrically constrained paleogeographic model (Fig. 15; Shaw and Johnston, 2012) demonstrates that 500-1000 km northward displacement of the eastern Mediterranean can be accommodated by 50% shortening (1100 km) in the Carpathian-Balkan orogen if (1) the orogen had an initial northwest-southeast strike (310-330º) and (2) northward displacement of the eastern Mediterranean was coupled with a similar magnitude component of westward directed latitudinal displacement. Though a latitudinal-parallel component eastern Mediterranean displacement would not be visible in the paleomagnetic record, it is consistent with westward-directed tectonic escape of the Anatolian block (Turkey) out of the African–Arabian collision zone, ongoing since the mid-Miocene (Tatar et al., 2012). The required initial 310-330º strike for an originally linear Carpathian–Balkan belt is parallel with the present-day trend of the Dinaride–Hellenide belt, supporting the notion that Miocene eastward extrusion of the Alcapa block bifurcated an originally singular and bivergent Carpathian–Dinaride orogen (Burtman, 1986). Escape tectonics may therefore be a significant mechanism involved in both the initiation and accommodation of orocline formation.

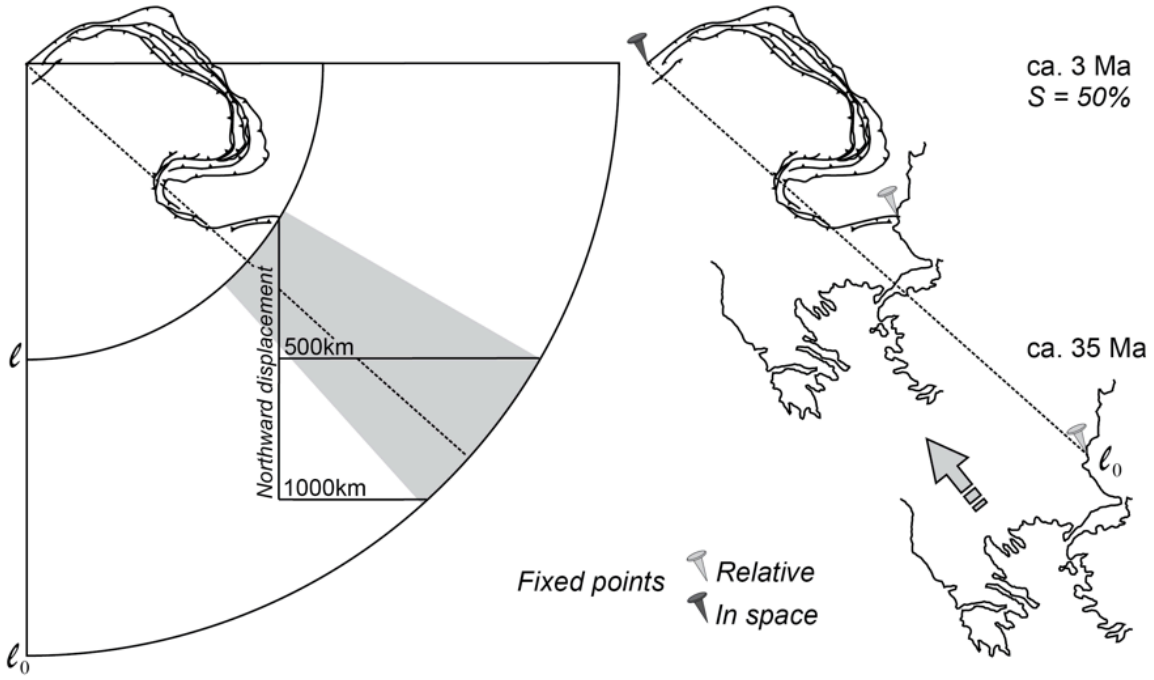

Figure 5-15 Geometric model showing 50% shortening of the Carpathian–Balkan orogen with a fixed northwest corner reveals the necessity for a component of westward directed displacement of the eastern Mediterranean. Length of originally linear orogen (l_0) = 2100 km; current length of orogen (l) measured linearly from northwest to southeast endpoint = 1050 km. The shaded region corresponds to the range of possible pathways of a point marking the southeastern end of the orogen starting along an arc of radius l_0 between 500 and 1000 km vertical distance from its current location and spanning trends between 310 and 330º. The dashed line illustrates one potential geometry for the originally linear orogen. After Shaw and Johnston (2012).

5.7 Conclusions

Significant amounts of orogen parallel translations associated with the formation of the Alaskan, Iberian, and Carpathian-Balkan coupled oroclines are recorded by paleomagnetic inclinations that are shallow with respect to cratonic reference values for the North American Cordillera, Western European Variscan belt, and Eastern European Alpine system, respectively. Palinspastic restoration of the Alaskan coupled oroclines brings terranes of the western North American Cordillera 2000-3000 km south of their early Eocene positions to the low Cretaceous paleolatitudes which they record and which spawned the controversial "Baja BC" hypothesis. Palinspastic restoration of the Carpathian–Balkan coupled oroclines shows that 500-1000 km of Late Oligocene to recent northward translation recorded by the

eastern Mediterranean inclination anomaly was accommodated by 50% shortening within the Carpathian–Balkan belt. Palinspastic restoration of the coupled Iberian oroclines suggests the existence of an Armorican ribbon continent and major mid-Paleozoic Paleotethys ocean, initially defined on the basis of seemingly anomalous Variscan paleomagnetic data. Restoration of the Iberian coupled oroclines and the Variscan paleomagnetic data set further collectively suggest that oroclinal buckling of the Variscan belt provides the true European record of Pangean amalgamation. The rapid rates of translation required for formation of the Alaskan and Iberian coupled oroclines suggests that buckling within the North American Cordilleran and Variscan orogenic belts was driven by a subduction-related driving mechanism. More modest rates of translation are required for formation of the Carpathian–Balkan oroclines, which is both partially driven and partially accommodated by extrusion tectonics within the greater Eastern Alpine orogenic system. The recognition of secondary oroclines within orogenic belts reconciles inclination anomalies with the structure of orogenic belts, and suggests that the amount of margin parallel translation accommodated with orogens is orders of magnitude greater than the amount of margin-normal shortening.

Chapter 6. Conclusions

An *S*-shaped pair of coupled oroclines characterizes the Iberian segment of the Western European Variscan belt. Continuity of the well-exposed Cantabrian orocline with the newly documented Central Iberian orocline directly to its south explains sedimentological and structural patterns within Iberia and across an orogen of typical across-strike width (300-400 km). A Central Iberian orocline geometry consistent with structural trends, the distribution of allochthonous terranes, available paleomagnetic data, and aeromagnetic anomalies, is defined by an axial trace along the previously defined Central Iberian boundary between a northerly domain of upright folds and a southerly domain of recumbent folds. Correlation of the West Asturian Leonese zone with the Luso Alcudian southern division of the Central Iberian zone is implied, defining an external hinterland that is continuous around the buried hinge of the Central Iberian orocline. Interpretation of the Cantabrian orocline as the core of the larger Ibero-Armorican arc is inconsistent with the existence of the Iberian coupled oroclines.

A model of formation of the Iberian coupled oroclines by vertical-axis buckling of an originally linear Iberian Variscan belt is supported by structural patterns around the hinge of the Cantabrian orocline that indicate its accommodation by a component of flexural shear. The Iberian coupled oroclines therefore palinspastically restore to a 2300-km-long linear orogen bound on either side by oceanic sutures, and with a paleomagnetically defined Late Carboniferous north-south trend (e.g. Weil et al., 2010). Paleocurrent data collected from the Lower Ordovician Armorican Quartzite along a 1500 km segment of the restored Cantabrian–Central Iberian Paleozoic passive margin (CCIM) indicate offshore paleoflow to the west (in modern day coordinates) defining a westerly oceanic domain and an easterly landward direction. The Lower Ordovician detrital zircon age spectra of the CCIM is best explained as a product of erosion of source terranes exposed, in modern day coordinates, to the south of the Saharan hinterland and Arabian Nubian shield. A paleogeographic model in which the palinspastically restored CCIM forms a component of the Ediacaran–Early Paleozoic Central to East African Gondwanan margin extending along the northern limits of the then low-relief Saharan hinterland and Arabian–Nubian Shield satisfies known

sedimentary, petrologic and paleontological constraints. Mid-Paleozoic separation of the CCIM from the north Gondwana margin is suggested by (1) the presence of an ophiolitic suture (Beja Acebuches) and continental allochthon (South Portuguese zone) on the landward side of the margin, (2) paleomagnetic inclination data that place all regions of the Variscan autochthon at lower mid to Late Paleozoic latitudes than the North African Gondwana margin, and (3) the requirement of 90º of counterclockwise rotation to bring the CCIM from an Ediacaran–Early Paleozoic position as a component of the north facing Gondwana passive margin to a pre-oroclinal (Late Carboniferous) north-south trend.

Palinspastic restoration of the Iberian coupled oroclines implies >1100 km of orogen parallel shortening acquired over a 10-20 My time interval between the Late Carboniferous cessation of east-west Variscan shortening (in modern-day coordinates) and the onset Early Permian deposition of post-oroclinal terrigenous sedimentary successions. Palinspastic restorations of the geometrically similar Alaskan and Carpathian–Balkan coupled oroclines require similarly large components of orogen parallel translation within the North American Cordillera (>3000 km) and Eastern Alpine system (>1000 km), respectively. Palinspastic restoration of the Alaskan coupled oroclines fully resolves a paleomagnetically defined paleolatitudinal disparity between the Cordilleran mobile belt and North American craton; palinspastic restoration of the Carpathian–Balkan coupled oroclines similarly resolves seemingly anomalous paleomagnetic inclination data within the Eastern European Alpine system. Though palinspastic restoration of the coupled Iberian oroclines confirms the existence of an Armorican ribbon continent and major mid-Paleozoic Paleotethys ocean, it cannot fully reconcile the paleomagnetically defined mid to Late Paleozoic paleolatitudinal separation between regions of the Variscan autochthon and North African Gondwana. A model in which the Armorican Ribbon stretched north-south across the Paleotethys seems the most plausible way of explaining sedimentological and paleontological ties to North Gondwana throughout the Paleozoic. Although the known 2100 km length of the restored Armorican ribbon is less than the maximum 3500 km width of Paleotethys, this restoration does not include the Armorican and Bohemian massifs, within which at least one other orocline (the Bohemian) is known.

The rapid rates of translation required for formation of the coupled Iberian oroclines are difficult to reconcile with paleogeographic and tectonic models that place orocline formation

within the continental core of Pangea. In addition, paleomagnetic data indicate that Gondwana collision is not coincident with Variscan orogeny (i.e. closure of the Rheic), but with formation of the Iberian coupled oroclines. The fundamental implication is that Pangea was not amalgamated by Variscan orogenesis, but by the closure of Paleotethys and associated buckling of a preexisting Variscan orogen.

6.1 Suggestions for further work

The model of formation of the Iberian coupled oroclines by vertical-axis buckling of an intitially linear Variscan belt (or Armorican continental ribbon) presented herein has been disputed. Martínez-Catalán (2011, 2012) accepts the existence of a Central Iberian orocline, but suggests that it formed by lithospheric-scale dextral transpressive shear driven by oblique Variscan collision; Sengor (2013) describes application of a Cordilleran-type terrane wreck model to the Variscan belt as "entirely inappropriate". Further testing of the model is therefore required. Many of the variable detailed structural and paleomagnetic studies that test and support a model of secondary formation of the Cantabrian orocline would be difficult to apply to the Central Iberian orocline as the bulk of its hinge is buried beneath post Variscan-sedimentary cover. However, some tests may be conducted with data collected solely within the southern limb of the Central Iberian orocline now that a suggested geometry has been established; these include (1) paleomagnetic assessment of the full extent of vertical-axis rotations, and (2) the documentation of vertical-axis structures which may be attributable to flexural shear (Chapter 4).

The location of the axial trace of the Central Iberian orocline with relation to allochthonous terranes of the Galicia–Trás-os-Montes zone is not clearly established. The axial trace may split the Galicia–Trás-os-Montes allochthon along the Malpica-Tui suture (as proposed in Chapter 1), or it may deflect along either its southern or northern limit, indicating that ophiolites of the Galicia–Trás-os-Montes allochthon may not have been continuous along the entire palinspastically restored (pre-orocline) length of the Iberian autochthon. Constraining the orientation of kinematic indicators developed during nappe emplacement will enable an assessment of the degree of orogenic curvature within the Galicia–Trás-os-Montes allochthon, and thus further constrain the location of the axial trace of the Central Iberian orocline in the northwesternmost massif.

The manner in which the tectonostratigraphic zones defined within the Iberian coupled oroclines geometrically connect and correlate across the remainder of Variscan belt is also unclear. Further faunal, geochronological and geochemical tests are required to establish terrane correlations within Iberia, across the Western European Variscan belt, and into northern Africa. The Armorican Quartzite correlates across the entirety of the Western European Variscan belt (e.g. Gutiérrez-Alonso et al., 2007), and would be an excellent target for continued paleocurrent study to further constrain orogenic geometry within the Armorican and Bohemian massifs.

References

Ábalos, B., Gil Ibarguchi, J.I., Sánchez-Lorda, M.E., and Paquette, J.L., 2012, African/Amazonian Proterozoic correlations of Iberia: A detrital zircon U-Pb study of early Cambrian conglomerates from the Sierra de la Demanda (northern Spain): Proterozoic Correlations of Iberia: Tectonics, v. 31, p. n/a–n/a, doi: 10.1029/2011TC003041.

Ábalos, B., Carreras, J., Druguet, E., Viruete, J.E., Gómez Pugnaire, M.T., Alvarez, L.R., Quesada, C., Rodríguez Fernández, and Gil-Ibarguchi, J.I., 2002, Variscan and pre-Variscan tectonics, *in* Gibbons, W., and Moreno, T., eds., The Geology of Spain: London, The Geological Society of London, p. 155-183.

Ábalos, B., Ibarguchi, J.I.G., and Eguiluz, L., 1991, Cadomian subduction / collision and Variscan transpression in the Badajoz-Córdoba shear belt, southwestern Spain: Tectonophysics, v. 199, p. 51-72.

Abati, J., Aghzer, A.M., Gerdes, A., and Ennih, N., 2010, Detrital zircon ages of Neoproterozoic sequences of the Moroccan Anti-Atlas belt: Precambiran Research, v. 181, p. 115-128.

Abdelsalam, M.G., Liégeois, J.-P., and Stern, R.J., 2002, The Saharan Metacraton: Journal of African Earth Sciences, v. 34, p. 119–136.

Aerden, D.G.A.M., 2004, Correlating Deformation in Variscan NW Iberia using porphyroblasts; implicatons for the Ibero-Armorican Arc: Journal of Structural Geology, v. 26, p. 177-196.

Allmendinger, R.W., Cardozo, N., and Fisher, D., 2012, Structural geology algorithms: Vectors and tensors in structural gelogy: Cambridge University Press, 302 p.

Allmendinger, R.W., Smalley, R., Bevis, M., Caprio, H., and Brooks, B., 2005, Bending the Bolivian orocline in real time: Geology, v. 33, no. 11, p. 905–908, doi: 10.1130/G21779.1.

Altumi, M.M., Elicki, O., Linnemann, U., Hoffman, M., Sawage, A., and Gärtner, A., 2013, U-Pb LA-ICP-MS detrital zircon ages from the Cambrian of AlQardaf Arch, central-western Libya: Provenance of the West Gondwanan sand sea at the dawn of the Early Paleozoic: Journal of African Earth Sciences, v. 79, p. 74-97.

Amidon, W.H., Burbank, D.W., and Gehrels, G.E., 2005, Construction of detrital mineral populations: insights from mixing of U-Pb zircon ages in Himalayan rivers: Basin Research, v. 17, p. 463-485.

Anderson, S.P., Dietrich, W.E., and Brimhall, G.H., 2002, Weathering profiles, mass-balance analysis, and rates of solute loss: Linkages between weathering and erosion in a small, steep catchment: Geological Society of America Bulletin, v. 114, p. 1143–1158.

Aramburu, C., 1989, El Cambro-Ordovícico de la Zona Cantábrica (NO de España): Oviedo, Universidad de Oviedo.

Aramburu, C., and García-Ramos, J.C., 1993, La Sedimentación Cambro-Ordovicica en la Zona Cantabrica (No de España): Trabajos de Geologia, v. 19, p. 45-73.

Aramburu, C., Méndez-Bedia, I., Arbizu, M., and García-López, S., 2004, La secuencia preorogénica, *in* Vera, J.A., ed., Geología de España: Madrid Sociedad Geológica de España-Instituto Geológico y Minero de España, p. 27-34.

Ardizone, J., Mezcua, J., and Socías, I., 1989, Mapa aeromagnético de España Peninsular 1:1,000,000: Instituto Geográfico Nacional, Madrid.

Atzemoglou, A., Kondopoulou, D., Papamarinopoulos, S., and Dimitriadis, S., 1994, Palaeomagnetic evidence for block rotations in the western Greek Rhodope: Geophysical Journal International, v. 118, p. 221–230, doi: 10.1111/j.1365-246X.1994.tb04685.x.

Avigad, D., Gerdes, A., Morag, N., and Bechstädt, T., 2012, Coupled U-Pb-Hf of detrital zircons of Cambrian sandstones from Morocco and Sardinia: Implications for provenance and Precambrian crustal evolution of North Africa: Gondwana Research, v. 21, p. 690-703.

Avigad, D., Stern, R.J., Beyth, M., Miller, N., and McWilliams, M.O., 2007, Detrital zircon U-Pb geochronology of Cryogenian diamictites and Lower Paleozoic sandstone in Ethiopia (Tigrai): Age constraints on Neoproterozoic glaciation and crustal evolution of the southern Arabian-Nubian Shield: Precambiran Research, v. 154, p. 88-106.

Azor, A., Rubatto, D., Simancas, J.F., González Lodeiro, F., Martínez Poyatos, D., Martín Parra, L.M., and Matas, J., 2008, Rheic Ocean ophiolitic remnants in southern Iberia questioned by SHRIMP U-Pb zircon ages on the Beja-Acebuches amphibolites: Tectonics, v. 27, p. TC5006, doi: 10.1029/2008TC002306.

Azor, A., González Lodeiro, F., and Simancas, J.F., 1994, Tectonic evolution of the boundary between the Central Iberian and Ossa-Morena zones (Varsican belt, southwest Spain): Tectonics, v. 13, p. 45-61.

Azor, A., González Lodeiro, F., Marcos, A., and Simancas, J.F., 1991, Edad y estructura de las rocas de Sierra Albarrana (Sw del Macizo Hespérico). Implicaciones regionales: Geogaceta, v. 10, p. 119-124.

Bachtadse, V., Heller, F., and Kröner, A., 1983, Palaeomagnetic investigations in the Hercynian mountain belt of central Europe: Tectonophysics, v. 91, p. 285–299, doi: 10.1016/0040-1951(83)90046-X.

Ballevre, M., Paris, F., and Robardet, M., 1992, Corrélations ibéro-armoricaines au Paléozïque: une confrontation des données paléobiogéographiques et tectonométamorphique: Comptes Rendus de Academie de Sciences, Serie 2, Mecanique, Physique, Chimie, Sciences de L'Univers, Sciences de la Terre, v. 315, p. 1783-1789.

Bandres, A., Eguiluz, L., Gil Ibarguchi, J.I., and Palacios, T., 2002, Geodynamic evolution of a Cadomian arc region: the northern Ossa-Morena zone, Iberian Massif: Tectonophysics, v. 362, p. 105-120.

Barbeau, J.D.L., Davis, J.T., Murray, K.E., Valencia, V., Gehrels, G.E., Zahid, K.M., and Gombosi, D.J., 2009, Detrital-zircon geochronology of the metaszedimentary rocks of north-western Graham Land: Antarctic Science, v. 22, p. 65-78, doi:10.1017/s095410200999054X.

Barr, S.M., Davis, D.W., Kamo, S., and White, C.E., 2003, Significance of U-Pb detrital zircon ages in quartzite from peri-Gondwanan terranes, New Brunswick and Nova Scotia, Canada: Precambrian Research, v. 126, p. 123-145.

Bastida, F., Martínez Catalán, J.R., and Pulgar, J.A., 1986, Structural, metamorphic and magmatic history of the Mondoñedo nappe (Hercynian belt, NW Spain): Journal of Structural Geology, v. 8, p. 415-430.

Beck, M.E., Burmester, R.F., Kondopoulou, D.P., and Atzemoglou, A., 2001, The palaeomagnetism of Lesbos, NE Aegean, and the eastern Mediterranean inclination anomaly: Geophysical Journal International, v. 145, p. 233–245.

Beck, M.E., Jr., and Schermer, E.R., 1994, Aegean paleomagnetic inclination anomalies. Is there a tectonic explanation? Tectonophysics, v. 231, p. 281–292.

Be'eri-Shlevin, Y., Katzir, Y., Whitehouse, M.J., and Kleinhanns, I.C., 2009, Contribution of pre-Pan-African crust to formation of the Arabian Nubian Shield: New Secondary ionization mass spectrometry U-Pb and O studies of zircon: Geology, v. 37, p. 889-902.

Bea, F., Montero, P., Talavera, C., Abu Anbar, M., Scarrow, J.H., Molina, J.F., and Moreno, J.A., 2010, The paleogeographic position of Central Iberia in Gondwana during the Ordovician: evidence from zircon chronology and Nd isitopes: Terra Nova, v. 22, p. 341-346.

Berry, R.F., Jenner, G.A., Meffre, S., and Tubrett, M.N., 2001, A North American provenance for Neoproterozoic to Cambrian sandstones in Tasmania?: Earth and Planetary Science Letters, v. 192, p. 207-222.

Bonhommet, N., Cobbold, P.R., Perroud, H., and Richardson, A., 1981, Paleomagnetism and cross-folding in a key area of the Asturian Arc (Spain): Journal of Geophysical Research: Solid Earth, v. 86, p. 1873–1887, doi: 10.1029/JB086iB03p01873.

Box, S.E., 1985, Early Cretacous orogenic belt in northwestern Alaska: Internal organization, lateral extent, and tectonicjohns interpretation, *in* Howell, D.G. ed., Tectonostratigraphic Terranes of the Circum-Pacific Region, Earth Science Series 1, Circum Pacific Council for Energy and Mineral Resources, Houston, TX, p. 137–145.

Braid, J.A., Murphy, J.B., Quesada, C., and Mortensen, J., 2011, Tectonic escape of a crustal fragment during the closure of the Rheic Ocean: U-Pb detrital zircon data from the Late Paleozoic Pulo do Lobo and South Portuguese zones, southern Iberia: Journal of the Geological Society of London, v. 168, p. 383-392.

Brun, J.-P., and Burg, J.-P., 1982, Combined thrusting and wrenching in the Ibero-Armorican arc: a corner effect during continental collision: Earth and Planetary Science Letters, v. 61, p. 319–332.

Burchfiel, B.C., 1980, Eastern European Alpine system and the Carpathian orocline as an example of collision tectonics: Tectonophysics, v. 63, no. 1, p. 31–61, doi:10.1016/0040-1951(80)90106-7.

Burchfiel, B.C., Cowan, D.S., and Davis, G.A., 1992, Tectonic overview of the Cordilleran Orogen in the Western United States The geology of North America, *in* United States, Geol. Soc. Am., United States, p. 407–479.

Burtman, V.S., 1986, Origin of structural arcs of the Carpathian-Balkan region: Tectonophysics, v. 127, p. 245–260.

Byerly, G.R., Kroener, A., Lowe, D.R., Todt, W., and Walsh, M.M., 1996, Prolonged magmatism and time constraints for sediment deposition in the early Archean Barberton greenstone belt; evidence from the upper Onverwacht and Fig Tree groups: Precambrian Research, v. 78, p. 125–138.

Cawood, P.A., Nemchi, A.A., Freeman, M., and Sircombe, K., 2003, Linking source and sedimentary basin: Detrital zircon record of sediment flux along a modern river sytem and implications for provenance studies: Earth and Planetary Science Letters, v. 210, p. 259-268.

Cahen, L., Snelling, N.J., Delhal, T., and Vail, J.R., 1984, The Geochronology and Evolution of Africa: London, Oxford Science.

Carey, S.W., 1955, The orocline concept in geotectonics, part I: Papers and proceedings of the Royal Society of Tasmania, v. 89, p. 255–288.

Chamberlain, V.E., and Lambert, R.S.J., 1985, Cordilleria, a newly defined Canadian microcontinent: Nature, v. 314, p. 707–713, doi: 10.1038/314707a0.

Channell, J.E.T., and Horváth, F., 1976, The African/Adriatic promontory as a palaeogeographical premise for alpine orogeny and plate movements in the Carpatho-Balkan region: Tectonophysics, v. 35, p. 71–101, doi: 10.1016/0040-1951(76)90030-5.

Cogné, J.P., 1987, Paleomagnetic direction obtained by strain removal in the Pyrenean Permian redbeds at the "Col du Somport" (France): Earth and Planetary Science Letters, v. 85, p. 162–172, doi: 10.1016/0012-821X(87)90029-X.

Cogné, J.-P., 1988, Strain, Magnetic Fabric, and Paleomagnetism of the Deformed Red Beds of the Pont-Rean Formation, Brittany, France: Journal of Geophysical Research: Solid Earth, v. 93, p. 13673–13687, doi: 10.1029/JB093iB11p13673.

Crespo-Blanc, A., and Orozco, M., 1991, The boundary between the Ossa-Morena Zone and Southportuguese Zone (Southern Iberian Massif): a major suture in the European Hercynian Chain: Geologische Rundschau, v. 30, p. 691-702.

Csontos, L., and Vörös, A., 2004, Mesozoic plate tectonic reconstruction of the Carpathian region: Palaeogeography, Palaeoclimatology, Palaeoecology, v. 210, no. 1, p. 1–56, doi: 10.1016/j.palaeo.2004.02.033.

Dahn, D.R.L., Braid, J.A., Murphy, J.B., Quesada, C., Dupuis, N., and McFarlane, C.R.M., 2014, Geochemistry of the Peramora Mélange and Pulo do Lobo schist: geochemical investigation and tectonic interpretation of mafic mélange in the Pangean suture zone, Southern Iberia: International Journal of Earth Sciences, v. 103, p. 1415–1431, doi: 10.1007/s00531-014-1024-7.

Dallmeyer, R.D., Martínez Catalán, J.R., Arenas, R., Ibarguchi, J.I.G., Gutiérrez Alonso, G., Farias, P., Bastida, F., and Aller, J., 1997, Diachronous Variscan tectonothermal activity in the NW Iberian Massif: Evidence from $^{40}Ar/^{39}Ar$ dating of regional fabrics: Tectonophysics, v. 277, p. 307-377.

De Waele, B., Fitzsimons, I.C.W., Wingate, M.T.D., Tembo, F., Mapani, B., and Belousova, A., 2009, The Geochronological framework of the Irumide Belt: A prolonged crustal history along the margin of the Bangweulu Craton: American Journal of Science, v. 309, p. 132-187.

DeGraaf-Surpless, K., Mahoney, J.B., Wooden, J.L., and McWilliams, M.O., 2003, Lithofacies in detrital zircon provenance studies: Insights from the Cretaceous Methow basin, southern Canadian Cordillera: GSA Bulletin, v. 118, p. 899-915.

Díaz García, F., 2002, Tectónica y magmatismo Ordovícicos en la área de Sanabia, Macizo Ibérico: Geogaceta, v. 32, p. 119-122.

Dickinson, W.R., Gehrels, G.E., and Stern, R.J., 2010, Late Triassic Texas uplift preceeding Jurassic opening of the Gulf of Mexico: Evidence from U-Pb ages of detrital zircons: Geosphere, v. 6, p. 641-662.

Díez Balda, M.A., Vegas, R., and González Lodeiro, F., 1990, Structure, *in* Dallmeyer, R.D., and Martínez García, E., eds., Pre-Mesozoic Geology of Iberia: Berlin, Heidelberg, New York, Springer-Verlag, p. 172-188.

Díez Fernández, R., Martínez Catalán, J.R., Arenas Martín, R., and Abati Gómez, J., 2011, Tectonic evolution of a continental subduction-exhumation channel: Variscan structure of the basal allochthonous units in NW Spain: Tectonics, v. 30, p. TC3009.

Díez Montes, A., 2006, La Geología del Dominio "Ollo de Sappo" en las comarcas de Sanabria y Terra do Bolo. PhD Thesis, Universidad de Salamanca, 496 pp.

Díez Fernández, R., Foster, A.R., Gómez Barreiro, J., and Alonso García, M., 2013, Rheological control on the tectonic evolution of a continental suture zone: the Variscan example from NW Iberia (Spain): International Journal of Earth Sciences, DOI 10.1007/s00531-013-0885-5.

Díez Fernández, R., Martínez Catalán, J.R., Arenas, R., Abati, J., Gerdes, A., and Fernández-Suárez, J., 2012, U-Pb detrital zircon analysis of the lower allochthon of NW Iberia: age constraints, provenance and links with the Variscan mobile belt and Gondwanan cratons: Journal of the Geological Society, v. 169, p. 655-665.

Díez Fernández, R., Martínez Catalán, J.R., Gerdes, A., Abati, J., Arenas, R., and Fernández-Suárez, J., 2010, U-Pb ages of detrital zircons from the Basal allocthonous units of NW Iberia: Provenance and paleoposition on the northern margin of Gondwana during the Neoproterozoic and Pelozoic: Gondwana Research, v. 18, p. 385-399.

Díez Montes, A., 2006, La Geología del Dominio "Ollo de Sappo" en las comarcas de Sanabria y Terra do Bolo. PhD Thesis, Universidad de Salamanca, 496 pp.

Dover, G.H., 1994, Geology of part of east-central Alaska, *in* Plafker, G. and Berg, H.C. eds., The Geology of Alaska: Boulder, Colorado, Geological Society of America, The Geology of North America, v. G-1, p. 153–204.

Du Toit, A., L., 1937, Our Wandering Continents: Edinburgh, Greenwood Press, 379 p.

Ducea, M.N., 2011, Fingerprinting orogenic delamination: Geology, v. 39, no. 2, p. 191–192, doi: 10.1130/focus022011.1.

Duff, B.A., 1979, The palaeomagnetism of Cambro-Ordovician redbeds, the Erquy Spilite Series and the Tregastel-Ploumanac'h granite complex, Armorican Massif (France and the Channel Islands): Geophysical Journal International, v. 59, p. 345–365.

Duff, B.A., 1980, The palaeomagnetism of Jersey volcanics and dykes, and the Lower Palaeozoic apparent polar wander path for Europe: Geophysical Journal International, v. 60, p. 355–375, doi: 10.1111/j.1365-246X.1980.tb04813.x.

El-Khayal, A.A., 1985, *Hanadirella:* A new problematic arthropod(?) from the Lower Ordovician (Llanvirn) Tabuk Formation, central Saudi Arabia: Scripta Geologica, v. 80, p. 1-13.

Edel, J.B., 1987, Paleomagnetic evolution of the Central Massif (France) during the Carboniferous: Earth and Planetary Science Letters, v. 82, p. 180–192, doi: 10.1016/0012-821X(87)90118-X.

Edel, J.-B., Coulon, M., and Hernot, M.-P., 1984, Mise en evidence par le paleomagnetisme d'une importante rotation antihoraire des Vosges meridionales entre le Viseen terminal et le Westphalien superieur: Tectonophysics, v. 106, p. 239–257, doi: 10.1016/0040-1951(84)90179-3.

Edel, J.B., Montigny, R., and Thuizat, R., 1981, Late Paleozoic rotations of Corsica and Sardinia: New evidence from paleomagnetic and K-Ar studies: Tectonophysics, v. 79, p. 201–223, doi: 10.1016/0040-1951(81)90113-X.

Enkin, R.J., 2006, Paleomagnetism and the case for Baja British Columbia: Special Paper - Geological Association of Canada, v. 46, p. 233–253.

Enkin, R.J., Johnston, S.T., Larson, K.P., and Baker, J., 2006, Paleomagnetism of the 70 Ma Carmacks Group at Solitary Mountain, Yukon, confirms and extends controversial results; further evidence for the Baja British Columbia model: Special Paper - Geological Association of Canada, v. 46, p. 221–232.

Enkin, R.J., Osadetz, K.G., Baker, J., and Kisilevsky, D., 2000, Orogenic remagnetizations in the Front Ranges and Inner Foothills of the southern Canadian Cordillera: Chemical harbinger and thermal handmaiden of Cordilleran deformation: Geological Society of America Bulletin, v. 112, p. 929–942, doi: 10.1130/0016-7606(2000)112<929:ORITFR>2.0.CO;2.

Eyal, M., Be'eri-Shlevin, Y., Eyal, Y., Whitehouse, M.J., and Litvinovsky, B., 2013, Three successive Proterozoic island arcs in the Northern Arabian-Nubian Shield: Evidence from SIMS U-Pb dating of zircon: Gondwana Research, DOI 10.1016/j.gr.2013.03.016.

Farias, P., Gallastequi, G., Gonzalez Lodeiro, F., Marquinez, J., Martin Parra, L.M.,

Martínez Catalán, J.R., de Pablo Macia, J.G., and Rodriguez Fernandez, L.R., 1987, Aportaciones al conocimiento de la estratigrafía y estructura de Galicia central.Lithostratigrphy and structure of Central Galicia: Memorias - Museu e Laboratorio Mineralogico e Geologico, Faculdade de Ciencias, Universidade do Porto, v. 1, p. 411-431.

Fernández-Suárez, J., Gutiérrez-Alonso, G., Pastor-Galán, D., Hofmann, M., Murphy, J.B., and Linnemann, U., 2013, The Ediacaran–Early Cambrian detrital zircon record of NW Iberia: possible sources and paleogeographic constraints: International Journal of Earth Sciences, v. 18, no. 10, p. 1217-1229, doi: 10.1007/s00531-013-0923-3.

Fernández-Suárez, J., Gutiérrez Alonso, G., Cox, R., and Jenner, G.A., 2002a, Assembly of the Armorica microplate: A strike-slip terrane delivery? Evidence from U-Pb ages of detrital zircons: The Journal of Geology, v. 110.

Fernández-Suárez, J., Gutiérrez Alonso, G., and Jeffries, T.E., 2002b, The importance of along-margin terrane transport in northern Gondwana: insights from detrital zircon parentage in Neoproterozoic rocks from Iberia and Brittany: Earth and Planetary Science Letters, v. 204, p. 75-88.

Fernández-Suárez, J., Gutiérrez Alonso, G., and Jenner, G.A., 2000a, New ideas on the Proterozoic-Early plaeozoic evolution of NW Iberia: Insights from U-Pb detrital zircon ages: Precambiran Research, v. 102, p. 185-206.

Fernández-Suárez, J., Dunning, G.R., Jenner, G.A., and Gutierrez-Alonso, G., 2000b, Variscan collisional magmatism and deformation in NW Iberia; constraints from U-Pb geochronology of granitoids: Journal of the Geological Society of London, v. 157, Part 3, p. 565–576.

Fernández Suárez, J., Gutiérrez-Alonso, G., Jenner, G.A., and Tubrett, M.N., 1999, Crustal sources in Lower Paleozoic rocks from NW Iberia: insights from laser ablation U-Pb ages of detrital zircons: Journal of the Geological Society of London, v. 156, p. 1065-1068.

Fernández-Suárez, J., Gutiérrez-Alonso, G., Jenner, G.A., and Jackson, S.E., 1998, Geochronology and geochemistry of the Pola de Allande granitoids (northern Spain): their bearing on the Cadomian-Avalonian evolution of northwest Iberia: Canadian Journal of Earth Sciences, v. 35, no. 12, p. 1439–1453.

Fonseca, P.E., and Ribeiro, A., 1993, Tectonics of the Beja-Acebuches Ophiolite: a major suture in the Iberian Variscan Foldbelt: Geologische Rundschau, v. 82, p. 440-447.

Fortey, R.A., and Morris, S.F., 1982, The Ordovician trilobite *Neseuretus* from Saudi Arabia, and the paleogeography of the *Neseuretus* fauna related to Gondwanaland in the elarier Ordovician: Bulletin of the British Musuem (Natural history), v. 36, p. 63-75.

Frei, D., and Gerdes, A., 2009, Precise and accurate *in-situ* U-Pb dating of zircon with high sample throughput by automated LA-SF-ICP-MS: Chemical Geology, v. 261, p. 261-270.

Friedl, G., Finger, F., McNaughton, N.J., and Fletcher, I.R., 2000, Deducing the ancestry of terranes: SHRIMP evidence for South America - derived Gonwanan fragments in central Europe: Geology, v. 28, p. 1035-1038.

Gabrielse, H., Murphy, D.C., and Mortensen, J.K., 2006, Cretaceous and Cenozoic dextral orogen-parallel displacements, magmatism, and paleogeography, north-central Canadian Cordillera: Special Paper - Geological Association of Canada, v. 46, p. 255–276.

Garzanti, E., Vermeesch, P., Andò, S., Vezzoli, G., Valagussa, M., Allen, K., Kadi, K.A., and Al-Juboury, A.I.A., 2013, Provenance and recycling of Arabian desert sand: Earth Science Reviews, v. 120, p.1-19.

Gibbons, W., and Moreno, J.A., 2002, Introduction and Overview, *in* Gibbons, W., and Moreno, J.A., eds., The Geology of Spain: London, The Gological Society p. 1-6.

Gladwin, K., and Johnston, S.T., 2006, Mid-Cretaceous pinning of accreted terranes to miogeoclinal assemblages in the northern Cordillera; irreconcilable with paleomagnetic data? Special Paper - Geological Association of Canada, v. 46, p. 299–306.

Gómez-Pugnaire, M.T., Azor, A., Férnandez-Soler, J.M., and Sánchez-Vizcaíno, L., 2003, The amphibolite from the Ossa Morena / Central Iberian Variscan suture (Southwestern Iberian Massif): Geochemistry and tectonic interpretation: Lithos, v. 68, p. 23-42.

Gordon, R.G., 1998, The plate tectonic approximation; plate nonrigidity, diffuse plate boundaries, and global plate reconstructions: Annual Review of Earth and Planetary Sciences, v. 26, p. 615–642.

Gutiérrez-Alonso, G., 1996, Strain partitioning in the footwall of the Somiedo Nappe: structural evolution of the Narcea Tectonic Window, NW Spain: Journal of Structural Geology, v. 18, no. 10, p. 1217–1229.

Gutiérrez-Alonso, G., Collins, A.S., Fernández-Suárez, J., Pastor-Galán, D., González-Clavijo, E., Jourdan, F., Weil, A.B., and Johnston, S.T., 2015, Dating of lithospheric buckling: 40Ar/39Ar ages of syn-orocline strike-slip shear zones in northwestern Iberia: Tectonophysics, doi: 10.1016/j.tecto.2014.12.009.

Gutiérrez-Alonso, G., Johnston, S.T., Weil, A.B., Pastor-Galán, D., and Fernádez-Suárez, J., 2012, Buckling an Orogen: The Cantabrian Orocline: GSA TODAY, v. 22, no. 7, p. 1–4.

Gutiérrez-Alonso, G., Fernández-Suárez, J., Jeffries, T.E., Johnston, S.T., Pastor-Galán, D., Murphy, J.B., Franco, M.P., and Gonzalo, J.C., 2011a, Diachronous post-orogenic magmatism within a developing orocline in Iberia, European Variscides: Tectonics, v. 30, p. TC5008, doi: 10.1029/2010TC002845.

Gutiérrez-Alonso, G., Murphy, J.B., Fernández-Suárez, J., Weil, A.B., Franco, M.P., and Gonzalo, J.C., 2011b, Lithospheric delamination in the core of Pangea: Sm-Nd insights from the Iberian mantle: Geology, v. 39, no. 2, p. 155–158, doi: 10.1130/G31468.1.

Gutiérrez-Alonso, G., Fernández-Suárez, J., Weil, A.B., Murphy, J.B., Nance, R.D., Corfú, F., and Johnston, S.T., 2008a, Self-subduction of the Pangaean global plate: Nature Geoscience, v. 1, p. 649-663.

Gutiérrez-Alonso, G., Murphy, J.B., Fernández-Suárez, J., and Hamilton, M.A., 2008b, Rifting along the northern Gondwana margin and the evolution of the Rheic Ocean: A Devonian age for the El Castillo volcanic rocks (Salamanca, Central Iberian Zone): Tectonophysics, v. 461, p. 157–165, doi: 10.1016/j.tecto.2008.01.013.

Gutiérrez-Alonso, G., Fernández-Suárez, J., Gutiérrez-Marco, J.C., Corfu, F., Murphy, J.B., and Suárez, M., 2007, U-Pb depositional age for the upper Barrios Formation (Armorican quartzite facies) in the Cantabrian zone of Iberia: Implications for stratigraphic correlation and paleogeography, *in* Linnemann, U., Nance, R.D., Kraft, P., and Zulauf, G., eds., The evolution of the Rheic Ocean; from Avalonian-Cadomian active margin to Alleghenian-Variscan collision, Volume 423: Boulder, CO, United States (USA), Geological Society of America (GSA), p. 287-296.

Gutiérrez-Alonso, G., Fernández-Suárez, J., and Weil, A.B., 2004, Orocline triggered lithospheric delamination: Orogenic Curvature: Integrating Paleomagnetic and Structural Analyses: Geological Society of America Special Paper, v. 383, p. 121–130.

Gutiérrez-Alonso, G., Fernández-Suárez, J., Jeffries, T.E., Jenner, G.A., Tubrett, M.N., Cox, R., and Jackson, S.E., 2003, Terrane accretion and dispersal in the northern Gondwana margin. An Early Paleozoic analogue of a long-lived active margin: Tectonophysics, v. 365, p. 221–232, doi: 10.1016/S0040-1951(03)00023-4.

Gutiérrez-Marco, J.C., Robardet, M., Rábano, I., Sarmiento, G.N., San José Lancha, M.Á., and Herranz, P.A., 2002, Ordovician, *in* Gibbons, W., and Moreno, T., eds., The Geology of Spain: London, The Geological Society.

Gutiérrez-Marco, J.C., and Rabáno, I., 1996, First Iberian representatives of the genus *Hanadirella* (problematica, Ordovician) and reevaluation of its biostratigraphic significance, *in* Baldis, B., and Aceñolaza, F.G., eds., Early Paleozoic evolution in NW Gondwana, Volume 12, Serie Correlacion Geologica, p. 271-272.

Guynn, J., and Gehrels, G.E., 2010, Comparison of detrital zircon age distributions using the k-S test. Arizona LaserChron Center. Web Address: https://sites.google.com/a/laserchron.org/laserchron/home/.

Handy, M.R., Ustaszewski, K., and Kissling, E., 2015, Reconstructing the Alps-Carpathians-Dinarides as a key to understanding switches in subduction polarity, slab gaps and surface motion: International Journal of Earth Sciences = Geologische Rundschau, v. 104, p. 1–26, doi: 10.1007/s00531-014-1060-3.

Hargraves, R.B., Dawson, E.M., and Houten, F.B., 1987, Palaeomagnetism and age of mid-Palaeozoic ring complexes in Niger, West Africa, and tectonic implications: Geophysical Journal International, v. 90, p. 705–729, doi: 10.1111/j.1365-246X.1987.tb00750.x.

Hargrove, U.S., Stern, R.J., Kimura, J.-I., Manton, W.I., and Johnson, P.R., 2006, How juvenile is the Arabian - Nubian Shield? Evidence from Nd Isotopes and pre-Neoproterozoic inherited Zr in the Bi'r Umq suture zone, Saudi Arabia: Earth and PLanetary Science Letters, v. 252, p. 308-326.

Hoffman, P.F., 1991, Did the breakout of Laurentia turn Gondwanaland inside-out?: Science, v. 252, p. 1409-1412.

Hildebrand, R.S., 2013, Mesozoic assembly of the North American Cordillera: Special Paper - Geological Society of America, v. 495.

Hildebrand, R.S., 2009, Did westward subduction cause Cretaceous-Tertiary orogeny in the North American Cordillera? Special Paper - Geological Society of America, v. 457.

Isacks, B.L., 1988, Uplift of the Central Andean Plateau and bending of the Bolivian Orocline: Journal of Geophysical Research, v. 93, no. B4, p. 3211–3231, doi: 10.1029/JB093iB04p03211.

Irving, E., 1985, Tectonics: Whence British Columbia? Nature, v. 314, p. 673–674, doi: 10.1038/314673a0.

Irving, E., and Wynne, P.J., 1992, Paleomagnetism; review and tectonic implications The geology of North America, *in* Canada, Geol. Surv. Can. : Ottawa, ON, Canada, p. 63–86.

Johnson, S.P., De Waele, B., Tembo, F., Katongo, C., Tani, K., Chang, Q., Iizuka, T., and Dunkley, D., 2007, Geochemistry, geochronology and isotope evolution of the Chwore - Rufansa terrane, Southern Irumide Belt: A Mesoproterozoic continental arc: Journal of Petrology, v. 48, p. 1411-1441.

Johnston, S.T., 2008, The Cordilleran Ribbon Continent of North America: Annual Review of Earth and Planetary Sciences, v. 36, p. 495–530, doi: 10.1146/annurev.earth.36.031207.124331.

Johnston, S.T., 2001, The Great Alaskan Terrane Wreck: reconciliation of paleomagnetic and geological data in the northern Cordillera: Earth and Planetary Science Letters, v. 193, p. 259–272.

Johnston, S.T., and Borel, G.D., 2007, The odyssey of the Cache Creek terrane, Canadian Cordillera: Implications for accretionary orogens, tectonic setting of Panthalassa, the Pacific superwell, and break-up of Pangea: Earth and Planetary Science Letters, v. 253, p. 415–428, doi: 10.1016/j.epsl.2006.11.002.

Johnston, S.T., Weil, A.B., and Gutierrez-Alonso, G., 2013, Oroclines: Thick and thin: Geological Society of America Bulletin, v. 125, no. 5-6, p. 643–663, doi: 10.1130/B30765.1.

Johnston, S.T., Wynne, P.J., Francis, D., Hart, C.J.R., Enkin, R.J., and Engebretson, D.C., 1996, Yellowstone in Yukon; the Late Cretaceous Carmacks Group: Geology [Boulder], v. 24, p. 997–1000, doi: 10.1130/0091-7613(1996)024<0997:YIYTLC>2.3.CO;2.

Julivert, M., 1971, Decollement tectonics in the Hercynian Cordillera of Northwest Spain: American Journal of Science, v. 270, no. 1, p. 1–29, doi: 10.2475/ajs.270.1.1.

Julivert, M., and Marcos, A., 1973, Superimposed folding under flexural conditions in the Cantabrian Zone (Hercynian Cordillera, northwest Spain): American Journal of Science, v. 273, no. 5, p. 353–375, doi: 10.2475/ajs.273.5.353.

Kissel, C., Kondopoulou, D., Laj, C., and Papadopoulos, P., 1986, New paleomagnetic data from Oligocene formations of northern Aegea: Geophysical Research Letters, v. 13, p. 1039–1042, doi: 10.1029/GL013i010p01039.

Kissel, C., Laj, C., and Mazaud, A., 1986, First paleomagnetic results from Neocene Formations in Evia, Skyros and the Volos Region and the deformation of Central Aegea: Geophysical Research Letters, v. 13, p. 1446–1449.

Keppie, J.D., Davis, D.W., and Krogh, T.E., 1998, U-Pb geochronological constraints on Precambrian stratified units in the Avalon Composite Terrane of Nova Scotia, Canada: tectonic implications: Canadian Journal of Earth Science, v. 35, p. 222-236.

Kollmeier, J.M., van der Pluijim, B.A., and Van der Voo, R., 2000, Analysis of Variscan dynamics; early bending of the Cantabria-Asturias Arc, northern Spain: Earth and Planetary Science Letters, v. 181, p. 203-216.

Kondopoulou, D., and Lauer, J.P., 1984, Palaeomagnetic data from Tertiary units of the North Aegean Zone: Geological Society Special Publications, v. 17, p. 681–686.

Kolodner, K., Avigad, D., McWilliams, M., Wooden, J.L., Weissbrod, T., and Feinstein, S., 2006, Provenance of north Gondwana Cambrian - Ordovician sansdstone: U-Pb SHRIMP dating of detrital zircons from Israel and Jordan: Geological Magazine, v. 143, p. 367-391.

Kröner, A., 2001, The Mozambique belt of East Africa and Madagascar: Sugnificance of zircon and Nd model ages for Rodinia and Gondwana supercontinent formation and dispersal: South African Journal of Geology, v. 18, p. 1186-1190.

Lamb, S., 2001, Vertical axis rotation in the Bolivian orocline, South America; 2, Kinematic and dynamical implications: Journal of Geophysical Research, v. 106, no. B11, p. 26,633–26,553

Lambert, R.S.J., and Chamberlain, V.E., 1988, Cordilleria revisited, with a three-dimensional model for Cretaceous tectonics in British Columbia: Journal of Geology, v. 96, p. 47–60.

Lawrence, R.L., Cox, R., Mapes, R.W. and Coleman, D.S., 2011. Hydrodynamic fractionation of zircon age populations: Geological Society of America Bulletin, v. 123, no. 1-2, p. 295-305.

Lewandowski, M., 1987, Results of the preliminary paleomagnetic investigations of some lower Paleozoic rocks from the Holy Cross Mts (Poland): Kwartalnik Geologiczny, v. 31, p. 543–556.

Link, P.K., Fanning, C.M., and Beranek, L.P., 2005, Reliability and longitudinal change of detrital-zircon age spectra in the Snake River system, Idaho and Wyoming: An example of reproducing the bumpy barcode: Sedimentary Geology, v. 182, p. 101–142, doi: 10.1016/j.sedgeo.2005.07.012.

Linnemann, U., Ouzegane, K., Drareni, A., Hofman, M., Becker, S., Gärtner, A., and Sagawe, A., 2011, Sands of West Gondwana: An archive of secular magmatism and plate interactions - A case study from the Cambro-Ordovician section of the Tassili Ouan Ahaggar (Algerian Sahara) using U-Pb-LA-ICP-MS detrital zircon ages: Lithos, v. 123.

Linnemann, U., Pereira, F.M., Jeffries, T.E., Drost, K., and Gerdes, A., 2008, The Cadomian Orogeny and the opening of the Rheic Ocean: The diacrony of geotectonic processes constrained by LA-ICP-MS U-Pb zircon dating (Ossa-Morena and sao-Thuringian Zones, Iberian and Bohermian Massifs): Tectonophysics, v. 481, p. 21-43.

López Sánchez-Vizcaíno, V., Gómez-Pugnaire, M.T., Azor, A., and Férnandez-Soler, J.M., 2003, Pahse diagram sections applied to amphibolites: a case study from the Ossa Morena / Central Iberian Variscan Suture (Southwestern Iberian Massif): Lithos, v. 68, p. 1-21.

Lotze, F., 1945, Zur Gliederung der Varisziden der Iberischen Meseta: Geotektonische Forschungen, v. 6, p. 78-92.

Lowe, D.R., and Byerly, G.R., 1999, Stratigraphy of the west-central part of the Barberton greenstone belt, South Africa: Special Paper - Geological Society of America, v. 329, p. 1–36.

Ludwig, K., 2009, Errors of isotope ratios acquired by double interpolation: Chemical Geology, v. 268, p. 24-26.

Marcos, A., Azor, A., González-Loderio, F., and Simancas, J.F., 1991, Early Phanerozoic trace fossils from the Sierra Albarrana quartzites (Ossa-Morena Zone, Southwst Spain): Scripta Geologica, v. 97, p. 47-53.

Marcos, A., and Pulgar, J.A., 1982, An approach to the tectonostratigraphic evoultion of the Cantabrian foreland thrust and fold belt, Hercynian Corcillera of NW Spain: Neues Jahrbuch fuer Geologie und Palaeontologie. Abhandlungen, v. 163, p. 256-260.

Marquis, G., and Globerman, B.R., 1988, Northward motion of the Whitehorse Trough: paleomagnetic evidence from the Upper Cretaceous Carmacks Group: Canadian Journal of Earth Sciences, v. 25, p. 2005–2016, doi: 10.1139/e88-187.

Marshak, S., 2004, Salients, recesses, arcs, oroclines, and syntaxes—A review of ideas concerning the formation of map-view curves in fold-thrust belts, *in* McClay, K.R. ed., Thrust tectonics and hydrocarbon systems, AAPG Memoir 82, p. 131–156.

Marshak, S., 1988, Kinematics of orocline and arc formation in thin-skinned orogens: Tectonics, v. 7, no. 1, p. 73–86, doi: 10.1029/TC007i001p00073.

Marshak, S., and Flöttmann, T., 1996, Structure and origin of the Fleurieu and Nackara Arcs in the Adelaide fold-thrust belt, South Australia: Salient and recess development in the Delamerian Orogen: Journal of Structural Geology, v. 18, no. 7, p. 891–908, doi: 10.1016/0191-8141(96)00016-8.

Marshak, S., Geiser, P.A., Alvarez, W., and Engelder, T., 1982, Mesoscopic fault array of the northern Umbrian Apennine fold belt, Italy: Geometry of conjugate shear by pressure-solution slip: Geological Society of America Bulletin, v. 93, no. 10, p. 1013–1022, doi: 10.1130/0016-7606(1982)93<1013:MFAOTN>2.0.CO;2.

Marshak, S., and Tabor, J.R., 1989, Structure of the Kingston orocline in the Appalachian fold-thrust belt, New York: Geological Society of America Bulletin, v. 101, no. 5, p. 683–701, doi: 10.1130/0016-7606(1989)101<0683:SOTKOI>2.3.CO;2.

Martínez Catalán, J.R., 2012, The Central Iberian Arc, an orocline centered in the Iberian Massif and some implications for the Variscan Belt: International Journal of Earth

Sciences = Geologische Rundschau, v. 101, p. 1299–1314, doi: 10.1007/s00531-011-0715-6.

Martínez Catalán, J.R., 2011, Are the oroclines of the Variscan belt related to late Variscan strike-slip tectonics?: Terra Nova, v. 00, p. 1-7.

Martínez Catalán, J.R., 2008, U-Pb detrital zircon ages in synorogenic deposits of the NW Iberian Massif (Variscan belt): interplay of Devonian-Carboniferous sedimentation and thrust tectonics: Journal of the Geological Society, London, v. 165, p. 687-698.

Martínez Catalán, J.R., Arenas, R., Abati, J., Sánchez Martínez, S., Díaz García, F., Fernández Suárez, J., González Cuadra, P., Castiñeiras, P., Gómez Barrerio, J., Díez Montes, A., González Clavijo, E., Rubio Pascual, F.J., Andonaegui, P., Jeffries, T.E., Alcock, J.E., Díez Fernández, R., and López Carmona, A., 2009, A rootless suture and the loss of the roots of a mountain chain: The Variscan belt of NW Iberia: Tectonics, v. 341, p. 114-126.

Martínez Catalán, J.R., Arenas, R., Díaz García, F., González Cuadra, P., Gómez-Barriero, J., Abati, J., Castiñeiras, P., Fernández-Suárez, J., Sánchez Martínez, S., Adonaegui, P., González Clavijo, E., Díez Montes, A., Rubio Pascual, F.J., and Valle Aguado, B., 2007, Space and time in the tectonic evolution of the northwestern Iberian Massif: Implications for the Variscan belt, *in* Hatcher, R.D., Jr., Carlosn, M.P., McBride, J.H., and Martínez Catalán, J.R., eds., 4-D Framework of Continental Crust: Geological Society of America Memoir 200, The Geological Society of America, p. 403-423.

Martínez Catalán, J.R., Fernández Suárez, J., Jenner, G.A., Belousova, E., and Díez Montes, A., 2004, Provenance contraints from detrital zircon U-Pb ages in the NW Iberian Massif: implications for Paleozoic plate configuration and Variscan evolution: Journal of the Geological Society of London, v. 161, p. 463-476.

Martínez Catalán, J.R., Arenas, R., Diaz García, F., and Abati, J., 1997, Variscan accretionary complex of NW Iberia: Terrane correlation and succession of tectonothermal events: Geology, v. 25, p. 1103-1106.

Martínez Catalán, J.R., Perez Estuan, A., Bastida, F., Pulgar, J.A., and Marcos, A., 1990, Structure, *in* Dallmeyer, R.D., and Martínez García, E., eds., Pre-Mesozoic Geology of Iberia: Berlin, Heidelberg, New York, Springer-Verlag, p. 103-114.

Mattauer, M., Collot, B., and Driessche, J.V. den, 1983, Alpine model for the internal metamorphic zones of the North American Cordillera: Geology, v. 11, p. 11–15, doi: 10.1130/0091-7613(1983)11<11:AMFTIM>2.0.CO;2.

Matte, P., 1991, Accretionary history and crustal evolution of the Variscan belt in Western Europe: Tectonophysics, v. 196, p. 309-337.

Matte, P., 2001, The Variscan collage and orogeny (480-290) Ma and the tectonic definition of the Amorica microplate: a review: Terra Nova, v. 13, p. 122-128.

McCausland, P.J.A., Symons, D.T.A., Hart, C.J.R., and Blackburn, W.H., 2006, Assembly of the northern Cordillera; new paleomagnetic evidence for coherent, moderate Jurassic to Eocene motion of the Intermontane Belt and Yukon-Tanana terranes: Special Paper - Geological Association of Canada, v. 46, p. 147–170.

McKerrow, W.S., Mac Niocailll, C., Ahlberg, P.E., Clayton, G., Cleal, C.J., and Eagar, R.M.C., 2000, The Late Paleozoic relations between Gondwana and Laurussia: The Geological Society of London Special Publications, v. 179, p. 9-20.

McLeish, D.F., and Johnston, S.T., 2011, Geology of the Aley Creek area: A record of Devonian orogeny in the foreland balt of the Canadian Cordillera?: Geological Society of Canada Abstracts with Programs, v.34, p. 138.

McLeish, D.F., Johnston, S.T., Mihalynuk, M.G., and Mortensen, J.K., 2010, Geology of the Aley Creek area, Northeastern BC Rocky Mountains: A record of Mississippian orogenesis in the Cordilleran foreland belt?: GeoCanada 2010, May 10-14, Calgary, Alberta.

McMechan, M.E., Thompson, R.I., Cook, D.G., Gabrielse, H., and Yorath, C.J., 1992, Structural styles; Foreland Belt The geology of North America, *in* Canada, Geol. Surv. Can. : Ottawa, ON, Canada, p. 634–650.

Medvedev, S., Podladchikov, Y., Handy, M.R., and Scheuber, E., 2006, Controls on the deformation of the central and southern Andes (10–35 S): insight from thin-sheet numerical modeling, *in* Oncken, O., et al., eds., The Andes, Berlin, Springer, p. 475–494.

Meinhold, G., Morton, A.C., Fanning, C.M., Frei, D., Howard, J.P., Phillips, R.J., Strogen, D., and Whitham, A.G., 2011, Evidence from detrital zircons for recycling of Mesoproterozoic and Neoproterozoic crust recorded in Paleozoic and Mesozoic sandstones of soutehrn Libya: Earth and Planetary Science Letters, v. 312, p. 164-175.

Mélou, M., Oulesbir, L., and Paris, F., 1999, Brachiopodes et chitinozoaires Ordoviciens dans le NE du Sahara Algérien: implicationsw stratigraphiques et paléogéographicques: Goebios, v. 32, p. 823-839.

Merino-Tomé, O.A., Bahamonde, J.R., Colmenero, J.R., Heredia, N., Villa, E., and Farias, P., 2009, Emplacement of the Cuera and Picos de Europa imbricate system at the core of the Iberian-Armorican arc (Cantabrian zone, north Spain): New precisions concerning the timing of arc closure: Geological Society of America Bulletin, v. 121, p. 729–751, doi: 10.1130/B26366.1.

Moores, E.M., 1998, Ophiolites, the Sierra Nevada, "Cordilleria," and Orogeny along the Pacific and Caribbean Margins of North and South America: International Geology Review, v. 40, p. 40–54, doi: 10.1080/00206819809465197.

Moores, E., 1970, Ultramafics and Orogeny, with Models of the US Cordillera and the Tethys: Nature, v. 228, p. 837–842, doi: 10.1038/228837a0.

Montero, O., Bea, F., González-Loderio, F., Talavera, C., and Whitehouse, M.J., 2007, Zircon ages of the metavolcanic rocks and metagranites of the Ollo de Sapo domain in central Spain: implications for the Neoproterozoic to Early Paleozoic evolution of Iberia: Geological Magazine, v. 144, p. 963-976.

Morag, N., Avigad, D., Gerdes, A., Belousova, E., and Harlavan, Y., 2011, Detrital zircon Hf isotopic composition indicates long-distance transport of North Gondwana Cambrian-Ordovician sandstones: Geology, v. 39, p. 955-958.

Morton, A.C., Whitham, A.G., Howard, J.P., Phillips, R.J., Strogen, D., Abutarrama, Y., El Dieb, M., Elktararry, F.M., Hamhoom, A.M., Lüning, S., Phillips, R., and Thusus, B., 2012, Using heavy minerals to test the stratigraphic framework of the Ak Kufrah basin *in* Salam, M.J., ed., Geology of Southern Libya.

Murphy, J.B., and Gutierrez-Alonso, G., 2008, The origin of the Variscan upper allochthons in the Ortegal Complex, northwestern Iberia; Sm-Nd isotopic constraints on the closure of the Rheic Ocean: Canadian Journal of Earth Sciences = Revue Canadienne des Sciences de la Terre, v. 45, p. 651–668, doi: 10.1139/E08-019.

Murphy, J.B., Gutiérrez-Alonso, G., Nance, R.D., Fernández-Suárez, J., Keppie, J.D., Quesada, C., Strachan, R.A., and Dostal, J., 2006, Origin of the Rheic Ocean: Rifting along a Neoproterozoic suture? Geology, v. 34, p. 325–328.

Murphy, J.B., Pisarevsky, S.A., Nance, R.D., and Keppie, J.D., 2004, Neoproterozoic - Early Paleozoic evolution of peri-Gondwanan terranes: implications for Laurentia-Gondwana connections: International Journal of Earth Sciences, v. 93, p. 659–682, doi: 10.1007/s00531-004-0412-9.

Nance, R.D., and Linnemann, U., 2008, The Rheic Ocean: Origin, Evolution, and Significance: GSA Today, v. 18, p. 4-12.

Nance, R.D., and Murphy, J.B., 1994, Contrasting basement isotopic signatures and the palinspastic restoration of peripheral orogens; example from the Neoproterozoic Avalonian-Cadomian Belt: Geology [Boulder], v. 22, p. 617–620, doi: 10.1130/0091-7613(1994)022<0617:CBISAT>2.3.CO;2.

Nance, R.D., Gutiérrez-Alonso, G., Keppie, J.D., Linnemann, U., Murphy, J.B., Quesada, C., Strachan, R.A., and Woodcock, N.H., 2012, A brief history of the Rheic Ocean: Geoscience Frontiers, v. 3, p. 125–135, doi: 10.1016/j.gsf.2011.11.008.

Nance, R.D., Gutiérrez-Alonso, G., Keppie, J.D., Linnemann, U., Murphy, J.B., Quesada, C., Strachan, R.A., and Woodcock, N.H., 2010, Evolution of the Rheic Ocean: Gondwana Research, v. 17, p. 194–222, doi: 10.1016/j.gr.2009.08.001.

Nance, R.D., Murphy, J.B., Strachan, R.A., Keppie, J.D., Gutiérrez-Alonso, G., Fernández-Suárez, J., Quesada, C., Linnemann, U., D'Lemos, R., and Pisarevsky, S.A., 2008, Neoproterozoic - early Paleozoic tectonostratigraphy and paleogeography of the per-Gondwanan terranes: Amazonian vs. West Africa, *in* Ennin, N., and Liégeois, J.-P., eds., The Boundaries of the West Africa Craton, Volume Special Publications, 297: London, Geologica Society, p. 345-383.

Nemcok, M., Pospisil, L., Lexa, J., and Donelick, R.A., 1998, Tertiary subduction and slab break-off model of the Carpathian–Pannonian region: Tectonophysics, v. 295, p. 307–340.

Noblet, C., and Lefort, J.P., 1990, Sedimentological evidence for a limited separation between Armorica and Gondwana during the Early Ordovician: Geology, v. 18, p. 303-306.

Orchard, M.J., 2000, An overview of terrane conodonts; what do they tell us? Abstracts with Programs - Geological Society of America, v. 32, p. 60–60.

Orchard, M.J., 2006, Late Paleozoic and Triassic conodont faunas of Yukon and northern British Columbia and implications for the evolution of the Yukon-Tanana Terrane: Special Paper - Geological Association of Canada, v. 45, p. 229–260.

Parés, J.M., and Van der Voo, R., 1992, Paleozoic paleomagnetism of Almaden, Spain: A cautionary note: Journal of Geophysical Research, v. 97, p. 9353-9356.

Parés, J.M., Van der Voo, R., Stamatakos, J., and Pérez-Estaún, A., 1994, Remagnetizations and post folding oroclinal rotations in the Cantabrian/Asturian arc, northern Spain: Tectonics, v. 13, p. 1461–1471, doi: 10.1029/94TC01871.

Pastor-Galán, D., Gutiérrez-Alonso, G., Murphy, J.B., Fernández Suáre, J., Hofman, M., and Linnemann, U., 2013, Provenance analysis of the Paleozoic sequences of the northern Gondwana margin in NW Iberia: Passive margin to Variscan collision and orocline development: Gondwana Research, v. 23, p. 1089-1103.

Pastor-Galán, D., Gutiérrez-Alonso, G., and Weil, A.B., 2011, Orocline timing through joint analysis: Insights from the Ibero-Armorican Arc: Tectonophysics, v. 507, p. 31–46, doi: 10.1016/j.tecto.2011.05.005.

Pérez-Estaún, A., and Bastida, F., 1990, Cantabrian Zone, *in* Dallmeyer, R.D., and Martínez Catalán, J.R., eds., Pre-Mesozoic Geology of Iberia: Berlin, Heidelberg, New York, Springer-Verlager, p. 55-69.

Pérez-Estaún, A., Pulgar, J.A., Banda, E., and Alvarez-Marrón, J., 1994, Crustal structure of the external Variscides in northwest Spain from deep seismic reflection profiling: Tectonophysics, v. 232, p. 91–118, doi: 10.1016/0040-1951(94)90078-7.

Pérez-Estaún, A., Bastida, F., Alonso, J.L., Marquínez, J., Aller, J., Alvarez-Marrón, J., Marcos, A., and Pulgar, J.A., 1988, A thin-skinned tectonics model for an arcuate fold and thrust belt; the Cantabrian Zone (Variscan Ibero-Armorican Arc): Tectonics, v. 7, p. 517–537, doi: 10.1029/TC007i003p00517.

Pereira, E., and Silva, J.B., 2002, Neoproterozoic-Paleozoic tectonic evolution of the Coimbra-Córdoba shear zone and related areas of the Ossa-Morena and Central Iberian zones (Northeast Alentejo, Portugal): Comunições Instituto Geológico e Mineiro, Lisboa, v. 89.

Pereira, M.F., Linnemann, U., Hoffman, M., Chicorro, M., Solá, A.R., Medina, J., and Silva, J.B., 2012, The provenance of Late Ediacaran and Early Ordovician siliciclastic rocks in the Southwest Central Iberian Zone: Constraints from detrital zircon data on northern Gondwana margin evolution during the late Neoproterozoic: Precambiran Research, v. 192-195, p. 166-189.

Pereira, E., Silva, J.B., and Ribeiro, A., 2010, The role of bedding in the formation of fault-fold structures. Portalegre-Esperança transpressional shear zone, SW Iberia: Geological Journal, v. 45, p. 521-535.

Pérez-Estaún, A., Bastida, F., Alonso, J.L., Marquinez, J., Aller, J., Alvarez-Marron, J., Farias, P., Marcos, A., and Pulgar, J.A., 1991, The Cantabrian Zone: an interpretation for an arcuate foreland thrust belt: Tectonophysics, v. 191, p. 243-253.

Perroud, H., 1983, Palaeomagnetism of Palaeozoic rocks from the Cabo de Penas, Asturia, Spain: Geophysical Journal International, v. 75, p. 201–215, doi: 10.1111/j.1365-246X.1983.tb01920.x.

Perroud, H., and Bonhommet, N., 1984, A Devonian paleomagnetic pole for Armorica: Geophysical Journal of the Royal Astronomical Society v. 77, p. 839-845.

Perroud, H., and Van der Voo, R., 1985, Paleomagnetism of the Late Ordovician Thouars Massif, Vendee Province, France: Journal of Geophysical Research: Solid Earth, v. 90, p. 4611–4625, doi: 10.1029/JB090iB06p04611.

Perroud, H., Calza, F., and Khattach, D., 1991, Paleomagnetism of the Silurian Volcanism ad Almaden, Southern Spain: Journal of Geophysical Research, v. 96, p. 1949-1962.

Perroud, H., Bonhommet, N., and Voo, R.V. der, 1983, Palaeomagnetism of the Ordovician dolerites of the Crozon Peninsula (France): Geophysical Journal International, v. 72, p. 307–319, doi: 10.1111/j.1365-246X.1983.tb03785.x.

Price, R.A., 1981, The Cordilleran foreland thrust and fold belt in the southern Canadian Rocky Mountains: Geological Society, London, Special Publications, v. 9, p. 427–448, doi: 10.1144/GSL.SP.1981.009.01.39.

Quesada, C., and Dallmeyer, R.D., 1994, Tectonothermal evolution of the Badajoz-Cordoba shear zone (SW Iberia); characteristics and (super 40) Ar/ (super 39) Ar mineral age constraints: Tectonophysics, v. 231, p. 195–213.

Ribeiro, A., 1990, Introduction, *in* Dallmeyer, R.D., and Martínez García, E., eds., Pre-Mesozoic Geology of Iberia: Berlin, Heidelberg, New York, Sporinger-Verlager, p. 143-144.

Ribeiro, A., Dias, R., and Silva, J.B., 1995, Genesis of the Ibero-Armorican Arc: Geodinamica Acta, v. 8, p. 173–184.

Ribeiro, A., Munhá, J., Dias, R., Mateus, A., Pereira, E., Ribeiro, L., Fonseca, P., Araújo, A., Oliveira, T., Romão, J., Chaminé, H., Coke, C., and Pedro, J., 2007, Geodynamic evolution of the SW Europe Variscides: Tectonics, v. 26, p. TC6009, doi: 10.1029/2006TC002058.

Robardet, M., 2003, The Armorica "microplate": fact or fiction? Critical review of the concept and contradictory palaeobiogeographical data: Palaeogeography, Palaeoclimatology, Palaeoecology, v. 195, p. 125–148, doi: 10.1016/S0031-0182(03)00305-5.

Robardet, M., 2002, Alternative approack to the Variscan Belt in southwestern Europe: Preorogenic paleobiogeographical constraints, *in* Martínez Catalán, J.R., Hatcher, R.D., Jr., Arenas, R., and Díaz García, F., eds., Variscan Appalachian dynamics: The building of the late Palaeozoic basment: Boulder, Colorado, Geological Society of America Special Paper 364, p. 1-15.

Robardet, M., and Gutiérrez-Marco, 2004, The Ordovician, Silurian and Devonian sedimentary rocks of the Ossa-Morena Zone (SW Ibreian Peninsula, Spain): Journal of Iberian Geology, v. 30, p. 73-92.

Robardet, M., and Gutiérrez-Marco, J.C., 1990a, Sedimentary and Faunal Domains in the Iberian Peninsula During Lower Paleozoic Times, *in* Dallmeyer, R.D., and Martínez García, E., eds., Pre-Mesozoic Geology of Iberia: Berlin, Springer-Verlag, p. 383-395.

Robardet, M., and Gutiérrez-Marco, J.C., 1990b, Ossa-Morena Zone, Stratigraphy, Passive Margin Phase (Ordovician - Silurian - Devonian), *in* Dallmeyer, R.D., and Martínez García, E., eds., Pre-Mesozoic Geology of Iberia: Berlin, Springer-Verlag, p. 262-272.

Rocci, G., Bronner, G., and Deschamps, M., 1991, Crystalline basement of the West African Craton, *in* Dallmeyer, R.D., and Lécorché, J.P., eds., The West African orogens and circum-Atlantic correlatives: Berlin, Springer-Verlag, p. 31-61.

Ross, G.M., Patchett, P.J., Hamilton, M., Heaman, L., DeCelles, P.G., Rosenberg, E., and Giovanni, M.K., 2005, Evolution of the Cordilleran orogen (southwestern Alberta, Canada) inferred from detrital mineral geochronology, geochemistry, and Nd isotopes in the foreland basin: Geological Society of America Bulletin, v. 117, p. 747–763, doi: 10.1130/B25564.1.

Royden, L., and Burchfiel, B.C., 1989, Are systematic variations in thrust belt style related to plate boundary processes? (the Western Alps versus the Carpathians): Tectonics, v. 8, p. 51–61, doi: 10.1029/TC008i001p00051.

Rubio-Ordóñez, A., Gutiérrez-Alonso, G., Valverde-Vaquero, P., Cuesta, A., Gallastegui, G., Gerdes, A., and Cárdenas, V., 2015, Arc-related Ediacaran magmatism in the northern margin of Gondwana. Geochronology and isotopic geochemistry from northern Iberia: Gondwana Research, v. 27, no. 1, p. 216-227.

Ruffet, G., 1990, ^{40}Ar-^{39}Ar Dating of the Beja Gabbro: Timing of teh accretion of Southern Portugal: Geophysical Research Letters, v. 17, p. 2121-2124.

Şengör, A.M.C., 2013, The Pyrenean Hercynian Keirogen and the Cantabrian Orocline as genetically coupled structures: Journal of Geodynamics, v. 65, p. 3–21, doi: 10.1016/j.jog.2012.10.003.

Sanchez Martinez, S., Arenas, R., Andonaegui, P., Martinez Catalan, J.R., and Pearce, J.A., 2007, Geochemistry of two associated ophiolites from the Cabo Ortegal Complex (Variscan belt of NW Spain): Memoir - Geological Society of America, v. 200, p. 445–467, doi: 10.1130/2007.1200(23).

Schmid, S.M., Bernoulli, D., Fügenschuh, B., Matenco, L., Schefer, S., Schuster, R., Tischler, M., and Ustaszewski, K., 2008, The Alpine-Carpathian-Dinaridic orogenic system: correlation and evolution of tectonic units: Swiss Journal of Geosciences, v. 101, p. 139–183, doi: 10.1007/s00015-008-1247-3.

Shaw, J., and Johnston, S.T., 2012, The Carpathian-Balkan bends: An oroclinal record of ongoing Arabian–Eurasian collision: Oroclines: Journal of the Virtual Explorer, E lectronic Edition, ISSN 1441-8142, volume 43, paper 4, doi:10.3809/jvirtex.2012.00310.

Shaw, J., Gutiérrez-Alonso, G., Johnston, S.T., and Galán, D.P., 2014, Provenance variability along the Early Ordovician north Gondwana margin: Paleogeographic and tectonic implications of U-Pb detrital zircon ages from the Armorican Quartzite of the Iberian Variscan belt: Geological Society of America Bulletin, v. 126, p. 702–719, doi: 10.1130/B30935.1.

Shaw, J., Johnston, S.T., Gutiérrez-Alonso, G., and Weil, A.B., 2012, Oroclines of the Variscan orogen of Iberia: Paleocurrent analysis and paleogeographic implications: Earth and Planetary Science Letters, v. 329-330, p. 60–70, doi: 10.1016/j.epsl.2012.02.014.

Simancas, J.F., Azor, A., Martínez-Poyatos, D., Tahiri, A., El Hadi, H., González-Loderio, F., and Pérez-Estaún, A., 2009, Tectonic relationships of Southwest Iberia with the allochthons of Northwest Iberia and the Moroccan Variscides: Tectonics, v. 341, p. 103-113.

Simancas, J.F., Martínez Poyatos, D., Expósito, I., Azor, A., and González Lodeiro, F., 2001, The structure of a major suture zone in the SW Iberian Massif: the Ossa-Morena/Central Iberian contact: Tectonophysics, v. 322, p. 295-308.

Sircombe, K.N., 2004, AgeDisplay: an EXCEL workbook to evaluate and display univariate geochronological data using binned frequency histograms and probability density distributions: Computers & Geosciences, v. 30, p. 21–31, doi:10.1016/j.cageo.2003.09.006.

Sircombe, K.N., Bleeker, W., and Stern, R.A., 2001, Detrital zircon geochronology and grain-size analysis of a ~2800 Ma Mesoarchean proto-cratonic cover successtion, Slave Province, Canada: Earth and Planetary Science Letters, v. 189, p. 207-220.

Socias, I., and Mezcua, J., 2002, Mapa de Anomalias Magneticas de la Peninsula Ibérica, Insitutio Geografico Nacional

Stacey, J.S., and Kramers, J.D., 1975, Approximation of terrestrial lead isotope evolutionby a two-stage model: Earth and Planetary Science Letters, v. 26, p. 207-221.

Stampfli, G., 2005, Plate tectonics of the Apulia-Adria microcontinents: CROP Project-Deep Seismic explorations of the Central Mediterranean and Italy, Section, v. 11, p. 747–766.

Stampfli, G.M., and Borel, G.D., 2002, A plate tectonic model for the Paleozoic and Mesozoic constrained by dyanimic plate boundaries and restored synthetic oceanic isochrons: Earth and Planetary Science Letters, v. 196, p. 17-33.

Tait, J., 1999, New Early Devonian paleomagnetic data from NW France; paleogeography and implications for the Armorican microplate hypothesis: Journal of Geophysical Research, v. 104, p. 2831–2839, doi: 10.1029/98JB02787.

Tait, J.A., Bachtadse, V., and Dinarés-Turell, 2000a, Paleomagnetism of Siluro-Devonian sequences, NE Spain: Journal of Geophysical Research, v. 105, p. 23,595-23,603.

Tait, J.A., Schäta, M., Bachtadse, V., and Soffel, H.C., 2000b, Paleomagnetism and Palaeozoic paleogeography of Gondwana and European terranes, *in* Franke, W., Haak, V., Onicken, O., and Tanner, D., eds., Orogenic Processes: Quantifications and Modelling in the Variscan Belt, Volume 179: Geological Society, London, Special Publications: London, The Geological Society of London, p. 21-34.

Tait, J.A., Bachtadse, V., and Soffel, H., 1994, Silurian paleogeography of Armorica; new paleomagnetic data from Central Bohemia: Journal of Geophysical Research, v. 99, p. 2897–2907, doi: 10.1029/93JB02642.

Tatar, O., Poyraz, F., Gürsoy, H., Cakir, Z., Ergintav, S., Akpınar, Z., Ko\ccbulut, F., Sezen, F., Türk, T., and Hastao\uglu, K.Ö., 2012, Crustal deformation and kinematics of the Eastern Part of the North Anatolian Fault Zone (Turkey) from GPS measurements: Tectonophysics, v. 518, p. 55–62.

Talavera, C., Montero, P., Martínez Poyatos, D., and Williams, I.S., 2012, Ediacaran to Lower Ordovician age for rocks ascribed to the Schist–Graywacke Complex (Iberian Massif, Spain): Evidence from detrital zircon SHRIMP U–Pb geochronology: Gondwana Research, v. 22, p. 928–942, doi: 10.1016/j.gr.2012.03.008.

Teixeira, W., Tassanari, C.C.G., Cordani, U.G., and Kawashita, K., 1989, A Review of the geochronology of the Amazonian Craton: Tectonic implications: Precambiran Research, v. 42, p. 213-227.

Tempelman-Kluit, D.J., 1979, Transported cataclasite, ophiolite and granodiorite in Yukon; evidence of arc-continent collision: Paper - Geological Survey of Canada,.

Torsvik, T.H., and Cocks, L.R.M., 2013, Gondwana from top to base in space and time: Gondwana Research, v. 24, p. 999–1030, doi: 10.1016/j.gr.2013.06.012.

Torsvik, T.H., Van der Voo, R., Preede, U., Mac Niocaill, C., Steinberger, B., Doubrovine, P.V., van Hinsbergen, D.J.J., Domeier, M., Gaina, C., Tohver, E., Meert, J.G., McCausland, P.J.A., and Cocks, L.R.M., 2012, Phanerozoic polar wander, paleogeography and dynamics: Earth Science Reviews, v. 114, p. 325-368.

Ugidos, J.M., 1990, Granites as a paradigm of genetic processes of granitic rocks: I-types vs S-types, *in* Dallmeyer, R.D., and Martínez García, E., eds., Pre-Mesozoic geology of Iberia: Berlin, Heidelberg, New York, Springer-Verlag, p. 190-206.

Unrug, R., 1997, Rodinia and Gondwana: The geodynamic map of Gondwana supercontinent assembly: GSA Today, v. 7, p. 1-6.

Valverde-Vaquero, P., Marcos, A., Farias, P., and Gallastegui, G., 2005, U-Pb dating of Ordovician Felsic volcanism in the Schistose Domain of the Galicia-Trás-os-Montes Zone, near Cabo Ortegal (NW Spain): Geologica Acta, v. 3, p. 27-37.

Van der Pluijm, B.A., Vrolijk, P.J., Pevear, D.R., Hall, C.M., and Solum, J., 2006, Fault dating in the Canadian Rocky Mountains: Evidence for late Cretaceous and early Eocene orogenic pulses: Geology, v. 34, p. 837–840, doi: 10.1130/G22610.1.

Van der Voo, R., 1982, Pre-Mesozoic paleomagnetism and plate tectonics: Annual Review of Earth and Planetary Sciences, v. 10, p. 191–220.

Van der Voo, R., 1979, Paleozoic assembly of Pangea; a new plate tectonic model for the Taconic, Caledonian, and Hercynian orogenies: Eos (Washington, D.C.), v. 60, p. 746.

Van der Voo, R., 1969, Paleomagnetic evidence for the rotation of the Iberian Peninsula: Tectonophysics, v. 7, p. 5–56, doi: 10.1016/0040-1951(69)90063-8.

Van der Voo, R., Stamatakos, J.A., and Parés, J.M., 1997, Kinematic constraints on thrust-belt curvature from syndeformational magnetizations in the Lagos del Valle Syncline in the Cantabrian Arc, Spain: Journal of Geophysical Research: Solid Earth, v. 102, p. 10105–10119, doi: 10.1029/97JB00263.

Vermeesch, P., 2004, How many grains are needed for a provenance study? Earth and Planetary Science Letters, v. 224, p. 441–451, doi: 10.1016/j.epsl.2004.05.037.

Vermeesch, P., 2012, On the visualisation of detrital age distributions: Chemical Geology, v. 312-313, p. 190–194, doi: 10.1016/j.chemgeo.2012.04.021.

Warr, L.N., 2012, The Variscan Orogeny: the Welding of Pangea, *in* Woodcock, N.H. and Strachan, R.A. eds., Geological History of Britain and Ireland, Blackwell Publishing Ltd.

Wegener, A., 1929, The origin of continents and oceans: United Kingdom, Methuen : London, United Kingdom.

Weil, A.B., 2006, Kinematics of orocline tightening in the core of an arc; paleomagnetic analysis of the Ponga Unit, Cantabrian Arc, northern Spain: Tectonics, v. 25, no. 3, P. TC3012, doi: 10.1029/2005TC001861.

Weil, A.B., and Sussman, A.J., 2004, Classifying curved orogens based on timing relationships between structural development and vertical-axis rotations: Special Paper - Geological Society of America, v. 383, p. 1–15.

Weil, A.B., Gutiérrez-Alonso, G., and Wicks, D., 2013a, Investigating the kinematics of local thrust sheet rotation in the limb of an orocline: a paleomagnetic and structural analysis of the Esla tectonic unit, Cantabrian–Asturian Arc, NW Iberia: International Journal of Earth Sciences, v. 102, p. 43–60, doi: 10.1007/s00531-012-0790-3.

Weil, A.B., Gutiérrez Alonso, G., Johnston, S.T., and Pastor-Galán, D., 2013b, Kinematic constraints on buckling a lithospheric-scale orocline along the northern margin of Gondwana: A geologic synthesis. Tectonophysics: Tectonophysics, v. 582, p. 25-49.

Weil, A., Gutiérrez-Alonso, G., and Conan, J., 2010, New time constraints on lithospheric-scale oroclinal bending of the Ibero-Armorican Arc: a palaeomagnetic study of earliest Permian rocks from Iberia: Journal of the Geological Society, v. 167, p. 127–143, doi: 10.1144/0016-76492009-002.

Weil, A.B., Voo, R.V. der, and van der Pluijm, B.A., 2001, Oroclinal bending and evidence against the Pangea megashear: The Cantabria-Asturias arc (northern Spain): Geology, v. 29, p. 991, doi: 10.1130/0091-7613(2001)029<0991:OBAEAT>2.0.CO;2.

Weil, A.B., Van der Voo, R., van der Pluijm, B.A., and Pares, J.M., 2000, The formation of an orocline by multiphase deformation; a paleomagnetic investigation of the Cantabria-Asturias Arc (northern Spain): Journal of Structural Geology, v. 22, p. 735–756.

Westphal, M., 1993, Did a large departure from the geocentric axial dipole hypothesis occur during the Eocene? Evidence from the magnetic polar wander path of Eurasia: Earth and Planetary Science Letters, v. 117, p. 15–28, doi: 10.1016/0012-821X(93)90114-O.

Woodcock, N.H., Soper, N.J., and Strachan, R.A., 2007, A Rheic cause for the Acadian deformation in Europe: Journal of the Geological Society, v. 164, p. 1023–1036, doi: 10.1144/0016-76492006-129.

Woodsworth, G.J., Anderson, R.G., Armstrong, R.L., Struik, L.C., and Van der Heyden, P., 1992, Plutonic regimes The geology of North America, *in* Canada, Geol. Surv. Can. : Ottawa, ON, Canada, p. 493–531.

Wynne, P.J., Enkin, R.J., Baker, J., Johnston, S.T., and Hart, C.J., 1998, The big flush: paleomagnetic signature of a 70 Ma regional hydrothermal event in displaced rocks of the northern Canadian Cordillera: Canadian Journal of Earth Sciences, v. 35, p. 657–671, doi: 10.1139/e98-014.

Appendix

Table A-1 Paleocurrent collection site coordinates, Armorican Quartzite, Iberian Massif

	Amalgam name	Sites	n	**N**	Lat°	Lon°	**Lat°**	**Lon°**
1	Cantabrian-W. Asturian North	CZ-04	37	**61**	43.656505	-5.846343	**43.603505**	**-6.161496**
		WALZ-01	24		43.550505	-6.476648		
2	Cantabrian West	CZ-03	22	**45**	43.214548	-6.048352	**43.26197**	**-6.183054**
		CZ-05	23		43.309228	-6.318860		
3	West Asturian West	WALZ-04	14	**41**	43.026772	-6.782984	**43.07201**	**-6.918468**
		WALZ-05	7		43.080349	-6.943977		
		WALZ-06	3		43.09628	-7.135336		
		WALZ-07	17		43.084637	-6.811573		
4	Cantabrian South	CZ-01	28	**64**	42.945448	-5.553614	**42.897561**	**-5.712485**
		CZ-02	36		42.849348	-5.871355		
5	West Asturian South	WALZ-02	28	**36**	42.843713	-6.467004	**42.747586**	**-6.491805**
		WALZ-03	8		42.651458	-6.516606		
6	Truchas syncline	GCZ-04	19	**32**	42.205006	-6.545018	**42.285643**	**-6.455439**
		GCZ-05	11		42.249607	-6.317437		
		GCZ-06	2		42.402317	-6.503861		
7	Alcañices syncline	GCZ-01	24	**44**	41.702489	-5.814551	**41.785929**	**-6.075192**
		GCZ-02	5		41.738742	-6.027326		
		GCZ-03	15		41.916555	-6.383698		
8	Spanish Central System	SCS-02A	12	**50**	41.091223	-3.204785	**41.136808**	**-3.157464**
		SCS-02B	19		41.091223	-3.204785		
		SCS-03	4		41.181562	-3.184845		
		SCS-05A	9		41.146795	-3.091712		
		SCS-05B	6		41.173235	-3.101191		
9	Iberian Ranges West	IBR-03A	22	**44**	41.114049	-1.565633	**41.107061**	**-1.558599**
		IBR-03B	22		41.100073	-1.551564		
10	Iberian Ranges East	IBR-01	21	**67**	41.144588	-1.167659	**41.241556**	**-1.221861**
		IBR-02	24		41.168032	-1.106298		
		IBR-04	22		41.412047	-1.391627		
11	Tamames and Peña de Francia synclines	GCZ-07	15	**61**	40.604556	-6.063056	**40.511836**	**-6.118089**
		GCZ-08	15		40.465056	-6.120000		
		GCZ-09	20		40.462083	-6.118972		
		GCZ-10	11		40.515649	-6.170329		
12	Cañaveral-Monfragüe synform	LAZ-01	3	**27**	39.865768	-6.708472	**39.84291**	**-6.321674**
		LAZ-02	7		39.80754	-6.475354		
		LAZ-35	10		39.869369	-6.045200		
		LAZ-36	7		39.828962	-6.057670		
13	Guadarranque synform SE	LAZ-03	5	**49**	39.378606	-5.375877	**39.429225**	**-5.144756**
		LAZ-04	3		39.143574	-5.185504		
		LAZ-05	8		39.31843	-4.985680		
		LAZ-06	11		39.471862	-5.152862		
		LAZ-07	7		39.621662	-4.905224		
		LAZ-08	15		39.641216	-5.263388		
14	Vadelacasa antiform NE	LAZ-9	17	**65**	39.686384	-4.583959	**39.564749**	**-4.47965**
		LAZ-10	28		39.521014	-4.352585		
		LAZ-18	11		39.613937	-4.503279		
		LAZ-19	2		39.572159	-4.522645		
		LAZ-20	7		39.430249	-4.435783		

Amalgam name		Sites	n	**N**	Lat°	Lon°	**Lat°**	**Lon°**
15	Valdelacasa antiform	LAZ-11	12		39.74879	-3.850742		
		LAZ-12	12		39.578605	-3.921896		
		LAZ-14	7	**58**	39.350903	-3.972747	**39.514521**	**-4.043112**
		LAZ-15	12		39.368854	-4.249905		
		LAZ-16	15		39.525452	-4.220272		
16	Guadarranque synform SE	LAZ-21	26		39.098028	-4.323026		
		LAZ-22A	7		39.138606	-4.499828		
		LAZ-22B	3	**65**	39.121778	-4.488285	**39.170052**	**-4.47967**
		LAZ-23	15		39.243341	-4.598162		
		LAZ-24	14		39.248509	-4.489049		
17	Almadén synform	LAZ-32	15		38.78267	-4.832332		
		LAZ-33	15	**46**	38.85852	-4.873829	**38.849341**	**-4.885882**
		LAZ-34	16		38.906833	-4.951486		
18	Alcudia antiform West	LAZ-26	20		38.690409	-4.056090		
		LAZ-29	18	**69**	38.694783	-4.108301	**38.570878**	**-4.079795**
		LAZ-30	20		38.479194	-4.099110		
		LAZ-31	11		38.419124	-4.055679		
19	Alcudia antiform East	LAZ-27	17		38.667264	-3.844700		
		LAZ-28A	5	**36**	38.391691	-3.506867	**38.4804**	**-3.621601**
		LAZ-28B	14		38.382246	-3.513236		
	Sites with no current data	LAZ-13	0		39.48233	-3.901171		
		LAZ-17	0		39.186741	-4.497643		
		LAZ-25	0		39.137726	-4.119040		
		SCS-01	0		41.203131	-2.904855		
		SCS-05	0		41.172006	-3.405019		

Coordinates of data collection sites and calculated average coordinate for paleoflow roses plotted in Fig. 5. n = number of data for each field site; **N** = total number of data plotted on each amalgam paleocurrent rose. Number of data (n) were not weighted in determining average coordinates for groups of sites excepting the exclusion of sites with no data.

Table A-2 Paleocurrent field data and calculated paleoflow azimuths, Armorican Quartzite, Iberian Massif

Site No.	Indicator	S_0		L_C / S_0 - S_F Intersection		S_F		P-Flow Direction	Calculated Azimuth
		Strike	Dip	Plunge	Trend	Strike	Dip		
CZ-01	Ripples	302	59	11	107			SSW	212
	Ripples	294	62	53	074			NW	344
	Ripples	293	68	48	313			SW	278
	Foreset Traces	299	62	32	313			SW	264
	Foreset Traces	302	62	25	315			SW	257
	Foresets	317	68	17	324	306	45	SW	255
	Foresets	304	68	57	085	342	58	SE	156
	Foresets	303	72	32	111	315	57	SSW	200
	Foresets	313	65	45	106	322	59	S	184
	Foresets	307	67	16	314	304	59	SW	250
	Foresets	318	80	23	134	331	55	SW	211
	Foresets	300	69	54	088	332	57	SE	169
	Foresets	291	78	22	106	308	47	S	201
	Foresets	287	70	07	290	284	52	SSW	223
	Foresets	299	78	05	118	302	50	SW	224
	Foresets	285	71	20	098	293	54	SSW	189
	Foresets	291	72	42	094	304	61	SE	181
	Foresets	285	65	11	100	288	54	SSW	214
	Foresets	258	62	60	012	290	60	E	129
	Foresets	292	71	24	103	306	49	S	198
	Foresets	288	72	45	089	311	56	SE	176
	Foresets	292	71	46	091	316	56	SE	176
	Foresets	288	66	10	293	285	54	SW	235
	Foresets	290	74	20	104	298	56	SSW	203

Site No.	Indicator	S_0		L_C / S_0 - S_F Intersection		S_F		P-Flow Direction	Calculated Azimuth
		Strike	Dip	Plunge	Trend	Strike	Dip		
CZ-01 continued	Foresets	296	73	26	108	308	54	SSW	201
	Foresets	295	68	48	089	308	60	SE	175
	Foresets	288	67	42	086	306	54	SE	178
	Foresets	286	72	53	080	324	56	SE	166
CZ-02	Ripples	297	73	18	114			SW	210
	Ripples	297	73	32	309			SW	262
	Ripples	297	73	07	112			SW	220
	Ripples	117	88	32	116			SW	195
	Ripples	117	88	15	120			SW	213
	Ripples	117	88	10	295			SW	237
	Ripples	288	83	20	110			SSW	208
	Ripples	282	86	11	285			SSW	234
	Ripples	285	88	06	288			SW	233
	Ripples	098	84	28	107			SW	197
	Ripples	283	83	30	103			SSW	194
	Ripples	283	83	80	346			SW	132
	Ripples	098	82	59	098			SW	227
	Foresets	126	75	64	273	148	68	NW	282
	Foresets	129	88	30	308	302	80	SW	260
	Foresets	129	88	08	129	312	71	SW	225
	Foresets	306	88	13	306	303	75	SW	242
	Foresets	122	89	24	302	296	78	SSW	253
	Foresets	092	79	65	247	067	90	SE	095
	Foresets	091	87	09	091	273	80	SSW	171
	Foresets	093	85	03	273	272	78	SSW	161

Site No.	Indicator	S_0		L_C / S_0 - S_F Intersection		S_F		P-Flow Direction	Calculated Azimuth
		Strike	Dip	Plunge	Trend	Strike	Dip		
CZ-02 continued	Foresets	282	85	31	099	291	71	SSE	195
	Foresets	102	86	26	104	292	74	SW	193
	Foresets	104	80	19	107	292	77	SW	186
	Foresets	106	81	22	110	298	70	SW	189
	Foresets	106	84	18	108	294	72	SW	184
	Foresets	104	83	20	107	287	89	SSW	186
	Foresets	115	81	13	293	118	69	NNE	334
	Foresets	102	86	09	103	285	75	SW	176
	Foresets	096	80	21	100	284	79	SW	190
	Foresets	114	83	37	289	281	80	SE	130
	Foresets	094	89	00	094	274	77	S	166
	Foresets	275	87	80	078	258	90	WNW	249
	Foresets	110	83	28	286	283	84	S	140
	Foresets	302	90	83	302	256	85	WNW	311
	Foresets	302	90	09	122	304	77	SW	223
CZ-03	Ripples	241	56	28	033			NW	292
	Ripples	247	43	08	059			Symmetric	326
									146
	Ripples	236	53	14	045			SE	128
	Ripples	211	54	51	307			SW	215
	Sand Wave	239	48	10	049			Symmetric	135
									315
	Foresets	321	89	21	321	155	58	NE	072
	Foresets	240	42	27	274	259	63	NE	012
	Foresets	352	83	16	354	349	73	WNW	278

Site No.	Indicator	S_0		L_C / S_0 - S_F Intersection		S_F		P-Flow Direction	Calculated Azimuth
		Strike	Dip	Plunge	Trend	Strike	Dip		
CZ-03 continued	Foresets	352	83	47	360	326	63	NW	310
	Foresets	238	57	04	055	237	68	NW	313
	Foresets	205	48	30	354	186	70	WSW	253
	Foresets	240	48	20	041	235	56	NE	302
	Foresets	226	30	05	037	222	47	NW	306
	Foresets	233	46	20	033	229	52	NW	295
	Foresets	228	42	34	277	246	53	NE	015
	Foresets	234	50	41	281	258	66	NE	023
	Foresets	235	51	34	268	247	62	NNE	011
	Foresets	203	55	25	222	210	66	NW	304
	Foresets	202	52	41	339	183	65	W	236
	Foresets	202	54	27	224	189	42	SE	146
CZ-04	Ripples	046	37	31	187			W	088
	Ripples	052	49	16	212			WNW	297
	Ripples	048	36	24	087			S	183
	Ripples	052	44	38	162			SW	247
	Ripples	041	24	14	194			WNW	281
	Ripples	040	32	30	115			SSW	207
	Ripples	037	41	39	132			SW	221
	Ripples	051	39	36	114			SSW	209
	Ripples	043	36	34	150			SW	237
	Ripples	050	21	12	087			Symmetric	359
									179
	Channel*	052	47	44	168	072	35	Symmetric	167
						075	44		347

Site No.	Indicator	S_0		L_C / S_0 - S_F Intersection		S_F		P-Flow Direction	Calculated Azimuth
		Strike	Dip	Plunge	Trend	Strike	Dip		
CZ-04 continued	Foreset Traces	051	38	21	083			Bidirectional	359
									179
	Foresets	066	42	16	084	055	30	NNE	000
	Foresets	098	32	07	109	068	10	NE	021
	Foresets	083	39	35	143	050	35	NE	059
	Foresets	071	37	27	114	093	55	SW	210
	Foresets	342	35	33	050	305	34	N	324
	Foresets	064	34	19	095	052	27	NNE	010
	Foresets	006	37	32	131	058	33	SW	210
	Foresets	067	46	45	142	055	45	NE	056
	Foresets	067	46	23	092	037	28	NE	057
	Foresets	082	40	38	150	064	38	ENE	065
	Foresets	037	33	33	131	078	39	SW	220
	Foresets	067	36	27	202	147	32	NW	286
	Foresets	052	42	26	199	108	26	WNW	281
	Foresets	036	36	28	169	072	28	SW	253
	Foresets	065	40	24	212	053	52	SE	115
	Foresets	067	37	09	079	056	22	NNW	352
	Foresets	038	32	05	210	042	23	NW	299
	Foresets	052	41	33	184	125	37	WSW	266
	Foresets	036	39	20	063	307	22	NW	339
	Foresets	044	39	11	210	050	30	NW	296
	Foresets	045	37	09	058	037	25	WNW	331
	Foresets	052	39	24	086	028	28	NNE	003

Site No.	Indicator	S_0		L_C / S_0 - S_F Intersection		S_F		P-Flow Direction	Calculated Azimuth
		Strike	Dip	Plunge	Trend	Strike	Dip		
CZ-05	Ripples	058	54	04	054			SE	141
	Ripples	033	52	27	192			E	090
	Ripples	031	50	09	203			NW	289
	Ripples	035	47	32	191			NW	265
	Ripples	033	54	12	209			NW	291
	Ripples	028	50	17	198			NW	280
	Ripples	035	46	09	199			SE	107
	Foresets	050	55	22	066	054	62	SSE	162
	Foresets	050	50	23	209	042	62	ESE	103
	Foresets	300	14	14	019	241	20	WNW	287
	Foresets	218	11	09	343	189	20	NNE	075
	Foresets	020	12	07	054	245	33	NW	323
	Foresets	320	09	08	020	217	25	WNW	292
	Foresets	224	14	00	043	223	37	NW	313
	Foresets	227	04	02	009	193	33	WNW	283
	Foresets	295	14	14	014	213	37	WNW	282
	Foresets	036	54	43	173	038	53	SW	248
	Foresets	034	47	18	196	029	56	ESE	099
	Foresets	236	23	17	010	212	39	WNW	280
	Foresets	237	25	22	356	213	34	WSW	264
	Foresets	207	31	14	003	193	54	WSW	272
	Foresets	206	40	27	244	221	53	NW	347
	Foresets	243	07	05	283	270	19	NNE	013

Site No.	Indicator	S_0		L_C / S_0 - S_F Intersection		S_F		P-Flow Direction	Calculated Azimuth
		Strike	Dip	Plunge	Trend	Strike	Dip		
GCZ-01	Ripples	131	48	06	303			NE	030
	Ripples	318	45	04	132			SW	220
	Ripples	318	41	15	332			SW	247
	Ripples	102	33	07	111			Symmetric	022
									202
	Ripples	306	45	09	117			SW	206
	Foresets	131	48	03	308	134	29	NE	031
	Foresets	118	33	07	129	122	45	SW	222
	Foresets	312	50	12	122	304	81	NE	026
	Foresets	130	22	15	170	150	37	W	261
	Foresets	130	22	16	174	155	41	W	263
	Foresets	130	22	11	160	028	15	NE	071
	Foresets	109	28	02	286	107	59	SW	195
	Foresets	107	33	02	111	108	42	SW	201
	Foresets	122	32	17	151	137	51	SW	243
	Foresets	317	41	34	007	286	34	WNW	283
	Foresets	137	21	08	296	119	71	SW	205
	Foresets	309	44	04	313	283	08	SW	243
	Foresets	315	31	00	135	318	04	SW	225
	Foresets	299	48	02	117	305	15	SW	207
	Foresets	288	32	02	291	121	11	SW	205
	Foresets	303	46	06	117	335	10	SW	207
	Foresets	299	40	16	099	319	24	SW	185
	Foresets	125	32	06	295	120	51	SW	203

Site No.	Indicator	S_0		L_C / S_0 - S_F Intersection		S_F		P-Flow Direction	Calculated Azimuth
		Strike	Dip	Plunge	Trend	Strike	Dip		
GCZ-02	Ripples	113	49	14	282			SW	186
	Ripples	120	52	13	288			SW	192
	Ripples	109	52	16	116			SW	216
	Foresets	132	57	16	143	124	42	NE	061
	Foresets	118	44	24	146	126	53	SW	244
GCZ-03	Ripples	145	40	05	316			NE	045
	Ripples	162	39	04	164			SE	256
	Ripples	162	39	04	329			NE	059
	Ripples	134	40	10	142			SW	237
	Ripples	124	58	24	143			SW	244
	Ripples	140	43	38	202			NW	298
	Ripples	140	38	12	298			SW	205
	Ripples	138	39	16	304			SW	117
	Ripples	141	44	07	145			SW	239
	Ripples	143	40	10	311			SW	217
	Ripples	127	24	21	280			SW	184
	Ripples	118	61	30	150			Symmetric	070 250
	Foresets	131	63	09	307	290	28	NE	031
	Foresets	112	60	12	285	123	35	NE	008
GCZ-04	Foresets	098	45	45	181	118	48	W	273
	Foresets	102	45	13	115	106	55	SW	210
	Foresets	111	30	12	269	241	24	N	356
	Foresets	134	47	28	284	122	60	SSW	184
	Foresets	134	47	12	303	126	75	SW	208

Site No.	Indicator	S_0		L_C / S_0 - S_F Intersection		S_F		P-Flow Direction	Calculated Azimuth
		Strike	Dip	Plunge	Trend	Strike	Dip		
GCZ-04 continued	Foresets	114	40	15	133	128	72	SW	228
	Foresets	093	77	07	095	094	85	S	190
	Foresets	102	68	03	281	101	84	SSW	189
	Foresets	098	48	00	098	278	82	S	188
	Foresets	093	32	01	095	094	52	S	185
	Foresets	103	53	11	275	100	64	S	179
	Foresets	088	32	32	170	130	44	WSW	262
	Foresets	071	38	13	233	116	15	NW	319
	Foresets	081	34	11	245	075	47	SE	152
	Foresets	080	32	13	101	092	55	SSW	195
	Foresets	078	32	25	210	122	25	NW	295
	Foresets	092	26	17	130	110	41	SW	213
	Foresets	096	24	08	115	107	47	SW	207
	Foresets	094	30	26	150	114	39	SW	244
GCZ-05	Ripples	125	65	33	289			Symmetric	018
									198
	Ripples	207	17	15	274			S	184
	Ripples	229	34	21	273			S	185
	Foresets	274	50	49	346	218	55	WSW	253
	Foresets	282	55	55	017	252	60	WNW	262
	Foresets	127	70	02	306	306	84	SW	232
	Foresets	234	40	29	275	163	31	SW	190
	Foresets	263	59	59	344	235	60	WSW	245
	Foresets	286	87	28	104	302	60	SSE	150
	Foresets	125	84	00	125	305	77	SSW	234

Site No.	Indicator	S_0		L_C / S_0 - S_F Intersection		S_F		P-Flow Direction	Calculated Azimuth
		Strike	Dip	Plunge	Trend	Strike	Dip		
GCZ-06	Foresets	118	52	04	295	130	16	NE	013
	Foresets	121	27	05	131	126	46	SW	222
GCZ-07	Ripples	161	87	60	336			NE	009
	Ripples	161	87	62	336			NE	009
	Ripples	161	87	62	332			NE	011
	Ripples	161	87	58	336			NE	009
	Ripples	161	87	62	336			NE	013
	Ripples	128	72	19	134			NE	038
	Foresets	152	88	44	330	163	77	NE	018
	Foresets	152	88	52	155	143	81	NE	114
	Foresets	152	88	07	332	153	80	NE	055
	Foresets	148	87	48	325	162	75	NE	010
	Foresets	148	87	30	326	157	72	NE	028
	Foresets	148	87	22	327	160	60	NE	036
	Foresets	128	76	22	302	139	54	NE	015
	Foresets	132	70	02	311	133	48	NE	040
	Foresets	136	83	14	138	127	54	NE	060
GCZ-08	Ripples	216	57	11	032			NW	295
	Ripples	234	50	54	341			NE	054
	Ripples	234	50	51	342			NE	055
	Ripples	234	50	36	017			SE	094
	Ripples	234	50	35	024			SE	099
	Ripples	223	59	39	006			W	261
	Ripples	223	59	38	026			SE	092
	Ripples	216	57	12	032			SE	114

Site No.	Indicator	S_0		L_C / S_0 - S_F Intersection		S_F		P-Flow Direction	Calculated Azimuth
		Strike	Dip	Plunge	Trend	Strike	Dip		
GCZ-08 continued	Ripples	216	57	29	012			NW	269
	Ripples	209	68	23	024			Bidirectional	096
									276
	Ripples	231	52	26	042			Symmertric	115
									295
	Foresets	210	75	43	015	204	81	NW	255
	Foresets	210	75	30	021	207	80	NW	269
GCZ-09	Ripples	173	71	10	350			NE	073
		173	71	11	349			NE	071
		173	71	09	352			NE	074
		173	71	02	352			NE	081
	Ripples	190	75	31	359			NE	067
		190	75	47	350			NE	050
	Ripples	178	73	08	357			ENE	080
	Ripples	192	77	13	195			SE	115
		192	77	16	195			SE	118
	Ripples	148	68	00	328			NE	058
	Ripples	148	68	22	325			NE	036
	Ripples	162	71	17	333			NE	053
	Ripples	201	87	24	207			SE	135
	Ripples	201	87	16	207			SE	135
	Ripples	171	68	62	218			NW	332
	Ripples	171	75	27	349			NE	054
	Ripples	174	70	16	181			Symmertric	101
									281

GCZ-09 continued	Ripples	174	70	33	342			Symmertric	039 219
Site No.	Indicator	S_0		L_C / S_0 - S_F Intersection		S_F		P-Flow Direction	Calculated Azimuth
		Strike	Dip	Plunge	Trend	Strike	Dip		
GCZ-10	Ripples	129	29	08	288			NE	017
	Ripples	140	32	19	297			NE	021
	Ripples	127	26	07	141			NE	052
	Slump Folds	008	16	18	065			NW	337
	Foresets	330	10	02	340	162	34	SW	250
		330	10	02	141	139	37	SW	231
	Foresets	145	47	24	300	160	35	NE	021
		145	47	45	254	177	46	NW	338
		145	47	18	308	184	21	NE	030
		145	47	14	312	286	30	NE	036
IBR-01	Ripples	046	30	14	068			SSE	226
	Ripples	357	46	29	140			NE	041
	Ripples	008	29	06	015			NW	287
	Ripples	007	32	06	018			NW	290
	Ripples	009	58	38	157			SW	231
	Ripples	031	34	20	066			NNW	341
	Ripples	014	44	40	097			N	008
	Ripples	027	34	30	101			Symmetric	013 193
	Ripples	012	50	11	184			ESE	089
	Foreset traces	007	36	09	176			W	263
	Foresets	001	52	23	020	350	40	NW	275
	Foresets	352	54	45	126	030	45	W	263

Site No.	Indicator	S_0		L_C / S_0 - S_F Intersection		S_F		P-Flow Direction	Calculated Azimuth
		Strike	Dip	Plunge	Trend	Strike	Dip		
IBR-01 continued	Foresets	358	54	04	175	001	35	W	164
	Foresets	007	46	16	171	014	36	W	278
	Foresets	353	67	54	028	342	62	NW	239
	Foresets	008	36	14	167	019	26	SW	277
	Foresets	006	36	16	029	342	21	NW	277
IBR-02	Ripples	357	30	27	078			N	356
	Ripples	008	29	14	017			NW	301
	Ripples	031	29	29	121			NE	036
	Ripples	011	30	27	097			N	015
	Ripples	012	20	06	034			NW	311
	Foresets	038	19	19	127	098	35	SW	217
	Foresets	018	30	28	086	036	35	S	183
	Foresets	030	27	03	205	028	40	SE	119
	Foresets	016	34	18	166	032	25	WSW	255
	Foresets	054	37	05	227	052	46	SE	136
	Foresets	355	39	31	044	013	50	SE	152
	Foresets	004	37	37	104	317	54	NE	020
	Foresets	006	35	30	062	288	39	NW	345
	Foresets	042	02	01	188	184	15	WNW	284
	Foresets	061	40	03	064	059	27	NNW	336
	Foresets	066	36	04	240	074	17	NW	328
	Foresets	057	51	18	222	084	26	NW	307
	Foresets	356	40	39	070	031	52	SE	173
	Foresets	030	25	02	206	037	10	NW	300
	Foresets	058	40	22	210	084	26	NW	296

Site No.	Indicator	S_0		L_C / S_0 - S_F Intersection		S_F		P-Flow Direction	Calculated Azimuth
		Strike	Dip	Plunge	Trend	Strike	Dip		
IBR-02 continued	Foresets	035	44	10	045	020	22	NW	322
	Foresets	037	46	13	204	050	28	NW	293
	Foresets	057	30	17	090	015	18	NE	002
	Foresets	057	38	08	227	064	25	NW	313
IBR-03 A	Ripples	349	44	38	093			S	181
	Channel*	346	36	05	348	344	52		352
						337	24		172
	Foresets	352	30	28	060	046	66	SE	153
	Foresets	353	43	03	356	340	10	W	268
	Foresets	348	60	00	168	156	01	W	260
	Foresets	162	35	06	334	154	86	SW	245
	Foresets	336	47	14	349	322	28	WSW	266
	Foresets	337	42	13	352	313	20	WSW	268
	Foresets	332	43	06	339	314	15	SW	254
	Foresets	342	42	13	357	322	22	W	273
	Foresets	352	35	02	169	355	20	WSW	260
	Foresets	340	61	24	146	334	72	NE	049
	Foresets	328	49	34	112	317	58	NE	019
	Foresets	327	34	13	347	334	46	ENE	083
	Foresets	339	40	10	351	316	17	WSW	266
	Foresets	350	33	01	352	346	13	SW	263
	Foresets	352	34	02	169	357	15	WSW	260
	Foresets	352	34	17	145	339	52	NE	051
	Foresets	346	36	04	351	218	05	WSW	263
	Foresets	351	41	34	023	004	55	ESE	124

Site No.	Indicator	S_0		L_C / S_0 - S_F Intersection		S_F		P-Flow Direction	Calculated Azimuth
		Strike	Dip	Plunge	Trend	Strike	Dip		
IBR-03 A continued	Foresets	351	41	02	354	346	17	ESE	086
IBR-03 B	Ripples	133	21	17	197			W	278
	Sand Wave	145	41	24	182			W	276
	Foreset traces	133	34	27	172			W	272
	Foreset traces	124	36	28	171			W	272
	Foreset traces	135	42	27	177			W	273
	Foresets	186	35	24	226	164	27	SE	137
	Foresets	173	33	02	350	172	45	W	247
	Foresets	162	40	10	174	168	60	WSW	261
	Foresets	163	37	07	173	157	25	E	078
	Foresets	176	40	06	349	174	50	WSW	239
	Foresets	142	35	11	305	134	53	SW	220
	Foresets	143	40	14	160	151	58	SW	255
	Foresets	113	44	42	180	152	62	WNW	291
	Foresets	137	42	35	267	184	35	NNW	349
	Foresets	146	37	16	169	155	51	SW	262
	Foresets	154	32	17	305	194	18	NE	034
	Foresets	162	31	04	169	164	40	SW	252
	Foresets	148	33	29	268	125	43	S	170
	Foresets	144	38	24	179	157	50	W	274
	Foresets	159	44	22	184	119	24	SW	277
	Foresets	162	45	11	331	200	14	NE	049
IBR-04	Ripples	270	80	02	091			S	161
	Ripples	277	75	10	090			S	153

Site No.	Indicator	S_0		L_C / S_0 - S_F Intersection		S_F		P-Flow Direction	Calculated Azimuth
		Strike	Dip	Plunge	Trend	Strike	Dip		
IBR-04 continued	Ripples	278	83	25	288			SSW	195
	Ripples	264	84	06	267			S	167
	Ripples	264	86	19	082			NNW	324
	Ripples	271	40	14	272			N	357
	Ripples	098	86	19	275			Symmetric	001
									181
	Ripples	098	86	20	273			N	002
	Ripples	096	84	51	102			NE	078
	Ripples	094	82	18	270			S	177
	Ripples	097	78	13	272			N	356
	Ripples	102	85	72	154			NNW	293
	Foresets	272	75	33	082	082	90	NW	311
	Foresets	273	80	66	070	252	89	NW	273
	Foresets	270	75	33	280	259	61	SW	195
	Foresets	272	75	02	091	273	54	S	161
	Foresets	114	83	40	288	272	72	SE	167
	Foresets	249	82	15	251	077	70	NNW	346
	Foresets	093	78	14	270	097	64	N	355
	Foresets	114	65	38	136	099	53	NE	076
	Foresets	108	80	23	112	102	67	NE	059
LAZ-01	Ripple Crest	328	86	59	132			SW	178
	Ripple Crest	312	77	18	117			NE	021
	Foresets	297	66	24	105	290	80	NE	000
LAZ-02	Ripples	111	71	23	274			S	174
	Ripples	112	76	25	276			S	174

Site No.	Indicator	S_0		L_C / S_0 - S_F Intersection		S_F		P-Flow Direction	Calculated Azimuth
		Strike	Dip	Plunge	Trend	Strike	Dip		
LAZ-02 continued	Ripples	106	68	20	270			S	171
	Ripples	134	72	35	293			S	184
	Ripples	094	57	30	252			S	147
	Ripples	091	51	26	265			S	157
	Ripples	093	69	27	253			S	151
LAZ-03	Ripples	142	37	13	152			SW	239
	Ripples	113	61	15	121			SSW	219
	Ripples	097	37	20	124			S	220
	Ripples	133	52	11	303			SW	199
	Ripples	132	86	73	282			S	136
LAZ-04	Ripples	141	36	35	298			N	013
	Ball and pillow	246	52	29	250			S	182
	Foresets	233	56	35	261	242	65	N	007
LAZ-05	Ripples	332	58	45	011			E	119
	Foresets	002	57	10	175	357	80	ENE	080
	Foresets	352	62	43	022	003	71	SE	133
		352	61	59	058	008	65	SE	160
	Foresets	331	65	32	348	343	82	ESE	097
	Foresets	334	63	41	001	349	77	SE	112
	Foresets	328	56	48	016	004	79	SE	121
	Foresets	350	57	21	005	359	76	ESE	106
LAZ-06	Ripples	072	24	14	208			ESE	116
	Ripples	013	53	38	054			SE	156
	Ripples	070	24	05	244			NW	332

Site No.	Indicator	S_0		L_C / S_0 - S_F Intersection		S_F		P-Flow Direction	Calculated Azimuth
		Strike	Dip	Plunge	Trend	Strike	Dip		
LAZ-06 continued	Ripples	072	25	15	202			NW	291
	Ripples	035	34	29	149			SW	236
	Ripples	041	22	06	216			NW	304
	Ripples	359	49	39	113			NE	018
	Ripples	043	35	26	127			NE	038
	Ball and pillow	003	40	06	169			E	078
	Foresets	347	65	61	110	326	72	NE	012
	Foresets	003	39	27	143	336	67	NE	046
LAZ-07	Ripples	295	21	15	063			NW	333
	Ripples	326	17	02	132			NE	042
	Ripples	337	15	04	135			NE	044
	Ripples	354	02	01	138			NE	048
	Foresets	335	27	01	153	334	46	NE	062
	Foresets	304	28	28	026	353	44	SE	119
	Foresets	011	07	03	166	351	31	ENE	074
LAZ-08	Ripples	172	70	60	338			NE	022
		172	70	63	312			NE	012
		172	64	57	303			NE	013
		172	64	64	338			NE	018
	Ripples	190	84	56	006			E	044
	Ripples	142	67	59	198			NW	305
	Ripples	161	72	14	327			NE	053
	Ripples	144	72	16	312			NE	035
	Ripples	152	58	49	296			NE	004
	Ripples	164	80	61	334			NE	013

Site No.	Indicator	S_0		L_C / S_0 - S_F Intersection		S_F		P-Flow Direction	Calculated Azimuth
		Strike	Dip	Plunge	Trend	Strike	Dip		
LAZ-08 continued	Ripples	164	80	69	299				001
	Foresets	182	80	48	351	192	72	NE	043
	Foresets	016	83	11	017	200	76	SE	117
	Foresets	153	72	14	328	157	59	NE	048
	Herring bone	352	84	73	152	152	90	NNE	008
LAZ-09	Ripples	012	32	07	018			NW	294
	Ripples	016	35	10	180			W	270
	Ripples	007	36	08	176			W	268
	Ripples	082	18	14	164			Symmetric	075 255
	Ripples	124	26	20	171			ENE	080
	Ripples	007	25	16	166			NE	075
	Ripples	358	31	15	155			NE	067
	Ripples	000	21	17	153			NE	064
	Ripples	012	29	12	157			NE	069
	Ripples	123	43	13	150			Symmetric	062 242
	Ripples	102	21	19	168			Symmetric	077 257
	Ripples	098	15	10	156			SW	249
	Foresets	042	31	28	159	354	64	NE	070
	Foresets	097	47	03	274	253	08	N	000
LAZ-10	Mega ripple	038	15	08	064			SE	153
	Mega ripple	000	10	05	064			NW	334
	Ripples	293	40	24	064			SE	150

Site No.	Indicator	S_0		L_C / S_0 - S_F Intersection		S_F		P-Flow Direction	Calculated Azimuth
		Strike	Dip	Plunge	Trend	Strike	Dip		
LAZ-10 continued	Ripples	000	10	04	067			NW	337
	Ripples	258	07	02	294			Symmetric	024
									204
	Ripples	258	07	01	281			NE	011
	Ripples	258	07	05	292			NE	023
	Ripples	265	10	06	294			NE	025
	Ripples	265	10	05	297			NE	028
	Ripples	265	10	05	314			NE	044
	Ripples	278	07	01	088			SW	178
	Ripples	278	07	06	306			SW	217
	Ripples	259	05	03	009			E	099
	Ripples	284	14	02	288			NE	018
	Ripples	316	18	02	315			NE & SW	045
									225
	Ripples	277	19	13	306			NE	038
	Ripples	273	18	03	284			NNE	015
	Ripples	257	20	02	259			SE	170
	Ripples	287	16	06	313			NE	044
	Ripples	280	13	08	305			SW	216
	Ripples	273	11	09	327			SW	238
	Ripples	288	09	06	337			NE	067
	Ripples	271	11	01	089			SSE	179
	Foresets	250	09	08	307	304	71	NE	038
	Foresets	287	10	03	305	301	38	NE	035
	Foresets	287	20	08	085	276	36	NNW	354

Site No.	Indicator	S_0		L_C / S_0 - S_F Intersection		S_F		P-Flow Direction	Calculated Azimuth
		Strike	Dip	Plunge	Trend	Strike	Dip		
LAZ-11	Ripples	170	74	35	186			Symmetric	118
									298
	Ripples	170	74	28	190			Symmetric	113
									293
	Foresets	156	77	61	180	004	88	NW	310
	Foresets	154	80	63	174	002	86	NW	308
	Foresets	153	80	60	171	356	87	NW	305
	Foresets	158	87	68	166	001	84	NW	316
	Foresets	170	74	23	343	338	78	SW	236
	Foresets	157	69	03	158	155	45	NE	070
	Foresets	156	73	63	299	180	66	NNW	357
	Foresets	150	75	33	320	163	59	NE	026
LAZ-12	Foresets	292	56	45	070	324	46	SE	144
	Foresets	301	45	45	027	330	50	SE	118
	Foresets	292	56	55	038	312	55	SE	121
	Foresets	296	39	18	092	050	26	S	176
	Foresets	270	54	37	057	301	40	SE	132
	Foresets	295	42	15	312	287	32	SW	228
	Foresets	136	88	16	315	141	71	NE	030
	Foresets	293	78	07	295	115	86	NE	030
	Foresets	126	85	56	299	155	68	NW	340
	Foresets	158	70	70	254	192	72	NW	340
	Ripples	281	52	51	046				122
									302
LAZ-13	NO CURRENT DATA								

Site No.	Indicator	S_0		L_C / S_0 - S_F Intersection		S_F		P-Flow Direction	Calculated Azimuth
		Strike	Dip	Plunge	Trend	Strike	Dip		
LAZ-14	Ripples	287	36	34	347			SW	262
	Ripples	294	45	43	009			W	271
	Foresets	107	51	48	173	154	74	W	280
	Foresets	124	51	16	137	134	79	SW	237
	Foresets	136	90	33	316	278	47	SW	179
		136	90	52	316	288	70	SE	161
	Foresets	288	56	06	104	103	81	NE	012
LAZ-15	Ripples	295	75	74	062			NW	307
	Ripples	295	75	74	050			NW	305
	Ripples	295	75	67	078			NW	336
	Ripples	296	77	70	087			NW	335
	Ripples	296	77	69	073			NW	333
	Ripples	296	77	64	326			NW	276
	Foresets	332	39	24	006	254	26	WNW	280
	Foresets	313	25	13	102	296	45	NNE	010
	Foresets	283	55	41	066	297	48	SE	149
	Foresets	286	19	09	077	269	39	NW	348
	Foresets	274	38	14	076	266	54	NW	346
	Foresets	314	34	15	111	303	52	NE	017
LAZ-16	Ripples	314	63	44	342			NE	085
	Ripples	314	63	53	004			E	111
	Ripples	285	65	14	297			SW	213
	Ripples	318	63	20	330			Symmetric	071 251
	Ripples	318	63	26	334			Symmetric	078

Site No.	Indicator	S_0		L_C / S_0 - S_F Intersection		S_F		P-Flow Direction	Calculated Azimuth
		Strike	Dip	Plunge	Trend	Strike	Dip		
LAZ-16 continued									258
	Ripples	297	62	39	318			NE	070
	Ripples	282	69	21	293			NE	035
	Ripples	297	68	41	310			NE	069
	Ripples	293	64	29	098			NNE	351
	Ripples	303	73	27	317			symmetric	063
									243
	Scour	308	66	43	105			NE	350
	Scour	303	73	57	100			N	333
LAZ-17	NO CURRENT DATA								
LAZ-18-A	Ripples	107	46	21	136			SW	232
	Ripples	112	70	61	178			Bidirectional	101
									281
	Ripples	114	66	32	142			SW	245
	Ripples	134	55	12	136			SW	222
	Ripples	134	55	04	312			Symmetric	207
									027
	Climbing Ripples	130	55	28	156			NE	066
	Climbing Ripples	130	55	30	156			NE	067
	Climbing Ripples	130	55	21	145			NE	054
	Scour	142	49	47	250			SE	154
LAZ-19	Ripples	149	63	27	318			SW	210
	Foresets	147	62	05	324	149	47	NE	051
LAZ-20	Ripples	149	63	27	318			NE	030

Site No.	Indicator	S_0		L_C / S_0 - S_F Intersection		S_F		P-Flow Direction	Calculated Azimuth
		Strike	Dip	Plunge	Trend	Strike	Dip		
LAZ-20 continued	Ripples	333	44	38	047			Symmetric	140 320
	Ripples	329	59	16	337			SW	257
	Foresets	342	73	40	357	180	86	SE	114
	Foresets	342	72	21	155	152	83	NE	050
	Foresets	332	61	02	333	333	86	NE	064
LAZ-21	Ripples	288	66	55	050			NW	306
	Ripples	284	59	53	054			NW	307
	Ripples	292	67	44	086			NNW	332
	Ripples	272	55	54	028			NW	287
	Ripples	270	54	50	028			NW	288
	Riiples	276	55	53	014			Symmetric	281 101
	Ripples	274	60	59	004			W	274
	Ripples	272	54	50	036			NW	293
	Ripples	276	55	45	032			NW	294
	Ripples	250	52	41	032			NW	297
	Ripples	249	53	51	030			NW	279
	Ripples	282	62	52	068			NW	313
	Ripples	267	65	55	037			Symmetric	109 279
	Ripples	244	59	45	281			NE	030
	Ripples	264	60	33	290			NE	035
	Ripples	256	64	60	013			NW	269
	Ripples	256	64	52	316			SW	238

Site No.	Indicator	S_0		L_C / S_0 - S_F Intersection		S_F		P-Flow Direction	Calculated Azimuth
		Strike	Dip	Plunge	Trend	Strike	Dip		
LAZ-21 continued	Ripples	275	54	50	352			SE	087
	Ripples	248	47	22	037			SE	121
	Ripples	274	52	45	036			WNW	296
	Ripples	271	61	35	063			NW	317
	Ripples	259	62	48	057			SE	118
	Channel	284	59	39	312			NW	331
	Foresets	247	56	43	286	267	71	NE	032
LAZ-22-A	Ripples	131	47	01	130			NE	041
		131	47	15	143			NE	060
	Ripples	117	52	41	155			NE	080
	Ripples	112	48	18	129			Symmetric	047
									227
	Ripples	120	59	17	126			SW	228
	Ripples	119	60	19	134			SW	233
LAZ-22-B	Ripples	130	64	21	295			NNE	015
		130	64	27	140			NE	068
	Ripples	127	62	29	292			NW	347
LAZ-23	Ripples	302	85	02	308			NE	035
	Ripples	312	71	05	314			NE	047
	Ripples	290	81	51	100			NE	048
	Ripples	310	90	30	307			NE	070
		320	87	15	147			NE	035
	Ripples	132	87	86	142			NW	308
	Ripples	282	72	15	289			symmetric	208
									028

Site No.	Indicator	S_0		L_C / S_0 - S_F Intersection		S_F		P-Flow Direction	Calculated Azimuth
		Strike	Dip	Plunge	Trend	Strike	Dip		
LAZ-23 continued		282	72	49	306			symmetric	065 245
	Ripples	284	67	31	297			symmetric	047 227
	Ripples	117	88	86	210			NW	297
	Ripples	114	89	87	202			WNW	294
	Ripples	113	86	75	176			SW	286
LAZ-24	Ripples	332	52	41	016			E	119
	Ripples	326	55	32	352			E	096
		320	47	20	119			NE	011
	Ripples	319	62	29	125			NE	017
		319	62	20	124			NE	014
	Ripples	307	48	45	061			NW	314
	Ripples	308	50	12	121			NE	024
	Ripples	317	52	33	098			NNE	358
	Ripples	308	54	06	122			NE	030
	Ripples	297	55	15	106			symmetric	008 188
	Ripples	326	49	14	131			NE	036
	Forsets	334	74	58	002	302	62	NW	306
	Forsets	338	56	56	060	288	63	NW	334
LAZ-25	NO CURRENT DATA								
LAZ-26	Ripples	116	78	04	294			NE	026
	Ripples	126	59	22	142			NE	063

Site No.	Indicator	S_0		L_C / S_0 - S_F Intersection		S_F		P-Flow Direction	Calculated Azimuth
		Strike	Dip	Plunge	Trend	Strike	Dip		
LAZ-26 continued	Ripples	126	59	33	284			SW	175
	Ripples	134	61	15	303			NE	021
	Ripples	132	77	24	142			NE	065
	Ripples	126	62	07	130			NE	044
	Ripples	118	66	14	296			NE	016
	Ripples	118	80	21	292			NE	007
	Ripples	140	76	14	144			SW	249
	Ripples	118	60	05	125			NE	040
	Ripples	114	63	22	123			NE	052
	Ripples	108	63	32	125			NE	064
	Ripples	122	62	17	133			SW	234
	Ripples	111	57	22	121			Symmetric	052 232
	Ripples	106	64	15	284			NE	011
	Ripples	106	52	20	267			NE	356
	Ripples	085	59	06	106			NE	034
	Ripples	112	65	37	115			NE	065
	Ball and Pillow	107	74	32	111			NE	060
LAZ-27	Ripples	202	24	10	232			SE	143
	Ripples	352	06	06	060			NW	329
	Ripples	182	10	06	341			NE	071
	Ripples	204	16	04	204			NW	295
	Ripples	202	16	04	200			NW	291
	Ripples	200	17	04	198			NW	289
	Ripples	153	22	09	177			SW	269

Site No.	Indicator	S_0		L_C / S_0 - S_F Intersection		S_F		P-Flow Direction	Calculated Azimuth
		Strike	Dip	Plunge	Trend	Strike	Dip		
LAZ-27 continued	Ripples	157	10	08	231			Symmetric	142 322
	Ripples	173	08	05	231			NW	321
	Ripples	104	14	05	145			NE	056
	Ripples	142	20	07	152			NE	063
	Ripples	122	07	02	140			NE	050
	Ripples	050	25	20	200			NW	293
	Ripples	071	12	09	246			NW	337
	Channel			06	339			NW	339
LAZ-28 A	Ripples	309	70	51	102			NW	353
	Ripples	283	69	52	072			NW	330
	Ripples	283	68	49	077			NW	334
	Ripples	287	74	60	044			NW	311
	Ripples	292	70	65	035			NW	305
LAZ-28 B	Ripples	110	59	00	110			NE	017
	Ripples	110	59	55	208			NW	273
	Ripples	110	57	46	240			NW	306
	Ripples	110	57	09	116			NE	013
	Ripples	109	60	60	199			WNW	277
	Ripples	093	58	12	266			NW	346
	Ripples	093	52	30	113			NE	033
	Ripples	090	60	36	118			NE	040
	Ripples	095	59	27	111			NE	029
	Ripples	097	57	54	208			SE	104
	Ripples	097	57	21	106			NW	022

Site No.	Indicator	S_0		L_C / S_0 - S_F Intersection		S_F		P-Flow Direction	Calculated Azimuth
		Strike	Dip	Plunge	Trend	Strike	Dip		
LAZ-28 B continued	Ripples	083	53	39	120			NW	044
	Ripples	099	58	49	233			SW	121
	Channel	118	73	34	136			NW	322
LAZ-29	Ripples	132	42	36	186			Symmetric	104
									284
	Ripples	120	40	26	144			NE	067
	Ripples	120	40	27	252			NW	339
		120	40	08	288			N	018
	Ripples	140	48	04	143			NE	049
	Ripples	130	41	07	144			NE	055
	Ripples	096	34	19	242			NW	334
	Ripples	111	43	16	136			NE	058
	Ripples	118	46	11	133			NE	052
	Ripples	114	42	17	132			NE	055
	Ripples	097	42	00	097			Symmetric	017
									197
	Ball and Pillow	085	21	06	117			NE	032
	Slump fold	088	29	04	282			N	015
	Slump fold	078	22	07	091			N	006
	Foresets	139	40	30	182	101	30	WSW	099
	Foresets	139	40	39	211	110	39	WSW	114
	Foresets	131	42	42	221	062	22	WNW	311

Site No.	Indicator	S_0		L_C / S_0 - S_F Intersection		S_F		P-Flow Direction	Calculated Azimuth
		Strike	Dip	Plunge	Trend	Strike	Dip		
LAZ-30	Ripples	311	73	20	122			NE	019
	Ripples	311	73	53	342			NW	280
	Ripples	133	70	21	136			NE	064
	Ripples	133	70	64	222			NW	313
	Ripples	193	30	14	345			NE	072
	Ripples	193	30	14	211			SE	125
	Ripples	129	40	12	143			NE	003
	Ripples	293	72	24	310			NE	051
	Ripples	297	69	20	321			NE	055
	Ripples	114	62	18	282			NNE	003
	Ripples	114	62	60	227			NW	305
	Ripples	117	66	11	292			NE	015
	Ripples	103	52	18	114			Bidirectional	034 114
	Ripples	099	50	14	107			NE	025
	Ripples	112	53	05	117			NE	029
	Ripples	103	61	06	280			NNE	006
	Foresets	296	70	25	106	304	57	S	179
LAZ-31	Ripples	254	50	30	283			NE	025
	Ripples	254	50	20	260			NW	003
	Ripples	250	45	30	287			NE	026
	Ripples	250	45	20	049			NW	311
	Ripples	246	64	35	267			N	016
	Ripples	297	61	33	320			NE	066
	Ripples	301	23	02	305			NE	035

Site No.	Indicator	S_0		L_C / S_0 - S_F Intersection		S_F		P-Flow Direction	Calculated Azimuth
		Strike	Dip	Plunge	Trend	Strike	Dip		
LAZ-31 continued	Ripples	238	54	29	262			NW	005
	Ripples	232	66	41	254			NW	008
	Ripples	065	09	02	079			NW	349
	Ripples	353	14	10	011			ESE	103
LAZ-33	Ripples	092	53	04	265			N	005
	Ripples	332	77	24	140			NE	036
	Ripples	099	82	68	251			NNW	298
	Ripples	078	62	15	087			N	005
	Ripples	087	51	23	107			NE	027
	Ripples	079	77	21	247			N	326
	Ripples	091	70	12	097			NE	014
	Ripples	080	76	20	084			N	010
	Ripples	081	65	08	257			NNW	342
	Ripples	081	85	20	258			NW	331
	Ripples	079	65	14	253			NW	334
	Ripples	073	60	09	249			NW	333
	Slump fold	090	62	18	267			SSE	163
LAZ-34	Ripples	138	20	07	292			Symmetric	023
									203
	Ripples	136	28	26	256			SE	165
	Ripples	126	26	10	286			NE	016
	Ripples	119	30	29	208			WNW	282
		119	30	15	261			NW	351
	Ripples	114	18	13	161			NE	075
	Ripples	139	22	15	261			SE	171

Site No.	Indicator	S_0		L_C / S_0 - S_F Intersection		S_F		P-Flow Direction	Calculated Azimuth
		Strike	Dip	Plunge	Trend	Strike	Dip		
LAZ-34 continued	Ripples	139	22	16	267			N	357
	Ripples	119	20	14	233			SE	144
	Ripples	138	30	25	260			NW	349
	Ripples	138	30	27	226			SE	138
	Ripples	124	24	11	244			NW	295
	Ripples	130	26	24	239			NW	300
	Ripples	095	21	19	169			NE	084
	Ripples	122	23	11	146			NE	060
LAZ-35	Ripples	120	42	33	172			NE	089
	Ripples	110	39	34	247			Symmetric	147 327
	Ripples	103	46	22	123			NE	042
	Ripples	104	35	33	200			ESE	099
	Sand Wave	090	28	15	127			NE	040
	Sand Wave	093	44	37	140			NE	060
	Foresets	108	46	36	153	092	40	ENE	073
	Foresets	108	36	34	221	089	42	SE	127
	Foresets	122	75	50	141	097	60	ENE	085
LAZ-36	Ripples	310	85	07	312			NE	047
	Ripples	103	86	12	277			NNE	001
	Ripples	105	88	16	275			N	358
	Ripples	273	85	18	277			N	021
	Ripples	121	64	20	294			N	010
	Foresets	105	75	37	273	097	85	SSE	156
	Foresets	114	85	09	115	296	82	SW	213

Site No.	Indicator	S_0		L_C / S_0 - S_F Intersection		S_F		P-Flow Direction	Calculated Azimuth
		Strike	Dip	Plunge	Trend	Strike	Dip		
SCS-01	NO CURRENT DATA								
SCS-02 A	Ripples	163	53	16	331			SW	243
	Ripples	168	66	17	341			SW	247
	Ripples	165	72	06	343			SW	258
	Ripples	166	64	06	345			SW	260
	Foresets	196	79	38	205	172	55	SE	135
	Foresets	196	79	44	207	184	68	SE	141
	Foresets	196	79	17	199	187	55	SE	117
	Foresets	192	86	18	011	204	55	ENE	081
	Foresets	192	86	03	192	190	55	SE	101
	Foresets	164	66	40	186	179	82	WNW	308
	Foresets	152	62	23	165	157	72	WSW	288
	Foresets	168	59	35	323	157	71	SW	222
SCS-02 B	Ripples	193	30	15	342			Symmetric	252
								Symmetric	072
	Ripples	188	40	05	175			W	272
	Ripples	184	59	05	174			E	091
	Ripples	182	59	44	332			SW	225
	Ripples	182	54	04	002			E	092
	Ripples	188	40	10	195			ESE	109
	Ripples	151	42	13	167			NNE	095
	Ripples	342	51	15	150			Symmetric	049
									229
	Ripples	343	53	12	153			Symmetric	054
									234

Site No.	Indicator	S_0		L_C / S_0 - S_F Intersection		S_F		P-Flow Direction	Calculated Azimuth
		Strike	Dip	Plunge	Trend	Strike	Dip		
SCS-02 B continued	Ripples	339	49	07	150			NE	055
	Ripples	346	55	29	147			SW	216
	Ripples	336	61	12	148			SW	220
	Foresets	176	66	23	345	183	54	NE	066
	Foresets	165	72	30	334	183	50	NE	054
	Foresets	165	72	15	170	003	50	WNW	275
	Foresets	185	60	34	342	174	73	SW	236
SCS-03	Ripples	177	69	08	356			W	263
	Foresets	180	76	05	359	357	73	WSW	267
	Foresets	183	66	32	347	168	88	SW	249
	Foresets	168	75	16	344	172	63	ENE	071
SCS-04	NO CURRENT DATA								
SCS-05 A	Ripples	251	11	01	252			NNW	343
	Foresets	335	10	10	068	260	40	NW	333
	Foresets	314	10	10	054	244	45	NW	341
	Foresets	228	21	19	293	262	34	NE	034
	Foresets	256	23	16	034	240	33	NW	301
	Foresets	193	12	07	229	221	41	NW	317
	Foresets	202	09	02	011	194	29	WNW	274
	Foresets	225	10	00	044	224	40	NW	309
	Foresets	198	07	05	239	232	33	NW	328
SCS-05 B	Foresets	319	16	07	344	339	54	ENE	070
	Foresets	333	68	67	044	309	67	NW	318
	Foresets	337	56	25	138	330	67	NE	027

Site No.	Indicator	S_0		L_C / S_0 - S_F Intersection		S_F		P-Flow Direction	Calculated Azimuth
		Strike	Dip	Plunge	Trend	Strike	Dip		
SCS-05 B continued	Foresets	202	37	17	226	220	71	NW	314
	Foresets	318	55	12	327	323	73	NE	059
	Foresets	326	53	33	117	317	62	NNE	011
WALZ-01	Ripples	246	62	15	062			SE	141
	Ripples	222	78	02	040			NW	310
	Ripples	222	62	09	041			NW	304
	Ripples	223	73	17	037			NW	295
	Foresets	246	65	20	056	053	82	NNW	314
	Foresets	242	67	43	265	223	54	SW	200
	Foresets	241	73	14	245	066	87	NW	346
	Foresets	246	71	39	262	232	58	SW	198
	Foresets	239	76	11	242	062	89	NW	340
	Foresets	246	62	15	254	250	75	NNW	353
	Foresets	244	64	00	244	244	75	NW	334
	Foresets	261	87	31	263	248	67	SW	202
	Foresets	229	64	35	029	212	86	NW	279
	Foresets	225	60	29	244	237	78	NNW	349
	Foresets	133	02	02	223	222	59	NW	313
	Foresets	226	63	61	341	210	67	SW	238
	Foresets	225	70	38	242	232	78	N	356
	Foresets	233	72	12	237	236	86	NW	336
	Foresets	226	67	24	035	215	90	NW	290
	Foresets	224	72	04	043	042	81	NW	310
	Foresets	223	70	11	227	217	48	SE	145
	Foresets	226	77	41	237	234	86	NNW	358

Site No.	Indicator	S_0		L_C / S_0 - S_F Intersection		S_F		P-Flow Direction	Calculated Azimuth
		Strike	Dip	Plunge	Trend	Strike	Dip		
WALZ-01	Foresets	226	76	37	035	215	90	WNW	278
continued	Foresets	219	78	62	242	231	84	NNE	013
WALZ-02	Ripples	327	85	03	320			Symmetric	239
									059
	Ripples	317	85	21	321			Symmetric	068
									248
	Ripples	123	90	19	303			SSW	194
	Ripples	303	81	66	321			Symmetric	280
									100
	Ripples	132	86	03	308			NE	039
	Ripples	126	89	08	127			Symmetric	224
									044
	Ripples	135	86	09	311			SW	215
	Ripples	128	90	19	218			Symmetric	128
									308
	Ripples	315	82	19	130			SW	205
	Foresets	162	77	16	338	335	79	WSW	236
	Foresets	327	85	20	329	158	66	NE	077
	Foresets	327	85	62	336	264	63	NW	299
	Foresets	148	86	49	153	335	88	WNW	287
	Foresets	318	89	31	137	130	78	NE	017
	Foresets	120	86	22	298	294	79	SSW	188
	Foresets	130	88	16	131	318	65	SW	216
	Foresets	314	90	38	134	321	81	SSW	262
	Foresets	308	90	32	128	315	79	SSW	186

Site No.	Indicator	S_0		L_C / S_0 - S_F Intersection		S_F		P-Flow Direction	Calculated Azimuth
		Strike	Dip	Plunge	Trend	Strike	Dip		
WALZ-02 continued	Foresets	313	86	05	133	314	74	SW	218
	Foresets	311	81	23	315	306	70	SW	244
	Foresets	321	87	47	138	128	81	NNE	004
	Foresets	314	89	14	314	312	81	SSW	218
	Foresets	134	85	20	312	309	81	SSW	204
WALZ-03	Ripples	278	41	11	308			N	038
	Ripples	278	41	11	091			NE	356
	Ripples	131	81	23	305			SW	197
	Ripples	133	74	39	291			SW	179
	Ripples	137	75	25	307			SW	201
	Ripples	122	83	32	297			SSW	180
	Ripples	128	82	38	301			NNE	359
	Foresets	288	35	11	304	264	17	SW	217
WALZ-04	Ripples	075	51	35	111			NE	033
	Ripples	066	48	42	122			NE	041
	Ripples	063	50	32	092			S	195
	Ripples	065	49	36	102			SSW	205
	Ripples	068	57	41	103			SSW	210
	Ripples	062	58	29	094			S	194
	Ripples	072	59	28	085			S	192
	Ripples	067	60	33	090			S	196
	Ripples	075	59	36	107			S	212
	Foresets	076	46	01	255	077	31	NW	345
	Foresets	066	56	11	073	062	44	NNW	349
	Foresets	069	54	38	104	034	40	NE	029

Site No.	Indicator	S_0		L_C / S_0 - S_F Intersection		S_F		P-Flow Direction	Calculated Azimuth
		Strike	Dip	Plunge	Trend	Strike	Dip		
WALZ-04 continued	Foresets	065	52	38	102	080	64	SW	206
	Foresets	070	54	03	248	073	31	NW	336
WALZ-05	Ripples	003	61	45	163			SW	226
	Ripples	107	44	12	125			SW	218
	Sand Wave	106	36	21	142			SW	237
	Foresets	003	66	12	009	358	50	WNW	286
	Foresets	142	54	21	306	151	42	NE	026
	Foresets	139	25	14	171	154	40	WSW	264
	Foresets	349	66	05	167	352	45	WSW	254
WALZ-06	Ripples	156	66	09	165			SW	258
	Ripples	155	63	01	333			SW	243
	Foresets	172	54	26	331	161	71	SW	229
WALZ-07	Ripples	172	37	14	336			SW	241
	Ripples	177	35	11	341			SW	248
	Ripples	165	47	03	342			NE	071
	Ripples	161	43	19	327			SW	228
	Ripples	157	36	33	230			NW	323
	Ripples	157	39	08	327			SW	234
	Ripples	162	36	14	325			SW	230
	Ripples	167	38	09	332			Symmetric	240
	Ripples	168	36	04	343			SW	251
	Ripples	171	41	10	177			Symmetric	272
	Ripples	166	38	15	185			W	280
	Ripples	193	33	25	342			E	064
	Ripples	192	33	08	198			NW	291

Site No.	Indicator	S_0		L_C / S_0 - S_F Intersection		S_F		P-Flow Direction	Calculated Azimuth
		Strike	Dip	Plunge	Trend	Strike	Dip		
WALZ-07 continued	Foresets	193	33	04	007	190	53	WNW	276
	Foresets	163	40	17	322	154	55	SW	226
	Foresets	199	39	31	331	301	50	ENE	054
	Foresets	167	39	13	184	175	57	W	278

S_0—Bedding plane; S_F—Foreset plane; L_C—lineation of channel, ripple crest, etc. Unshaded rows in column 4 are field measurements (L_C). Shaded areas in column 4 are calculated (e.g. S_0-S_F intersections, intersections of channel flanks).
*Lineation of channel calculated from intersection of measured channel flanks.

Table A-3 Detrital zircon sample collection sites, Armorican Quartzite, Iberian Massif

Sample name	Location				
	UTM			Lat	Lon
	zone	mN	mW	(decimal ºN)	(decimal ºW)
WALZ-01	29T	703832	4825044	43.550505	6.476648
WALZ-02	29T	706120	4746062	42.839361	6.477806
CZ-02	30T	265832	4748083	42.849649	5.866177
GCZ-03	29T	716967	4643822	41.916555	6.383698
GCZ-06	29T	705423	4697465	42.402317	6.503861
IBR-02	30T	658862	4559139	41.168032	1.106298
SCS-05	30T	492304	4555057	41.146795	3.091712
LAZ-26	30S	408153	4282951	38.690409	4.056089
LAZ-05	30S	328823	4353994	39.318430	4.985692

Table A-4 Minor element geochemistry for the Armorican Quartzite of the Iberian Massif

		CZ-02	WALZ-01	WALZ-02	IBR-2	GC-03	GCZ-06	SCS-05	LAZ-05	LAZ-26
V	(ppm)	15.5	16.8	11.1	12.5	15.1	22	35.2	19.5	23.1
Cr	(ppm)	260.9	152.5	245.2	198.6	186.3	104.3	-0.1	206	198.9
Co	(ppm)	1.7	2	1.8	2.6	2.4	2.7	51.7	2.8	4.2
Ni	(ppm)	4.6	7.8	6	4.3	4.4	5.3	5	24.1	15.1
Cu	(ppm)	0.7	3.4	2.9	1.7	2.6	1.8	3.7	8.1	8
Zn	(ppm)	3.2	6.9	3.4	3.4	7	7.4	10.2	6.3	9.5
Ga	(ppm)	0.7	3.7	0.6	0.9	1.4	1.9	6.5	3.3	3.1
Rb	(ppm)	2.8	46.5	3.2	7.2	9.5	14.3	59.8	5.6	12.6
Sr	(ppm)	39.4	38.3	1.5	10.9	6.5	10.1	35.7	4.4	29.5
Y	(ppm)	6.5	11.1	6	3.9	6.6	12.1	22.7	9.4	8.6
Zr	(ppm)	193.3	104.2	117.8	202.4	211.6	627.3	569.4	58.4	174.3
Nb	(ppm)	3.6	4.1	3.8	3.9	3.5	8.2	11.9	4	6.6
Ba	(ppm)	94.3	619.3	35.4	170.8	95.1	134.9	542.5	43.8	155.4
La	(ppm)	20.3	20	17.2	19.3	22.4	26.6	47.5	14.2	25.2
Pb	(ppm)	7.9	33	7.8	7.6	15.6	11.7	40.8	8.5	10.2
Th	(ppm)	6.3	8.3	7	6.4	5.3	12.4	23	6.5	8.6
U	(ppm)	2.6	2	2.7	5.1	1.1	3.1	1	5.3	0.7
Ce	(ppm)	52.5	62.4	45.3	52.6	56.9	57.5	88.3	38.7	61.5
Nd	(ppm)	8.3	10.8	3.9	7.5	12.6	19.9	39.6	0.2	11.8
Cs	(ppm)	1.7	0	2.4	1.6	3.7	3.7	3.5	3.8	2.7

Note: SuperQ quantitative analysis of pressed powders conducted using a Phillips PW2400 spectrometer at the Regional Geochemical Centre, St Mary's University, Halifax, Nova Scotia B3H 3C3.

Table A-5 LA-ICP MS U-Pb analysis and results for detrital zircons from the Armorican Quartzite of the Iberian Massif

Sample WALZ-01	Isotopic ratios and 2σ (%) errors						Ages and 2σ absolute errors (Ma)						Reported Age		
Analysis	$^{206}Pb/^{238}U$	±2σ	$^{207}Pb/^{235}U$	±2σ	$^{207}Pb/^{206}Pb$	±2σ	$^{206}Pb/^{238}U$	±2σ	$^{207}Pb/^{235}U$	±2σ	$^{207}Pb/^{206}Pb$	±2σ	Age (Ma)	±2σ	conc %
b44	0.0871	1.51	0.7086	5.16	0.0590	4.94	538	8	544	22	567	107	**539**	**8**	95
a59	0.0909	2.13	0.7418	4.30	0.0592	3.73	561	11	563	19	574	81	**561**	**11**	98
c29	0.0935	1.74	0.7612	3.92	0.0591	3.51	576	10	575	17	570	76	**576**	**10**	101
a6	0.0939	1.37	0.7560	3.55	0.0584	3.28	578	8	572	16	545	72	**578**	**7**	106
c13	0.0938	1.47	0.7846	3.45	0.0606	3.12	578	8	588	16	627	67	**579**	**8**	92
a19	0.0956	1.99	0.7987	4.32	0.0606	3.83	589	11	596	20	625	83	**589**	**11**	94
b8	0.0959	2.15	0.7789	3.98	0.0589	3.35	591	12	585	18	563	73	**590**	**12**	105
a35	0.0958	1.35	0.8063	3.25	0.0610	2.95	590	8	600	15	640	63	**591**	**8**	92
c25	0.0968	1.61	0.8021	2.48	0.0601	1.90	596	9	598	11	607	41	**596**	**9**	98
a48	0.0976	1.81	0.7989	3.41	0.0594	2.88	600	10	596	15	581	63	**600**	**10**	103
c30	0.0990	1.45	0.8120	2.66	0.0595	2.23	609	8	604	12	584	49	**608**	**8**	104
b12	0.1002	1.40	0.8223	3.82	0.0595	3.56	616	8	609	18	586	77	**615**	**8**	105
c6	0.1005	1.25	0.8247	2.37	0.0595	2.01	618	7	611	11	585	44	**617**	**7**	106
c1	0.1008	1.53	0.8314	3.91	0.0598	3.59	619	9	614	18	597	78	**619**	**9**	104
a55	0.1013	1.23	0.8465	3.15	0.0606	2.90	622	7	623	15	625	63	**622**	**7**	99
c5	0.1025	1.23	0.8371	2.96	0.0592	2.69	629	7	618	14	575	58	**628**	**7**	109
b19	0.1031	2.29	0.8686	6.24	0.0611	5.80	633	14	635	30	642	125	**633**	**14**	99
b58	0.1048	1.77	0.8857	3.76	0.0613	3.32	643	11	644	18	650	71	**643**	**11**	99
b37	0.1052	1.74	0.8822	2.36	0.0608	1.59	645	11	642	11	634	34	**644**	**10**	102
a32	0.1056	1.27	0.8749	3.67	0.0601	3.44	647	8	638	18	606	75	**647**	**8**	107
c24	0.1085	1.23	0.9023	3.00	0.0603	2.74	664	8	653	15	615	59	**663**	**8**	108
c3	0.1094	1.68	0.9129	3.44	0.0605	3.00	669	11	659	17	623	65	**668**	**11**	107
c17	0.1096	1.42	0.9137	2.36	0.0605	1.88	671	9	659	12	620	41	**668**	**9**	108
b20	0.1092	1.51	0.9410	2.97	0.0625	2.56	668	10	673	15	691	54	**669**	**9**	97
b11	0.1098	1.46	0.9233	2.86	0.0610	2.46	671	9	664	14	639	53	**670**	**9**	105
b7	0.1097	1.43	0.9212	3.29	0.0609	2.96	671	9	663	16	635	64	**671**	**9**	106
a22	0.1119	1.92	0.9398	3.48	0.0609	2.90	684	12	673	17	636	62	**682**	**12**	108
a53	0.1119	1.29	0.9643	3.71	0.0625	3.48	684	8	685	19	691	74	**684**	**8**	99
a16	0.1137	0.86	0.9649	3.53	0.0616	3.42	694	6	686	18	659	73	**694**	**6**	105
b60	0.1140	1.61	0.9618	3.33	0.0612	2.92	696	11	684	17	646	63	**694**	**10**	108
c14	0.1142	1.34	0.9783	2.75	0.0621	2.41	697	9	693	14	679	51	**697**	**9**	103
a38	0.1156	1.46	0.9760	2.41	0.0612	1.92	705	10	692	12	647	41	**702**	**10**	109
c19	0.1152	1.36	0.9897	5.82	0.0623	5.66	703	9	699	30	685	121	**703**	**9**	103

Sample WALZ-01 continued	Isotopic ratios and 2σ (%) errors						Ages and 2σ absolute errors (Ma)						Reported Age		
	$^{206}Pb/^{238}U$	±2σ	$^{207}Pb/^{235}U$	±2σ	$^{207}Pb/^{206}Pb$	±2σ	$^{206}Pb/^{238}U$	±2σ	$^{207}Pb/^{235}U$	±2σ	$^{207}Pb/^{206}Pb$	±2σ	Age (Ma)	±2σ	conc %
a13	0.1164	1.63	0.9917	3.51	0.0618	3.11	710	11	700	18	667	67	**708**	**11**	106
b33	0.1176	3.49	1.0184	6.45	0.0628	5.42	717	24	713	34	703	115	**716**	**23**	102
b3	0.1176	1.79	1.0051	4.11	0.0620	3.70	717	12	706	21	674	79	**716**	**12**	106
b31	0.1184	1.38	1.0231	2.42	0.0627	1.99	721	9	715	12	698	42	**720**	**9**	103
b23	0.1202	1.88	1.0389	4.68	0.0627	4.29	732	13	723	25	698	91	**731**	**13**	105
c34	0.1223	0.72	1.0970	2.08	0.0650	1.95	744	5	752	11	776	41	**745**	**5**	96
a44	0.1252	1.88	1.0815	4.18	0.0627	3.74	760	13	744	22	697	80	**758**	**13**	109
c40	0.1263	0.96	1.1207	2.80	0.0643	2.63	767	7	763	15	753	56	**767**	**7**	102
a3	0.1270	1.19	1.1261	2.74	0.0643	2.47	771	9	766	15	752	52	**770**	**9**	102
a5	0.1270	1.73	1.1332	2.54	0.0647	1.86	771	13	769	14	765	39	**770**	**12**	101
a34	0.1274	1.46	1.1526	2.91	0.0656	2.52	773	11	778	16	795	53	**774**	**10**	97
a41	0.1315	1.20	1.1633	2.10	0.0642	1.72	796	9	783	12	747	36	**793**	**9**	107
c37	0.1256	1.74	1.1403	2.76	0.0658	2.15	763	13	773	15	801	45	**795**	**12**	95
c18	0.1325	0.67	1.1962	5.07	0.0655	5.03	802	5	799	28	789	106	**802**	**5**	102
b10	0.1322	1.73	1.2113	2.34	0.0664	1.58	801	13	806	13	820	33	**803**	**12**	98
b32	0.1329	1.45	1.2016	2.67	0.0656	2.24	804	11	801	15	793	47	**804**	**11**	101
c28	0.1330	2.25	1.2179	5.06	0.0664	4.53	805	17	809	29	820	95	**805**	**17**	98
b9	0.1358	1.51	1.2287	4.31	0.0656	4.04	821	12	814	24	794	85	**821**	**12**	103
c38	0.1397	1.54	1.2880	3.33	0.0669	2.95	843	12	840	19	834	62	**842**	**12**	101
a26	0.1426	1.30	1.3079	2.48	0.0665	2.11	859	10	849	14	823	44	**857**	**10**	104
a11	0.1438	2.16	1.3573	4.22	0.0685	3.63	866	18	871	25	882	75	**867**	**17**	98
a49	0.1528	1.07	1.5061	1.99	0.0715	1.68	917	9	933	12	971	34	**920**	**9**	94
a12	0.1567	2.10	1.4735	2.80	0.0682	1.33	938	11	920	11	875	28	**926**	**11**	107
a23	0.1589	1.59	1.5863	5.29	0.0724	5.05	951	14	965	33	998	103	**951**	**14**	95
a43	0.1605	1.76	1.5674	4.08	0.0708	3.69	960	16	957	26	952	75	**959**	**15**	101
c20	0.1605	1.30	1.6092	4.39	0.0727	4.19	959	12	974	28	1006	85	**960**	**12**	95
a37	0.1618	2.08	1.5783	2.68	0.0708	1.69	967	19	962	17	950	35	**963**	**16**	102
b17	0.1662	2.61	1.5834	3.73	0.0691	2.66	991	24	964	23	902	55	**977**	**24**	110
a24	0.1646	1.96	1.6300	3.04	0.0718	2.32	982	18	982	19	981	47	**982**	**17**	100
a10	0.1655	1.65	1.6267	3.33	0.0713	2.89	988	15	981	21	965	59	**986**	**15**	102
a50	0.1669	0.80	1.6871	1.92	0.0733	1.74	995	7	1004	12	1023	35	**996**	**7**	97
a60	0.1680	1.80	1.6818	3.23	0.0726	2.69	1001	17	1002	21	1003	55	**1001**	**16**	100
c2	0.1689	3.00	1.7048	6.74	0.0732	6.03	1006	28	1010	44	1020	122	**1007**	**27**	99
a27	0.1720	2.41	1.6833	3.34	0.0710	2.31	1023	23	1002	22	957	47	**1010**	**23**	107
b18	0.1686	2.83	1.7412	3.70	0.0749	2.38	1004	26	1024	24	1066	48	**1011**	**26**	94

Sample WALZ-01 continued	Isotopic ratios and 2σ (%) errors						Ages and 2σ absolute errors (Ma)						Reported Age		
	$^{206}Pb/^{238}U$	±2σ	$^{207}Pb/^{235}U$	±2σ	$^{207}Pb/^{206}Pb$	±2σ	$^{206}Pb/^{238}U$	±2σ	$^{207}Pb/^{235}U$	±2σ	$^{207}Pb/^{206}Pb$	±2σ	Age (Ma)	±2σ	conc %
b6	0.1700	1.61	1.7124	3.21	0.0730	2.77	1012	15	1013	21	1015	56	**1013**	**15**	100
c35	0.1713	0.96	1.7065	2.32	0.0722	2.11	1019	9	1011	15	993	43	**1018**	**9**	103
b24	0.1718	1.61	1.6957	3.12	0.0716	2.67	1022	15	1007	20	974	55	**1018**	**15**	105
c27	0.1710	1.18	1.7441	2.44	0.0740	2.14	1018	11	1025	16	1041	43	**1019**	**11**	98
c32	0.1715	1.99	1.7237	5.48	0.0729	5.10	1021	19	1017	36	1011	103	**1020**	**19**	101
b43	0.1723	1.37	1.7189	2.30	0.0724	1.85	1025	13	1016	15	996	38	**1021**	**12**	103
a20	0.1705	3.16	1.7842	4.48	0.0759	3.19	1015	30	1040	30	1092	64	**1027**	**30**	93
b1	0.1773	2.20	1.7486	3.50	0.0715	2.10	1052	18	1027	18	973	43	**1041**	**18**	108
b13	0.1757	1.53	1.7605	4.02	0.0727	3.72	1043	15	1031	26	1005	75	**1042**	**14**	104
a56	0.1764	2.71	1.7724	4.17	0.0729	3.18	1048	26	1035	27	1010	64	**1042**	**24**	104
c9	0.1766	2.01	1.7766	2.87	0.0730	2.04	1048	19	1037	19	1013	41	**1042**	**18**	103
b2	0.1755	1.37	1.8176	2.38	0.0751	1.95	1042	13	1052	16	1072	39	**1045**	**13**	97
b5	0.1766	2.41	1.7713	4.84	0.0727	4.20	1048	23	1035	32	1007	85	**1045**	**22**	104
b56	0.1771	1.49	1.7840	2.49	0.0731	1.99	1051	15	1040	16	1016	40	**1047**	**14**	104
a33	0.1747	1.90	1.8345	2.30	0.0761	0.97	1038	16	1058	13	1099	19	**1052**	**16**	94
a8	0.1777	1.21	1.7746	3.78	0.0724	3.58	1054	12	1036	25	998	73	**1053**	**12**	106
a21	0.1758	2.53	1.8343	3.32	0.0757	2.14	1044	24	1058	22	1086	43	**1054**	**21**	96
b34	0.1773	1.57	1.8326	2.67	0.0750	2.16	1052	15	1057	18	1067	43	**1054**	**14**	99
b15	0.1775	1.74	1.8528	2.82	0.0757	2.23	1053	17	1064	19	1087	45	**1057**	**16**	97
c12	0.1836	1.28	1.8314	2.98	0.0723	2.69	1087	13	1057	20	995	55	**1057**	**20**	109
b50	0.1814	1.46	1.8720	1.92	0.0748	1.24	1075	15	1071	13	1064	25	**1072**	**13**	101
c10	0.1820	1.43	1.8282	2.70	0.0728	2.29	1078	14	1056	18	1010	46	**1072**	**14**	107
c23	0.1817	1.12	1.8184	2.84	0.0726	2.61	1076	11	1052	19	1003	53	**1073**	**15**	107
b35	0.1827	1.62	1.8812	3.87	0.0747	3.51	1082	16	1074	26	1060	71	**1080**	**16**	102
a29	0.1827	1.80	1.8764	4.93	0.0745	4.59	1082	18	1073	33	1055	92	**1081**	**18**	103
a31	0.1834	0.71	1.8635	2.10	0.0737	1.97	1085	7	1068	14	1033	40	**1084**	**7**	105
b4	0.1837	1.07	1.8745	2.83	0.0740	2.62	1087	11	1072	19	1042	53	**1085**	**11**	104
b57	0.1850	2.87	1.9035	5.08	0.0746	4.19	1094	29	1082	34	1058	84	**1090**	**27**	103
a14	0.1855	1.87	1.9425	2.62	0.0760	1.83	1097	19	1096	18	1094	37	**1096**	**17**	100
a9	0.1868	1.66	1.9599	3.73	0.0761	3.34	1104	17	1102	25	1097	67	**1104**	**16**	101
a52	0.1927	2.33	2.0462	3.36	0.0770	2.41	1136	24	1131	23	1121	48	**1133**	**22**	101
b49	0.2018	1.76	2.1979	3.04	0.0790	2.48	1185	19	1180	21	1172	49	**1183**	**18**	101
b48	0.2067	2.53	2.3101	4.24	0.0811	3.40	1211	28	1215	31	1223	67	**1213**	**26**	99
b36	0.2088	2.01	2.3130	3.06	0.0803	2.31	1222	22	1216	22	1205	46	**1219**	**20**	101
b14	0.2364	1.11	2.8515	2.10	0.0875	1.78	1368	14	1369	16	1371	34	**1368**	**13**	100

Sample WALZ-01 continued	Isotopic ratios and 2σ (%) errors						Ages and 2σ absolute errors (Ma)						Reported Age		
	$^{206}Pb/^{238}U$	±2σ	$^{207}Pb/^{235}U$	±2σ	$^{207}Pb/^{206}Pb$	±2σ	$^{206}Pb/^{238}U$	±2σ	$^{207}Pb/^{235}U$	±2σ	$^{207}Pb/^{206}Pb$	±2σ	Age (Ma)	±2σ	conc %
a17	0.2389	2.39	3.0332	5.10	0.0921	4.51	1381	30	1416	40	1469	86	**1389**	**28**	94
c7	0.2451	1.95	2.9207	3.19	0.0864	2.52	1413	25	1387	24	1348	49	**1399**	**25**	105
a46	0.3427	1.32	5.2023	2.70	0.1101	2.35	1900	22	1853	23	1801	43	**1801**	**43**	105
a51	0.3184	1.99	4.9239	2.58	0.1122	1.65	1782	31	1806	22	1835	30	**1835**	**30**	97
a25	0.3514	1.38	5.4743	2.11	0.1130	1.59	1941	23	1897	18	1848	29	**1848**	**29**	105
b55	0.3136	1.09	5.0795	2.89	0.1175	2.68	1759	17	1833	25	1918	48	**1918**	**48**	92
b40	0.3386	1.17	5.5086	2.45	0.1180	2.16	1880	19	1902	21	1926	39	**1926**	**39**	98
b52	0.3259	1.61	5.3102	2.39	0.1182	1.76	1818	26	1871	21	1929	32	**1929**	**32**	94
a15	0.3695	1.66	6.0236	3.46	0.1182	3.04	2027	29	1979	31	1930	54	**1930**	**54**	105
c33	0.3495	1.80	5.7298	3.18	0.1189	2.62	1932	30	1936	28	1940	47	**1940**	**47**	100
b41	0.3400	1.21	5.5775	2.00	0.1190	1.59	1887	20	1913	17	1941	28	**1941**	**28**	97
b38	0.3786	1.16	6.3978	1.93	0.1225	1.54	2070	21	2032	17	1994	27	**1994**	**27**	104
a7	0.3475	1.52	5.9766	2.08	0.1247	1.43	1923	25	1972	18	2025	25	**2025**	**25**	95
b21	0.3525	2.08	6.1553	2.68	0.1266	1.70	1947	35	1998	24	2052	30	**2052**	**30**	95
b59	0.4060	1.43	7.0977	3.24	0.1268	2.90	2197	27	2124	29	2054	51	**2054**	**51**	107
b45	0.3969	2.08	7.0081	2.88	0.1281	2.00	2155	38	2112	26	2072	35	**2072**	**35**	104
b26	0.3596	1.70	6.3656	2.13	0.1284	1.29	1980	29	2028	19	2076	23	**2076**	**23**	95
a42	0.4361	1.84	8.0919	2.61	0.1346	1.86	2333	36	2241	24	2158	32	**2158**	**32**	108
b28	0.3991	1.39	7.5474	2.24	0.1372	1.76	2165	26	2179	20	2192	31	**2192**	**31**	99
a58	0.4139	1.56	8.7465	3.36	0.1533	2.98	2233	30	2312	31	2383	51	**2383**	**51**	94
c39	0.4639	1.34	10.3529	1.61	0.1619	0.88	2457	27	2467	15	2475	15	**2475**	**15**	99
a47	0.4862	1.54	11.2205	1.92	0.1674	1.15	2554	32	2542	18	2532	19	**2532**	**19**	101
c15	0.4697	1.10	10.8601	1.77	0.1677	1.39	2482	23	2511	17	2535	23	**2535**	**23**	98
c4	0.4963	1.44	11.9447	1.79	0.1746	1.06	2598	31	2600	17	2602	18	**2602**	**18**	100
a36	0.4563	1.43	10.9845	1.71	0.1746	0.95	2423	29	2522	16	2602	16	**2602**	**16**	93
a57	0.5189	0.85	12.5053	1.50	0.1748	1.24	2695	19	2643	14	2604	21	**2604**	**21**	103
b51	0.4742	0.83	11.4401	1.71	0.1750	1.50	2502	17	2560	16	2606	25	**2606**	**25**	96
a30	0.5028	1.48	12.1519	2.39	0.1753	1.87	2626	32	2616	23	2609	31	**2609**	**31**	101
a1	0.5197	1.71	12.5906	2.32	0.1757	1.56	2698	38	2650	22	2613	26	**2613**	**26**	103
c22	0.4898	1.20	11.8990	1.42	0.1762	0.76	2570	26	2596	13	2617	13	**2617**	**13**	98
a28	0.5480	1.69	13.3899	2.17	0.1772	1.37	2817	39	2708	21	2627	23	**2627**	**23**	107
a39	0.4913	1.62	12.0841	2.04	0.1784	1.23	2576	35	2611	19	2638	20	**2638**	**20**	98
b22	0.4827	1.59	11.9154	1.83	0.1790	0.92	2539	33	2598	17	2644	15	**2644**	**15**	96
a40	0.5362	1.57	13.3638	2.30	0.1808	1.68	2768	36	2706	22	2660	28	**2660**	**28**	104
b39	0.5359	1.60	13.4570	2.14	0.1821	1.42	2766	36	2712	20	2672	24	**2672**	**24**	104
b29	0.5260	1.16	15.0614	1.48	0.2077	0.91	2724	26	2819	14	2888	15	**2888**	**15**	94

Sample WALZ-02	Isotopic ratios and 2σ (%) errors						Ages and 2σ absolute errors (Ma)						Reported Age		
Analysis	$^{206}Pb/^{238}U$	±2σ	$^{207}Pb/^{235}U$	±2σ	$^{207}Pb/^{206}Pb$	±2σ	$^{206}Pb/^{238}U$	±2σ	$^{207}Pb/^{235}U$	±2σ	$^{207}Pb/^{206}Pb$	±2σ	Age (Ma)	±2σ	conc %
a16	0.0791	1.60	0.6247	4.21	0.0573	3.89	491	8	493	17	503	86	**491**	**8**	98
a5	0.0799	1.16	0.6361	2.14	0.0577	1.80	496	6	500	8	519	40	**496**	**6**	96
c24	0.0815	1.61	0.6422	2.55	0.0572	1.98	505	8	504	10	498	44	**505**	**8**	101
c50	0.0885	5.97	0.7004	6.97	0.0574	3.60	546	31	539	30	508	79	**541**	**29**	108
b18	0.0893	1.62	0.7269	4.43	0.0591	4.13	551	9	555	19	569	90	**551**	**9**	97
b8	0.0897	1.66	0.7339	3.14	0.0594	2.67	554	9	559	14	581	58	**554**	**9**	95
a26	0.0914	1.45	0.7439	4.34	0.0591	4.09	564	8	565	19	569	89	**564**	**8**	99
b2	0.0922	1.86	0.7681	4.77	0.0604	4.40	569	10	579	21	619	95	**569**	**10**	92
a10	0.0924	1.78	0.7566	4.48	0.0594	4.11	569	10	572	20	583	89	**570**	**10**	98
a25	0.0929	1.45	0.7728	2.72	0.0603	2.29	573	8	581	12	615	50	**574**	**8**	93
b28	0.0936	1.32	0.7746	3.78	0.0600	3.55	577	7	582	17	605	77	**577**	**7**	95
c28	0.0947	1.17	0.7743	2.48	0.0593	2.19	583	7	582	11	578	48	**583**	**7**	101
b4	0.0949	1.63	0.7818	6.27	0.0598	6.06	584	9	587	28	595	131	**584**	**9**	98
b24	0.0950	1.91	0.7799	6.81	0.0595	6.54	585	11	585	31	587	142	**585**	**11**	100
b15	0.0951	1.97	0.7795	3.88	0.0595	3.34	586	11	585	17	584	72	**586**	**11**	100
a12	0.0960	1.36	0.8065	1.95	0.0609	1.40	591	8	600	9	636	30	**591**	**8**	93
c55	0.0965	1.84	0.8040	2.71	0.0604	1.99	594	10	599	12	618	43	**595**	**10**	96
c57	0.0974	1.57	0.7958	3.29	0.0593	2.88	599	9	594	15	577	63	**599**	**9**	104
a15	0.0974	1.12	0.8250	3.36	0.0614	3.17	599	6	611	16	654	68	**600**	**6**	92
c2	0.0976	1.26	0.8093	2.47	0.0601	2.13	600	7	602	11	608	46	**601**	**7**	99
b46	0.0978	1.07	0.8172	4.34	0.0606	4.20	602	6	607	20	625	91	**602**	**6**	96
a19	0.0981	2.39	0.7984	6.92	0.0591	6.49	603	14	596	32	569	141	**603**	**14**	106
b21	0.0989	1.67	0.8256	4.43	0.0605	4.10	608	10	611	21	623	88	**608**	**10**	98
c27	0.1001	1.43	0.8341	4.03	0.0605	3.77	615	8	616	19	620	81	**615**	**8**	99
c19	0.1008	1.83	0.8480	4.19	0.0610	3.77	619	11	624	20	640	81	**619**	**11**	97
a6	0.1011	1.42	0.8314	3.30	0.0597	2.98	621	8	614	15	591	65	**620**	**8**	105
a24	0.1011	1.60	0.8575	3.20	0.0615	2.78	621	9	629	15	658	60	**622**	**9**	94
a20	0.1014	0.91	0.8638	2.94	0.0618	2.80	623	5	632	14	666	60	**623**	**5**	93
c11	0.1017	1.74	0.8656	3.30	0.0617	2.80	625	10	633	16	664	60	**626**	**10**	94
c39	0.1024	1.75	0.8654	3.27	0.0613	2.76	629	10	633	16	649	59	**629**	**10**	97
b14	0.1039	2.28	0.8611	4.62	0.0601	4.02	637	14	631	22	607	87	**637**	**14**	105
c20	0.1043	1.75	0.8894	3.26	0.0619	2.75	639	11	646	16	670	59	**640**	**11**	95
c9	0.1044	1.43	0.8961	2.58	0.0622	2.14	640	9	650	12	682	46	**642**	**9**	94
b44	0.1050	1.37	0.8776	2.88	0.0606	2.53	644	8	640	14	625	55	**643**	**8**	103
a9	0.1052	1.24	0.9072	2.56	0.0626	2.25	645	8	656	12	693	48	**646**	**8**	93

Sample WALZ-02 continued	Isotopic ratios and 2σ (%) errors						Ages and 2σ absolute errors (Ma)						Reported Age		
	$^{206}Pb/^{238}U$	±2σ	$^{207}Pb/^{235}U$	±2σ	$^{207}Pb/^{206}Pb$	±2σ	$^{206}Pb/^{238}U$	±2σ	$^{207}Pb/^{235}U$	±2σ	$^{207}Pb/^{206}Pb$	±2σ	Age (Ma)	±2σ	conc %
c41	0.1053	2.08	0.8979	5.32	0.0618	4.89	646	13	651	26	668	105	**646**	**13**	97
c31	0.1065	2.21	0.8919	4.58	0.0607	4.01	653	14	647	22	629	86	**652**	**14**	104
b27	0.1067	1.51	0.8901	7.05	0.0605	6.89	653	9	646	34	622	149	**653**	**9**	105
b58	0.1083	1.86	0.9293	3.88	0.0622	3.41	663	12	667	19	682	73	**663**	**12**	97
b52	0.1088	1.65	0.9066	6.47	0.0605	6.26	666	10	655	32	620	135	**665**	**10**	107
b7	0.1088	1.77	0.9312	3.74	0.0621	3.29	666	11	668	18	677	70	**666**	**11**	98
b55	0.1090	2.41	0.9191	5.37	0.0612	4.80	667	15	662	26	645	103	**666**	**15**	103
c46	0.1092	2.57	0.9394	5.81	0.0624	5.21	668	16	673	29	688	111	**668**	**16**	97
a30	0.1093	1.67	0.9546	4.65	0.0633	4.34	669	11	680	23	720	92	**669**	**11**	93
c40	0.1093	1.98	0.9328	4.16	0.0619	3.66	669	13	669	21	670	78	**669**	**12**	100
b35	0.1096	1.95	0.9316	5.30	0.0616	4.92	670	12	668	26	662	106	**670**	**12**	101
b42	0.1105	1.57	0.9244	2.63	0.0607	2.11	675	10	665	13	628	46	**673**	**10**	107
b17	0.1108	1.24	0.9757	2.93	0.0639	2.66	678	8	691	15	737	56	**679**	**9**	92
c43	0.1116	1.50	0.9439	3.07	0.0613	2.68	682	10	675	15	651	58	**681**	**10**	105
c34	0.1121	1.06	0.9745	3.79	0.0630	3.64	685	7	691	19	709	77	**685**	**7**	97
c3	0.1138	1.94	1.0030	5.34	0.0639	4.98	695	13	705	28	738	105	**696**	**13**	94
b57	0.1142	1.93	0.9783	5.95	0.0621	5.63	697	13	693	30	678	120	**697**	**13**	103
b33	0.1145	1.57	1.0161	4.03	0.0643	3.71	699	10	712	21	753	78	**700**	**10**	93
b54	0.1155	1.89	1.0074	4.94	0.0633	4.56	705	13	708	25	717	97	**705**	**13**	98
b32	0.1158	1.68	1.0073	3.19	0.0631	2.72	706	11	708	16	712	58	**706**	**11**	99
c22	0.1176	1.80	1.0187	2.91	0.0628	2.29	717	12	713	15	703	49	**716**	**12**	102
c48	0.1206	1.86	1.0664	3.08	0.0641	2.46	734	13	737	16	746	52	**735**	**13**	98
c30	0.1214	1.20	1.0650	2.37	0.0636	2.04	739	8	736	12	729	43	**738**	**8**	101
b31	0.1218	2.02	1.0732	4.56	0.0639	4.09	741	14	740	24	739	87	**741**	**14**	100
b12	0.1218	2.40	1.0782	8.67	0.0642	8.32	741	17	743	47	748	176	**741**	**17**	99
a21	0.1238	2.65	1.1072	5.90	0.0649	5.27	752	19	757	32	770	111	**753**	**19**	98
b30	0.1243	1.32	1.1002	2.85	0.0642	2.52	755	9	753	15	748	53	**755**	**9**	101
b11	0.1315	1.55	1.2172	2.81	0.0671	2.34	797	12	809	16	841	49	**799**	**11**	95
a17	0.1326	1.93	1.1819	6.41	0.0647	6.12	803	15	792	36	763	129	**802**	**14**	105
b48	0.1334	1.76	1.2024	3.80	0.0654	3.37	807	13	802	21	786	71	**807**	**13**	103
b59	0.1343	1.48	1.2280	2.72	0.0663	2.29	813	11	813	15	816	48	**813**	**11**	100
c38	0.1369	1.33	1.2590	2.74	0.0667	2.40	827	10	827	16	828	50	**827**	**10**	100
b23	0.1374	1.17	1.2801	2.57	0.0676	2.29	830	9	837	15	856	48	**831**	**9**	97
c32	0.1415	1.94	1.3332	5.43	0.0683	5.08	853	15	860	32	879	105	**854**	**15**	97
c14	0.1420	1.40	1.3151	2.61	0.0672	2.21	856	11	852	15	844	46	**855**	**11**	101
b9	0.1440	1.25	1.3479	3.03	0.0679	2.77	867	10	867	18	865	57	**867**	**10**	100

Sample WALZ-02 continued	Isotopic ratios and 2σ (%) errors						Ages and 2σ absolute errors (Ma)						Reported Age		
	$^{206}Pb/^{238}U$	±2σ	$^{207}Pb/^{235}U$	±2σ	$^{207}Pb/^{206}Pb$	±2σ	$^{206}Pb/^{238}U$	±2σ	$^{207}Pb/^{235}U$	±2σ	$^{207}Pb/^{206}Pb$	±2σ	Age (Ma)	±2σ	conc %
c13	0.1506	1.24	1.4943	2.83	0.0720	2.54	904	10	928	17	985	52	**907**	**10**	92
a11	0.1512	2.19	1.4644	6.54	0.0702	6.16	908	19	916	40	935	126	**908**	**18**	97
a14	0.1544	1.47	1.5399	2.05	0.0723	1.42	926	13	946	13	995	29	**955**	**29**	93
c17	0.1595	1.35	1.6258	1.97	0.0739	1.44	954	12	980	12	1040	29	**960**	**13**	92
b16	0.1591	2.28	1.6157	3.39	0.0737	2.51	952	20	976	21	1032	51	**961**	**20**	92
b36	0.1602	2.58	1.6134	4.43	0.0730	3.61	958	23	975	28	1015	73	**963**	**22**	94
a27	0.1620	1.43	1.6633	2.51	0.0745	2.06	968	13	995	16	1054	41	**970**	**13**	92
c1	0.1627	1.34	1.5774	3.28	0.0703	2.99	972	12	961	21	937	61	**970**	**12**	104
b20	0.1624	1.42	1.6450	3.44	0.0735	3.13	970	13	988	22	1027	63	**972**	**13**	94
b51	0.1635	1.50	1.5888	7.92	0.0705	7.78	976	14	966	51	942	159	**976**	**14**	104
c16	0.1659	1.45	1.7191	5.25	0.0751	5.04	990	13	1016	34	1072	101	**991**	**13**	92
c7	0.1663	1.67	1.7168	3.26	0.0749	2.80	991	15	1015	21	1066	56	**996**	**15**	93
a3	0.1669	3.60	1.6978	6.03	0.0738	4.84	995	33	1008	39	1035	98	**999**	**32**	96
c49	0.1667	1.16	1.7184	1.92	0.0748	1.53	994	11	1015	12	1062	31	**1000**	**11**	94
c53	0.1678	1.19	1.6890	2.87	0.0730	2.61	1000	11	1004	18	1015	53	**1000**	**11**	99
b1	0.1673	1.52	1.7124	3.01	0.0742	2.60	997	14	1013	19	1047	52	**1001**	**14**	95
b26	0.1701	3.25	1.6886	7.63	0.0720	6.90	1012	31	1004	50	986	140	**1011**	**30**	103
a29	0.1703	1.11	1.7780	2.43	0.0757	2.17	1014	10	1037	16	1088	43	**1017**	**10**	93
c23	0.1727	1.45	1.7166	2.52	0.0721	2.06	1027	14	1015	16	988	42	**1023**	**13**	104
b22	0.1727	1.56	1.7432	4.96	0.0732	4.71	1027	15	1025	33	1020	95	**1027**	**15**	101
b47	0.1734	1.52	1.7241	2.71	0.0721	2.24	1031	15	1018	18	989	46	**1027**	**14**	104
c26	0.1755	1.52	1.7255	2.45	0.0713	1.92	1042	15	1018	16	967	39	**1042**	**15**	108
c44	0.1785	1.66	1.8200	3.02	0.0740	2.53	1059	16	1053	20	1041	51	**1057**	**15**	102
b49	0.1790	1.36	1.8033	3.43	0.0731	3.14	1061	13	1047	23	1016	64	**1059**	**13**	104
c42	0.1790	1.95	1.8774	3.74	0.0761	3.19	1061	19	1073	25	1097	64	**1064**	**18**	97
b25	0.1820	1.94	1.8327	4.72	0.0730	4.30	1078	19	1057	31	1015	87	**1075**	**19**	106
c21	0.1862	1.68	1.8775	3.04	0.0731	2.53	1101	17	1073	20	1018	51	**1091**	**17**	108
c25	0.1870	1.56	1.8902	2.93	0.0733	2.49	1105	16	1078	20	1023	50	**1097**	**16**	108
b41	0.1886	1.77	1.9274	3.24	0.0741	2.72	1114	18	1091	22	1045	55	**1106**	**18**	107
c33	0.1895	1.33	1.9371	3.41	0.0741	3.14	1119	14	1094	23	1045	63	**1115**	**14**	107
a7	0.2040	1.17	2.2897	4.74	0.0814	4.60	1197	13	1209	34	1231	90	**1197**	**13**	97
a2	0.2318	1.16	2.8433	1.82	0.0890	1.40	1344	14	1367	14	1403	27	**1403**	**27**	96
a4	0.3107	1.12	4.6553	2.98	0.1087	2.77	1744	17	1759	25	1777	50	**1747**	**16**	98
b39	0.3285	1.87	5.0588	3.26	0.1117	2.67	1831	30	1829	28	1827	48	**1830**	**25**	100
c56	0.3415	1.28	5.3503	2.13	0.1136	1.70	1894	21	1877	18	1858	31	**1882**	**17**	102
c29	0.3451	1.18	5.4203	1.66	0.1139	1.17	1911	20	1888	14	1863	21	**1889**	**14**	103

Sample WALZ-02 continued	Isotopic ratios and 2σ (%) errors						Ages and 2σ absolute errors (Ma)						Reported Age		
	$^{206}Pb/^{238}U$	±2σ	$^{207}Pb/^{235}U$	±2σ	$^{207}Pb/^{206}Pb$	±2σ	$^{206}Pb/^{238}U$	±2σ	$^{207}Pb/^{235}U$	±2σ	$^{207}Pb/^{206}Pb$	±2σ	Age (Ma)	±2σ	conc %
a13	0.3342	1.13	5.5433	1.66	0.1203	1.21	1859	18	1907	14	1961	22	**1961**	**22**	95
c37	0.3507	1.81	5.8631	2.20	0.1213	1.25	1938	30	1956	19	1975	22	**1975**	**22**	98
c52	0.3546	1.19	5.9297	1.44	0.1213	0.81	1956	20	1966	13	1975	14	**1975**	**14**	99
c10	0.3475	1.55	5.8328	1.97	0.1217	1.21	1923	26	1951	17	1982	22	**1982**	**22**	97
b37	0.3708	2.12	6.2761	2.78	0.1228	1.79	2033	37	2015	25	1997	32	**2012**	**24**	102
b60	0.3745	1.13	6.4587	1.80	0.1251	1.40	2051	20	2040	16	2030	25	**2043**	**16**	101
a18	0.3459	0.93	6.0375	1.72	0.1266	1.44	1915	15	1981	15	2051	25	**2051**	**25**	93
c18	0.3653	1.45	6.3873	1.64	0.1268	0.77	2007	25	2031	15	2054	14	**2054**	**14**	98
c59	0.3922	1.67	7.0724	1.93	0.1308	0.97	2133	30	2121	17	2109	17	**2115**	**15**	101
a1	0.3568	1.26	6.5755	1.56	0.1337	0.91	1967	21	2056	14	2146	16	**2146**	**16**	92
a28	0.4863	1.08	11.6289	2.08	0.1734	1.77	2555	23	2575	20	2591	30	**2568**	**18**	99
b56	0.4983	2.18	11.8722	2.85	0.1728	1.84	2607	47	2594	27	2585	31	**2592**	**26**	101
b19	0.4546	1.38	10.9691	1.62	0.1750	0.85	2416	28	2521	15	2606	14	**2606**	**14**	93
c54	0.5023	1.05	12.2609	1.73	0.1770	1.38	2624	23	2625	16	2625	23	**2624**	**16**	100
b10	0.4733	1.30	11.5890	1.72	0.1776	1.12	2498	27	2572	16	2631	19	**2631**	**19**	95
c60	0.4851	1.41	11.8852	1.79	0.1777	1.11	2550	30	2595	17	2631	18	**2631**	**18**	97
b13	0.4595	1.53	11.3204	1.91	0.1787	1.15	2437	31	2550	18	2641	19	**2641**	**19**	92
a8	0.4638	1.21	11.5013	1.43	0.1799	0.76	2456	25	2565	13	2652	13	**2652**	**13**	93
c51	0.4925	1.61	12.2758	1.87	0.1808	0.94	2581	34	2626	18	2660	16	**2660**	**16**	97
b29	0.5110	1.77	12.9307	3.02	0.1835	2.44	2661	39	2675	29	2685	40	**2672**	**28**	99
b38	0.4704	1.37	11.8989	1.91	0.1834	1.34	2485	28	2596	18	2684	22	**2684**	**22**	93
c4	0.4960	1.32	13.1991	1.85	0.1930	1.30	2597	28	2694	18	2768	21	**2768**	**21**	94

Sample CZ-02	Isotopic ratios and 2σ (%) errors						Ages and 2σ absolute errors (Ma)						Reported Age		
Analysis	$^{206}Pb/^{238}U$	±2σ	$^{207}Pb/^{235}U$	±2σ	$^{207}Pb/^{206}Pb$	±2σ	$^{206}Pb/^{238}U$	±2σ	$^{207}Pb/^{235}U$	±2σ	$^{207}Pb/^{206}Pb$	±2σ	Age (Ma)	±2σ	conc %
a60	0.0819	1.10	0.6456	2.53	0.0572	2.28	508	5	506	10	498	50	**508**	**5**	102
b3	0.0955	1.29	0.7867	3.69	0.0597	3.45	588	7	589	17	594	75	**588**	**7**	99
a36	0.0966	1.48	0.7848	2.17	0.0589	1.59	595	8	588	10	563	35	**593**	**8**	106
b20	0.0981	1.62	0.8203	4.92	0.0607	4.65	603	9	608	23	627	100	**603**	**9**	96
b12	0.0986	1.57	0.8357	3.36	0.0615	2.96	606	9	617	16	657	64	**607**	**9**	92
a30	0.0987	1.49	0.8227	2.85	0.0604	2.42	607	9	610	13	619	52	**607**	**9**	98
b5	0.0989	2.19	0.8287	4.16	0.0608	3.54	608	13	613	19	631	76	**608**	**13**	96
a50	0.0982	2.08	0.8314	2.58	0.0614	1.53	604	12	614	12	654	33	**609**	**12**	92
b41	0.0995	1.06	0.8238	2.17	0.0600	1.90	612	6	610	10	605	41	**611**	**6**	101

Sample CZ-02 continued	Isotopic ratios and 2σ (%) errors						Ages and 2σ absolute errors (Ma)						Reported Age		
	$^{206}Pb/^{238}U$	±2σ	$^{207}Pb/^{235}U$	±2σ	$^{207}Pb/^{206}Pb$	±2σ	$^{206}Pb/^{238}U$	±2σ	$^{207}Pb/^{235}U$	±2σ	$^{207}Pb/^{206}Pb$	±2σ	Age (Ma)	±2σ	conc %
a45	0.0999	1.72	0.8196	2.81	0.0595	2.22	614	10	608	13	585	48	**613**	**10**	105
c1	0.1001	2.07	0.8139	3.39	0.0590	2.69	615	12	605	16	566	59	**613**	**12**	109
c10	0.0999	1.69	0.8332	4.09	0.0605	3.72	614	10	615	19	622	80	**614**	**10**	99
b15	0.1003	1.25	0.8513	3.36	0.0616	3.13	616	7	625	16	659	67	**617**	**7**	93
b40	0.1007	2.08	0.8612	2.53	0.0620	1.44	618	12	631	12	675	31	**618**	**12**	92
b28	0.1023	1.80	0.8493	3.02	0.0602	2.43	628	11	624	14	612	52	**627**	**11**	103
b18	0.1032	1.54	0.8536	3.00	0.0600	2.57	633	9	627	14	604	56	**632**	**9**	105
b52	0.1031	1.35	0.8729	2.95	0.0614	2.62	633	8	637	14	652	56	**633**	**8**	97
c15	0.1042	2.00	0.8664	4.49	0.0603	4.02	639	12	634	21	615	87	**638**	**12**	104
b13	0.1045	1.60	0.8683	2.72	0.0603	2.19	640	10	635	13	614	47	**639**	**10**	104
b31	0.1045	0.90	0.8791	1.99	0.0610	1.78	641	6	640	10	639	38	**641**	**6**	100
b57	0.1053	1.61	0.8710	4.12	0.0600	3.79	646	10	636	20	603	82	**645**	**10**	107
a2	0.1073	1.79	0.9049	3.86	0.0611	3.42	657	11	654	19	644	73	**657**	**11**	102
c8	0.1074	2.24	0.9140	4.12	0.0617	3.45	658	14	659	20	664	74	**658**	**14**	99
b47	0.1076	1.35	0.9124	2.96	0.0615	2.63	659	8	658	14	657	56	**659**	**8**	100
a25	0.1077	1.44	0.8972	3.95	0.0604	3.68	659	9	650	19	618	79	**659**	**9**	107
b1	0.1083	1.32	0.9033	3.51	0.0605	3.25	663	8	653	17	622	70	**662**	**8**	107
b43	0.1088	1.23	0.9138	2.87	0.0609	2.59	666	8	659	14	637	56	**665**	**8**	104
a59	0.1095	2.03	0.9371	4.46	0.0621	3.97	670	13	671	22	677	85	**670**	**13**	99
b37	0.1102	1.85	0.9381	2.61	0.0618	1.85	674	12	672	13	666	40	**673**	**11**	101
b21	0.1105	1.87	0.9274	3.00	0.0609	2.35	675	12	666	15	636	51	**673**	**12**	106
a14	0.1139	1.22	0.9988	2.58	0.0636	2.28	695	8	703	13	729	48	**696**	**8**	95
a33	0.1153	2.19	0.9798	3.35	0.0617	2.54	703	15	694	17	662	54	**700**	**14**	106
b51	0.1154	1.23	0.9929	2.58	0.0624	2.27	704	8	700	13	687	49	**704**	**8**	103
c2	0.1162	1.81	0.9956	3.05	0.0622	2.45	708	12	702	16	680	52	**707**	**12**	104
a42	0.1217	2.11	1.0658	4.87	0.0635	4.39	740	15	737	26	725	93	**740**	**15**	102
b10	0.1223	1.44	1.0826	3.50	0.0642	3.19	744	10	745	19	747	67	**744**	**10**	100
c4	0.1251	2.02	1.1072	3.60	0.0642	2.98	760	14	757	19	748	63	**759**	**14**	102
a43	0.1252	1.78	1.1058	3.08	0.0641	2.52	760	13	756	17	744	53	**759**	**12**	102
b16	0.1266	1.99	1.1115	3.95	0.0637	3.41	768	14	759	21	731	72	**767**	**14**	105
a19	0.1301	1.58	1.1536	2.43	0.0643	1.85	788	12	779	13	752	39	**785**	**11**	105
a31	0.1298	1.93	1.1906	2.65	0.0665	1.81	787	14	796	15	822	38	**791**	**14**	96
a12	0.1316	2.38	1.1949	3.45	0.0659	2.49	797	18	798	19	802	52	**797**	**17**	99
b25	0.1320	1.81	1.2069	5.21	0.0663	4.88	799	14	804	29	816	102	**800**	**13**	98
b26	0.1362	1.25	1.2798	4.35	0.0681	4.16	823	10	837	25	873	86	**824**	**10**	94
a26	0.1378	1.93	1.2316	3.41	0.0648	2.81	832	15	815	19	768	59	**828**	**15**	108

Sample CZ-02 continued	Isotopic ratios and 2σ (%) errors						Ages and 2σ absolute errors (Ma)						Reported Age		
	$^{206}Pb/^{238}U$	±2σ	$^{207}Pb/^{235}U$	±2σ	$^{207}Pb/^{206}Pb$	±2σ	$^{206}Pb/^{238}U$	±2σ	$^{207}Pb/^{235}U$	±2σ	$^{207}Pb/^{206}Pb$	±2σ	Age (Ma)	±2σ	conc %
a13	0.1372	2.14	1.2662	3.16	0.0670	2.32	829	17	831	18	836	48	**829**	**16**	99
b2	0.1397	1.54	1.2891	2.30	0.0669	1.71	843	12	841	13	836	36	**842**	**12**	101
a39	0.1388	1.70	1.3105	2.29	0.0685	1.53	838	13	850	13	883	32	**844**	**13**	95
b35	0.1517	1.59	1.4584	3.51	0.0697	3.13	910	13	913	21	921	64	**911**	**13**	99
a32	0.1545	1.55	1.4870	1.98	0.0698	1.24	926	13	925	12	923	26	**925**	**12**	100
a38	0.1565	1.37	1.4994	2.21	0.0695	1.73	938	12	930	14	913	36	**935**	**11**	103
a35	0.1577	1.55	1.4847	2.58	0.0683	2.06	944	14	924	16	878	43	**937**	**14**	108
a15	0.1579	1.63	1.5374	3.66	0.0706	3.28	945	14	945	23	947	67	**945**	**14**	100
b36	0.1596	3.06	1.5558	5.71	0.0707	4.82	955	27	953	36	949	99	**954**	**26**	101
a49	0.1596	1.58	1.5589	3.09	0.0708	2.65	955	14	954	19	953	54	**955**	**14**	100
b38	0.1605	1.81	1.5758	3.18	0.0712	2.62	959	16	961	20	964	53	**960**	**15**	100
a34	0.1610	1.18	1.5869	1.82	0.0715	1.39	962	11	965	11	972	28	**963**	**10**	99
a47	0.1614	1.58	1.5837	2.83	0.0712	2.34	965	14	964	18	962	48	**964**	**14**	100
a56	0.1620	1.46	1.5631	2.82	0.0700	2.41	968	13	956	18	928	50	**965**	**13**	104
a41	0.1638	4.11	1.5686	6.42	0.0695	4.93	978	37	958	41	912	102	**969**	**35**	107
a46	0.1626	1.22	1.5910	2.28	0.0710	1.93	971	11	967	14	957	39	**970**	**11**	101
b56	0.1629	1.17	1.5876	2.36	0.0707	2.04	973	11	965	15	948	42	**971**	**10**	103
b11	0.1633	0.82	1.6388	2.45	0.0728	2.31	975	7	985	16	1008	47	**976**	**7**	97
a37	0.1630	1.44	1.6556	2.55	0.0736	2.10	974	13	992	16	1032	42	**978**	**13**	94
b4	0.1648	1.91	1.6070	2.88	0.0707	2.16	983	17	973	18	949	44	**979**	**16**	104
b22	0.1645	1.68	1.6944	2.52	0.0747	1.88	982	15	1006	16	1061	38	**986**	**15**	93
a29	0.1651	1.18	1.6732	3.33	0.0735	3.11	985	11	998	21	1028	63	**986**	**11**	96
b9	0.1660	2.42	1.6387	3.34	0.0716	2.30	990	22	985	21	975	47	**987**	**20**	102
a3	0.1656	1.21	1.6043	1.64	0.0703	1.10	988	11	972	10	936	23	**988**	**11**	106
b44	0.1664	1.39	1.6357	2.03	0.0713	1.49	992	13	984	13	966	30	**988**	**12**	103
c3	0.1672	1.42	1.6684	2.29	0.0724	1.80	996	13	997	15	997	37	**997**	**12**	100
a48	0.1673	1.31	1.6126	1.97	0.0699	1.46	997	12	975	12	926	30	**997**	**12**	108
a11	0.1679	1.53	1.6484	2.13	0.0712	1.48	1001	14	989	14	963	30	**999**	**14**	104
b59	0.1696	1.94	1.6810	2.51	0.0719	1.58	1010	18	1001	16	983	32	**1003**	**16**	103
a5	0.1688	1.24	1.6768	2.09	0.0720	1.68	1006	12	1000	13	987	34	**1004**	**11**	102
a16	0.1692	1.55	1.6782	2.79	0.0720	2.32	1007	14	1000	18	985	47	**1005**	**14**	102
a10	0.1688	2.37	1.7007	2.99	0.0731	1.82	1005	22	1009	19	1016	37	**1008**	**19**	99
b8	0.1694	1.01	1.6984	3.15	0.0727	2.99	1009	9	1008	20	1006	61	**1009**	**9**	100
a9	0.1712	1.50	1.7019	2.57	0.0721	2.09	1019	14	1009	17	989	43	**1016**	**13**	103
b60	0.1710	1.64	1.7198	2.68	0.0730	2.12	1017	15	1016	17	1013	43	**1017**	**15**	100
b24	0.1728	1.29	1.7316	2.48	0.0727	2.13	1028	12	1020	16	1004	43	**1026**	**12**	102

Sample CZ-02 continued	Isotopic ratios and 2σ (%) errors						Ages and 2σ absolute errors (Ma)						Reported Age		
	$^{206}Pb/^{238}U$	±2σ	$^{207}Pb/^{235}U$	±2σ	$^{207}Pb/^{206}Pb$	±2σ	$^{206}Pb/^{238}U$	±2σ	$^{207}Pb/^{235}U$	±2σ	$^{207}Pb/^{206}Pb$	±2σ	Age (Ma)	±2σ	conc %
c11	0.1761	3.98	1.7487	5.25	0.0720	3.42	1046	39	1027	34	986	70	**1031**	**33**	106
b42	0.1744	1.86	1.7680	3.08	0.0735	2.46	1036	18	1034	20	1029	50	**1035**	**17**	101
a6	0.1756	1.30	1.7457	4.45	0.0721	4.26	1043	12	1026	29	988	87	**1042**	**12**	106
b30	0.1769	1.48	1.7679	3.73	0.0725	3.42	1050	14	1034	24	999	69	**1048**	**14**	105
b7	0.1802	1.13	1.8359	1.58	0.0739	1.11	1068	11	1058	10	1038	22	**1062**	**11**	103
b39	0.1814	1.75	1.8230	3.07	0.0729	2.53	1074	17	1054	20	1011	51	**1067**	**17**	106
b49	0.1812	1.62	1.8280	3.88	0.0732	3.53	1074	16	1056	26	1018	71	**1071**	**16**	105
c12	0.1814	2.10	1.8805	2.67	0.0752	1.64	1075	21	1074	18	1074	33	**1074**	**18**	100
c19	0.1858	2.08	1.9300	2.65	0.0753	1.64	1099	21	1092	18	1077	33	**1092**	**18**	102
c16	0.1859	1.41	1.9149	2.81	0.0747	2.43	1099	14	1086	19	1061	49	**1096**	**14**	104
c9	0.3227	1.92	4.7423	2.54	0.1066	1.66	1803	30	1775	22	1742	30	**1742**	**30**	104
c13	0.3349	1.55	4.9467	1.87	0.1071	1.04	1862	25	1810	16	1751	19	**1751**	**19**	106
a57	0.3237	2.46	4.9605	2.84	0.1112	1.41	1808	39	1813	24	1818	26	**1818**	**26**	99
a4	0.3583	1.49	5.5859	2.75	0.1131	2.31	1974	25	1914	24	1849	42	**1849**	**42**	107
b19	0.3158	1.15	4.9489	1.71	0.1136	1.27	1769	18	1811	15	1859	23	**1859**	**23**	95
b23	0.3318	1.14	5.2000	1.83	0.1137	1.43	1847	18	1853	16	1859	26	**1859**	**26**	99
b53	0.3319	1.16	5.2034	2.19	0.1137	1.86	1848	19	1853	19	1859	34	**1859**	**34**	99
a27	0.3101	0.93	4.9243	1.62	0.1152	1.33	1741	14	1806	14	1882	24	**1882**	**24**	93
a22	0.3325	1.29	5.3998	1.81	0.1178	1.27	1850	21	1885	16	1923	23	**1923**	**23**	96
a28	0.3294	1.72	5.3659	2.11	0.1181	1.21	1836	28	1879	18	1928	22	**1928**	**22**	95
a1	0.3567	1.35	5.8134	2.45	0.1182	2.05	1967	23	1948	21	1929	37	**1929**	**37**	102
a21	0.3409	2.29	5.6094	2.45	0.1193	0.86	1891	38	1918	21	1946	15	**1946**	**15**	97
b27	0.3321	1.05	5.4642	1.66	0.1193	1.29	1849	17	1895	14	1946	23	**1946**	**23**	95
a40	0.3385	1.45	5.5785	1.90	0.1195	1.23	1879	24	1913	16	1949	22	**1949**	**22**	96
c17	0.3486	1.67	5.8120	1.99	0.1209	1.09	1928	28	1948	17	1970	19	**1970**	**19**	98
b14	0.3354	1.09	5.6973	1.65	0.1232	1.23	1864	18	1931	14	2003	22	**2003**	**22**	93
c18	0.3538	2.08	6.0213	2.55	0.1235	1.48	1952	35	1979	22	2007	26	**2007**	**26**	97
a51	0.3477	1.78	5.9544	1.91	0.1242	0.69	1924	30	1969	17	2017	12	**2017**	**12**	95
b17	0.3533	0.92	6.0619	1.88	0.1245	1.64	1950	16	1985	17	2021	29	**2021**	**29**	96
a54	0.3757	1.24	6.4698	1.81	0.1249	1.32	2056	22	2042	16	2027	23	**2027**	**23**	101
b29	0.3730	2.16	6.5589	2.43	0.1275	1.10	2043	38	2054	22	2064	19	**2064**	**19**	99
a17	0.4809	1.97	10.7660	2.29	0.1624	1.16	2531	41	2503	21	2480	20	**2480**	**20**	102
a55	0.4612	1.98	10.9965	2.19	0.1729	0.95	2445	40	2523	21	2586	16	**2586**	**16**	95
a8	0.5095	1.40	12.2657	1.73	0.1746	1.01	2654	30	2625	16	2602	17	**2602**	**17**	102
a52	0.4644	0.95	11.2317	1.43	0.1754	1.06	2459	20	2543	13	2610	18	**2610**	**18**	94
a44	0.5470	1.51	13.7353	2.17	0.1821	1.56	2813	34	2732	21	2672	26	**2672**	**26**	105

Sample CZ-02 continued	Isotopic ratios and 2σ (%) errors						Ages and 2σ absolute errors (Ma)						Reported Age		
	$^{206}Pb/^{238}U$	±2σ	$^{207}Pb/^{235}U$	±2σ	$^{207}Pb/^{206}Pb$	±2σ	$^{206}Pb/^{238}U$	±2σ	$^{207}Pb/^{235}U$	±2σ	$^{207}Pb/^{206}Pb$	±2σ	Age (Ma)	±2σ	conc %
c14	0.4616	1.29	11.6638	1.63	0.1833	1.00	2447	26	2578	15	2683	17	**2683**	**17**	91
a24	0.4996	1.71	12.6552	2.18	0.1837	1.35	2612	37	2654	21	2687	22	**2687**	**22**	97
c5	0.5359	1.81	13.6118	2.03	0.1842	0.91	2766	41	2723	19	2691	15	**2691**	**15**	103
a7	0.5505	1.60	14.4421	1.85	0.1903	0.93	2827	37	2779	18	2745	15	**2745**	**15**	103

Sample GCZ-06	Isotopic ratios and 2σ (%) errors						Ages and 2σ absolute errors (Ma)						Reported Age		
Analysis	$^{206}Pb/^{238}U$	±2σ	$^{207}Pb/^{235}U$	±2σ	$^{207}Pb/^{206}Pb$	±2σ	$^{206}Pb/^{238}U$	±2σ	$^{207}Pb/^{235}U$	±2σ	$^{207}Pb/^{206}Pb$	±2σ	Age (Ma)	±2σ	conc %
a53	0.0847	1.26	0.6856	1.91	0.0587	1.43	524	6	530	8	556	31	**525**	**6**	94
b3	0.0856	1.19	0.6836	2.67	0.0579	2.39	529	6	529	11	528	52	**529**	**6**	100
c8	0.0870	1.76	0.6840	3.04	0.0570	2.49	538	9	529	13	492	55	**537**	**9**	109
a5	0.0939	1.54	0.7742	2.80	0.0598	2.33	579	9	582	12	595	50	**579**	**9**	97
b6	0.0941	1.80	0.7717	3.35	0.0595	2.83	579	10	581	15	586	61	**580**	**10**	99
c34	0.0960	1.40	0.7841	2.06	0.0593	1.51	591	8	588	9	577	33	**590**	**8**	102
b5	0.0971	1.44	0.8068	1.91	0.0602	1.25	598	8	601	9	612	27	**599**	**8**	98
c47	0.0972	1.42	0.8254	2.42	0.0616	1.96	598	8	611	11	659	42	**600**	**8**	91
d9	0.0990	2.26	0.8181	4.06	0.0599	3.38	609	13	607	19	601	73	**608**	**13**	101
c46	0.0998	1.59	0.8162	2.87	0.0593	2.39	613	9	606	13	578	52	**612**	**9**	106
a23	0.0997	1.56	0.8317	3.40	0.0605	3.02	613	9	615	16	622	65	**613**	**9**	98
a47	0.1017	3.15	0.8440	3.45	0.0602	1.41	624	19	621	16	610	31	**621**	**16**	102
b23	0.1027	2.22	0.8485	4.60	0.0599	4.03	630	13	624	22	601	87	**629**	**13**	105
c33	0.1029	1.92	0.8778	2.67	0.0619	1.86	631	12	640	13	669	40	**634**	**11**	94
d8	0.1034	1.49	0.8640	3.08	0.0606	2.70	634	9	632	15	625	58	**634**	**9**	102
a42	0.1043	1.56	0.8940	3.44	0.0622	3.06	639	10	649	17	680	65	**640**	**9**	94
c45	0.1051	1.94	0.8810	4.21	0.0608	3.73	644	12	642	20	632	80	**644**	**12**	102
a24	0.1053	1.81	0.8775	5.50	0.0604	5.20	645	11	640	26	619	112	**645**	**11**	104
a21	0.1055	1.20	0.8768	2.05	0.0603	1.66	647	7	639	10	613	36	**645**	**7**	105
c9	0.1071	1.93	0.9134	3.28	0.0618	2.65	656	12	659	16	669	57	**656**	**12**	98
a37	0.1072	2.74	0.9165	4.19	0.0620	3.17	657	17	661	21	674	68	**658**	**17**	97
a51	0.1080	1.69	0.8982	3.25	0.0603	2.77	661	11	651	16	615	60	**659**	**10**	107
c12	0.1081	1.89	0.9184	2.99	0.0616	2.32	662	12	662	15	661	50	**662**	**12**	100
a6	0.1098	1.88	0.9130	6.63	0.0603	6.36	672	12	659	33	614	137	**671**	**12**	109
c18	0.1107	1.02	0.9309	2.82	0.0610	2.63	677	7	668	14	639	57	**676**	**7**	106
c30	0.1111	1.68	0.9343	2.55	0.0610	1.92	679	11	670	13	639	41	**676**	**10**	106
c7	0.1116	1.62	0.9409	2.29	0.0611	1.62	682	11	673	11	644	35	**679**	**11**	106

Sample GCZ-06 continued	Isotopic ratios and 2σ (%) errors						Ages and 2σ absolute errors (Ma)						Reported Age		
	$^{206}Pb/^{238}U$	±2σ	$^{207}Pb/^{235}U$	±2σ	$^{207}Pb/^{206}Pb$	±2σ	$^{206}Pb/^{238}U$	±2σ	$^{207}Pb/^{235}U$	±2σ	$^{207}Pb/^{206}Pb$	±2σ	Age (Ma)	±2σ	conc %
b4	0.1111	2.21	0.9789	2.96	0.0639	1.96	679	14	693	15	738	42	**685**	**14**	92
c1	0.1124	2.42	0.9637	3.79	0.0622	2.91	687	16	685	19	681	62	**686**	**15**	101
a35	0.1129	1.53	0.9501	3.25	0.0610	2.87	690	10	678	16	641	62	**688**	**10**	108
c28	0.1123	2.30	0.9793	3.00	0.0632	1.92	686	15	693	15	716	41	**690**	**14**	96
d7	0.1141	1.56	0.9695	3.57	0.0616	3.22	696	10	688	18	661	69	**696**	**10**	105
a54	0.1164	1.53	0.9934	2.39	0.0619	1.84	710	10	700	12	671	39	**707**	**10**	106
c38	0.1152	1.81	1.0281	2.57	0.0647	1.83	703	12	718	13	766	39	**708**	**12**	92
a17	0.1171	1.83	0.9967	2.68	0.0617	1.96	714	12	702	14	665	42	**709**	**12**	107
b2	0.1169	1.15	1.0004	3.98	0.0621	3.81	713	8	704	20	677	81	**712**	**8**	105
c11	0.1178	1.58	1.0322	4.61	0.0635	4.33	718	11	720	24	726	92	**718**	**11**	99
a52	0.1184	2.06	1.0202	3.21	0.0625	2.47	721	14	714	17	692	53	**719**	**14**	104
a29	0.1198	1.32	1.0568	2.61	0.0640	2.26	729	9	732	14	741	48	**730**	**9**	98
a9	0.1231	2.03	1.0678	3.81	0.0629	3.23	748	14	738	20	705	69	**747**	**14**	106
b15	0.1240	1.98	1.0923	4.47	0.0639	4.01	753	14	750	24	738	85	**753**	**14**	102
c13	0.1254	2.22	1.0949	3.21	0.0633	2.33	762	16	751	17	719	49	**757**	**15**	106
d15	0.1258	1.88	1.0966	3.28	0.0632	2.69	764	14	752	18	715	57	**761**	**13**	107
c54	0.1266	1.68	1.1097	4.07	0.0636	3.71	768	12	758	22	728	79	**767**	**12**	105
d6	0.1360	1.99	1.2351	4.70	0.0659	4.26	822	15	817	27	803	89	**821**	**15**	102
d5	0.1362	1.25	1.2180	3.67	0.0649	3.45	823	10	809	21	770	73	**822**	**10**	107
a14	0.1384	1.88	1.2423	3.38	0.0651	2.81	836	15	820	19	778	59	**832**	**14**	107
a31	0.1376	1.68	1.2864	2.35	0.0678	1.64	831	13	840	13	863	34	**835**	**12**	96
b17	0.1384	1.68	1.2826	3.44	0.0672	3.00	836	13	838	20	844	62	**836**	**13**	99
c21	0.1389	2.01	1.3107	3.47	0.0685	2.83	838	16	850	20	882	59	**841**	**15**	95
a49	0.1389	2.79	1.3053	3.99	0.0681	2.84	839	22	848	23	873	59	**843**	**21**	96
a50	0.1409	2.54	1.2957	3.52	0.0667	2.43	850	20	844	20	829	51	**847**	**19**	102
c50	0.1416	1.51	1.2906	3.14	0.0661	2.76	853	12	842	18	810	58	**851**	**12**	105
c4	0.1428	1.94	1.3471	3.23	0.0684	2.59	861	16	866	19	881	53	**862**	**15**	98
d17	0.1475	1.23	1.3586	2.07	0.0668	1.67	887	10	871	12	832	35	**882**	**10**	107
b22	0.1461	2.15	1.4062	2.60	0.0698	1.46	879	18	892	16	922	30	**890**	**16**	95
a39	0.1488	1.29	1.4269	1.81	0.0696	1.27	894	11	900	11	915	26	**897**	**10**	98
a18	0.1527	1.67	1.4790	2.13	0.0703	1.33	916	14	922	13	936	27	**920**	**13**	98
a7	0.1539	1.86	1.4650	4.56	0.0691	4.16	923	16	916	28	900	86	**922**	**16**	102
a16	0.1574	1.62	1.5120	4.39	0.0697	4.08	943	14	935	27	918	84	**942**	**14**	103
a59	0.1593	1.78	1.5539	2.73	0.0708	2.07	953	16	952	17	950	42	**952**	**15**	100
c48	0.1606	2.94	1.5847	3.76	0.0716	2.35	960	26	964	24	974	48	**963**	**23**	99
d12	0.1641	1.86	1.6428	2.61	0.0726	1.83	980	17	987	17	1003	37	**983**	**15**	98

Sample GCZ-06 continued	Isotopic ratios and 2σ (%) errors						Ages and 2σ absolute errors (Ma)						Reported Age		
	$^{206}Pb/^{238}U$	±2σ	$^{207}Pb/^{235}U$	±2σ	$^{207}Pb/^{206}Pb$	±2σ	$^{206}Pb/^{238}U$	±2σ	$^{207}Pb/^{235}U$	±2σ	$^{207}Pb/^{206}Pb$	±2σ	Age (Ma)	±2σ	conc %
c15	0.1652	2.46	1.6715	3.22	0.0734	2.07	986	23	998	21	1025	42	**994**	**20**	96
c58	0.1663	2.07	1.7191	3.55	0.0750	2.89	992	19	1016	23	1067	58	**998**	**19**	93
a45	0.1680	1.56	1.6503	2.90	0.0713	2.45	1001	14	990	19	965	50	**998**	**14**	104
b7	0.1677	1.58	1.6772	2.67	0.0725	2.16	999	15	1000	17	1001	44	**999**	**14**	100
d10	0.1679	1.71	1.7487	3.35	0.0756	2.88	1000	16	1027	22	1083	58	**1001**	**16**	92
a60	0.1679	2.58	1.6812	3.26	0.0726	1.99	1001	24	1001	21	1003	40	**1001**	**21**	100
c52	0.1690	2.00	1.6763	2.63	0.0720	1.71	1006	19	1000	17	985	35	**1001**	**16**	102
a34	0.1693	1.55	1.6623	2.66	0.0712	2.16	1008	15	994	17	964	44	**1004**	**14**	105
a13	0.1701	1.58	1.6867	2.56	0.0719	2.02	1012	15	1004	16	984	41	**1009**	**14**	103
a11	0.1713	1.75	1.6762	2.56	0.0710	1.86	1019	17	1000	16	957	38	**1009**	**17**	107
b14	0.1698	2.37	1.7519	5.04	0.0748	4.45	1011	22	1028	33	1064	89	**1014**	**22**	95
c56	0.1717	1.53	1.6727	3.43	0.0707	3.07	1021	15	998	22	948	63	**1017**	**15**	108
d19	0.1716	1.40	1.7426	2.58	0.0737	2.16	1021	13	1024	17	1032	44	**1022**	**13**	99
c5	0.1730	2.18	1.7180	3.81	0.0720	3.13	1028	21	1015	25	987	64	**1024**	**20**	104
a27	0.1743	2.42	1.7303	3.22	0.0720	2.11	1036	23	1020	21	986	43	**1024**	**23**	105
c25	0.1724	2.59	1.8126	3.23	0.0762	1.94	1025	25	1050	21	1101	39	**1025**	**25**	93
c6	0.1747	2.14	1.7710	2.82	0.0735	1.84	1038	21	1035	18	1028	37	**1036**	**18**	101
a48	0.1762	1.83	1.7645	2.91	0.0726	2.25	1046	18	1032	19	1004	46	**1040**	**16**	104
c14	0.1782	2.08	1.7866	4.23	0.0727	3.69	1057	20	1041	28	1006	75	**1053**	**19**	105
a26	0.1799	1.56	1.8006	2.45	0.0726	1.89	1067	15	1046	16	1002	38	**1057**	**15**	106
c2	0.1791	1.34	1.8124	3.03	0.0734	2.72	1062	13	1050	20	1025	55	**1060**	**13**	104
a44	0.1798	2.21	1.8010	6.43	0.0727	6.04	1066	22	1046	43	1005	123	**1064**	**21**	106
a40	0.1799	1.66	1.8247	3.53	0.0736	3.12	1066	16	1054	23	1030	63	**1064**	**16**	104
c41	0.1810	1.55	1.8235	2.96	0.0731	2.52	1073	15	1054	20	1016	51	**1067**	**15**	106
c29	0.1816	1.47	1.8635	3.49	0.0744	3.16	1076	15	1068	23	1053	64	**1074**	**14**	102
c57	0.1826	1.56	1.8724	2.63	0.0744	2.12	1081	16	1071	18	1052	43	**1077**	**15**	103
a10	0.1835	1.51	1.8826	4.51	0.0744	4.25	1086	15	1075	30	1052	86	**1085**	**15**	103
c3	0.1837	1.34	1.8462	2.10	0.0729	1.63	1087	13	1062	14	1011	33	**1087**	**15**	108
a15	0.1850	1.78	1.8571	3.68	0.0728	3.22	1094	18	1066	25	1009	65	**1087**	**18**	108
b24	0.1863	2.30	1.8812	4.90	0.0732	4.33	1101	23	1074	33	1021	88	**1095**	**22**	108
a41	0.1864	1.76	1.8898	2.63	0.0735	1.95	1102	18	1078	18	1029	39	**1102**	**18**	107
d4	0.1879	1.45	1.9484	3.53	0.0752	3.22	1110	15	1098	24	1074	65	**1108**	**14**	103
c51	0.1927	1.34	1.9940	2.08	0.0750	1.59	1136	14	1113	14	1069	32	**1136**	**15**	106
c36	0.1967	1.35	2.0441	3.93	0.0754	3.70	1158	14	1130	27	1079	74	**1154**	**14**	107
b1	0.2222	1.53	2.5985	2.01	0.0848	1.31	1294	18	1300	15	1311	25	**1299**	**15**	99
d16	0.3033	3.77	4.6098	3.98	0.1102	1.28	1707	57	1751	34	1803	23	**1803**	**23**	95

Sample GCZ-06 continued	Isotopic ratios and 2σ (%) errors						Ages and 2σ absolute errors (Ma)						Reported Age		
	$^{206}Pb/^{238}U$	±2σ	$^{207}Pb/^{235}U$	±2σ	$^{207}Pb/^{206}Pb$	±2σ	$^{206}Pb/^{238}U$	±2σ	$^{207}Pb/^{235}U$	±2σ	$^{207}Pb/^{206}Pb$	±2σ	Age (Ma)	±2σ	conc %
a38	0.3080	1.34	4.8744	2.18	0.1148	1.72	1731	20	1798	19	1876	31	**1876**	**31**	92
d11	0.3310	1.35	5.2405	1.88	0.1148	1.32	1843	22	1859	16	1877	24	**1877**	**24**	98
a12	0.3469	1.92	5.5394	2.25	0.1158	1.17	1920	32	1907	20	1893	21	**1893**	**21**	101
a58	0.3379	1.86	5.4088	2.42	0.1161	1.54	1876	30	1886	21	1897	28	**1897**	**28**	99
a43	0.3795	1.75	6.1915	2.27	0.1183	1.45	2074	31	2003	20	1931	26	**1931**	**26**	107
a4	0.3836	1.19	6.2978	2.12	0.1191	1.76	2093	21	2018	19	1942	31	**1942**	**31**	108
c10	0.3632	1.13	6.0762	2.19	0.1213	1.88	1997	19	1987	19	1976	33	**1976**	**33**	101
c20	0.3701	2.50	6.2180	3.07	0.1219	1.79	2030	44	2007	27	1984	32	**1984**	**32**	102
a8	0.3617	1.86	6.1061	2.16	0.1224	1.10	1990	32	1991	19	1992	20	**1992**	**20**	100
a55	0.3642	1.68	6.3263	1.93	0.1260	0.94	2002	29	2022	17	2042	17	**2042**	**17**	98
a57	0.3838	1.78	6.7476	2.12	0.1275	1.14	2094	32	2079	19	2064	20	**2064**	**20**	101
a33	0.4028	1.96	7.5787	2.27	0.1364	1.14	2182	36	2182	21	2183	20	**2183**	**20**	100
c42	0.4274	1.71	9.4005	2.14	0.1595	1.29	2294	33	2378	20	2450	22	**2450**	**22**	94
a30	0.4208	1.99	9.5361	2.16	0.1644	0.85	2264	38	2391	20	2501	14	**2501**	**14**	91
c60	0.4726	1.40	11.1830	1.67	0.1716	0.90	2495	29	2538	16	2574	15	**2574**	**15**	97
a3	0.4584	1.59	11.0026	1.71	0.1741	0.63	2433	32	2523	16	2597	11	**2597**	**11**	94
b10	0.4946	1.36	11.9907	1.63	0.1758	0.90	2590	29	2604	15	2614	15	**2614**	**15**	99
d20	0.5510	1.80	13.5470	2.26	0.1783	1.38	2829	41	2719	22	2637	23	**2637**	**23**	107
a36	0.5063	2.80	12.5300	3.13	0.1795	1.42	2641	61	2645	30	2648	24	**2648**	**24**	100
c23	0.5256	2.02	13.0774	2.66	0.1804	1.74	2723	45	2685	25	2657	29	**2657**	**29**	102
a1	0.5516	1.76	13.8086	2.77	0.1815	2.14	2832	41	2737	27	2667	35	**2667**	**35**	106
d3	0.6347	1.39	22.5344	2.35	0.2575	1.90	3168	35	3207	23	3232	30	**3232**	**30**	98

Sample GCZ-03	Isotopic ratios and 2σ (%) errors						Ages and 2σ absolute errors (Ma)						Reported Age		
Analysis	$^{206}Pb/^{238}U$	±2σ	$^{207}Pb/^{235}U$	±2σ	$^{207}Pb/^{206}Pb$	±2σ	$^{206}Pb/^{238}U$	±2σ	$^{207}Pb/^{235}U$	±2σ	$^{207}Pb/^{206}Pb$	±2σ	Age (Ma)	±2σ	conc %
a29	0.0955	1.02	0.8024	1.59	0.0610	1.22	588	6	598	7	638	26	**589**	**6**	92
a10	0.0963	2.00	0.7801	6.72	0.0587	6.42	593	11	586	30	558	140	**593**	**11**	106
b16	0.0965	1.56	0.8142	4.40	0.0612	4.11	594	9	605	20	646	88	**594**	**9**	92
a3	0.0971	1.51	0.8059	2.66	0.0602	2.18	598	9	600	12	610	47	**598**	**9**	98
b25	0.0974	1.40	0.7910	3.97	0.0589	3.71	599	8	592	18	564	81	**599**	**8**	106
b18	0.0985	0.89	0.8052	3.19	0.0593	3.07	606	5	600	15	577	67	**606**	**5**	105
a27	0.0987	1.67	0.8068	3.10	0.0593	2.61	607	10	601	14	578	57	**606**	**10**	105
a42	0.0990	1.62	0.8117	2.73	0.0594	2.20	609	9	603	13	584	48	**608**	**9**	104
c15	0.0990	1.76	0.8421	3.48	0.0617	3.01	608	10	620	16	664	64	**610**	**10**	92

Sample GCZ-03 continued	Isotopic ratios and 2σ (%) errors						Ages and 2σ absolute errors (Ma)						Reported Age		
	$^{206}Pb/^{238}U$	±2σ	$^{207}Pb/^{235}U$	±2σ	$^{207}Pb/^{206}Pb$	±2σ	$^{206}Pb/^{238}U$	±2σ	$^{207}Pb/^{235}U$	±2σ	$^{207}Pb/^{206}Pb$	±2σ	Age (Ma)	±2σ	conc %
a24	0.0991	2.02	0.8376	4.17	0.0613	3.65	609	12	618	19	649	78	**610**	**12**	94
b6	0.0993	1.68	0.8107	3.67	0.0592	3.26	611	10	603	17	574	71	**610**	**10**	106
c12	0.0996	1.24	0.8213	3.10	0.0598	2.84	612	7	609	14	596	62	**612**	**7**	103
a18	0.1000	1.43	0.8454	3.81	0.0613	3.53	615	8	622	18	649	76	**615**	**8**	95
a9	0.1006	2.02	0.8248	5.26	0.0595	4.85	618	12	611	24	584	105	**617**	**12**	106
c4	0.1007	0.94	0.8247	2.74	0.0594	2.58	619	6	611	13	581	56	**618**	**6**	107
c23	0.1010	1.83	0.8343	4.28	0.0599	3.86	620	11	616	20	599	84	**620**	**11**	104
b40	0.1010	1.10	0.8604	2.40	0.0618	2.13	620	6	630	11	666	46	**621**	**7**	93
a12	0.1020	1.13	0.8429	2.34	0.0599	2.05	626	7	621	11	601	44	**625**	**7**	104
c18	0.1019	2.20	0.8649	4.50	0.0615	3.92	626	13	633	21	658	84	**626**	**13**	95
a5	0.1026	1.52	0.8587	2.43	0.0607	1.89	630	9	629	11	629	41	**630**	**9**	100
b15	0.1026	0.90	0.8566	1.55	0.0605	1.26	630	5	628	7	622	27	**630**	**5**	101
a43	0.1035	1.26	0.8579	2.55	0.0601	2.22	635	8	629	12	608	48	**634**	**8**	104
b60	0.1036	1.16	0.8855	3.04	0.0620	2.81	636	7	644	15	673	60	**636**	**7**	94
a56	0.1036	1.94	0.8789	6.95	0.0615	6.68	636	12	640	34	657	143	**636**	**12**	97
b28	0.1036	1.37	0.8884	2.44	0.0622	2.03	636	8	645	12	680	43	**637**	**8**	93
a57	0.1038	1.30	0.8719	2.74	0.0609	2.41	637	8	637	13	636	52	**637**	**8**	100
c1	0.1052	1.39	0.8903	3.52	0.0614	3.23	645	9	647	17	653	69	**645**	**9**	99
b45	0.1055	1.33	0.8880	3.41	0.0610	3.14	647	8	645	16	640	68	**647**	**8**	101
c11	0.1058	2.54	0.8850	5.18	0.0607	4.52	648	16	644	25	627	97	**648**	**15**	103
b52	0.1060	1.48	0.8998	3.04	0.0615	2.65	650	9	652	15	658	57	**650**	**9**	99
b14	0.1061	1.41	0.8939	2.83	0.0611	2.45	650	9	648	14	642	53	**650**	**9**	101
b12	0.1064	1.43	0.8882	2.71	0.0605	2.31	652	9	645	13	622	50	**651**	**9**	105
a17	0.1064	1.36	0.8876	3.48	0.0605	3.20	652	8	645	17	621	69	**652**	**8**	105
b36	0.1068	1.08	0.8892	2.99	0.0604	2.79	654	7	646	14	618	60	**653**	**7**	106
a39	0.1069	1.00	0.9200	3.69	0.0624	3.56	655	6	662	18	688	76	**655**	**6**	95
a25	0.1072	1.16	0.8908	3.07	0.0603	2.84	657	7	647	15	613	61	**656**	**7**	107
c24	0.1083	1.16	0.9068	2.23	0.0607	1.91	663	7	655	11	629	41	**662**	**7**	105
a41	0.1084	1.88	0.9066	3.91	0.0607	3.43	663	12	655	19	628	74	**662**	**12**	106
c3	0.1084	1.05	0.9027	1.95	0.0604	1.64	664	7	653	9	617	35	**662**	**7**	107
b57	0.1084	0.98	0.9187	4.00	0.0615	3.87	664	6	662	20	655	83	**664**	**6**	101
b30	0.1086	1.71	0.9185	3.73	0.0613	3.31	665	11	662	18	651	71	**664**	**11**	102
c29	0.1097	1.39	0.9261	2.13	0.0612	1.62	671	9	666	10	647	35	**670**	**9**	104
b49	0.1101	1.41	0.9661	2.90	0.0636	2.53	673	9	686	15	730	54	**675**	**9**	92
b3	0.1105	1.28	0.9265	3.77	0.0608	3.55	676	8	666	19	632	76	**675**	**8**	107
a55	0.1106	2.21	0.9391	4.37	0.0616	3.77	676	14	672	22	659	81	**676**	**14**	103

Sample GCZ-03 continued	Isotopic ratios and 2σ (%) errors						Ages and 2σ absolute errors (Ma)						Reported Age		
	$^{206}Pb/^{238}U$	±2σ	$^{207}Pb/^{235}U$	±2σ	$^{207}Pb/^{206}Pb$	±2σ	$^{206}Pb/^{238}U$	±2σ	$^{207}Pb/^{235}U$	±2σ	$^{207}Pb/^{206}Pb$	±2σ	Age (Ma)	±2σ	conc %
a38	0.1107	1.26	0.9411	3.11	0.0617	2.84	677	8	673	15	663	61	**676**	**8**	102
c6	0.1108	2.05	0.9407	5.41	0.0616	5.01	678	13	673	27	659	107	**677**	**13**	103
a37	0.1111	0.88	0.9330	2.47	0.0609	2.31	679	6	669	12	636	50	**678**	**6**	107
b17	0.1117	1.45	0.9470	3.31	0.0615	2.97	683	9	677	16	656	64	**682**	**9**	104
a40	0.1120	1.65	0.9548	2.42	0.0618	1.76	684	11	681	12	669	38	**683**	**10**	102
c22	0.1120	1.36	0.9683	3.56	0.0627	3.29	685	9	688	18	698	70	**685**	**9**	98
b19	0.1129	1.41	0.9628	3.92	0.0619	3.66	690	9	685	20	669	78	**689**	**9**	103
c9	0.1136	1.25	0.9679	2.61	0.0618	2.29	694	8	687	13	667	49	**693**	**8**	104
c5	0.1137	1.90	0.9602	4.47	0.0613	4.05	694	13	683	23	649	87	**693**	**12**	107
b9	0.1147	1.12	0.9656	3.30	0.0611	3.10	700	7	686	17	641	67	**699**	**7**	109
a22	0.1160	1.51	0.9937	3.19	0.0621	2.81	708	10	701	16	678	60	**707**	**10**	104
b11	0.1162	1.64	0.9840	3.36	0.0614	2.93	709	11	696	17	654	63	**707**	**11**	108
b4	0.1162	0.75	0.9913	3.17	0.0619	3.07	708	5	699	16	671	66	**708**	**5**	106
a33	0.1174	2.47	1.0223	5.62	0.0632	5.05	715	17	715	29	714	107	**715**	**17**	100
a35	0.1184	1.33	1.0629	2.31	0.0651	1.89	721	9	735	12	779	40	**724**	**9**	93
a6	0.1204	1.36	1.0345	2.38	0.0623	1.96	733	9	721	12	685	42	**730**	**9**	107
a60	0.1235	0.99	1.0734	2.41	0.0630	2.20	751	7	740	13	709	47	**750**	**7**	106
a32	0.1237	1.12	1.0720	2.20	0.0629	1.90	752	8	740	12	703	40	**750**	**8**	107
b1	0.1296	1.31	1.2069	2.63	0.0675	2.28	786	10	804	15	854	47	**788**	**10**	92
b20	0.1301	2.09	1.1568	4.99	0.0645	4.53	789	16	780	28	757	96	**788**	**15**	104
a58	0.1331	2.03	1.2298	2.56	0.0670	1.55	805	15	814	14	839	32	**811**	**14**	96
b10	0.1353	1.46	1.2492	2.62	0.0670	2.18	818	11	823	15	837	45	**819**	**11**	98
a50	0.1534	2.45	1.4715	3.74	0.0696	2.82	920	21	919	23	916	58	**920**	**20**	100
b23	0.1536	3.26	1.4379	11.12	0.0679	10.63	921	28	905	69	866	220	**920**	**28**	106
b46	0.1541	0.74	1.4778	2.00	0.0696	1.86	924	6	921	12	916	38	**923**	**6**	101
b37	0.1546	1.62	1.4521	3.21	0.0681	2.77	927	14	911	19	872	57	**923**	**14**	106
a21	0.1536	1.47	1.4879	1.97	0.0703	1.32	921	13	925	12	936	27	**924**	**11**	98
b55	0.1606	1.79	1.5386	2.64	0.0695	1.94	960	16	946	16	913	40	**953**	**16**	105
a26	0.1610	1.96	1.5734	2.92	0.0709	2.16	962	17	960	18	954	44	**961**	**16**	101
b5	0.1610	2.05	1.5783	2.81	0.0711	1.92	962	18	962	18	960	39	**962**	**17**	100
a52	0.1598	1.90	1.6017	2.49	0.0727	1.60	956	17	971	16	1005	32	**966**	**17**	95
c2	0.1629	1.26	1.5735	1.78	0.0700	1.26	973	11	960	11	930	26	**966**	**11**	105
a13	0.1634	1.95	1.5902	3.09	0.0706	2.39	976	18	966	19	945	49	**972**	**17**	103
a7	0.1629	1.61	1.6777	3.79	0.0747	3.43	973	15	1000	24	1060	69	**976**	**15**	92
c27	0.1662	2.27	1.5903	3.48	0.0694	2.64	991	21	966	22	911	54	**980**	**21**	109
c21	0.1680	1.55	1.6556	3.38	0.0715	3.00	1001	14	992	22	971	61	**999**	**14**	103

Sample GCZ-03 continued	Isotopic ratios and 2σ (%) errors						Ages and 2σ absolute errors (Ma)						Reported Age		
	$^{206}Pb/^{238}U$	±2σ	$^{207}Pb/^{235}U$	±2σ	$^{207}Pb/^{206}Pb$	±2σ	$^{206}Pb/^{238}U$	±2σ	$^{207}Pb/^{235}U$	±2σ	$^{207}Pb/^{206}Pb$	±2σ	Age (Ma)	±2σ	conc %
a59	0.1691	1.20	1.6778	3.01	0.0720	2.77	1007	11	1000	19	985	56	**1006**	**11**	102
b8	0.1698	1.36	1.7085	2.92	0.0730	2.58	1011	13	1012	19	1014	52	**1011**	**12**	100
c26	0.1713	2.12	1.6924	3.37	0.0717	2.62	1019	20	1006	22	977	53	**1014**	**19**	104
a4	0.1737	1.48	1.6916	2.15	0.0706	1.55	1033	14	1005	14	946	32	**1020**	**15**	109
b26	0.1724	1.11	1.7150	2.02	0.0722	1.69	1025	11	1014	13	991	34	**1022**	**10**	103
a2	0.1736	1.40	1.7654	3.74	0.0737	3.47	1032	13	1033	25	1034	70	**1032**	**13**	100
b50	0.1744	1.42	1.7380	2.82	0.0723	2.44	1037	14	1023	18	993	50	**1033**	**13**	104
b29	0.1735	1.65	1.7775	2.62	0.0743	2.04	1031	16	1037	17	1050	41	**1034**	**15**	98
a31	0.1739	0.97	1.7999	2.23	0.0751	2.00	1034	9	1045	15	1070	40	**1036**	**9**	97
b59	0.1750	0.74	1.7982	2.27	0.0745	2.14	1040	7	1045	15	1056	43	**1040**	**7**	98
b33	0.1756	1.37	1.7957	2.49	0.0742	2.08	1043	13	1044	16	1046	42	**1043**	**13**	100
a47	0.1770	1.50	1.7628	2.50	0.0722	1.53	1051	12	1032	13	992	31	**1044**	**12**	106
c19	0.1779	1.08	1.7832	3.35	0.0727	3.17	1056	11	1039	22	1005	64	**1054**	**10**	105
a34	0.1779	1.21	1.8213	2.58	0.0742	2.27	1056	12	1053	17	1048	46	**1055**	**11**	101
c28	0.1782	1.99	1.8465	3.52	0.0751	2.90	1057	19	1062	23	1072	58	**1059**	**19**	99
c8	0.1811	1.72	1.8313	3.70	0.0734	3.28	1073	17	1057	25	1024	66	**1070**	**16**	105
a36	0.1812	2.27	1.8420	5.05	0.0737	4.51	1074	22	1061	34	1034	91	**1071**	**22**	104
b43	0.1820	1.31	1.9728	2.80	0.0786	2.48	1078	13	1106	19	1162	49	**1083**	**13**	93
c16	0.1836	0.96	1.8629	3.47	0.0736	3.34	1086	10	1068	23	1031	68	**1085**	**10**	105
b42	0.1856	1.09	1.9109	2.45	0.0747	2.19	1097	11	1085	16	1060	44	**1095**	**11**	104
c10	0.1930	1.28	2.0656	2.54	0.0776	2.19	1138	13	1137	17	1137	44	**1138**	**13**	100
b39	0.2286	1.22	2.7530	2.48	0.0874	2.15	1327	15	1343	19	1368	41	**1331**	**14**	97
c20	0.3467	0.87	5.3800	1.42	0.1125	1.12	1919	15	1882	12	1841	20	**1841**	**20**	104
b41	0.3373	1.00	5.3962	2.14	0.1160	1.89	1873	16	1884	19	1896	34	**1878**	**15**	99
a20	0.3406	2.53	5.3642	3.37	0.1142	2.24	1889	42	1879	29	1868	40	**1878**	**29**	101
a15	0.3535	1.47	5.8339	1.62	0.1197	0.69	1951	25	1951	14	1952	12	**1952**	**12**	100
a1	0.3555	1.42	6.0245	2.21	0.1229	1.69	1961	24	1979	19	1999	30	**1975**	**24**	98
a45	0.3752	0.98	6.3588	1.71	0.1229	1.41	2054	17	2027	15	1999	25	**1999**	**25**	103
c30	0.3734	0.84	6.3485	1.39	0.1233	1.11	2045	15	2025	12	2005	20	**2005**	**20**	102
a8	0.3406	1.99	5.9162	2.92	0.1260	2.15	1890	33	1964	26	2043	38	**2043**	**38**	93
c14	0.3832	0.76	6.9227	1.31	0.1310	1.06	2091	14	2102	12	2112	19	**2098**	**11**	99
b34	0.3834	1.42	6.9644	2.01	0.1317	1.41	2092	25	2107	18	2121	25	**2107**	**18**	99
a44	0.3999	0.80	7.8364	1.20	0.1421	0.89	2169	15	2212	11	2253	15	**2253**	**15**	96
a53	0.4116	1.26	8.1400	1.80	0.1434	1.29	2222	24	2247	16	2269	22	**2269**	**22**	98
b58	0.4453	1.58	9.5166	2.14	0.1550	1.45	2374	31	2389	20	2402	25	**2391**	**20**	99
b22	0.4924	0.91	11.8433	1.37	0.1745	1.02	2581	19	2592	13	2601	17	**2601**	**17**	99

Sample GCZ-03	Isotopic ratios and 2σ (%) errors						Ages and 2σ absolute errors (Ma)						Reported Age		
continued	$^{206}Pb/^{238}U$	±2σ	$^{207}Pb/^{235}U$	±2σ	$^{207}Pb/^{206}Pb$	±2σ	$^{206}Pb/^{238}U$	±2σ	$^{207}Pb/^{235}U$	±2σ	$^{207}Pb/^{206}Pb$	±2σ	Age (Ma)	±2σ	conc %
a30	0.4838	1.10	11.6529	1.52	0.1747	1.04	2544	23	2577	14	2603	17	**2603**	**17**	98
a14	0.4556	1.01	11.0203	1.21	0.1754	0.67	2420	20	2525	11	2610	11	**2610**	**11**	93
a48	0.5364	1.24	13.2199	1.74	0.1787	1.21	2769	28	2695	17	2641	20	**2641**	**20**	105
a23	0.5068	1.24	12.5859	1.80	0.1801	1.31	2643	27	2649	17	2654	22	**2649**	**17**	100
b2	0.7122	1.98	28.6709	2.42	0.2920	1.39	3467	53	3442	24	3428	22	**3434**	**21**	101

Sample IBR-02	Isotopic ratios and 2σ (%) errors						Ages and 2σ absolute errors (Ma)						Reported Age		
Analysis	$^{206}Pb/^{238}U$	±2σ	$^{207}Pb/^{235}U$	±2σ	$^{207}Pb/^{206}Pb$	±2σ	$^{206}Pb/^{238}U$	±2σ	$^{207}Pb/^{235}U$	±2σ	$^{207}Pb/^{206}Pb$	±2σ	Age (Ma)	±2σ	conc %
a6	0.0809	1.99	0.6464	4.41	0.0580	3.94	501	10	506	18	529	86	**502**	**10**	95
a7	0.0829	1.28	0.6692	2.91	0.0586	2.61	513	6	520	12	551	57	**514**	**6**	93
a8	0.0888	0.85	0.7266	5.99	0.0594	5.93	548	4	555	26	581	129	**548**	**5**	94
a9	0.0916	1.52	0.7537	2.80	0.0597	2.35	565	8	570	12	591	51	**566**	**8**	96
a10	0.0917	1.47	0.7531	3.32	0.0596	2.98	565	8	570	15	588	65	**566**	**8**	96
a11	0.0925	2.26	0.7677	3.45	0.0602	2.60	571	12	578	15	609	56	**572**	**12**	94
a12	0.0931	2.20	0.7659	2.79	0.0596	1.72	574	12	577	12	591	37	**576**	**12**	97
a13	0.0946	2.19	0.7645	4.90	0.0586	4.38	583	12	577	22	553	96	**582**	**12**	105
a14	0.0951	1.37	0.7930	2.04	0.0605	1.51	586	8	593	9	620	33	**588**	**8**	94
a15	0.0955	2.02	0.8013	2.95	0.0609	2.15	588	11	598	13	635	46	**590**	**11**	93
a16	0.0965	1.20	0.7908	2.79	0.0594	2.52	594	7	592	13	583	55	**594**	**7**	102
a17	0.0968	1.52	0.7938	2.32	0.0595	1.76	596	9	593	10	585	38	**595**	**8**	102
a18	0.0971	1.76	0.8163	4.01	0.0610	3.60	598	10	606	18	638	77	**598**	**10**	94
a19	0.0973	1.54	0.8179	3.09	0.0610	2.68	598	9	607	14	639	58	**599**	**9**	94
a20	0.0973	2.04	0.8153	2.92	0.0608	2.10	598	12	605	13	632	45	**600**	**11**	95
a21	0.0983	1.59	0.8023	4.11	0.0592	3.78	605	9	598	19	573	82	**604**	**9**	106
a23	0.0985	2.43	0.8042	4.33	0.0592	3.58	606	14	599	20	575	78	**605**	**14**	105
a22	0.0985	1.84	0.8250	3.90	0.0607	3.45	606	11	611	18	630	74	**606**	**11**	96
a24	0.0995	2.11	0.8372	3.25	0.0611	2.48	611	12	618	15	641	53	**613**	**12**	95
a25	0.1000	1.95	0.8298	3.07	0.0602	2.36	614	11	613	14	611	51	**614**	**11**	101
a27	0.1004	3.67	0.8479	5.03	0.0613	3.44	616	22	624	24	649	74	**619**	**21**	95
a28	0.1014	2.41	0.8319	4.34	0.0595	3.61	623	14	615	20	585	78	**621**	**14**	106
a29	0.1015	1.10	0.8373	3.33	0.0598	3.14	623	7	618	16	597	68	**623**	**7**	104
a31	0.1020	2.04	0.8358	3.15	0.0594	2.40	626	12	617	15	582	52	**624**	**12**	108
a30	0.1020	1.77	0.8517	3.01	0.0606	2.43	626	11	626	14	625	52	**626**	**10**	100
a32	0.1025	1.56	0.8469	2.37	0.0599	1.78	629	9	623	11	600	39	**628**	**9**	105
a33	0.1027	2.19	0.8609	4.89	0.0608	4.37	630	13	631	23	632	94	**630**	**13**	100

Sample IBR-02 continued	Isotopic ratios and 2σ (%) errors						Ages and 2σ absolute errors (Ma)						Reported Age		
	$^{206}Pb/^{238}U$	±2σ	$^{207}Pb/^{235}U$	±2σ	$^{207}Pb/^{206}Pb$	±2σ	$^{206}Pb/^{238}U$	±2σ	$^{207}Pb/^{235}U$	±2σ	$^{207}Pb/^{206}Pb$	±2σ	Age (Ma)	±2σ	conc %
a34	0.1028	0.99	0.8530	2.18	0.0602	1.95	631	6	626	10	611	42	**630**	**6**	103
a35	0.1031	1.58	0.8706	2.70	0.0612	2.18	633	10	636	13	647	47	**633**	**9**	98
a38	0.1070	1.88	0.8923	4.36	0.0605	3.93	656	12	648	21	620	85	**655**	**12**	106
a40	0.1074	2.20	0.9282	5.53	0.0627	5.07	658	14	667	27	697	108	**658**	**14**	94
a42	0.1081	2.89	0.9289	5.60	0.0623	4.80	661	18	667	28	686	102	**662**	**18**	96
a43	0.1083	1.76	0.9117	4.04	0.0611	3.63	663	11	658	20	642	78	**662**	**11**	103
a44	0.1084	1.11	0.9168	2.40	0.0613	2.13	663	7	661	12	651	46	**663**	**7**	102
a46	0.1091	2.24	0.9233	4.45	0.0614	3.85	668	14	664	22	652	83	**667**	**14**	102
a45	0.1090	1.28	0.9368	2.37	0.0623	2.00	667	8	671	12	685	43	**668**	**8**	97
a48	0.1118	2.33	0.9808	3.88	0.0636	3.10	683	15	694	20	729	66	**685**	**15**	94
a49	0.1125	1.52	0.9749	2.52	0.0629	2.00	687	10	691	13	704	43	**688**	**10**	98
a50	0.1130	1.96	0.9511	3.54	0.0610	2.94	690	13	679	18	640	63	**688**	**13**	108
a53	0.1146	2.27	0.9808	3.58	0.0621	2.77	699	15	694	18	677	59	**698**	**15**	103
a52	0.1144	4.25	1.0003	4.65	0.0634	1.90	698	28	704	24	723	40	**706**	**23**	97
a55	0.1171	1.14	1.0337	2.02	0.0640	1.67	714	8	721	10	742	35	**715**	**8**	96
a54	0.1169	1.98	1.0293	2.44	0.0639	1.42	712	13	719	13	738	30	**716**	**12**	97
a56	0.1181	1.77	1.0605	2.78	0.0651	2.14	720	12	734	15	778	45	**723**	**12**	93
a57	0.1205	1.48	1.0440	2.13	0.0628	1.53	734	10	726	11	703	33	**731**	**10**	104
a58	0.1247	1.42	1.0909	2.20	0.0635	1.68	757	10	749	12	724	36	**755**	**10**	105
a60	0.1370	1.68	1.2374	3.38	0.0655	2.93	828	13	818	19	791	62	**826**	**13**	105
b1	0.1378	1.18	1.2824	2.65	0.0675	2.37	832	9	838	15	853	49	**833**	**9**	98
b2	0.1385	1.23	1.3018	2.30	0.0682	1.94	836	10	847	13	874	40	**838**	**9**	96
b3	0.1389	1.75	1.3028	3.68	0.0680	3.24	839	14	847	21	869	67	**840**	**14**	97
b4	0.1395	1.06	1.2981	2.08	0.0675	1.79	842	8	845	12	852	37	**843**	**8**	99
b5	0.1405	1.48	1.3276	2.38	0.0685	1.86	848	12	858	14	884	38	**851**	**11**	96
b7	0.1424	1.71	1.3140	3.06	0.0669	2.54	858	14	852	18	835	53	**857**	**13**	103
b6	0.1422	1.54	1.3485	2.41	0.0688	1.85	857	12	867	14	892	38	**860**	**12**	96
b8	0.1434	1.46	1.3779	4.35	0.0697	4.10	864	12	880	26	920	84	**865**	**12**	94
b9	0.1486	2.49	1.4189	6.70	0.0693	6.22	893	21	897	41	907	128	**893**	**21**	98
b10	0.1505	1.03	1.4326	2.27	0.0691	2.02	904	9	903	14	901	42	**903**	**9**	100
b11	0.1516	1.65	1.4594	4.00	0.0698	3.65	910	14	914	24	923	75	**910**	**14**	99
b12	0.1530	1.34	1.5012	3.16	0.0712	2.86	918	11	931	19	962	58	**919**	**11**	95
b13	0.1550	2.51	1.4732	3.27	0.0690	2.09	929	22	919	20	897	43	**922**	**19**	103
b14	0.1557	1.42	1.5272	2.17	0.0711	1.63	933	12	941	13	961	33	**936**	**12**	97
b15	0.1575	1.13	1.5386	2.03	0.0709	1.69	943	10	946	13	953	35	**944**	**10**	99
b16	0.1581	1.56	1.5542	2.83	0.0713	2.36	946	14	952	18	965	48	**948**	**13**	98

Sample IBR-02 continued	Isotopic ratios and 2σ (%) errors						Ages and 2σ absolute errors (Ma)						Reported Age		
	$^{206}Pb/^{238}U$	±2σ	$^{207}Pb/^{235}U$	±2σ	$^{207}Pb/^{206}Pb$	±2σ	$^{206}Pb/^{238}U$	±2σ	$^{207}Pb/^{235}U$	±2σ	$^{207}Pb/^{206}Pb$	±2σ	Age (Ma)	±2σ	conc %
b17	0.1587	0.90	1.5682	1.62	0.0717	1.35	950	8	958	10	976	27	**952**	**8**	97
b18	0.1588	1.62	1.5602	2.34	0.0713	1.69	950	14	955	15	965	34	**952**	**13**	98
b20	0.1604	1.16	1.5644	2.25	0.0707	1.92	959	10	956	14	950	39	**958**	**10**	101
b19	0.1596	2.42	1.6049	3.33	0.0729	2.29	955	21	972	21	1012	46	**964**	**20**	94
b21	0.1613	2.23	1.5813	3.45	0.0711	2.64	964	20	963	22	960	54	**964**	**19**	100
b22	0.1621	2.14	1.6197	3.84	0.0725	3.19	968	19	978	24	999	65	**971**	**19**	97
b23	0.1623	1.34	1.6161	2.15	0.0722	1.68	970	12	976	14	992	34	**972**	**11**	98
b24	0.1654	1.73	1.6097	2.83	0.0706	2.24	987	16	974	18	945	46	**982**	**15**	104
b28	0.1664	1.07	1.6180	1.90	0.0705	1.57	992	10	977	12	944	32	**988**	**10**	105
b26	0.1663	1.25	1.6506	1.84	0.0720	1.35	991	11	990	12	986	27	**991**	**11**	101
b27	0.1664	1.55	1.6450	3.05	0.0717	2.63	992	14	988	19	978	54	**991**	**14**	101
b29	0.1667	1.65	1.6582	2.53	0.0721	1.92	994	15	993	16	989	39	**994**	**14**	100
b31	0.1669	1.71	1.6728	2.37	0.0727	1.64	995	16	998	15	1005	33	**997**	**14**	99
b30	0.1668	1.61	1.7202	2.98	0.0748	2.51	994	15	1016	19	1063	50	**999**	**15**	94
b25	0.1655	2.72	1.6645	2.90	0.0730	1.03	987	25	995	19	1013	21	**1002**	**16**	97
b33	0.1691	1.49	1.6778	2.27	0.0720	1.72	1007	14	1000	15	985	35	**1004**	**13**	102
b32	0.1689	1.76	1.6874	3.27	0.0725	2.75	1006	16	1004	21	999	56	**1005**	**16**	101
b34	0.1695	1.47	1.7084	2.72	0.0731	2.28	1010	14	1012	18	1016	46	**1010**	**13**	99
b35	0.1697	1.28	1.7071	2.37	0.0729	1.99	1011	12	1011	15	1012	40	**1011**	**11**	100
b36	0.1702	1.79	1.7081	2.69	0.0728	2.01	1013	17	1012	17	1008	41	**1013**	**16**	101
b37	0.1711	1.36	1.7671	2.74	0.0749	2.38	1018	13	1033	18	1066	48	**1021**	**12**	96
b38	0.1723	1.39	1.7285	2.29	0.0728	1.82	1025	13	1019	15	1008	37	**1023**	**12**	102
b39	0.1738	1.59	1.7427	2.70	0.0727	2.18	1033	15	1024	18	1006	44	**1030**	**14**	103
b40	0.1744	1.87	1.7574	2.96	0.0731	2.30	1036	18	1030	19	1016	47	**1034**	**17**	102
b41	0.1751	1.50	1.7721	4.52	0.0734	4.27	1040	14	1035	30	1025	86	**1040**	**14**	101
b42	0.1756	1.37	1.7911	2.04	0.0740	1.50	1043	13	1042	13	1041	30	**1043**	**12**	100
b43	0.1769	2.24	1.8179	3.63	0.0745	2.86	1050	22	1052	24	1056	58	**1051**	**20**	99
b44	0.1797	2.10	1.8081	3.81	0.0730	3.19	1065	21	1048	25	1014	65	**1060**	**20**	105
b46	0.1802	1.77	1.8076	2.87	0.0728	2.26	1068	17	1048	19	1007	46	**1060**	**17**	106
b45	0.1801	1.46	1.8509	4.44	0.0745	4.20	1068	14	1064	30	1056	84	**1067**	**14**	101
b48	0.1836	2.47	1.9006	3.93	0.0751	3.06	1087	25	1081	27	1071	61	**1084**	**23**	102
b49	0.1867	2.61	1.9640	7.40	0.0763	6.93	1104	27	1103	51	1103	139	**1104**	**26**	100
b50	0.1912	0.81	2.0398	2.15	0.0774	1.99	1128	8	1129	15	1131	40	**1128**	**8**	100
b54	0.2372	1.43	2.8597	2.58	0.0875	2.15	1372	18	1371	20	1370	41	**1372**	**16**	100
b59	0.2900	2.86	4.2342	3.43	0.1059	1.90	1642	42	1681	29	1730	35	**1730**	**35**	95
a4	0.3301	1.97	5.0457	2.62	0.1109	1.73	1839	32	1827	22	1814	31	**1826**	**22**	101

Sample IBR-02	Isotopic ratios and 2σ (%) errors						Ages and 2σ absolute errors (Ma)						Reported Age		
continued	$^{206}Pb/^{238}U$	±2σ	$^{207}Pb/^{235}U$	±2σ	$^{207}Pb/^{206}Pb$	±2σ	$^{206}Pb/^{238}U$	±2σ	$^{207}Pb/^{235}U$	±2σ	$^{207}Pb/^{206}Pb$	±2σ	Age (Ma)	±2σ	conc %
a5	0.3307	1.76	5.0810	2.58	0.1114	1.88	1842	28	1833	22	1823	34	**1834**	**22**	101
b60	0.3150	1.81	4.8847	2.39	0.1125	1.56	1765	28	1800	20	1840	28	**1840**	**28**	96
a2	0.3244	1.43	5.1848	1.94	0.1159	1.31	1811	23	1850	17	1894	24	**1894**	**24**	96
a8	0.3488	2.32	5.5185	2.81	0.1148	1.57	1929	39	1903	24	1876	28	**1895**	**24**	103
c1	0.3224	1.39	5.2636	1.90	0.1184	1.30	1801	22	1863	16	1932	23	**1932**	**23**	93
a3	0.3247	0.97	5.3682	2.50	0.1199	2.30	1813	15	1880	22	1955	41	**1955**	**41**	93
a6	0.3395	1.94	5.6725	2.29	0.1212	1.22	1884	32	1927	20	1974	22	**1974**	**22**	95
a12	0.3743	1.35	6.2582	2.30	0.1213	1.86	2050	24	2013	20	1975	33	**1975**	**33**	104
a13	0.3811	1.10	6.4631	1.86	0.1230	1.49	2081	20	2041	16	2000	27	**2000**	**27**	104
a7	0.3399	2.34	5.7667	2.89	0.1231	1.69	1886	38	1941	25	2001	30	**2001**	**30**	94
a9	0.3636	1.91	6.2894	2.95	0.1254	2.25	1999	33	2017	26	2035	40	**2014**	**26**	98
a10	0.3649	1.81	6.2794	1.99	0.1248	0.82	2005	31	2016	18	2026	15	**2022**	**14**	99
a16	0.3836	2.04	6.5901	2.92	0.1246	2.09	2093	37	2058	26	2023	37	**2059**	**26**	103
a15	0.3830	1.81	7.3545	2.42	0.1393	1.60	2090	32	2155	22	2218	28	**2218**	**28**	94
a17	0.4170	1.80	7.6967	6.22	0.1339	5.95	2247	34	2196	57	2149	104	**2236**	**32**	105
a18	0.4419	1.13	9.4431	1.69	0.1550	1.26	2359	22	2382	16	2402	21	**2402**	**21**	98
a20	0.4515	1.28	10.2375	1.49	0.1644	0.76	2402	26	2456	14	2502	13	**2502**	**13**	96
a22	0.4633	2.40	10.6287	2.53	0.1664	0.80	2454	49	2491	24	2522	13	**2522**	**13**	97
a24	0.4698	1.47	11.1712	1.80	0.1724	1.05	2483	30	2538	17	2582	17	**2582**	**17**	96
a21	0.4618	0.92	11.0328	1.36	0.1733	1.01	2447	19	2526	13	2590	17	**2590**	**17**	95
a27	0.4980	1.23	11.8528	1.80	0.1726	1.31	2605	26	2593	17	2583	22	**2593**	**17**	101
a23	0.4688	1.84	11.2262	2.21	0.1737	1.23	2478	38	2542	21	2593	20	**2593**	**20**	96
a26	0.4892	1.36	11.9062	1.83	0.1765	1.22	2567	29	2597	17	2621	20	**2621**	**20**	98
a25	0.4710	2.01	11.4653	2.57	0.1765	1.60	2488	42	2562	24	2621	27	**2621**	**27**	95
a28	0.5176	2.00	13.1076	2.24	0.1837	1.01	2689	44	2687	21	2686	17	**2687**	**17**	100
a29	0.5349	1.72	13.6770	1.90	0.1855	0.80	2762	39	2728	18	2702	13	**2702**	**13**	102

Sample SCS-05	Isotopic ratios and 2σ (%) errors						Ages and 2σ absolute errors (Ma)						Reported Age		
Analysis	$^{206}Pb/^{238}U$	±2σ	$^{207}Pb/^{235}U$	±2σ	$^{207}Pb/^{206}Pb$	±2σ	$^{206}Pb/^{238}U$	±2σ	$^{207}Pb/^{235}U$	±2σ	$^{207}Pb/^{206}Pb$	±2σ	Age (Ma)	±2σ	conc %
b30	0.0827	1.69	0.6598	3.06	0.0578	2.54	512	8	514	12	523	56	**513**	**8**	98
c47	0.0900	2.88	0.7300	5.81	0.0588	5.04	556	15	557	25	561	110	**556**	**15**	99
a43	0.0979	1.69	0.8156	4.18	0.0604	3.82	602	10	606	19	618	83	**603**	**10**	97
a58	0.0987	3.67	0.8381	7.58	0.0616	6.64	607	21	618	36	661	142	**608**	**21**	92
a49	0.0992	1.42	0.8108	2.21	0.0593	1.70	610	8	603	10	577	37	**608**	**8**	106

Sample SCS-05 continued	Isotopic ratios and 2σ (%) errors						Ages and 2σ absolute errors (Ma)						Reported Age		
	$^{206}Pb/^{238}U$	±2σ	$^{207}Pb/^{235}U$	±2σ	$^{207}Pb/^{206}Pb$	±2σ	$^{206}Pb/^{238}U$	±2σ	$^{207}Pb/^{235}U$	±2σ	$^{207}Pb/^{206}Pb$	±2σ	Age (Ma)	±2σ	conc %
a17	0.0992	1.31	0.8179	3.94	0.0598	3.71	609	8	607	18	597	80	**609**	**8**	102
a44	0.0993	2.77	0.8281	5.17	0.0605	4.37	610	16	613	24	622	94	**610**	**16**	98
a3	0.0993	1.82	0.8482	3.89	0.0620	3.44	610	11	624	18	673	74	**611**	**11**	91
c31	0.0994	2.01	0.8352	3.68	0.0609	3.09	611	12	616	17	636	66	**612**	**12**	96
a4	0.1005	1.15	0.8536	2.63	0.0616	2.37	618	7	627	12	660	51	**618**	**7**	94
c43	0.1009	2.03	0.8365	2.96	0.0601	2.16	620	12	617	14	608	47	**619**	**12**	102
a39	0.1018	1.54	0.8338	2.54	0.0594	2.02	625	9	616	12	582	44	**623**	**9**	107
c5	0.1025	1.95	0.8556	4.44	0.0605	3.99	629	12	628	21	623	86	**629**	**12**	101
b40	0.1022	2.99	0.8712	4.30	0.0618	3.10	627	18	636	21	668	66	**630**	**17**	94
c46	0.1034	2.03	0.8775	2.88	0.0616	2.04	634	12	640	14	659	44	**636**	**12**	96
c12	0.1051	1.86	0.8727	3.47	0.0602	2.93	644	11	637	17	612	63	**643**	**11**	105
c33	0.1054	1.21	0.8779	3.31	0.0604	3.08	646	7	640	16	619	66	**646**	**7**	104
c35	0.1055	0.99	0.9181	2.90	0.0631	2.73	646	6	661	14	713	58	**647**	**6**	91
b19	0.1064	1.69	0.8827	3.71	0.0602	3.31	652	10	642	18	610	72	**651**	**10**	107
a7	0.1065	1.80	0.9000	4.42	0.0613	4.04	653	11	652	21	649	87	**653**	**11**	101
b29	0.1067	1.67	0.9208	4.15	0.0626	3.80	654	10	663	20	694	81	**654**	**10**	94
a2	0.1074	1.81	0.9303	2.62	0.0628	1.90	658	11	668	13	703	40	**661**	**11**	94
c10	0.1085	1.29	0.9119	2.68	0.0610	2.35	664	8	658	13	638	50	**663**	**11**	104
a8	0.1084	1.72	0.9280	4.23	0.0621	3.86	664	11	667	21	677	83	**664**	**11**	98
c50	0.1090	1.50	0.9296	3.13	0.0618	2.74	667	10	667	15	669	59	**667**	**9**	100
a23	0.1094	1.31	0.9110	1.99	0.0604	1.50	669	8	658	10	618	32	**667**	**8**	108
c27	0.1099	1.42	0.9294	2.28	0.0613	1.79	672	9	667	11	651	38	**671**	**9**	103
b46	0.1101	2.62	0.9216	6.57	0.0607	6.03	673	17	663	33	629	130	**673**	**17**	107
b34	0.1106	2.08	0.9593	5.75	0.0629	5.36	676	13	683	29	705	114	**677**	**13**	96
b17	0.1119	1.22	0.9458	1.73	0.0613	1.22	684	8	676	9	649	26	**681**	**8**	105
b10	0.1120	3.13	0.9540	4.80	0.0618	3.64	684	20	680	24	667	78	**683**	**20**	103
c23	0.1125	1.60	0.9426	2.58	0.0608	2.02	687	10	674	13	632	44	**684**	**10**	109
c30	0.1122	1.26	0.9573	5.11	0.0619	4.95	685	8	682	26	671	106	**685**	**8**	102
b56	0.1129	1.82	0.9746	3.71	0.0626	3.23	689	12	691	19	695	69	**690**	**12**	99
a15	0.1137	2.24	0.9991	5.19	0.0637	4.68	694	15	703	27	732	99	**695**	**15**	95
c49	0.1143	1.93	1.0025	3.97	0.0636	3.47	698	13	705	20	729	74	**698**	**13**	96
b13	0.1153	2.78	0.9846	4.82	0.0619	3.94	704	19	696	25	671	84	**702**	**18**	105
c16	0.1218	1.88	1.0763	2.62	0.0641	1.82	741	13	742	14	745	39	**741**	**12**	99
c41	0.1242	1.37	1.0869	3.91	0.0635	3.66	755	10	747	21	725	78	**754**	**10**	104
a9	0.1283	3.90	1.1484	4.50	0.0649	2.24	778	29	777	25	772	47	**776**	**24**	101
b22	0.1299	3.82	1.1666	5.25	0.0651	3.61	787	28	785	29	779	76	**786**	**26**	101

Sample SCS-05 continued	Isotopic ratios and 2σ (%) errors						Ages and 2σ absolute errors (Ma)						Reported Age		
	$^{206}Pb/^{238}U$	±2σ	$^{207}Pb/^{235}U$	±2σ	$^{207}Pb/^{206}Pb$	±2σ	$^{206}Pb/^{238}U$	±2σ	$^{207}Pb/^{235}U$	±2σ	$^{207}Pb/^{206}Pb$	±2σ	Age (Ma)	±2σ	conc %
a27	0.1300	1.58	1.1896	3.20	0.0664	2.79	788	12	796	18	818	58	**789**	**12**	96
c48	0.1329	1.66	1.2130	3.11	0.0662	2.64	804	13	807	17	813	55	**805**	**12**	99
b12	0.1347	2.24	1.1918	4.25	0.0642	3.62	815	17	797	24	747	76	**811**	**17**	109
c15	0.1361	1.14	1.2660	3.09	0.0674	2.87	823	9	831	18	851	60	**823**	**9**	97
b24	0.1361	1.82	1.2628	2.99	0.0673	2.37	823	14	829	17	846	49	**825**	**14**	97
b4	0.1399	0.98	1.2766	2.28	0.0662	2.05	844	8	835	13	813	43	**843**	**8**	104
a14	0.1401	1.70	1.2736	3.29	0.0659	2.81	845	14	834	19	804	59	**843**	**13**	105
b45	0.1402	1.38	1.2654	2.82	0.0655	2.46	846	11	830	16	789	52	**843**	**11**	107
a57	0.1401	2.17	1.3229	3.07	0.0685	2.17	845	17	856	18	883	45	**850**	**16**	96
c24	0.1426	1.36	1.2960	3.88	0.0659	3.64	859	11	844	23	804	76	**858**	**11**	107
a26	0.1438	1.28	1.3283	2.61	0.0670	2.27	866	10	858	15	838	47	**865**	**10**	103
b20	0.1467	1.09	1.3414	3.04	0.0663	2.83	882	9	864	18	817	59	**881**	**9**	108
a5	0.1504	2.22	1.4804	4.26	0.0714	3.64	903	19	922	26	969	74	**907**	**18**	93
a10	0.1549	1.82	1.5063	2.69	0.0705	1.98	928	16	933	17	944	41	**930**	**15**	98
b47	0.1560	0.92	1.4632	2.30	0.0680	2.11	934	8	915	14	869	44	**932**	**8**	107
a46	0.1568	1.02	1.4960	3.02	0.0692	2.84	939	9	929	19	904	59	**938**	**9**	104
b38	0.1597	4.52	1.6411	10.67	0.0745	9.67	955	40	986	70	1056	195	**959**	**39**	90
a52	0.1626	2.39	1.5593	3.41	0.0696	2.43	971	22	954	21	915	50	**962**	**22**	106
a41	0.1619	1.65	1.6137	6.17	0.0723	5.94	967	15	976	39	994	121	**968**	**15**	97
c2	0.1630	2.20	1.5529	4.68	0.0691	4.13	973	20	952	29	902	85	**969**	**19**	108
b31	0.1639	1.10	1.6002	2.41	0.0708	2.15	979	10	970	15	952	44	**977**	**10**	103
c34	0.1645	1.04	1.6753	2.40	0.0739	2.16	982	9	999	15	1037	44	**984**	**9**	95
a42	0.1648	3.61	1.6890	9.21	0.0743	8.47	983	33	1004	61	1051	171	**985**	**32**	94
c11	0.1657	1.65	1.6228	3.54	0.0710	3.13	988	15	979	22	958	64	**987**	**15**	103
c29	0.1668	1.58	1.6072	3.14	0.0699	2.71	994	15	973	20	925	56	**989**	**15**	108
a25	0.1659	1.05	1.5895	2.17	0.0695	1.90	990	10	966	14	913	39	**990**	**10**	108
c25	0.1656	2.15	1.7132	4.07	0.0750	3.45	988	20	1013	26	1069	69	**993**	**20**	92
b54	0.1672	1.79	1.6782	2.93	0.0728	2.33	996	17	1000	19	1009	47	**998**	**16**	99
c21	0.1685	1.33	1.6804	3.79	0.0723	3.55	1004	12	1001	24	996	72	**1003**	**12**	101
c7	0.1681	1.51	1.7220	2.19	0.0743	1.58	1001	14	1017	14	1050	32	**1004**	**14**	95
a50	0.1685	1.20	1.7214	1.57	0.0741	1.01	1004	11	1017	10	1045	20	**1007**	**11**	96
c44	0.1699	2.36	1.7043	3.97	0.0728	3.20	1011	22	1010	26	1007	65	**1011**	**21**	100
a13	0.1712	1.54	1.7586	3.17	0.0745	2.77	1019	15	1030	21	1055	56	**1021**	**14**	97
a40	0.1719	1.43	1.7534	2.77	0.0740	2.37	1023	14	1028	18	1040	48	**1024**	**13**	98
c22	0.1729	1.70	1.7112	3.75	0.0718	3.35	1028	16	1013	24	980	68	**1025**	**16**	105
b60	0.1726	1.04	1.7533	3.68	0.0737	3.53	1026	10	1028	24	1033	71	**1026**	**10**	99

Sample SCS-05 continued	Isotopic ratios and 2σ (%) errors						Ages and 2σ absolute errors (Ma)						Reported Age		
	$^{206}Pb/^{238}U$	±2σ	$^{207}Pb/^{235}U$	±2σ	$^{207}Pb/^{206}Pb$	±2σ	$^{206}Pb/^{238}U$	±2σ	$^{207}Pb/^{235}U$	±2σ	$^{207}Pb/^{206}Pb$	±2σ	Age (Ma)	±2σ	conc %
b1	0.1727	2.21	1.7335	4.42	0.0728	3.83	1027	21	1021	29	1008	78	**1026**	**20**	102
a54	0.1732	2.51	1.7561	3.08	0.0735	1.78	1030	24	1029	20	1028	36	**1029**	**20**	100
a60	0.1743	1.47	1.7940	3.82	0.0747	3.53	1036	14	1043	25	1060	71	**1036**	**14**	98
b15	0.1768	2.45	1.7802	3.31	0.0730	2.23	1050	24	1038	22	1014	45	**1042**	**21**	103
a35	0.1780	2.19	1.7756	4.30	0.0723	3.70	1056	21	1037	28	995	75	**1051**	**20**	106
c36	0.1787	0.99	1.7894	2.04	0.0726	1.79	1060	10	1042	13	1003	36	**1056**	**10**	106
b51	0.1779	2.34	1.8488	5.21	0.0754	4.65	1056	23	1063	35	1078	93	**1057**	**22**	98
a19	0.1791	1.65	1.8152	4.39	0.0735	4.06	1062	16	1051	29	1028	82	**1061**	**16**	103
b26	0.1809	2.32	1.8052	3.77	0.0724	2.97	1072	23	1047	25	997	60	**1061**	**23**	108
b59	0.1796	2.60	1.8492	3.82	0.0747	2.80	1065	26	1063	26	1060	56	**1064**	**23**	100
c18	0.1807	1.59	1.8367	2.78	0.0737	2.29	1071	16	1059	18	1034	46	**1067**	**15**	104
a45	0.1823	1.68	1.8312	3.03	0.0729	2.52	1079	17	1057	20	1010	51	**1072**	**17**	107
a22	0.1818	1.29	1.8514	2.42	0.0739	2.05	1077	13	1064	16	1038	41	**1073**	**12**	104
b25	0.1815	1.47	1.8809	2.30	0.0752	1.78	1075	15	1074	15	1073	36	**1075**	**13**	100
c6	0.1826	1.23	1.8433	3.17	0.0732	2.93	1081	12	1061	21	1020	59	**1078**	**12**	106
b6	0.1811	2.66	1.9379	3.97	0.0776	2.95	1073	26	1094	27	1137	59	**1083**	**26**	94
c37	0.1853	1.08	1.8947	2.46	0.0742	2.21	1096	11	1079	16	1046	45	**1093**	**11**	105
a36	0.1867	1.34	1.8882	3.11	0.0734	2.80	1103	14	1077	21	1024	57	**1098**	**14**	108
b8	0.1872	1.43	1.8899	3.38	0.0732	3.06	1106	15	1078	23	1020	62	**1101**	**15**	108
b27	0.1878	1.76	1.9627	3.84	0.0758	3.41	1109	18	1103	26	1090	68	**1108**	**17**	102
b53	0.1913	0.78	1.9494	3.62	0.0739	3.53	1128	8	1098	25	1039	71	**1127**	**8**	109
b2	0.1917	2.18	2.0070	4.77	0.0759	4.24	1130	23	1118	33	1094	85	**1128**	**22**	103
a34	0.1943	1.42	2.1768	4.63	0.0813	4.41	1145	15	1174	33	1228	87	**1147**	**15**	93
b7	0.1993	2.12	2.0885	3.58	0.0760	2.89	1171	23	1145	25	1095	58	**1160**	**23**	107
a33	0.2168	1.56	2.5114	3.07	0.0840	2.65	1265	18	1275	23	1292	52	**1268**	**17**	98
b32	0.3162	1.30	4.7473	1.98	0.1089	1.49	1771	20	1776	17	1781	27	**1781**	**27**	99
c3	0.3028	1.11	4.6229	1.82	0.1107	1.44	1705	17	1753	15	1812	26	**1812**	**26**	94
b48	0.3646	1.63	5.6326	2.28	0.1121	1.60	2004	28	1921	20	1833	29	**1833**	**29**	109
a56	0.3000	2.24	4.6605	4.24	0.1127	3.60	1691	33	1760	36	1843	65	**1843**	**65**	92
b49	0.3493	1.12	5.4463	1.79	0.1131	1.39	1931	19	1892	15	1849	25	**1849**	**25**	104
c8	0.3265	3.27	5.0969	3.75	0.1132	1.83	1821	52	1836	32	1852	33	**1852**	**33**	98
b36	0.3474	0.81	5.4795	1.40	0.1144	1.14	1922	13	1897	12	1870	21	**1870**	**21**	103
a30	0.3500	1.04	5.6627	1.64	0.1173	1.27	1935	17	1926	14	1916	23	**1916**	**23**	101
c38	0.3282	1.16	5.3367	1.59	0.1179	1.08	1830	19	1875	14	1925	19	**1925**	**19**	95
b55	0.3767	1.25	6.1611	1.81	0.1186	1.30	2061	22	1999	16	1935	23	**1935**	**23**	106
a59	0.3301	1.25	5.4153	1.76	0.1190	1.23	1839	20	1887	15	1941	22	**1941**	**22**	95

Sample SCS-05 continued	Isotopic ratios and 2σ (%) errors						Ages and 2σ absolute errors (Ma)						Reported Age		
	$^{206}Pb/^{238}U$	±2σ	$^{207}Pb/^{235}U$	±2σ	$^{207}Pb/^{206}Pb$	±2σ	$^{206}Pb/^{238}U$	±2σ	$^{207}Pb/^{235}U$	±2σ	$^{207}Pb/^{206}Pb$	±2σ	Age (Ma)	±2σ	conc %
b50	0.3652	1.42	6.0914	1.69	0.1210	0.90	2007	25	1989	15	1971	16	**1971**	**16**	102
b44	0.3464	1.92	5.8505	3.06	0.1225	2.38	1917	32	1954	27	1993	42	**1993**	**42**	96
b37	0.3442	1.41	5.9622	2.72	0.1256	2.33	1907	23	1970	24	2038	41	**2038**	**41**	94
a20	0.3657	2.67	6.3589	3.39	0.1261	2.09	2009	46	2027	30	2044	37	**2044**	**37**	98
c39	0.3935	1.62	6.9127	3.01	0.1274	2.53	2139	30	2100	27	2062	45	**2062**	**45**	104
b23	0.3875	1.12	6.9246	2.07	0.1296	1.75	2111	20	2102	19	2092	31	**2092**	**31**	101
c42	0.3948	1.13	7.1099	1.92	0.1306	1.55	2145	21	2125	17	2106	27	**2106**	**27**	102
b28	0.3727	1.13	7.0604	1.82	0.1374	1.43	2042	20	2119	16	2195	25	**2195**	**25**	93
a53	0.4526	1.18	8.6627	1.34	0.1388	0.64	2407	24	2303	12	2212	11	**2212**	**11**	109
a12	0.4092	1.30	8.8284	2.07	0.1565	1.61	2211	24	2320	19	2418	27	**2418**	**27**	91
c26	0.4537	1.53	10.4734	1.80	0.1674	0.94	2412	31	2478	17	2532	16	**2532**	**16**	95
c14	0.4995	4.68	11.6205	4.76	0.1687	0.90	2612	101	2574	46	2545	15	**2545**	**15**	103
b41	0.4603	2.41	10.8522	2.57	0.1710	0.92	2441	49	2511	24	2567	15	**2567**	**15**	95
c1	0.4915	1.28	11.6090	1.97	0.1713	1.49	2577	27	2573	19	2570	25	**2570**	**25**	100
a6	0.4455	1.82	10.6041	1.94	0.1726	0.69	2375	36	2489	18	2583	11	**2583**	**11**	92
c19	0.5167	2.39	12.4188	2.68	0.1743	1.21	2685	53	2637	25	2599	20	**2599**	**20**	103
b52	0.5053	1.33	12.1727	2.37	0.1747	1.96	2637	29	2618	22	2603	33	**2603**	**33**	101
a18	0.4955	2.50	11.9932	3.30	0.1755	2.15	2594	54	2604	31	2611	36	**2611**	**36**	99
a48	0.4999	1.55	12.1284	2.05	0.1760	1.34	2613	33	2614	19	2615	22	**2615**	**22**	100
b35	0.4781	1.33	11.6153	1.78	0.1762	1.18	2519	28	2574	17	2617	20	**2617**	**20**	96
c45	0.5106	1.49	12.4313	1.99	0.1766	1.32	2659	33	2638	19	2621	22	**2621**	**22**	101
a47	0.5348	1.68	13.1913	1.95	0.1789	0.99	2762	38	2693	19	2642	16	**2642**	**16**	105
a38	0.5541	1.52	13.7443	1.90	0.1799	1.14	2842	35	2732	18	2652	19	**2652**	**19**	107
b9	0.5525	2.16	13.7499	3.58	0.1805	2.86	2836	50	2733	34	2657	47	**2657**	**47**	107
a21	0.5267	1.95	13.1564	2.07	0.1812	0.69	2728	44	2691	20	2664	11	**2664**	**11**	102
c40	0.5375	0.86	13.5270	1.27	0.1825	0.94	2773	19	2717	12	2676	16	**2676**	**16**	104
c17	0.5234	1.07	15.0642	1.21	0.2087	0.57	2714	24	2819	12	2896	9	**2896**	**9**	94

Sample LAZ-26	Isotopic ratios and 2σ (%) errors						Ages and 2σ absolute errors (Ma)						Reported Age		
Analysis	$^{206}Pb/^{238}U$	±2σ	$^{207}Pb/^{235}U$	±2σ	$^{207}Pb/^{206}Pb$	±2σ	$^{206}Pb/^{238}U$	±2σ	$^{207}Pb/^{235}U$	±2σ	$^{207}Pb/^{206}Pb$	±2σ	Age (Ma)	±2σ	conc %
d3	0.0816	2.64	0.6538	4.00	0.0581	3.00	506	13	511	16	533	66	**507**	**13**	95
a2	0.0832	1.85	0.6664	6.04	0.0581	5.75	515	9	518	25	533	126	**515**	**9**	97
c3	0.0835	2.28	0.6679	4.24	0.0580	3.57	517	11	519	17	531	78	**517**	**11**	97
b9	0.0845	4.38	0.6691	6.68	0.0574	5.05	523	22	520	28	507	111	**523**	**22**	103
c14	0.0850	1.73	0.6889	3.35	0.0588	2.87	526	9	532	14	559	63	**526**	**9**	94
a48	0.0893	1.36	0.7270	3.76	0.0591	3.50	551	7	555	16	569	76	**551**	**7**	97
a1	0.0896	1.29	0.7295	2.97	0.0591	2.68	553	7	556	13	569	58	**553**	**7**	97
a23	0.0897	2.02	0.7444	3.15	0.0602	2.42	554	11	565	14	610	52	**556**	**11**	91
a4	0.0903	1.39	0.7349	3.38	0.0590	3.08	557	7	559	15	567	67	**558**	**7**	98
c8	0.0912	2.59	0.7454	4.34	0.0593	3.48	562	14	566	19	578	76	**563**	**14**	97
a33	0.0918	2.97	0.7506	6.65	0.0593	5.95	566	16	569	29	578	129	**566**	**16**	98
c48	0.0923	2.12	0.7614	3.00	0.0598	2.12	569	12	575	13	598	46	**571**	**11**	95
a8	0.0925	1.14	0.7755	3.53	0.0608	3.35	571	6	583	16	631	72	**571**	**6**	90
c57	0.0931	3.23	0.7731	7.06	0.0602	6.28	574	18	582	32	611	136	**575**	**18**	94
c51	0.0936	1.87	0.7663	4.21	0.0594	3.77	577	10	578	19	580	82	**577**	**10**	99
b29	0.0957	1.23	0.7961	2.80	0.0603	2.51	589	7	595	13	615	54	**590**	**7**	96
a18	0.0960	1.89	0.8019	4.41	0.0606	3.98	591	11	598	20	625	86	**591**	**11**	94
c36	0.0961	1.68	0.7960	3.13	0.0601	2.65	592	9	595	14	606	57	**592**	**9**	98
a46	0.0960	2.89	0.8075	3.93	0.0610	2.67	591	16	601	18	638	57	**594**	**16**	93
c15	0.0961	2.04	0.8139	3.06	0.0614	2.27	592	12	605	14	654	49	**594**	**12**	91
b3	0.0971	2.36	0.7940	5.03	0.0593	4.44	598	13	593	23	578	96	**597**	**13**	103
b30	0.0970	2.08	0.8135	4.21	0.0608	3.66	597	12	604	19	633	79	**598**	**12**	94
d9	0.0971	1.85	0.8012	4.33	0.0598	3.92	598	11	597	20	597	85	**598**	**11**	100
a28	0.0973	1.60	0.8207	3.86	0.0612	3.52	599	9	608	18	645	76	**599**	**9**	93
a54	0.0981	1.91	0.8001	4.03	0.0592	3.55	603	11	597	18	573	77	**602**	**11**	105
b19	0.0980	1.54	0.8225	2.72	0.0609	2.24	603	9	609	13	635	48	**604**	**9**	95
c27	0.0982	2.61	0.8154	4.67	0.0602	3.86	604	15	606	22	612	83	**604**	**15**	99
c31	0.0985	2.20	0.8181	3.43	0.0602	2.63	606	13	607	16	612	57	**606**	**12**	99
a43	0.0993	1.33	0.8224	2.45	0.0600	2.06	610	8	609	11	605	45	**610**	**8**	101
b28	0.0996	1.40	0.8094	2.70	0.0589	2.31	612	8	602	12	565	50	**611**	**8**	108
b7	0.0996	1.88	0.8150	4.64	0.0593	4.24	612	11	605	21	579	92	**612**	**11**	106
b22	0.1004	1.69	0.8205	2.28	0.0593	1.53	617	10	608	10	578	33	**613**	**10**	107
a55	0.0996	1.88	0.8466	3.56	0.0616	3.02	612	11	623	17	661	65	**614**	**11**	93
a34	0.0998	2.58	0.8438	4.52	0.0613	3.70	613	15	621	21	650	80	**615**	**15**	94
a50	0.1001	2.22	0.8249	7.97	0.0598	7.66	615	13	611	37	595	166	**615**	**13**	103
c39	0.1009	2.53	0.8482	3.49	0.0610	2.41	620	15	624	16	638	52	**621**	**14**	97

Sample LAZ-26 continued	Isotopic ratios and 2σ (%) errors						Ages and 2σ absolute errors (Ma)						Reported Age		
	$^{206}Pb/^{238}U$	±2σ	$^{207}Pb/^{235}U$	±2σ	$^{207}Pb/^{206}Pb$	±2σ	$^{206}Pb/^{238}U$	±2σ	$^{207}Pb/^{235}U$	±2σ	$^{207}Pb/^{206}Pb$	±2σ	Age (Ma)	±2σ	conc %
d10	0.1011	1.26	0.8497	2.43	0.0610	2.08	621	7	624	11	638	45	**621**	**7**	97
a57	0.1017	2.30	0.8374	3.52	0.0597	2.66	624	14	618	16	593	58	**623**	**13**	105
c50	0.1020	1.55	0.8514	3.51	0.0605	3.15	626	9	625	17	623	68	**626**	**9**	100
a30	0.1021	2.64	0.8524	3.56	0.0605	2.39	627	16	626	17	623	52	**627**	**15**	101
b16	0.1024	1.17	0.8437	3.37	0.0598	3.16	628	7	621	16	596	68	**628**	**7**	105
c58	0.1029	1.82	0.8504	2.74	0.0600	2.05	631	11	625	13	602	44	**629**	**11**	105
a24	0.1037	1.60	0.8570	4.22	0.0600	3.91	636	10	628	20	602	85	**635**	**10**	106
a31	0.1043	1.86	0.8751	4.75	0.0608	4.37	640	11	638	23	634	94	**639**	**11**	101
d7	0.1047	1.68	0.8708	3.52	0.0603	3.09	642	10	636	17	614	67	**641**	**10**	105
c34	0.1047	1.92	0.8813	5.66	0.0611	5.33	642	12	642	27	641	115	**642**	**12**	100
a6	0.1050	1.48	0.8674	2.54	0.0599	2.07	643	9	634	12	602	45	**642**	**9**	107
a51	0.1042	2.98	0.9011	4.19	0.0627	2.95	639	18	652	20	698	63	**643**	**18**	92
a36	0.1051	1.55	0.9062	4.25	0.0625	3.96	644	9	655	21	692	84	**645**	**10**	93
b4	0.1053	2.28	0.8877	6.52	0.0612	6.11	645	14	645	32	645	131	**645**	**14**	100
d8	0.1057	1.97	0.8779	3.55	0.0602	2.95	648	12	640	17	612	64	**646**	**12**	106
a42	0.1057	1.59	0.8846	3.05	0.0607	2.61	647	10	643	15	630	56	**647**	**10**	103
b14	0.1068	2.01	0.8931	5.18	0.0607	4.77	654	13	648	25	628	103	**653**	**12**	104
a44	0.1068	1.54	0.8826	3.17	0.0599	2.77	654	10	642	15	601	60	**653**	**10**	109
c20	0.1072	1.56	0.9066	2.74	0.0613	2.25	657	10	655	13	650	48	**656**	**10**	101
c47	0.1075	2.25	0.8970	5.74	0.0605	5.28	658	14	650	28	623	114	**657**	**14**	106
b27	0.1077	2.19	0.9128	3.39	0.0615	2.59	659	14	659	17	656	56	**659**	**13**	100
c13	0.1077	3.47	0.8961	9.58	0.0603	8.93	659	22	650	47	616	193	**659**	**22**	107
a47	0.1079	2.35	0.9045	4.16	0.0608	3.44	661	15	654	20	632	74	**659**	**14**	105
c30	0.1079	2.70	0.9456	4.00	0.0636	1.36	660	11	676	11	727	29	**663**	**11**	91
c45	0.1089	1.37	0.9163	3.03	0.0610	2.70	666	9	660	15	641	58	**666**	**9**	104
c9	0.1091	1.78	0.9264	4.04	0.0616	3.63	667	11	666	20	660	78	**667**	**11**	101
b10	0.1091	1.39	0.9223	4.57	0.0613	4.35	667	9	664	23	651	93	**667**	**9**	103
a13	0.1092	3.10	0.9434	11.19	0.0626	10.75	668	20	675	57	696	229	**669**	**20**	96
a14	0.1095	2.72	0.9279	7.38	0.0615	6.86	670	17	667	37	655	147	**670**	**17**	102
c4	0.1101	1.65	0.9191	2.81	0.0606	2.28	673	11	662	14	624	49	**671**	**11**	108
c44	0.1097	2.15	0.9466	3.55	0.0626	2.82	671	14	676	18	694	60	**672**	**13**	97
b26	0.1099	3.15	0.9253	6.78	0.0610	6.00	672	20	665	34	641	129	**672**	**20**	105
b20	0.1104	1.64	0.9333	3.72	0.0613	3.34	675	11	669	18	650	72	**675**	**10**	104
c52	0.1111	2.57	0.9551	4.22	0.0624	3.35	679	17	681	21	686	72	**679**	**16**	99
b21	0.1118	1.01	0.9418	2.11	0.0611	1.86	683	7	674	10	643	40	**682**	**7**	106
a15	0.1125	1.87	0.9519	3.31	0.0614	2.73	687	12	679	17	652	59	**686**	**12**	105

Sample LAZ-26 continued	Isotopic ratios and 2σ (%) errors						Ages and 2σ absolute errors (Ma)						Reported Age		
	$^{206}Pb/^{238}U$	±2σ	$^{207}Pb/^{235}U$	±2σ	$^{207}Pb/^{206}Pb$	±2σ	$^{206}Pb/^{238}U$	±2σ	$^{207}Pb/^{235}U$	±2σ	$^{207}Pb/^{206}Pb$	±2σ	Age (Ma)	±2σ	conc %
a17	0.1125	2.47	0.9481	4.50	0.0611	3.76	687	16	677	22	643	81	**686**	**16**	107
b12	0.1125	2.01	0.9636	5.21	0.0621	4.81	687	13	685	26	679	103	**687**	**13**	101
c5	0.1121	2.28	0.9858	3.36	0.0638	2.47	685	15	697	17	734	52	**688**	**14**	93
c19	0.1141	1.77	1.0117	4.71	0.0643	4.37	697	12	710	24	751	92	**698**	**12**	93
a29	0.1152	1.77	0.9847	3.65	0.0620	3.19	703	12	696	19	673	68	**702**	**12**	104
b23	0.1232	1.91	1.0891	3.84	0.0641	3.33	749	14	748	21	746	70	**749**	**13**	100
a35	0.1238	2.87	1.0726	7.67	0.0628	7.11	752	20	740	41	703	151	**751**	**20**	107
a32	0.1294	2.74	1.1401	3.95	0.0639	2.85	784	20	773	22	739	60	**779**	**19**	106
a38	0.1292	2.10	1.1836	3.76	0.0665	3.12	783	16	793	21	821	65	**785**	**15**	95
b6	0.1312	3.36	1.1704	3.84	0.0647	1.88	795	25	787	21	765	40	**786**	**21**	104
c35	0.1325	3.25	1.2048	4.75	0.0659	3.47	802	25	803	27	805	73	**802**	**23**	100
b17	0.1320	3.16	1.2515	5.15	0.0687	4.07	799	24	824	30	891	84	**805**	**24**	90
c43	0.1394	1.95	1.2731	4.00	0.0662	3.49	841	15	834	23	814	73	**840**	**15**	103
c23	0.1411	1.41	1.3177	3.18	0.0677	2.86	851	11	854	19	860	59	**851**	**11**	99
b25	0.1506	0.98	1.4678	1.83	0.0707	1.54	904	8	917	11	948	32	**907**	**8**	95
d2	0.1536	1.92	1.4996	2.54	0.0708	1.66	921	17	930	16	952	34	**927**	**15**	97
c25	0.1554	1.95	1.4966	4.46	0.0698	4.01	931	17	929	27	923	82	**931**	**17**	101
b2	0.1556	1.97	1.5685	4.14	0.0731	3.64	932	17	958	26	1018	74	**936**	**17**	92
b18	0.1576	2.24	1.5412	3.92	0.0709	3.22	943	20	947	24	955	66	**944**	**19**	99
a45	0.1586	1.35	1.5040	2.48	0.0688	2.07	949	12	932	15	892	43	**945**	**12**	106
c49	0.1597	2.05	1.5435	3.38	0.0701	2.68	955	18	948	21	932	55	**952**	**17**	102
b13	0.1596	2.04	1.5592	4.25	0.0709	3.72	954	18	954	27	954	76	**954**	**18**	100
c41	0.1604	1.85	1.5740	2.59	0.0712	1.81	959	16	960	16	962	37	**960**	**15**	100
a16	0.1611	1.38	1.5953	3.30	0.0718	3.00	963	12	968	21	980	61	**964**	**12**	98
c17	0.1618	1.55	1.5981	1.77	0.0716	0.86	967	14	969	11	976	18	**970**	**11**	99
a49	0.1627	2.41	1.5833	5.16	0.0706	4.56	972	22	964	33	945	93	**970**	**21**	103
b24	0.1627	1.27	1.5906	2.37	0.0709	2.00	972	11	967	15	955	41	**970**	**11**	102
c40	0.1636	1.46	1.6574	2.70	0.0735	2.27	977	13	992	17	1028	46	**980**	**13**	95
c18	0.1661	2.37	1.6084	4.00	0.0702	1.25	991	22	973	17	934	26	**985**	**21**	106
a21	0.1664	1.33	1.6224	4.16	0.0707	3.95	992	12	979	27	949	81	**991**	**12**	104
a41	0.1690	1.82	1.7336	3.26	0.0744	2.70	1007	17	1021	21	1052	54	**1010**	**16**	96
c56	0.1702	2.08	1.7624	5.19	0.0751	4.76	1013	19	1032	34	1071	96	**1015**	**19**	95
c54	0.1715	2.45	1.7205	3.71	0.0728	2.79	1020	23	1016	24	1008	57	**1018**	**21**	101
a9	0.1715	2.44	1.7319	4.32	0.0732	3.57	1021	23	1020	28	1020	72	**1021**	**22**	100
a10	0.1718	1.17	1.7455	2.58	0.0737	2.30	1022	11	1026	17	1033	46	**1023**	**11**	99
a40	0.1742	2.21	1.7270	4.11	0.0719	3.47	1035	21	1019	27	983	71	**1030**	**20**	105

Sample LAZ-26 continued	Isotopic ratios and 2σ (%) errors						Ages and 2σ absolute errors (Ma)						Reported Age		
	$^{206}Pb/^{238}U$	±2σ	$^{207}Pb/^{235}U$	±2σ	$^{207}Pb/^{206}Pb$	±2σ	$^{206}Pb/^{238}U$	±2σ	$^{207}Pb/^{235}U$	±2σ	$^{207}Pb/^{206}Pb$	±2σ	Age (Ma)	±2σ	conc %
b11	0.1736	1.66	1.7525	3.65	0.0732	3.25	1032	16	1028	24	1020	66	**1031**	**15**	101
a27	0.1748	2.10	1.7182	3.70	0.0713	1.38	1038	13	1015	13	966	28	**1031**	**13**	107
a11	0.1734	1.78	1.8034	3.73	0.0754	3.27	1031	17	1047	25	1079	66	**1034**	**17**	96
c10	0.1775	1.66	1.7588	3.51	0.0719	3.10	1054	16	1030	23	982	63	**1049**	**16**	107
c60	0.1783	1.34	1.8415	2.87	0.0749	2.53	1058	13	1060	19	1066	51	**1058**	**13**	99
c53	0.1788	1.91	1.8523	3.26	0.0751	2.64	1060	19	1064	22	1072	53	**1062**	**18**	99
d1	0.1818	1.14	1.8272	2.24	0.0729	1.92	1077	11	1055	15	1011	39	**1071**	**11**	106
a26	0.1811	2.10	1.9375	4.00	0.0776	1.33	1073	15	1094	14	1136	26	**1076**	**15**	94
c6	0.1838	2.98	1.8773	4.42	0.0741	3.26	1088	30	1073	30	1044	66	**1080**	**27**	104
a52	0.1924	2.08	2.0095	6.38	0.0757	6.04	1135	22	1119	44	1088	121	**1133**	**21**	104
a60	0.2087	1.12	2.3449	2.42	0.0815	2.15	1222	12	1226	17	1233	42	**1223**	**12**	99
c28	0.2914	1.21	4.1644	2.78	0.1037	2.50	1648	18	1667	23	1691	46	**1691**	**46**	98
a5	0.3159	4.00	4.6039	5.83	0.1057	4.24	1770	62	1750	50	1727	78	**1727**	**50**	102
a58	0.2936	1.65	4.4195	2.32	0.1092	1.63	1659	24	1716	19	1786	30	**1786**	**30**	93
a25	0.3306	4.28	5.0539	5.48	0.1109	3.42	1841	69	1828	48	1814	62	**1814**	**62**	102
c16	0.3165	2.16	4.9095	2.70	0.1125	1.62	1772	33	1804	23	1840	29	**1840**	**29**	96
b8	0.3489	1.55	5.5970	2.81	0.1163	2.34	1930	26	1916	24	1901	42	**1901**	**42**	102
c22	0.3639	2.23	6.0638	2.57	0.1209	1.29	2001	38	1985	23	1969	23	**1969**	**23**	102
d5	0.3980	0.57	6.6447	1.91	0.1211	1.82	2160	10	2065	17	1972	32	**1972**	**32**	109
a20	0.3705	2.85	6.3270	3.40	0.1238	1.84	2032	50	2022	30	2012	33	**2012**	**33**	101
c26	0.3521	1.53	6.3229	2.18	0.1302	1.55	1945	26	2022	19	2101	27	**2101**	**27**	93
c32	0.3929	1.32	7.4114	1.89	0.1368	1.35	2136	24	2162	17	2187	23	**2187**	**23**	98
c42	0.4616	1.25	9.0809	1.89	0.1427	1.42	2446	25	2346	17	2260	25	**2260**	**25**	108
a12	0.4100	1.47	8.6505	2.04	0.1530	1.41	2215	28	2302	19	2380	24	**2380**	**24**	93
a39	0.4688	1.94	10.5222	2.21	0.1628	1.06	2478	40	2482	21	2485	18	**2485**	**18**	100
c21	0.5328	2.00	12.2667	2.47	0.1670	1.45	2753	45	2625	23	2528	24	**2528**	**24**	109
a59	0.4364	1.19	10.1507	1.77	0.1687	1.31	2335	23	2449	16	2545	22	**2545**	**22**	92
a53	0.4506	1.35	10.6391	1.61	0.1712	0.88	2398	27	2492	15	2570	15	**2570**	**15**	93
a56	0.4918	2.03	11.7183	2.31	0.1728	1.11	2578	43	2582	22	2585	18	**2585**	**18**	100
c37	0.4553	1.71	10.8878	1.88	0.1734	0.77	2419	35	2514	18	2591	13	**2591**	**13**	93
c55	0.4588	1.61	11.0766	2.55	0.1751	1.98	2434	33	2530	24	2607	33	**2607**	**33**	93
c38	0.5145	1.57	12.5357	1.88	0.1767	1.04	2676	34	2645	18	2622	17	**2622**	**17**	102
c59	0.6524	1.47	25.5044	1.77	0.2835	0.98	3238	38	3328	17	3382	15	**3382**	**15**	96

Sample LAZ-05	Isotopic ratios and 2σ (%) errors						Ages and 2σ absolute errors (Ma)						Reported Age		
Analysis	$^{206}Pb/^{238}U$	±2σ	$^{207}Pb/^{235}U$	±2σ	$^{207}Pb/^{206}Pb$	±2σ	$^{206}Pb/^{238}U$	±2σ	$^{207}Pb/^{235}U$	±2σ	$^{207}Pb/^{206}Pb$	±2σ	Age (Ma)	±2σ	conc %
c28	0.0773	2.30	0.6129	4.51	0.0575	3.88	480	11	485	18	510	85	**481**	**11**	94
c8	0.0794	1.36	0.6181	2.30	0.0565	1.86	493	6	489	9	470	41	**492**	**6**	105
c10	0.0800	1.41	0.6228	3.07	0.0565	2.73	496	7	492	12	471	60	**496**	**7**	105
c3	0.0800	1.25	0.6398	3.66	0.0580	3.43	496	6	502	15	530	75	**496**	**6**	94
c30	0.0802	1.39	0.6350	3.27	0.0574	2.96	497	7	499	13	509	65	**497**	**7**	98
a18	0.0805	1.76	0.6356	2.92	0.0573	2.33	499	8	500	12	501	51	**499**	**8**	100
a49	0.0806	1.32	0.6266	2.73	0.0564	2.39	500	6	494	11	468	53	**499**	**6**	107
b26	0.0809	1.56	0.6299	2.98	0.0565	2.54	501	8	496	12	472	56	**501**	**8**	106
b2	0.0810	2.10	0.6452	3.55	0.0578	2.86	502	10	506	14	520	63	**503**	**10**	97
a40	0.0813	1.46	0.6307	3.00	0.0563	2.61	504	7	497	12	464	58	**503**	**7**	109
a9	0.0812	2.40	0.6511	4.65	0.0582	3.99	503	12	509	19	536	87	**504**	**12**	94
b29	0.0815	1.64	0.6532	3.84	0.0581	3.47	505	8	510	16	535	76	**505**	**8**	94
c9	0.0815	1.80	0.6415	3.02	0.0571	2.43	505	9	503	12	495	53	**505**	**9**	102
a15	0.0815	2.16	0.6478	5.11	0.0576	4.63	505	10	507	21	516	102	**505**	**10**	98
a16	0.0816	1.62	0.6369	2.64	0.0566	2.08	505	8	500	10	477	46	**505**	**8**	106
b54	0.0817	1.52	0.6444	2.66	0.0572	2.18	506	7	505	11	500	48	**506**	**7**	101
a14	0.0819	1.21	0.6357	2.78	0.0563	2.50	507	6	500	11	465	55	**507**	**6**	109
b11	0.0826	1.07	0.6501	3.16	0.0571	2.98	512	5	509	13	494	66	**512**	**5**	104
b24	0.0827	1.33	0.6499	4.19	0.0570	3.98	512	7	508	17	492	88	**512**	**7**	104
b58	0.0853	1.45	0.6753	2.87	0.0574	2.47	527	7	524	12	508	54	**527**	**7**	104
a36	0.0860	1.45	0.6767	3.85	0.0571	3.57	532	7	525	16	495	79	**531**	**7**	107
a2	0.0874	2.56	0.6909	4.77	0.0573	4.03	540	13	533	20	504	89	**539**	**13**	107
a1	0.0880	2.20	0.6955	6.45	0.0573	6.06	544	11	536	27	505	133	**543**	**11**	108
a6	0.0881	1.67	0.7058	4.12	0.0581	3.77	545	9	542	17	533	82	**544**	**9**	102
b28	0.0885	2.03	0.7135	5.74	0.0585	5.37	547	11	547	25	547	117	**547**	**11**	100
b7	0.0921	1.26	0.7600	2.56	0.0598	2.23	568	7	574	11	598	48	**569**	**7**	95
b1	0.0925	2.14	0.7398	3.62	0.0580	2.92	570	12	562	16	531	64	**569**	**11**	107
c27	0.0932	1.65	0.7551	2.66	0.0588	2.09	574	9	571	12	559	46	**574**	**9**	103
b20	0.0945	2.18	0.7739	4.63	0.0594	4.08	582	12	582	21	581	89	**582**	**12**	100
c17	0.0946	1.12	0.7943	4.13	0.0609	3.98	583	6	594	19	636	86	**583**	**6**	92
c23	0.0949	1.31	0.7723	2.85	0.0591	2.52	584	7	581	13	569	55	**584**	**7**	103
a26	0.0962	1.30	0.8044	2.70	0.0606	2.37	592	7	599	12	627	51	**593**	**7**	95
b10	0.0968	1.29	0.7912	1.75	0.0593	1.19	596	7	592	8	578	26	**594**	**7**	103
c22	0.0971	1.54	0.7899	2.63	0.0590	2.14	598	9	591	12	566	46	**597**	**9**	106
a38	0.0977	1.32	0.7912	1.97	0.0587	1.46	601	8	592	9	557	32	**598**	**8**	108
b47	0.0974	1.87	0.8000	3.32	0.0596	2.74	599	11	597	15	587	60	**599**	**11**	102

Sample LAZ-05 continued	Isotopic ratios and 2σ (%) errors						Ages and 2σ absolute errors (Ma)						Reported Age		
	$^{206}Pb/^{238}U$	±2σ	$^{207}Pb/^{235}U$	±2σ	$^{207}Pb/^{206}Pb$	±2σ	$^{206}Pb/^{238}U$	±2σ	$^{207}Pb/^{235}U$	±2σ	$^{207}Pb/^{206}Pb$	±2σ	Age (Ma)	±2σ	conc %
c14	0.0975	1.78	0.7960	4.24	0.0592	3.85	600	10	595	19	576	84	**599**	**10**	104
c11	0.0978	1.36	0.7966	2.86	0.0590	2.52	602	8	595	13	569	55	**601**	**8**	106
b5	0.0984	2.09	0.8053	5.81	0.0593	5.42	605	12	600	27	579	118	**605**	**12**	104
b15	0.0984	2.08	0.8082	4.32	0.0595	3.78	605	12	601	20	587	82	**605**	**12**	103
c12	0.0989	1.54	0.8090	2.33	0.0593	1.75	608	9	602	11	579	38	**606**	**9**	105
a22	0.0982	1.84	0.8249	2.39	0.0609	1.52	604	11	611	11	637	33	**607**	**10**	95
c6	0.0991	1.49	0.8063	2.68	0.0590	2.23	609	9	600	12	567	49	**608**	**9**	107
b19	0.0988	2.92	0.8398	5.29	0.0617	4.41	607	17	619	25	662	95	**609**	**17**	92
b16	0.0989	1.93	0.8327	3.42	0.0610	2.82	608	11	615	16	641	61	**609**	**11**	95
b6	0.0998	1.62	0.8196	2.85	0.0596	2.35	613	9	608	13	587	51	**612**	**9**	104
b4	0.0999	1.78	0.8366	3.83	0.0608	3.39	614	10	617	18	631	73	**614**	**10**	97
c7	0.1000	1.17	0.8238	3.13	0.0598	2.91	614	7	610	14	595	63	**614**	**7**	103
a8	0.1002	1.11	0.8248	1.91	0.0597	1.56	616	6	611	9	592	34	**615**	**6**	104
c2	0.1004	1.40	0.8293	3.16	0.0599	2.84	617	8	613	15	601	61	**616**	**8**	103
a53	0.1004	2.19	0.8342	7.06	0.0603	6.71	617	13	616	33	613	145	**617**	**13**	101
a35	0.1011	1.61	0.8450	3.70	0.0606	3.33	621	10	622	17	625	72	**621**	**10**	99
b41	0.1014	1.86	0.8432	4.33	0.0603	3.91	623	11	621	20	615	84	**622**	**11**	101
c21	0.1015	0.96	0.8359	2.94	0.0598	2.78	623	6	617	14	595	60	**623**	**6**	105
a11	0.1013	1.66	0.8662	2.94	0.0620	2.42	622	10	634	14	675	52	**624**	**10**	92
a57	0.1018	1.41	0.8470	3.45	0.0604	3.14	625	8	623	16	616	68	**625**	**8**	101
a42	0.1027	3.70	0.8504	4.18	0.0600	1.95	630	22	625	20	605	42	**625**	**20**	104
a29	0.1022	1.98	0.8361	4.35	0.0593	3.87	627	12	617	20	580	84	**626**	**12**	108
a7	0.1027	1.69	0.8606	3.06	0.0608	2.56	630	10	630	14	631	55	**630**	**10**	100
a3	0.1027	3.55	0.8697	5.45	0.0614	4.13	630	21	635	26	654	89	**631**	**21**	96
c26	0.1035	0.80	0.8548	2.70	0.0599	2.58	635	5	627	13	601	56	**634**	**5**	106
c5	0.1041	1.43	0.8574	3.41	0.0597	3.10	638	9	629	16	594	67	**638**	**9**	107
b22	0.1041	2.78	0.8822	5.64	0.0614	4.91	639	17	642	27	655	105	**639**	**17**	98
c4	0.1057	1.33	0.8762	2.33	0.0601	1.91	648	8	639	11	608	41	**646**	**8**	106
b52	0.1056	1.22	0.8860	3.02	0.0608	2.76	647	8	644	15	633	59	**647**	**8**	102
b21	0.1057	1.48	0.8817	3.29	0.0605	2.94	648	9	642	16	621	64	**647**	**9**	104
b30	0.1059	1.69	0.8862	3.28	0.0607	2.81	649	10	644	16	628	61	**648**	**10**	103
b13	0.1061	1.74	0.8793	2.80	0.0601	2.20	650	11	641	13	606	47	**648**	**10**	107
a27	0.1061	2.29	0.8981	4.94	0.0614	4.38	650	14	651	24	653	94	**650**	**14**	99
b51	0.1063	1.78	0.9027	4.00	0.0616	3.59	651	11	653	19	660	77	**651**	**11**	99
a55	0.1063	1.58	0.8897	3.26	0.0607	2.86	651	10	646	16	628	62	**651**	**10**	104
b39	0.1067	1.96	0.9093	3.71	0.0618	3.15	654	12	657	18	667	67	**654**	**12**	98

Sample LAZ-05 continued	Isotopic ratios and 2σ (%) errors						Ages and 2σ absolute errors (Ma)						Reported Age		
	$^{206}Pb/^{238}U$	±2σ	$^{207}Pb/^{235}U$	±2σ	$^{207}Pb/^{206}Pb$	±2σ	$^{206}Pb/^{238}U$	±2σ	$^{207}Pb/^{235}U$	±2σ	$^{207}Pb/^{206}Pb$	±2σ	Age (Ma)	±2σ	conc %
a30	0.1069	2.06	0.8949	5.33	0.0607	4.92	655	13	649	26	630	106	**654**	**13**	104
b55	0.1069	2.12	0.8926	4.62	0.0606	4.11	655	13	648	22	624	89	**654**	**13**	105
b25	0.1073	1.39	0.8972	5.02	0.0606	4.82	657	9	650	24	627	104	**657**	**9**	105
a13	0.1076	1.98	0.9010	2.79	0.0607	1.96	659	12	652	14	629	42	**657**	**12**	105
b53	0.1078	1.58	0.9128	4.46	0.0614	4.17	660	10	659	22	653	90	**660**	**10**	101
a17	0.1087	2.27	0.9204	3.32	0.0614	2.42	665	14	663	16	655	52	**664**	**14**	102
b50	0.1091	1.49	0.9125	3.25	0.0607	2.88	667	9	658	16	628	62	**666**	**9**	106
a4	0.1099	1.45	0.9182	2.74	0.0606	2.32	672	9	661	13	624	50	**671**	**9**	108
b9	0.1102	1.79	0.9273	4.25	0.0611	3.86	674	11	666	21	641	83	**673**	**11**	105
a31	0.1102	3.25	0.9400	4.63	0.0618	3.31	674	21	673	23	668	71	**674**	**20**	101
b59	0.1116	1.25	0.9394	2.63	0.0611	2.31	682	8	673	13	642	50	**681**	**8**	106
a47	0.1121	2.98	0.9444	4.81	0.0611	3.78	685	19	675	24	643	81	**682**	**19**	107
a48	0.1121	1.63	0.9690	5.12	0.0627	4.86	685	11	688	26	698	103	**685**	**11**	98
a43	0.1122	1.68	0.9554	3.01	0.0618	2.49	685	11	681	15	666	53	**685**	**11**	103
a52	0.1126	1.61	0.9503	3.21	0.0612	2.78	688	11	678	16	646	60	**687**	**10**	106
b37	0.1129	1.95	0.9612	3.27	0.0617	2.63	690	13	684	16	665	56	**688**	**12**	104
b36	0.1133	1.65	0.9620	2.71	0.0616	2.15	692	11	684	14	659	46	**690**	**12**	105
a25	0.1146	1.27	0.9697	3.86	0.0614	3.65	700	8	688	20	652	78	**699**	**8**	107
b23	0.1152	1.81	0.9768	3.86	0.0615	3.41	703	12	692	20	656	73	**702**	**12**	107
b60	0.1157	1.29	0.9829	2.43	0.0616	2.05	705	9	695	12	662	44	**704**	**9**	107
a60	0.1183	1.56	1.0327	3.91	0.0633	3.59	721	11	720	20	719	76	**721**	**11**	100
a39	0.1199	1.64	1.0735	3.59	0.0649	3.19	730	11	740	19	772	67	**731**	**11**	95
a33	0.1203	1.74	1.0432	3.70	0.0629	3.27	732	12	726	19	705	70	**731**	**12**	104
b56	0.1268	2.50	1.1171	3.58	0.0639	2.57	769	18	762	19	739	54	**766**	**17**	104
a12	0.1274	1.43	1.1204	2.43	0.0638	1.96	773	10	763	13	735	42	**770**	**10**	105
b31	0.1287	1.58	1.1250	3.12	0.0634	2.69	781	12	765	17	721	57	**778**	**12**	108
b18	0.1292	1.94	1.1486	2.78	0.0645	1.99	783	14	777	15	758	42	**780**	**13**	103
b8	0.1341	1.73	1.2061	3.88	0.0652	3.47	811	13	803	22	781	73	**810**	**13**	104
b34	0.1363	1.27	1.2150	3.26	0.0646	3.01	824	10	807	18	763	63	**823**	**10**	108
b12	0.1415	2.16	1.2928	5.76	0.0663	5.34	853	17	843	34	815	112	**852**	**17**	105
c25	0.1445	0.99	1.3202	2.55	0.0663	2.35	870	8	855	15	815	49	**868**	**8**	107
a46	0.1468	2.68	1.3664	4.93	0.0675	4.14	883	22	875	29	853	86	**881**	**21**	104
b27	0.1487	1.76	1.3989	2.82	0.0683	2.20	893	15	888	17	876	46	**892**	**14**	102
c24	0.1518	1.54	1.4357	2.42	0.0686	1.88	911	13	904	15	886	39	**909**	**12**	103
b3	0.1543	1.50	1.4515	3.14	0.0682	2.76	925	13	910	19	875	57	**922**	**13**	106
a54	0.1556	1.17	1.4835	3.06	0.0691	2.83	932	10	924	19	903	58	**931**	**10**	103

Sample LAZ-05 continued	Isotopic ratios and 2σ (%) errors						Ages and 2σ absolute errors (Ma)						Reported Age		
	$^{206}Pb/^{238}U$	±2σ	$^{207}Pb/^{235}U$	±2σ	$^{207}Pb/^{206}Pb$	±2σ	$^{206}Pb/^{238}U$	±2σ	$^{207}Pb/^{235}U$	±2σ	$^{207}Pb/^{206}Pb$	±2σ	Age (Ma)	±2σ	conc %
a10	0.1588	2.30	1.4973	2.90	0.0684	1.22	950	13	929	12	880	25	**933**	**13**	108
c16	0.1571	1.35	1.5807	2.69	0.0730	2.33	941	12	963	17	1013	47	**945**	**12**	93
a19	0.1640	1.08	1.6627	2.94	0.0735	2.73	979	10	994	19	1028	55	**981**	**10**	95
b40	0.1647	0.94	1.6885	2.66	0.0744	2.49	983	9	1004	17	1051	50	**984**	**9**	93
b45	0.1685	2.18	1.6701	3.49	0.0719	2.73	1004	20	997	22	983	56	**1001**	**19**	102
a24	0.1685	1.06	1.6639	1.71	0.0716	1.35	1004	10	995	11	975	27	**1001**	**9**	103
a56	0.1681	1.85	1.6871	3.97	0.0728	3.51	1002	17	1004	26	1008	71	**1002**	**17**	99
c1	0.1707	1.24	1.7079	2.02	0.0726	1.59	1016	12	1011	13	1002	32	**1014**	**11**	101
a34	0.1759	1.69	1.7540	2.60	0.0723	1.98	1044	16	1029	17	995	40	**1037**	**16**	105
a20	0.1772	1.52	1.7816	2.77	0.0729	2.32	1052	15	1039	18	1012	47	**1048**	**14**	104
b33	0.1769	1.43	1.8511	2.07	0.0759	1.49	1050	14	1064	14	1092	30	**1057**	**14**	96
b42	0.1939	1.71	2.1010	2.63	0.0786	1.99	1142	18	1149	18	1162	39	**1146**	**16**	98
c19	0.3096	1.97	4.3890	2.61	0.1028	1.71	1739	30	1710	22	1675	32	**1675**	**32**	104
a44	0.3116	1.92	4.5700	3.59	0.1064	3.03	1749	30	1744	30	1738	56	**1738**	**56**	101
b57	0.3404	1.38	5.4690	2.01	0.1165	1.46	1889	23	1896	17	1904	26	**1904**	**26**	99
b14	0.3605	1.24	5.8755	1.47	0.1182	0.78	1985	21	1958	13	1929	14	**1929**	**14**	103
a50	0.3725	1.78	6.2561	2.31	0.1218	1.47	2041	31	2012	20	1983	26	**1983**	**26**	103
a28	0.4020	1.38	6.7835	1.90	0.1224	1.31	2178	26	2084	17	1991	23	**1991**	**23**	109
a32	0.3622	1.77	6.2532	2.84	0.1252	2.22	1993	30	2012	25	2032	39	**2032**	**39**	98
b46	0.3850	2.36	6.9563	2.72	0.1310	1.36	2100	42	2106	24	2112	24	**2112**	**24**	99
c15	0.3694	1.65	6.7492	2.44	0.1325	1.80	2027	29	2079	22	2132	32	**2132**	**32**	95
a59	0.4301	1.32	8.0084	1.84	0.1350	1.28	2306	26	2232	17	2164	22	**2164**	**22**	107
a5	0.4626	1.69	10.3053	3.03	0.1616	2.51	2451	34	2463	28	2472	42	**2472**	**42**	99
b38	0.5590	1.23	13.5783	2.00	0.1762	1.58	2862	28	2721	19	2617	26	**2617**	**26**	109
a51	0.4933	1.65	12.0093	1.84	0.1766	0.81	2585	35	2605	17	2621	14	**2621**	**14**	99
c13	0.5322	1.51	14.9841	1.80	0.2042	0.98	2751	34	2814	17	2860	16	**2860**	**16**	96

Table A-6 Paleozoic paleomagnetic data for autochthonous regions of the Western European Variscan belt (WEVB)

Place Name		Location	Age Range (Ma)	*Period*	D	I	α_{95}	P.Lat.	Reference
Col du Somport	CS	Pyrennees	268-286	Early-Mid Permian	157.5	1.5	4	0.8 S ± 2.0	Cogné, 1987
Viar Intrustions and red beds	VIR	South Meseta (Iberia)	263-296	Early-Mid Permian	153.2	6.3	6	3.2 S ± 3.0	Van der Voo, 1969
Buçaco Red Beds Remagnetization	BR*	N. Portugal (Iberia)	268-291	Early Permian	149	+11	5	5.6 S ± 2.5	Van der Voo, 1969
Atienza Andesites	AA	Central Spain (Iberia)	275-299	Early Permian	159	18.5	5	9.5 S ± 2.5	Van der Voo, 1969
Trégastel-Ploumanac'h Granite	TPG	Trégor (Armorica)	295-306	Carbo-Permian	200	+9	7	4.5 S ± 3.5	Duff, 1979
Group B. Metamorphic	BM	Massif Central (Armorica)	310-320	Mid Carb	249	+7	6	3.5 S ± 3.0	Edel, 1987
Flamanville Granite	FG	Norrmandy (Armorica)	300-340	Carboniferous	203	+14	15	7.1 S ± 7.6	Van der Voo and Klootwijk, 1972
St Malo Dikes	StM	Brittany (Armorica)	313-331	Mid Carboniferous	206	+ 14	4	7.1 S ± 2.0	Perroud et al., 1986b
Group C. Metamorphic	MC	Massif Central (Armorica)	320-335	Mid Carboniferous	301	+24	8	12.6 S ± 4.0	Edel, 1987
Laval Syncline Volcanics and Seds	LVS	Brittany (Armorica)	300-360	Carboniferous	220	-6	12	3.0 S ± 6.1	Edel et al., 1984
Cabo de Peñas Remagnetization	CP*	Asturias (Iberia)	315-352	Carboniferous	178	+19	9	9.8 S ± 4.5	Perroud, 1983
Alba Griotte	AG	Asturias (Iberia)	315-352	Carboniferous	101.8	+13.1	2	6.6 S ± 0.8	Bonhommet et al., 1981
Vosges Greywacke-1	VG1	Germany (Bohemia)	320-360	Mississippian	17.4	2.4	7	1.2 S ± 3.3	Bachtadse et al., 1983
Franconian Chert	FC	Germany (Bohemia)	320-360	Mississippian	201.7	-7.8	10	3.9 S ± 5.1	Bachtadse et al., 1983
Vosges Visean Volcanics	VVV	France (Armorica)	333-348	Early Carb	323	-17	9	8.7 S ± 4.5	Edel et al., 1984
Visean Volcanics	VV	Massif Central (Armorica)	333-352	Early Carb	78	-2	12	1.0 S ± 6.1	Edel et al., 1981
Group D. Metamorphic	DM	Massif Central (Armorica)	350-379	Late Devonian	288	+57	9	37.6 S ± 4.5	Edel, 1987
Vosges Greywacke-2	VG2	Germany (Bohemia)	360-385	Late Devonian	182.5	+22.9	9	11.9 S ± 4.6	Bachtadse et al., 1983
Almaden Dolerites	AD	Extremadura (Iberia)	360-385	Late Devoninan	128	+32	7	17.4 S ± 3.5	Parés & Van der Voo, 1992

Place Name		Location	Age Range (Ma)	*Period*	D	I	α_{95}	P.Lat.	Reference
Franconian Diabase	FD	Germany (Bohemia)	360-397	Mid-Late Devonian	176.9	+28.9	7	15.4 S ± 3.5	Bachtadse et al., 1983
Franconian Limestone	FL	Germany (Bohemia)	385-397	Mid Devonian	190.6	+22.2	12	11.5 S ± 5.8	Bachtadse et al., 1983
San Pedro Red Beds	SP	Asturias (Iberia)	401-421	Early Devonian	113	+34	10	18.6 S ± 5.0	Perroud & Bonhommet, 1984
Pointe de l'Armorique	PA	Armorica	407-416	Early Devonian	222	+35	4	19.3 S ± 2.1	Tait, 1999
Griotte (Pyrennes)	Gr	Pyrennes	411-419	Siluro-Devonian	224	+51	9	31.7 S ± 4.3	Tait et al., 2000b
Holy Cross Ludlowvian Sandstones	HCL	Poland (Bohemia)	418-423	Late Silurian	223.2	+17.1	20	8.7 S ± 10.3	Lewandowski, 1987
Jersey Lamprphyre Dikes	JL	Jersey, UK (Armorica)	400-440	Late Silurian	234	+64	24	45.7 S ± 12.6	Duff, 1980
Barrandian Basin Seds and Volcanics	BSV	Czech Republic (Bohemia)	416-428	Late Silurian	208	-40	6	22.8 S ± 2.9	Tait et al., 1994
Almaden Spillites	AS	Iberia	421-438	Early-Mid Silurian	62	-36	14	20.0 S ± 7.1	Perroud et al., 1991; Parés and Van der Voo, 1992
Thouars Massif	TM	Brittany (Armorica)	435-453	Ordo-Silurian	160	83	7	76.2 S ± 3.5	Perroud and Van der Voo, 1985
Crozon Dolerites	CD	Brittany (Armorica)	438-458	Ordo-Silurian	356	-64	8	45.7 S ± 3.9	Perroud et al. 1983
Cabo de Peñas	CP	Asturias (Iberia)	438-476	Late Ordovician	202	+78	6	67.0 S ± 3.0	Perroud, 1983
Erquy Volcanics	EV	Brittany (Armorica)	472-493	Mid Ordovician	221	+82	11	74.3 S ± 5.6	Duff, 1979
Moulin de Chateaupanne Fm	MC	Brittany (Armorica)	480-486	Early Ordovician	228	+81	6	72.4 S ± 3.0	Perroud et al., 1986
Pont Réan Formation	PR	Brittany (Armorica)	478-488	Early Ordovician	235	+75	7	61.8 S ± 3.3	Cogné, 1988
Holy Cross Arenig Sandstones	HCA	Poland (Bohemia)	478-488	Early Ordovician	197	+77	10	65.2 S ± 5.0	Lewandowski, 1987
Buçaco Red Beds	BR	Portugal (Iberia)	458-523	Cambrian-Early Ord.	208	+78	6	67.0 S ± 3.0	Perroud and Bonhommet, 1981

Age constraints not given in original publications are taken form the compilation of Van der Voo (1992).
*Remagnetization

P.Lat.—corresonding paleolatitude; errors on paleolatitude reported calculated from α95 radius